Scaling of Inorganic Minerals from Potable Water in Appliances and Systems

A thesis submitted

By

Amthal Al-Gailani

Submitted in accordance with the requirements for the degree of Doctor of Philosophy

The University of Leeds

School of Mechanical Engineering

Institute of Functional Surfaces (iFS)

September, 2021

Acknowledgements

First and foremost, I am extremely grateful to my former supervisor, Professor Anne Neville, for her invaluable advice, continuous support, understanding, encouragement, and for giving me the opportunity to carry out my PhD study in the School of Mechanical Engineering. I would like to express my sincere gratitude to Dr Richard Barker and Dr Thibaut Charpentier for their trust, continued support, mentorship, and outstanding advice. I am also grateful to Professor Harvey Thompson for his help in reviewing my thesis.

I would like to appreciate the project sponsors; Philips, Fernox, WLN, and Bekaert, for their financial support and technical contributions towards the success of this project. I would like to extend my sincere thanks to the administrative staff and technicians of the iFS research group for their involvement and contributions, especially Fiona, Tom, Judith, Michael, Jordan, and Ryan. The support I received from my colleagues in the School of Mechanical Engineering was tremendous. A very special thanks to Waleed, Olujide, Alaaeddin, Al-Khateeb, Kabir, Alex, Amir, Hazim, Eniola, and Aran.

My acknowledgement cannot be complete without recognizing the continuous support and encouragement of my mother, father and siblings, without whom I would never have the chance to accomplish any successes.

My deepest appreciation and words beyond gratitude go to my beloved wife, Nadia, who shared this tough time with me. My daughter, Ghina has been a blessing throughout this time. You are my treasures beyond measures.

Abstract

Scale formation has long been a concern in domestic appliances such as electric boilers, steam irons, washing machines, dishwashers, coffee makers and potable water distribution systems in general. Potable water contains a variety of ions prone to precipitate over a range of concentrations depending on water quality and its geographic location. The kinetics and mechanisms of mineral scaling from potable water in the open and closed household systems have received no attention.

The present study aims to gain an understanding of the mechanisms and structure of inorganic fouling from potable water in household appliances conditions. Four experimental setups and methodologies were developed to achieve the work goals, namely boiling static setup, flow visualization rig, flow-evaporation scaling cell, and pressurised flow-evaporation scaling cell. The bulk precipitation in closed systems during pool boiling conditions was evaluated. Then, the surface deposition of inorganic minerals from potable water under the convective heat transfer was investigated. Finally, the effects of water evaporation were examined at various surface conditions, key operating conditions, and water ionic species.

The effects of solution temperature, surface material, surface roughness, evaporation area, water composition, heating and cooling rates on the bulk precipitation and surface deposition in closed systems were investigated using the boiling static setup. The solution temperature promotes the bulk precipitation and the polymorphic transformation from both calcite and vaterite to aragonite. The results also showed that the faster the cooling and heating rates the lower the scaling rate. However, $CaCO_3$ formed in the cooling period was greater than in the heating period.

The inorganic scaling kinetics during the convective heat transfer were studied using a once-through flow visualisation setup through investigating the effects of surface temperature, material, roughness, flow rate and vapour bubbles. The study showed that all parameters, especially vapour bubbles, play a vital role in the scaling kinetics and scale morphology.

The influence of surface temperature, pressure, surface roughness and the ionic species on the fouling mechanism and structure was evaluated during the boiling convective heat transfer using the flow-evaporation scaling cell. The water species examined include sodium, chloride, magnesium, sulphate, total organic carbon (TOC) and zinc. The pressure significantly minimises the fouling resistance as well as the amount of the deposits. However, the impact of different ionic

species varies from negligible to strong. Understanding the kinetics of surface deposition and bulk precipitation of inorganic minerals from potable water allows for better design and development of household appliances and systems.

Publications

1. **Al-Gailani, A.**, Sanni, O., Charpentier, T.V., Crisp, R., Bruins, J.H. and Neville, A., 2020. Inorganic Fouling of Heat Transfer Surface from Potable Water during Convective Heat Transfer. *Applied Thermal Engineering*, 184, p.116271.

2. **Al-Gailani, A.**, Sanni, O., Charpentier, T.V., Crisp, R., Bruins, J.H. and Neville, A., 2020. Examining the Effect of Ionic Constituents on Crystallization Fouling on Heat Transfer Surfaces. *International Journal of Heat and Mass Transfer*, 160, p.120180.

3. **Al-Gailani, A.**, Charpentier, T.V., Sanni, O., Crisp, R., Bruins, J.H. and Neville, A., 2020. Inorganic Mineral Precipitation from Potable Water on Heat Transfer Surfaces. *Journal of Crystal Growth*, 537, p.125621.

4. **Al-Gailani, A.**, Charpentier, T.V., Sanni, O. and Neville, A., 2021. Crystallization Fouling in Domestic Appliances and Systems. *Heat Transfer Engineering*, pp.1-9.

5. **Al-Gailani, A.**, Sanni, O., Charpentier, T.V., Barker, R., Crisp, R., Bruins, J.H. and Neville, A., 2021. Role of Temperature, Roughness and Pressure in Crystallization Fouling from Potable Water on Aluminium Surface. *Thermal Science and Engineering Progress*, 23, p.100911.

Table of Contents

Table of Figures

XIII

XV

XVI

XVII

List of Tables

Nomenclature and Abbreviations

Nomenclature

Symbol	Definition	Units
A	Pre-exponential constant	Nuclei/s.m^3
A and B	Nucleation theoretical time equation constants	
A_H	Hamaker constant	N. m
A_{ij}	Interfacial area	m^2
C	Constant in the shear stress expression	
C_b	Bulk concentration of solute	kg. m^3
C_i	Interfacial concentration of solute	kg. m^3
C_{sat}	Saturated concentration of solute	kg. m^3
D	Diffusion coefficient	m^2. s^{-1}
D_h	Hydraulic diameter	m
d	Average distance between asperities	m
E_a	Activation energy of crystallisation reaction	kJ. mol
E_{ad}	Adhesive energy per surface area	kJ. m^2
F_{ad}	Adhesion force	N
F_{vdW}	Lifshitz-van der Waals forces	N
F_{chem}	Chemical bonding	N
F_H	Hydrogen bonding	N
F_{el}	Electrostatic force	N
F_{wp}	van der Waals force	N. m^{-2}

F_τ	Shear stress	N. m^{-2}
G	Growth rate	kg. m^2. s
ΔG_{Het}	Free energy change coupled with heterogenous nucleation	kJ. mol^{-1}
ΔG^*_{Hom}	Free energy change coupled with homogenous nucleation	kJ. mol^{-1}
ΔG_s	Surface excess of free energy change	kJ. mol^{-1}
ΔG_v	Volume excess of free energy change	kJ. mol^{-1}
ΔH_{vap}	Molar heat of vaporization	kJ. mol^{-1}
I_0	Intensity of incident beam	
I_L	Intensity of transmitted beam	
J	Nucleation rate	Nuclei/s.m^3
K	Proportionality constant	
k_B	Boltzmann constant	m^2 . kg. s^{-2}. K^{-1}
K_{eq}	Equilibrium constant	
K_G	Overall crystal growth coefficient	m^4. kg^{-1} s^{-1}
K_H	Henry's law coefficient	mol. kg^{-1}. kPa^{-1}
K_r	Reaction rate constant	m^4. kg^{-1} s^{-1}
K_{sp}	Solubility product constant	mol^2. dm^{-6}
K_t	Mass transfer coefficient	m. s^{-1}
k_1	First ionisation constant of the carbonic acid	mol. dm^{-3}
K_1	Proportionality factor	
k_2	Second ionization constant	mol. dm^{-3}

l	Optical path length	m
M_a	Amount of mineral scale in absence of inhibitor	mg
M_p	Amount of mineral scale in presence of inhibitor	mg
m_d	Mass deposition rate	kg. m^2. s
m_f	Mass fouling rate	kg. m^2. s
m_r	Mass removal rate	kg. m^2. s
n	Order of crystallisation reaction	
P	Pressure	kPa
Q	Heat flux	W
R	Gas constant	J. mol^{-1} K^{-1}
Re	Reynolds number	
R_f	Fouling resistance	m^2 ^{0}C. W^{-1}
R_f^*	Asymptotic fouling resistance	m^2 ^{0}C. W^{-1}
r_{rms}	Root mean square roughness	μm
S	Salinity	ppt
Sh	Sherwood number	
t	Time	s
T	Temperature	^{0}C
T_b	Solution bulk temperature	^{0}C
T_h	Heater temperature	^{0}C
T_i	Interfacial temperature	^{0}C
$T_{Nucleation}$	Theoretical time of nucleation	s

T_s	Surface temperature	^{0}C
t_λ	Turbidity	FTU
U_f	overall heat transfer coefficient of fouled surface	W. m^{-2} ^{0}C^{-1}
U_o	overall heat transfer coefficient of clean surface	W. m^{-2} ^{0}C^{-1}
v	Overall flow velocity	m. s^{-1}
V	Molecular volume	m^3
x	Distance between the interacting bodies	m
x_f	Fouling layer thickness	m

Greek symbols

Symbol	Definition	Units
σ	Degree of supersaturation	
$\emptyset$	Correction factor of free energy change	
γ_{ij}	Interfacial energy	J.m^{-2}
θ	Contact angle	^{0}
γ	Interfacial energy	kJ. m^2
ψ	Deposit strength	N. m^{-2}
Γ	Removal probability	
$\chi_I, \chi_{II},$ and χ_{III}	Weibull parameters	
ρ	Solution density	kg. m^{-3}
ρ_f	Fouling layer density	kg. m^{-3}
λ_f	Fouling layer thermal conductivity	W. m^{-1}. K^{-1}

Abbreviations

Abbreviation	Definition
A	Calcium carbonate as aragonite
AAS	Atomic absorption spectroscopy
ACC	Amorphous calcium carbonate
BSE	Back-scattered electrons
C	Calcium carbonate as calcite
CA	Contact angle
CCD	Charged couple device
DOM	Dissolved organic matter
EDX	Energy-dispersive X-ray
FESC	Flow-evaporation scaling cell
FE-SEM	Field emission scanning electron microscopes
FTU	Formazin turbidity unit
IAP	Activity product of salt ions
ICP-MS	Inductively coupled plasma mass spectrometry
ICP-OES	Inductively coupled plasma atomic emission spectroscopy
ICSD	Inorganic crystal structure database
LSI	Langelier Saturation Index
M	Magnesium carbonate as magnesite
NOM	Natural organic matter
P	Magnesium oxide as periclase

PFESC	Pressurised flow-evaporation scaling cell
PID	Proportional–Integral–Derivative
PVS	Polyvinyl sulfonate
Ra	Arithmetical mean roughness value
RDC	Rotating disk crystalliser
RSI	Ryznar Stability Index
S	Anhydrite calcium sulphate
SE	Secondary electrons
SEM	Scanning electron microscope
SI	Saturation index
SR	Saturation ratio
TA	Total Alkalinity
TOC	Total organic carbon
V	Vaterite
XRD	X-ray diffraction

Subscript/superscript

Abbreviation	Definition
1	Initial state
2	Final state
b	Bulk
c	Clean surface
f	Fouled surface
i	Interface
s	Surface

Chapter 1: Introduction

Water heating/boiling is essential in different household appliances and systems, it is also involved in different industries such as the downstream oil and gas industry, power plants, water desalination and the food industry. The demand for water heating facilities and systems has increased due to the increase in population and standard of living. However, water heating is accompanied by several inevitable challenges that appear as very serious threats to the sustainability of systems. The most common issues in similar systems are inorganic fouling, corrosion fouling and biological fouling [1]. All types of fouling are responsible for increasing power consumption due to retarded heat transfer efficiency and reduced flow area [2].

Inorganic fouling or scale is diverse, complex, long-term and the second most common type of fouling after corrosion deposits. It is the formation of unwanted deposits either on the heated surfaces in contact with the solution or bulk fluid and occurs as a consequence of the supersaturation of salt. The formation of inorganic scale is thermodynamically possible when the aqueous solution is supersaturated with one of the sparingly soluble salts such as calcium carbonate ($CaCO_3$), calcium hydroxide ($Ca(OH)_2$), lithium carbonate (Li_2CO_3), sulphate salts of calcium, magnesium hydroxide ($Mg(OH)_2$), magnesium oxide (MgO), barium sulphate ($BaSO_4$) and calcium oxalate (CaC_2O_4) [3]. The formation of each salt depends on water composition and operating conditions. $CaCO_3$ fouling is the most frequent form of scale in a wide range of industrial processes which deals with water as a working fluid [4].

Fouling from water is classified into two categories, namely, surface deposition and bulk precipitation. In order to predict and mitigate fouling in a system, an understanding of the mechanisms and kinetics of scale formation should be achieved based on water composition, operating conditions and surface material [5]. Inadequate attention to fouling impact in the earliest stages of the design of heat transfer equipment may lead to serious consequences. These deposits increase the resistance to heat transfer and reduce the flow area of the working fluids in industrial, commercial and domestic systems [6-9]. The increasing resistance to heat flow and the high system pressure drop increases the energy consumption, pumping cost and maintenance cost, and lower the durability of the system [10, 11].

Studies of inorganic scaling have focused on four aspects, namely; kinetics and mechanism, morphology, inhibition and removal of deposits [12]. The investigation of the fouling mechanism, which is the first step in a way to mitigate fouling, allows us to predict the impact of fouling at different conditions. Moreover, understanding kinetics may contribute to controlling or inhibiting scale formation in a system. In the second step, examining the structure and composition of the fouling layer using various techniques provides essential information for the inhibition step in which chemical and physical methods can be employed [13].

Preventive means such as the addition of chemicals, surface modification, external techniques can be used to mitigate scale formation [14]. Scale build-up may lead to a complete shutdown of a system, therefore, the search for an efficient technique for the removal of deposits has been of interest for researchers [15]. Investigating the above four aspects might be necessary to control inorganic scaling.

1.1. Crystallisation fouling in domestic appliances

Fouling has long been a concern in domestic appliances such as electric boilers, gas boilers, steam irons, washing machines, dishwashers, coffee makers and potable water distribution systems in general. In the report of the Water Quality Research Foundation (WQRF) [16], it is estimated that the heat transfer efficiency of instantaneous gas water heaters is reduced by 30% over a 15-year lifecycle if hard water is used. Scale build-up on the metallic surfaces of such appliances diminishes the heat transfer and increases the power needed to fulfil the desired performance. The deposition of inorganic salts can also result in reduced flow area which can lead to the failure of the domestic devices subjected to fouling. Moreover, the precipitation of salts in the bulk solution also affects the quality of the produced water such as taste and colour [17].

Figure 1.1 shows a washing machine heater at 60 °C and 95 °C after 300 cycles of washing. The formation of inorganic scale in household appliances is a persistent problem owing to the severe conditions and water composition. The temperature in these appliances is usually high enough to make the mineral scaling thermodynamically favoured. In some devices, water evaporation is a common practice leading to unavoidable mineral scaling. The fouling phenomenon in domestic systems is also attributed to pressure, flow rate and surface substrate. Secondly, potable water and surface water contain a variety of ionic species that contribute to the formation of different types

of inorganic deposits in water distribution systems and domestic appliances. The composition and quality of potable water vary based on geographic location [18].

Figure 1.1. Washing machine heaters at 60°C (Left) and 95°C (Right) [19].

The heating of water in some household appliances is a complicated process allowing deposits to form on the surface and in the bulk solution. An Espresso machine provides hot water and steam from two different outlets, the brew water and steam are supplied from a heat exchanger and boiler, respectively, as shown in Figure 1.2. In the boiler, the minerals tend to adhere to the heating element and boiler surface, while scaling forms in the bulk solution, on the inner and outer surfaces of the heat exchanger. This reduces the heat flow from the heating element to water and increases the pressure drop of the system.
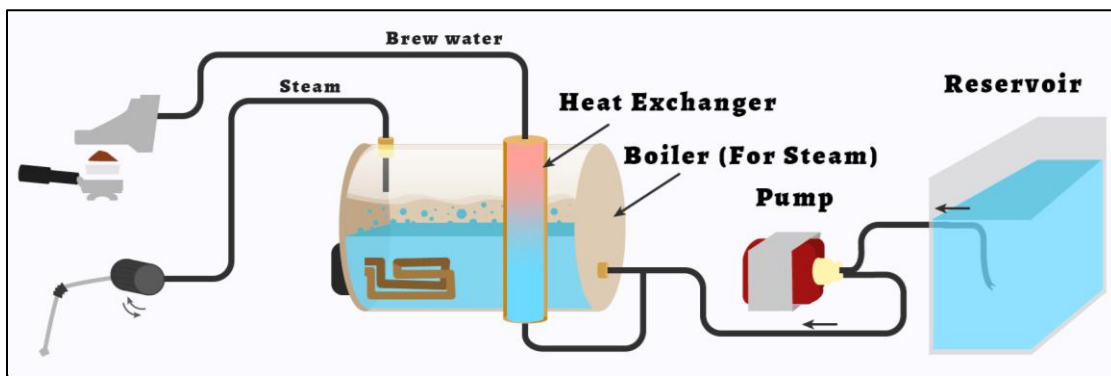
Figure 1.2. A basic representation of an Espresso machine [20].

The type of inorganic mineral formed in household systems depends on water composition. $CaCO_3$ is the common type of scale due to the abundance of calcium in potable water and its low solubility [21]. The formation of magnesium salts is likely from the water with a high content of magnesium. The composite fouling layer of different inorganic salts may also be observed on the heat transfer surface of domestic devices. Therefore, the structure and composition of deposited salt should be investigated to nominate a suitable mitigation technique.

1.2. Research background

To achieve a full understanding of deposits formation in domestic appliances, two research aspects need to be taken into account. The mechanism and kinetics of inorganic fouling is the first aspect that has been investigated in this work. The study of scale adhesion on the surface and potential mitigation methods is the second aspect that should be considered for future work. The first aspect involves the mechanism of surface deposition and bulk precipitation accounting for the following important elements:

- Complete and partial evaporation of water.

- Water composition.

The investigations began with a study of bulk precipitation from potable water in a closed system where no solution flow. The effects of substrate properties, key operating conditions and water composition on the kinetics of precipitation were examined. Simple domestic appliances adopt closed systems for economic and operational considerations. Water heating and cooling rates could also affect the amount of precipitated scale in closed systems. The effect of these parameters on crystallisation fouling associated with water evaporation has received little attention.

The effect of water flow plays a significant role in surface deposition and removal. Flow shear stress enhances the removal rate of scale crystals from the heated surface [22], the higher the flow velocity the lower the resistance to heat transfer [23]. However, the increase of flow velocity promotes the deposition rate of $CaCO_3$ when the flow Reynolds number ranges from 1,457 to 29,135 in a rotating cylinder electrode setup [24]. The influence of flow on the surface deposition was introduced using a once-through in-situ visualisation flow rig system while the amount and morphology of scale were monitored for different conditions.

4

The partial evaporation of water alongside surface fouling mimics the operation of household appliances. Heating the aluminium surface to the water boiling point allows the flowing potable water to partially evaporate. The evaporation and boiling conditions affect the local supersaturation in the vicinity of the surface. The presence of steam bubbles on the surface influences the fouling mechanism [25]. Fouling resistance is a common approach to determine the impact of deposits on heat transfer [26]. The resistance to heat transfer increases with time as a result of mineral deposition. However, the change rate of the fouling resistance and the asymptotic fouling resistance value is dependent on water constituents as well as the key conditions.

The operating conditions include surface temperature, bulk temperature, flow rate and pressure. The surface properties tested are the material and roughness of the surface. Regarding water composition, the effects of the most abundant constituents in potable water have been evaluated. Other parameters are the heating rate, cooling rate and evaporation rate. The kinetics information obtained from all experimental apparatuses can be combined with the morphology data for elaborating the inorganic fouling mechanism in household appliances.

1.3. Aims and objectives

This work aims to gain an understanding of the kinetics and structure of inorganic fouling from potable water in household appliances conditions. The research objectives are described below:

- To design and build a closed system setup and accompanying analysis protocols that enable the evaluation of bulk precipitation of composite scale followed by deposition on the metallic surface. The influence of key operating conditions, surface material, water ionic constituents, heating rate and the cooling rate will be studied on the kinetics of scale formation in the bulk solution.

- To investigate the surface deposition of inorganic salts from potable water under convective heat transfer in a once-through in-situ visualisation system.

- To develop a once-through Pressurised Flow-Evaporation Scaling Cell that allows the fouling of the heat transfer surface to be examined in a pressurised environment.

- To establish the influence of water evaporation in a Flow-Evaporation Scaling Cell under different surface conditions, operating conditions, and water ionic species.

The aim of the research can be achieved by addressing the specific objectives mentioned above. Figure 1.3 shows a representation of the research overview.
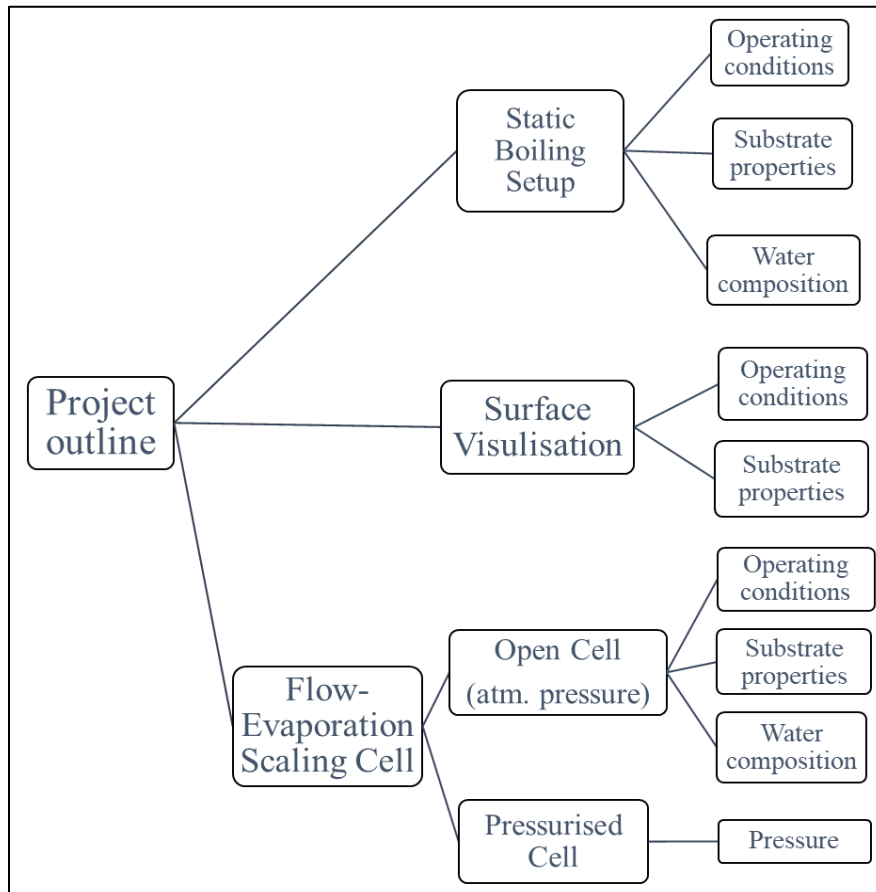
Figure 1.3. Schematic of a research outline.

1.4. Thesis outline

This work has been presented in ten chapters covering all research aspects as summarised below:

- An introduction of inorganic fouling in the domestic and industrial system is given in the first Chapter. Overview of scale formation in bulk solution and on the heat transfer surface in domestic appliances is highlighted. Chapter one also states the research aspects covered in the present work.

- Chapter two illustrates the theory behind crystallisation fouling and the consecutive processes which lead to mineral deposition. An insight into the relationship between water chemistry and deposited minerals and their morphology is given.

- A detailed literature review on crystallisation fouling mechanisms, morphology, affecting factors and mitigation techniques for different mineral deposits is given in the third chapter.

- The development of apparatuses and setups used in the research is described in Chapter four. This chapter also illustrates the purpose, design, inline analysis technique and working principle of each setup.

- Chapter five presents the methodology of experimental work done by each setup. The experimental methodology includes materials, solution preparation, conditions and procedures for all experiments. The post-experiment surface and solution characterisation methods are also given in the fifth chapter.

- The experimental findings of bulk precipitation and surface deposition in batch systems are shown in Chapter Six. The effect of different operating conditions, material properties and water chemistry on mineral scaling in closed systems is presented.

- Chapter Seven shows the results of surface crystallisation assessments in a once-through flow system. The surface deposition is examined for different conditions under subcooled flow boiling with no evaporation.

- Chapter Eight presents the outcomes from surface deposition during subcooled flow boiling with partial evaporation in a once-through flow system. The results showed the influence of key operating conditions, substrate and ionic constituents in the water on the scale build-up on the surface.

- Chapter Nine gives an overall discussion that links the experimental results to obtain a full understanding of inorganic fouling in different systems. The present results are also discussed with reference to the reported studies in the literature.

- Research conclusions, general synopsis and future work are given in Chapter Ten.

1.5. Summary

The present study is devoted to investigating the kinetics of inorganic fouling from potable water. The surface deposition and bulk precipitation of composite crystallisation fouling have been evaluated. The kinetics of scale formation and morphology of deposit crystal can be affected by operating conditions, design parameters and water chemistry. The aim and objectives of the study

were achieved through sets of experiments carried out in different experimental setups. The kinetics data were linked to scale structure and morphology for a better understanding of the fouling.

In this chapter, a general introduction to inorganic mineral scaling on the heat transfer surface is given. The crystallisation fouling in domestic appliances and systems is then described. It has been admitted that the complex chemistry of potable water and the extreme operating conditions are the main challenges that may face the mitigation efforts. It has been also explained the strategy followed to achieve the study goals.

Chapter 2: Theory

2.1. Crystallisation fouling

Crystallisation fouling of heat transfer surfaces coupled with heating water in domestic and industrial heat exchangers has been a long concern. The formation of minerals process includes different steps that occur in series and/or in parallel. Each step starting from the supersaturation of minerals to the removal of crystals from the surface has been reported in the literature according to theoretical models. The steps, which lead to scale formation, vary depending on the conditions. For instance, heterogeneous nucleation is the dominant nucleation in the presence of foreign particulates in the solution [27]. Also, the removal step of deposited particles becomes pronounced as the flow velocity increased [22, 28].

Bott [29] mentioned that the general sequence of steps that end with mineral deposition is supersaturation, nucleation, and crystal growth. However, the adhesion and removal of fouling particles are added to Bott [29] fouling process events. Figure 2.1 shows a schematic of the overall crystallisation fouling process and the sequence of events. The steps and their sequence can be predicted, nevertheless, it is challenging in some systems. Mineral formation on heat transfer surface might occur by two potential paths; homogenous nucleation and growth in the bulk fluid followed by adhesion of crystals to the surface or heterogenous nucleation, growth and adhesion to the surface [6, 30].

The fouling process steps and overall mechanism depend on the operating conditions and surface material. For instance, using a non-metal heat transfer surface such as glass or silicon carbide retards the heterogeneous nucleation and growth on the surface [31]. However, in the same system, the scale may form in the bulk solution by homogenous nucleation due to high supersaturation [32]. Similarly, the adhesion of crystals, which either form in the bulk fluid or on the surface, is dependent on the substrate nature and properties [33].
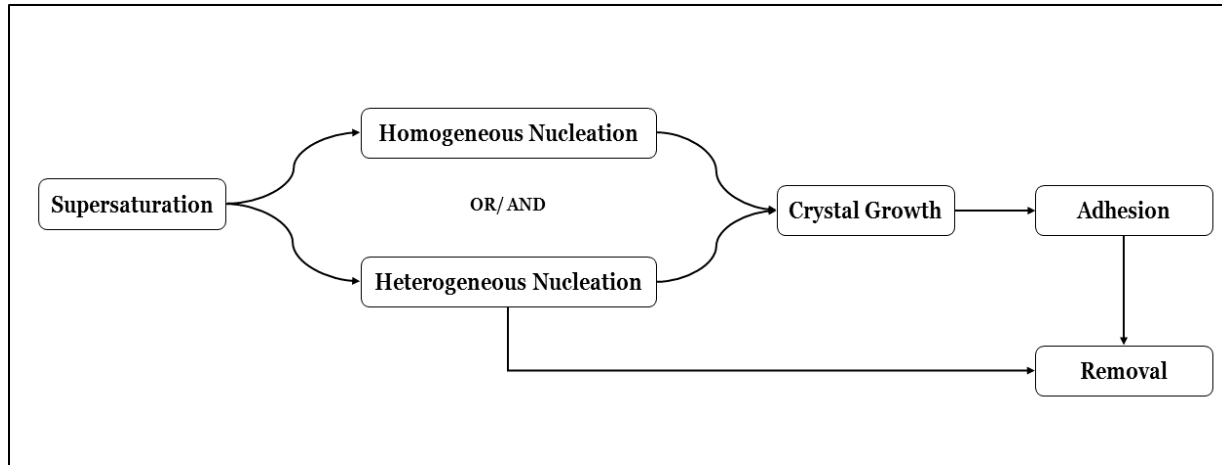
Figure 2.1. A schematic of the crystallisation fouling process.

2.1.1. Supersaturation

The dissolved ionic species in water crystallises in mineral salt form when solubility is exceeded due to different conditions. The majority of mineral salts have a normal solubility-temperature relationship in which the higher the temperature the higher the solubility in water [34]. The precipitation of these salts is expected at low-temperature applications. However, the salts, which have an inverse solubility-temperature relationship, are known as sparingly soluble materials; so, the temperature reduces the solubility and increases the rate of crystallisation [35]. The dissolved minerals start crystallisation when a solution is been supersaturated [5]. Figure 2.2 illustrates the solubility constant of common minerals as a function of temperature.
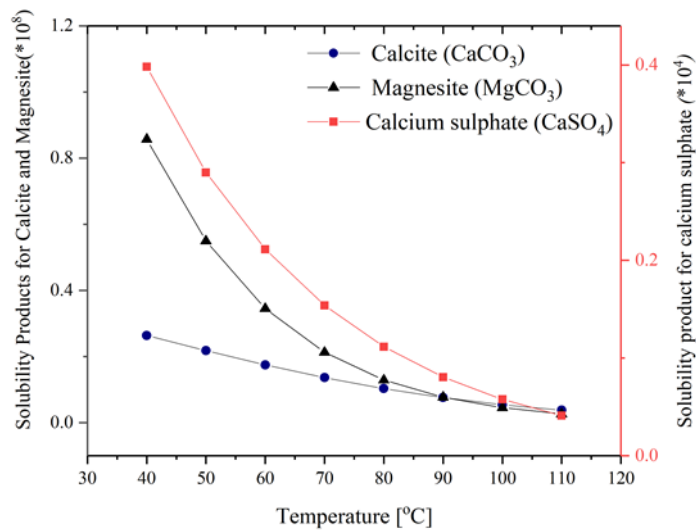
Figure 2.2.The solubility of CaCO$_3$, MgCO$_3$ and CaSO$_4$ as a function of temperature [36].

10

Supersaturation is a thermodynamic driving force for crystallisation fouling. Supersaturation of mineral salts in an aqueous solution is brought about through the concentration of water constituent ions, pressure and temperature variations, or by manipulating the water chemistry [37]. Supersaturation is a measure of scaling thermodynamic tendency of a solution, which can be expressed in terms of saturation ratio (SR) as a ratio of activity of dissolved ions to solubility constant of mineral salt. Table 2.1 shows the criteria of scale formation based on the value of SR with respect to a salt.

$$SR = \frac{IAP}{K_{sp}} \qquad (2.1)$$

Where, IAP is activity product of salt ions and K_{sp} is the solubility product constant. The ionic activity product is a function of the actual concentration of fouling ions.

Table 2.1. Prediction of solution saturation based on SR value.

SR>1	The solution is supersaturated corresponding to the thermodynamic possibilities of salt and scale formation.
SR=1	The solution is saturated, crystallisation and dissolution of fouling particles simultaneously occur at the same rate.
SR<1	The solution is under-saturated, fouling particles are likely to dissolve with no tendency for scaling.

The solubility product constant is a temperature-dependent parameter [38, 39]. Other parameters may influence the supersaturation such as solution pH and partial pressure of carbon dioxide (CO_2) through effecting the chemical equilibria leading to deposits formation [40, 41]. The supersaturation is also given in terms of the degree of supersaturation (σ) which corresponds to the natural logarithm of saturation ratio:

$$\sigma = \ln(SR) \qquad (2.2)$$

Regardless of salt solubility in water, Bott [42] summarised the conditions that may lead to supersaturate the solution and hence cause salt to crystallise: (1) mixing of saturated solutions of

common ions, (2) addition of water-soluble salt to saturated solution, (3) evaporation of water, and (4) dissolution of gas (e.g. CO_2) in water from the atmosphere. Solution supersaturation has been employed in a model to predict the rate of precipitation and the rate of crystal growth [43, 44]. However, the prediction model is valid for a batch system where a scaling fluid is being circulated. In such a system, the supersaturation decreases with time until reaching the chemical equilibrium between the scaling species.

2.1.1.1. *Mineral solubility and formation equilibria*

Several inverse solubility salts can form in domestic and industrial heat exchangers corresponding to the composition of potable and surface water. The possibility of salt deposition in a system is related to the concentration of ionic species that composes the salt and solubility of the salt. However, the solubility of salt varies with temperature and the presence of impurities [45, 46]. For the inverse solubility salts, the concentration of dissolved salt decreases during the heating, as shown in Figure 3.2.
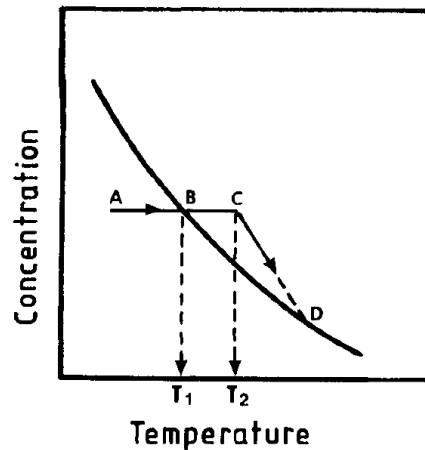
Figure 2.3. The concentration of sparingly soluble salt during heating [42].

The impact of salt solubility on the supersaturation and fouling process is expressed in terms of the solubility product constant (Eq^n 2.1). Researchers have proposed numerical correlations to estimate the solubility constant for common inversely soluble minerals [38, 39, 47].

Table 2.2. The solubility product constant of common scales

Mineral (crystalline form)	Solubility constant (K_{sp}) correlation	Ref.
Calcium carbonate (calcite)	$\log K_{sp} = -171.9065 - 0.077993\,T + \dfrac{2839.319}{T} + 71.595 \log T$	[38]
Calcium carbonate (aragonite)	$\log K_{sp} = -171.9773 - 0.077993\,T + \dfrac{2903.293}{T} + 71.595 \log T$	[38]
Calcium carbonate (vaterite)	$\log K_{sp} = -172.1295 - 0.077993\,T + \dfrac{3074.688}{T} + 71.595 \log T$	[38]
Magnesium carbonate (magnesite)	$\log K_{sp} = 7.267 - 0.033918\,T - \dfrac{1476.604}{T}$	[39]
Calcium sulphate (gypsum)	$\log K_{sp} = 390.9619 + 0.0818493\,T - \dfrac{12545.6}{T} - 152.6246 \log T$	[47]
Calcium sulphate (anhydrite)	$\log K_{sp} = -215.509 - 0.070707\,T + \dfrac{6075.2}{T} + 85.685 \log T$	[47]

Another important parameter that may affect the supersaturation of salt in water and scale formation is the ionic activity product, in other words, foulants concentration. Taking as an example, $CaCO_3$ is the dominant scale formed in domestic and industrial heat exchangers due to low solubility and abundance of calcium (Ca^{2+}), bicarbonate (HCO_3^-) and carbonate (CO_3^{2-}) ions in water [48]. The $CaCO_3$ forms when Ca^{2+} reacts with either CO_3^{2-} or HCO_3^-. The crystallisation reaction of $CaCO_3$ is sensitive to pH and CO_2 partial pressure, which both could affect the equilibria of $CaCO_3$ formation [49, 50], as presented below:

$$CO_{2\,(g)} + H_2O \leftrightarrow H_2CO_{3\,(aq)} \qquad\qquad K_{eq} = 1.3 \times 10^{-3} \qquad\qquad (2.3)$$

$$H_2CO_{3\,(aq)} \leftrightarrow HCO^-_{3\,(aq)} + H^+ \qquad\qquad K_{eq} = 4.60 \times 10^{-7} \qquad\qquad (2.4)$$

$$HCO^-_{3\,(aq)} \leftrightarrow CO^{2-}_{3\,(aq)} + H^+ \qquad\qquad K_{eq} = 5.14 \times 10^{-11} \qquad\qquad (2.5)$$

$$Ca^{2+} + CO^{2-}_{3\,(aq)} \leftrightarrow CaCO_3 \qquad\qquad K_{eq} = 2.1 \times 10^{8} \qquad\qquad (2.6)$$

$$Ca^{2+} + 2HCO^-_3 \leftrightarrow CaCO_{3(s)} + CO_{2\,(g)} + H_2O \qquad\qquad (2.7)$$

Solution pH enhances the transformation of dissolved CO_2 to HCO_3^-, then HCO_3^- to CO_3^{2-}, and eventually greater activity product and supersaturation (see Figure 2.4). The $MgCO_3$ formation rate is also dependent on carbonate equilibria. The formation of $MgCO_3$ and $CaSO_4$ are described by the following reactions:

$$Mg_{(aq)}^{2+} + 2HCO_{3\ (aq)}^- \leftrightarrow MgCO_{3\ (s)} + CO_{2\ (g)} + H_2O_{(l)} \tag{2.8}$$

$$Ca_{(aq)}^{2+} + SO_{4\ (aq)}^{2-} \leftrightarrow CaSO_{4\ (s)} \tag{2.9}$$
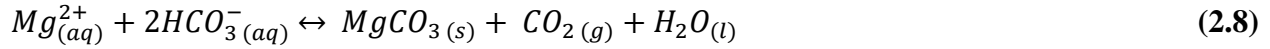
According to the reactions stated above (Eq[n] 2.6 to 2.9), the formation of inverse soluble salts may simultaneously take place either on the heat transfer surface or in the bulk solution. The solution could be supersaturated with more than one mineral salt at the same time as a result of temperature rise and concentration increase, therefore, leading to the formation of a composite fouling layer in some systems [51].
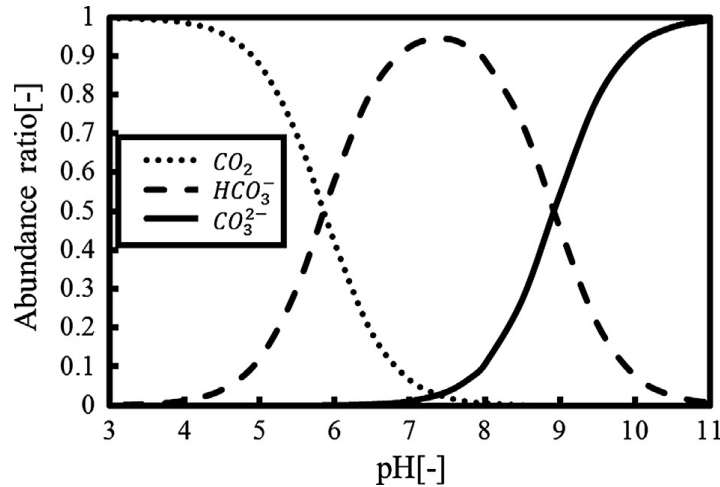
Figure 2.4. The abundance of scale species as a function of solution pH [52].

2.1.2. Fouling periods

The crystallisation fouling process is divided into two periods of time, which are experimentally identified. The first period lies between supersaturation attainment and the formation of stable crystalline nuclei, either by homogeneous or heterogeneous nucleation. This period is recognised as the "Induction period". In the following period "fouling period", the stable nuclei grow to visible

crystals forming a compact scale layer [5, 53]. Figure 2.5 presents fouling process periods regarding fouling resistance change with time. The fouling resistance was a measure of heat transfer retardation introduced by scale deposits. It can be determined using surface temperature, bulk temperatures, and heat flux.
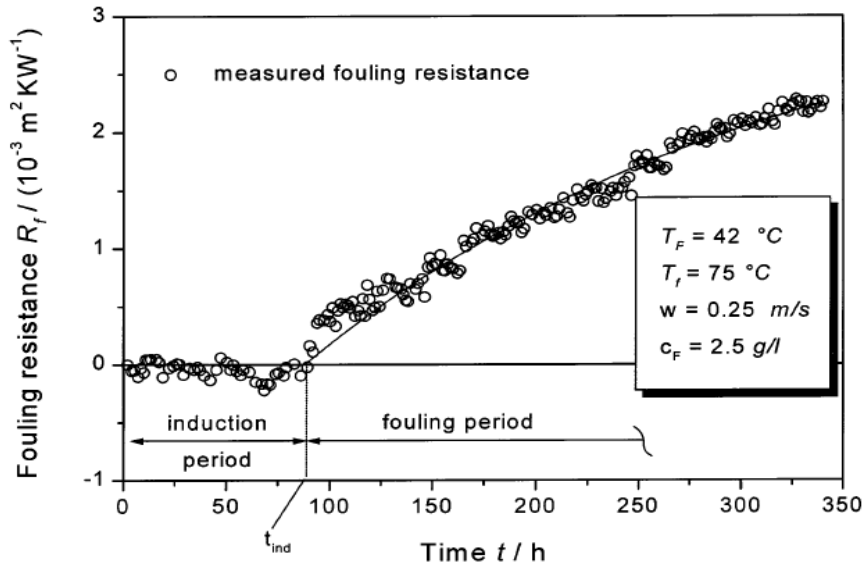
Figure 2.5. Measured fouling resistance with time for an aqueous CaSO₄ solution [54].

2.1.2.1. Induction period

The induction or initiation period, the first-time stage of the fouling process, has been defined in different ways based on research outcomes. The elapsed time until the first appearance of crystalline nuclei at the heat transfer surface is the induction time [55]. Harouaka, et al. [56] mentioned that the induction time is the time in which $CaCO_3$ crystals becomes detectable by various experimental techniques. In the field of crystallisation, Mullin [57] described induction time as the metastable state of supersaturated aqueous solution where spontaneous nucleation is not favourable. However, recent research pointed out that in the induction period, small discrete nuclei form at localised sites and lateral growth to stable large particles which does not cover the entire surface [58-60].

The heat transfer is not significantly decreased in the induction period, quite the contrary, the heat flow could be improved, represented by the negative fouling resistance in figure 1.5 [61]. Bohnet [30] demonstrated that the negative values for the deposition rate reveal an improved heat flow

compared to the clean surface, which might be caused by turbulent flow over the rough fouling layer. The approach of induction period prolongation, therefore, could be one of the modern anti-fouling strategies. Since both deposition and removal processes occur in that period, the length of induction time depends on the parameters that affect these processes [62, 63]. The end of crystallisation fouling induction interval could be experimentally detected through observing changes in some physical properties, e.g. turbidity, solution pH, conductivity, crystals appearance on the surface, and the surface temperature rising [5].

2.1.2.2. Fouling period

Once the induction period ends, the post-induction period or layer growth period starts, where the heat transfer efficiency of the system significantly drops due to the impact of fouling build-up [64]. Over time, the scale layer becomes tenacious and less porous, resulting in increased fouling thermal resistance [65]. The behaviour of fouling resistance in this period relies on the rates of removal and deposition. The amount of deposits on the heated surface is influenced by the removal of scale particles from the surface, hence altering fouling layer resistance to heat transfer. The fouling period is divided into regions, steady growth and plateau steady state. In a steady growth region, a competition between deposition and removal processes occurs until the removal rate approaches the deposition rate, so the plateau steady-state begins. No pronounced change in the fouling resistance and deposit thickness is observed in the plateau steady-state (or asymptote) zone [42]. Mayer, et al. [63] presented in figure 2.6 the possible trends of fouling thermal resistance.
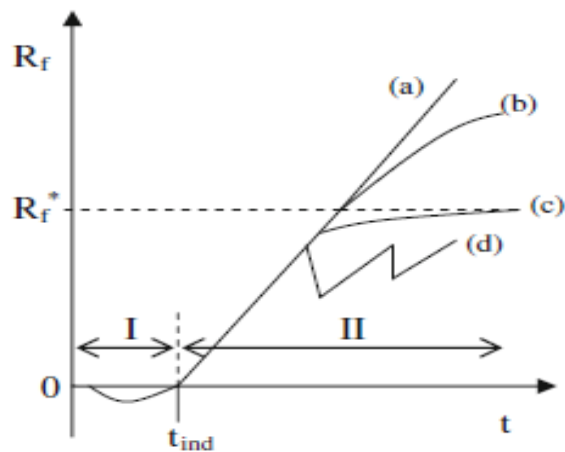
Figure 2.6. Trends of Fouling thermal resistance over time: (a) no removal, (b) Removal effect, (c) asymptotic fouling resistance, (d) saw teeth shape: removal of large fouling particles [63].

16

When scale building attains asymptotic behaviour, the fouling layer could include more than one crystal lining. Each sub-layer may differ from others in density, porosity, thermal conductivity, morphology, thickness, deposition rate and propensity to be removed by flow [66, 67]. The successive sub-layers are mostly weaker than the initial one which is bound directly to the surface due to the higher crystals-surface adhesion strength [68].

2.1.3. Nucleation

Nucleation in the crystallisation fouling is divided into heterogeneous and homogeneous nucleation. As a result of different mechanisms, there are several variances between the heterogeneous and homogeneous nucleation regarding supersaturation degree, crystal size, morphology and adhesion force [35, 69, 70]. Nucleation is also classified based on the host surface into primary and secondary nucleation. By primary nucleation, the nucleus is directly created from the solution for the homogeneous nucleation or on the solid surface for the heterogeneous.

Once scale particles forms, the creation of further nuclei can be induced by the existing crystals on the surface or bulk solution rather than a solid surface, this category is termed "Secondary nucleation" [57]. The resulting foreign crystals can lower the energy barrier in the secondary nucleation and accelerate the process. On the heat transfer surface, the fouling sub-layers form over the first layer results in the secondary nucleation, attrition of existed crystals, then the transport of the portions and finally their growth [71]. The fragments of main crystals may diffuse through the solution to other locations and grow to their parent's size. The secondary nucleation on the surface plays a vital role in doubling the scale thickness several times [72]. Figure 2.7 illustrates the types of crystallisation nucleation.
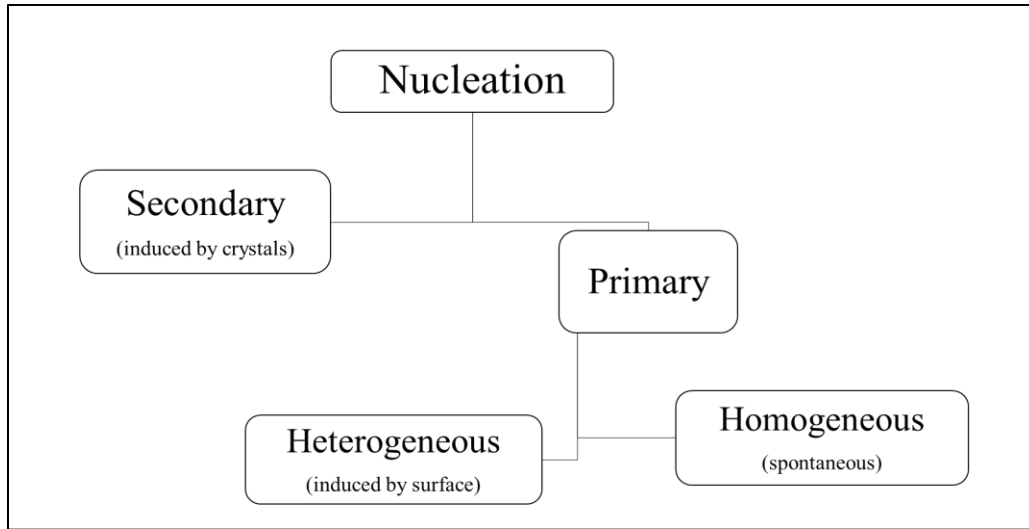
Figure 2.7. Types of crystallisation nucleation

2.1.3.1. Heterogeneous nucleation

The surface deposition process incorporates some steps, nucleation, growth, and attachment to the heat transfer surface. First, divalent metal cations like Ca^{2+} and anions such as CO_3^{2-} immigrate to liquid–crystal interface on the heated surface. As the surface temperature is greater than the bulk solution, a chemical reaction between foulants occurs to form $CaCO_3$ molecules [22, 73]. Bansal, et al. [74] revealed that the scale fouling could be controlled by mass transfer of ionic species, crystallisation reaction or a combination of both, relying on the key operating conditions. The ordering process of these molecules into the crystal lattice on the pre-existing surface is known as "heterogeneous nucleation". The salt molecules are absorbed into the active nucleation site of the hot surface [25, 75]. The heterogeneous nucleation is followed by crystal growth to the stable and visible crystal with different polymorphisms. Figure 2.8 illustrates the overall process of the scale surface deposition and the common $CaCO_3$ forms.
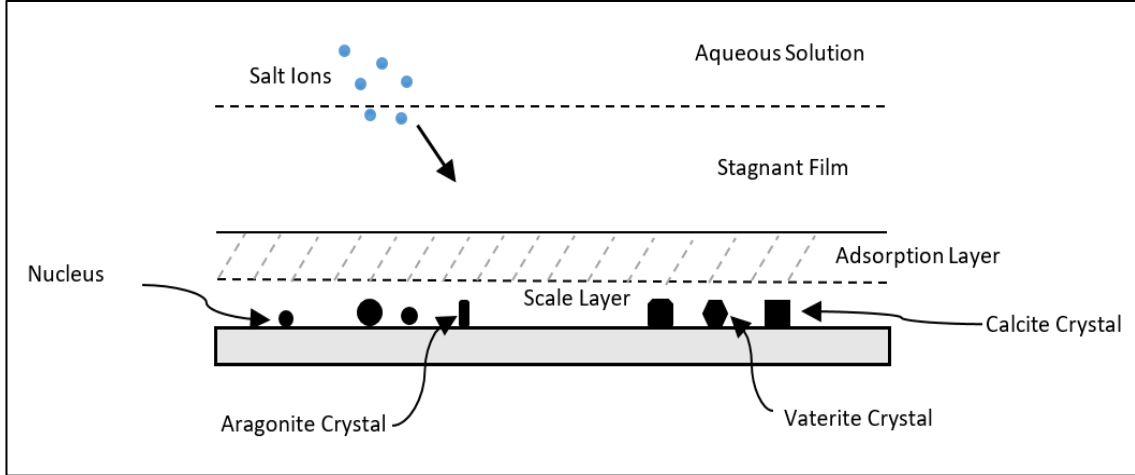
Figure 2.8. Schematic illustration of the surface deposition process.

The presence of a solid surface, including the surrounding surface and seeds, can significantly lower the energy barrier for nucleation occurrence on the surface (classical nucleation theory) [76]. In addition to operating conditions, the nucleation rate is closely related to surface characteristics. The kinetic model describes the nucleation rate (J) is given as

$$J = A \exp\left(-\frac{\Delta G_{Het}^*}{K_B T}\right) \qquad (2.10)$$

Where k_B is the Boltzmann constant, T is the temperature, A is a pre-exponential constant and ΔG_{Het} is the change of free energy during the heterogeneous nucleation, the greater the ΔG_{Het}; the higher the energy barrier needs to be beaten to achieve the first nucleus [77, 78]. The value of the energy barrier for the system can be determined by the summation of the product of the interfacial area A_{ij} and interfacial energies γ_{ij} between each of surface, crystal and liquid, as follow:

$$\Delta G_{Het}^* = \sum A_{ij} \gamma_{ij} \qquad (2.11)$$

Three interfacial free energies control the energy barrier of the heterogeneous nucleation; surface-liquid solution (γ_{sl}), surface-crystal nucleus (γ_{sc}) and crystal nucleus-liquid solution (γ_{cl}), as presented in figure 2.9. The contact angle (θ) between the crystal nucleus and surface outlines the thermodynamic equilibrium, as stated by Young equation (Eq^n 2.12).

$$\gamma_{sl} = \gamma_{sc} + \gamma_{cl} \cos\theta \qquad (2.12)$$

19
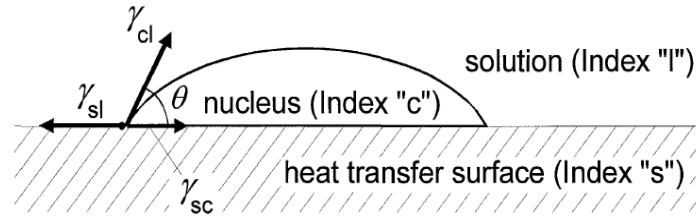
Figure 2.9. Interfacial energies during the formation of the nucleus.

2.1.3.2. Homogeneous nucleation

This phenomenon occurs less frequently than the heterogeneous nucleation due to the higher energy barrier. The absence of a nucleation agent and pre-existing surface hinders the spontaneous formation of deposit nuclei, therefore, requiring higher supersaturation concentration compared to surface heterogeneous nucleation. [79]. The kinetics of homogeneous nucleation is presented in the literature based on two theories: classical and non-classical nucleation (Fig. 2.10). According to the classical theory of nucleation, the formation of nanoscale nuclei can spontaneously occur if the system overcomes the energy barrier which is merely represented by the solution supersaturation [69].

In the non-classical theory, nuclei formation follows two common mechanisms; stepwise phase transition and aggregation, in which pre-critical nuclei (solute species) are colliding and binding themselves together to form a more stable aggregate [80, 81]. The aggregation process becomes more favourable when a large number of the pre-critical nuclei collides with a collision rate much higher than their dissolution rate [10]. The stepwise phase transition is believed to be one of the nucleation paths, which involves the conversion of mineral lattice ions to an amorphous phase, then the later yields a more stable crystalline phase of like calcite and magnesia [82, 83].
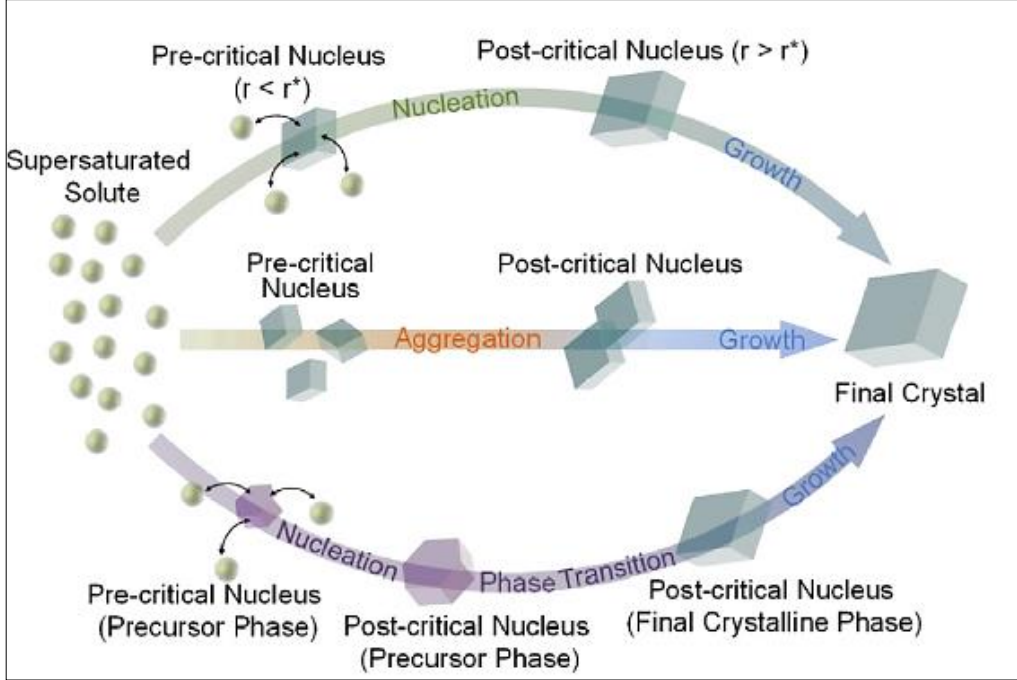
Figure 2.10. Schematic drawing of possible nucleation routes, top path shows the classical theory, then the middle and bottom routes represent aggregation and phase transition, respectively [10].

Similar to heterogeneous nucleation, the change in free energy coupled with homogenous nucleation (ΔG^*_{Hom}) is the energy barrier against the transformation of solute to solid particle [84]. The ΔG^*_{Hom} is estimated from the summation of components; the surface excess of free energy, ΔG_s, (positive component) and the volume excess of free energy, ΔG_v, (negative component):

$$\Delta G^*_{Hom} = \Delta G_s + \Delta G_v \qquad (2.13)$$

The ΔG_v is proportional to the supersaturation ratio (S) of the solution, therefore the homogeneous nucleation rate (J) is supersaturation dependent:

$$\Delta G_v = -\frac{K_B T \ln S}{v} \qquad (2.14)$$

Where, v is the molecular volume. During the process, the excess of free energy attains the critical maximum free energy change, ΔG^{crit}_{Hom}, that is corresponding to the critical nucleus radius. The tendency for nucleus formation in the bulk solution increases with ΔG^{crit}_{Hom} decrease. The excess free energy corresponding to heterogeneous nucleation, ΔG^{crit}_{Het}, is linked to ΔG^{crit}_{Hom} through applying the correction factor, Ø, that is a function of contact angle (θ) [53]:

$$\Delta G_{Het}^{crit} = \emptyset \, \Delta G_{Hom}^{crit} \qquad\qquad (2.15)$$

And
$$\emptyset = \frac{(2+\cos\theta)(1-\cos\theta)^2}{4} \qquad\qquad (2.16)$$

Fouling of industrial heat exchangers is unlikely to be attributed to homogeneous (spontaneous) nucleation as the working fluids of these systems are usually associated with solid particulate impurities which act as heterogeneous nucleation sites [85]. Besides the solution impurities, other solid species are considered as crystallisation seeds such as corrosion products [86].

2.1.4. Crystal growth

The process of crystal growth involves the size increase of minute nuclei to the visible larger crystal in different polymorphic phases. Once the nucleus reaches a size larger than the critical one, the growth process begins by adding new scale molecules to extend the overall size in all three dimensions [57]. On the surface, the growth step in the crystallisation fouling is often identified as including two mechanisms: diffusion of fouling ions from the bulk solution to the vicinity of the surface, and integration reaction of ions into the crystal lattice. The crystal growth behaviour and rate, either on the heated substrate or bulk solution, is prominently controlled by diffusion mass transfer, crystallisation reaction, or both [30, 74]. According to the investigations of Hasson, et al. [87] scale deposition of $CaCO_3$ on the heated surface is mass transfer controlled.

Ions diffusion from bulk fluid to the vicinity of the surface comprises two sequential steps. First, solute ions transport from the bulk through the liquid boundary layer and may pass through the pores of the scale layer. Later, surface diffusion occurs until the reaction of cations and anions takes place [42]. The driving force for ions mass flux to the heat transfer surface is the concentration difference between bulk solution (C_b) and interfacial concentration (C_i) (Fig. 2.11). When the growth rate on the surface is controlled by ions mass transfer, the mass deposition rate, m_d can be given as below [26, 61, 87]:

$$m_d = K_t(C_b - C_i) \qquad\qquad (2.17)$$

Where K_t is a mass transfer coefficient, which changes as a function of the hydrodynamics and liquid properties at the interfacial temperature (T_i) [88] by:

$$K_t = \frac{Sh.D}{D_h} \qquad (2.18)$$

Where, D_h is the hydraulic diameter, D is the diffusion coefficient and Sh is the Sherwood number that is calculated based on the flow geometry.
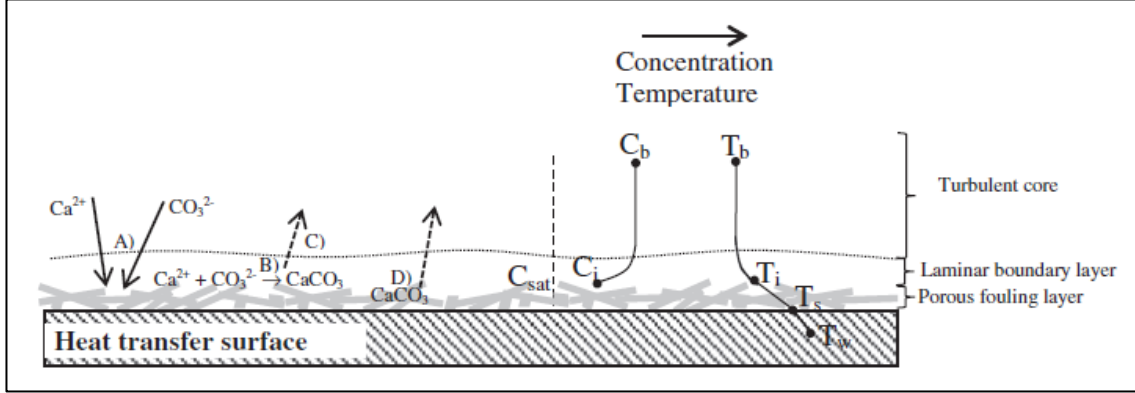
Figure 2.11. Schematic of the variation of concentration and temperature between bulk and surface, (A), (B), (C), and (D) different mechanisms of ions diffusions, surface reaction and crystal removal, respectively [89].

The deposition rate of minerals could be governed by the transport process of the solvated ions to the surface. Crystallisation reaction and the ions attachment into the crystal lattice are described by the below temperature-dependent formula:

$$m_d = K_r(C_i - C_{sat})^n \qquad (2.19)$$

Where, C_i is the concentration of solute at liquid-solid interface, C_{sat} is the saturated concentration of solute, n is the order of crystallisation reaction [90], and the reaction rate constant, K_r, is an interfacial temperature T_i dependent, which is predominantly following the Arrhenius-type equation, as follow [91]:

$$K_r = A_0 \, e^{-\frac{E_a}{RT_i}} \qquad (2.20)$$

Where A_0 is the pre-exponential constant, E_a is the activation energy of crystallisation reaction and R is the gas constant. In the case of a clean surface, the interfacial temperature (T_i) and surface temperature (T_s) are identical. Once the scale layer starts growing, T_i decreases and becomes lower than T_s. It implies that the reaction constant and reaction rate sequentially decrease for the incoming sub-layers [92].

Morse [93] suggested a model for describing the growth rate (G) of the precipitating scale particles normalised to surface area, as given next.

$$G = K_r(S - 1)^n \qquad (2.21)$$

The deposition rate of the salt crystals on the heated surface combines both the nucleation and growth stages. Once the stable crystal forms, either from the bulk solution or on the surface, the adhesion of the crystal to the surface takes place. However, along with the above stages, the flow shear stress attempts to remove the binding crystal from the surface [22, 73]. Figure 2.12 illustrates the surface fouling deposition and removal processes. Based on the approach of Kern (1959), the difference in the mass deposition rate and the mass removal rate from the surface is known as the fouling rate (m_f) (Eqn. 2.22), which changes depending on critical operating conditions, solution properties, and surface characteristics.

$$m_f = m_d - m_r \qquad (2.22)$$

m_r denotes the mass removal rate. In the ultimate stage, the ageing phenomena transform the participated/ surface crystals to harder or weaker scale layers [94].
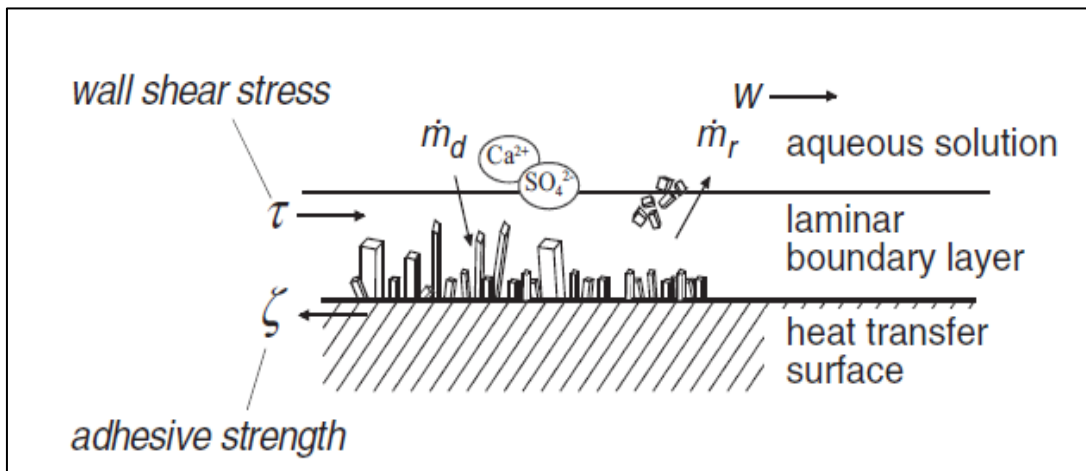
Figure 2.12. The surface fouling process [1].

2.1.4.1. Crystal growth theories

Three theories have been adopted to describe the process of crystal growth [57]. The common theories in crystal growth are surface energy theory, adsorption layer theory and diffusion-reaction

theory. Besides, other theories were used to explain how the crystal grows such as kinematic theories [95].

2.1.4.1.1. Surface energy theory

The surface energy theory was suggested based on the principle that "an isolated droplet of fluid is most stable when it's surface free energy, and thus its area, is a minimum'' [96, 97]. To achieve crystal growth, the summation of free energy in Eq^n 2.11, of a crystal in equilibrium with a solid surface would be a minimum at given operating conditions. In other words, the crystal obtains a minimum total surface free energy when its faces develop an equilibrium shape at an identical rate. As a result of differences between liquid droplets and crystallite, limitations were identified in Gibbs's analogy. Curie and Curie [98] has therefore estimated the crystal shape in equilibrium with the solution according to Gibbs theory.

Wulff [99] proposed that the crystal faces would develop in rates related to their surface energies by demonstrating that the crystal face energy determines the equilibrium shape of a crystal. However, the face energy, thus the rate of crystal growth, is inversely proportional to the lattice density of the face, the higher the lattice density, the faster the growth. The rate of face growth can be observed through the development in a direction perpendicular to that face. Figure 2.13a illustrates a crystal that grows in an ideal geometric pattern which is known as an 'invariant' crystal. The growth rate of crystal face increases with face area; faces A slowest, faces B medium and face C fastest growth. However, a crystal, in practice, does not follow the geometric pattern during the growth. In this case, the mode of growth is defined as ''overlapping'', in which smaller faster-growing faces gradually fade from the structure [100].
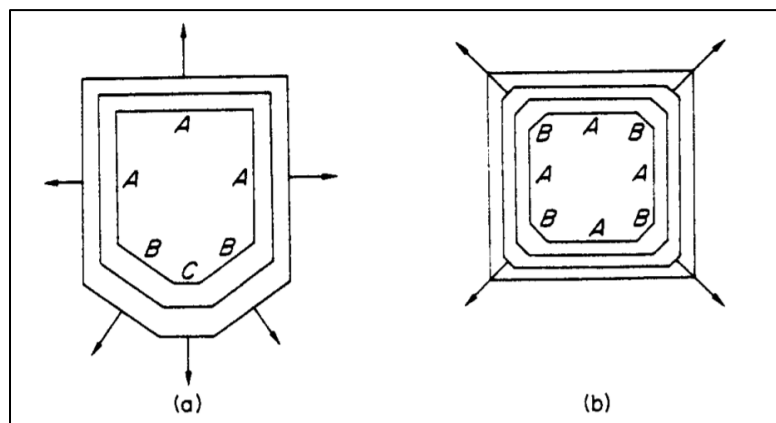
Figure 2.13. Growth of crystal growth faces: (a) invariant crystal; (b) overlapping mode [97].

25

2.1.4.1.2. Adsorption layer theory

Volmer [101] suggested, for the first time, the crystal growth mechanism of the adsorbed layer; he stated that an adsorbed layer of solute atoms or ions exists on a crystal face. According to this theory, or Gibbs-Volmer theory, the fouling species are unable to incorporate directly into the lattice, but they form a loose adsorption layer on the crystal and diffuse over the surface (surface diffusion). It has been believed that the adsorption layer contributes to heterogeneous nucleation and crystal growth. Once the adsorbed layer form on the crystal face, a thermodynamic equilibrium will be set up between the layer and the bulk solution [57, 102].

Atoms or ions will be attracted and linked to the active centres where the attraction force is the greatest. Once this is done, the construction of a whole plane face continues to completion as shown in Figures 2.14 a and b. The growth of the next layer on the crystal face begins when a 'centre of crystallisation' is being created. A single-layer island nucleus that forms by two-dimensional nucleation in the centre of the face, commences the second layer generation as stated by Gibbs-Volmer theory (Fig. 2.14c). The two-dimensional nucleation needs lower local supersaturation when compare with three-dimensional nucleation for similar conditions [97].
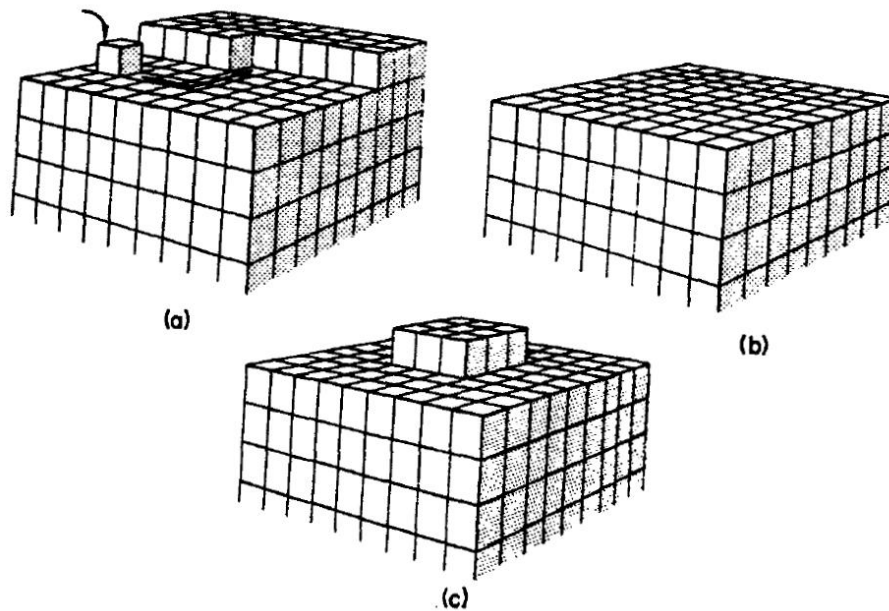
Figure 2.14. Adsorption layer theory of crystal growth (a) foulant transport and positioning, (b) full layer formation and (c) two-dimensional nucleation [97].

26

2.1.4.1.3. Diffusion-reaction theory

The diffusion theory was first proposed by Noyes and Whitney [103] who described the growth process based on a diffusional concept. They revealed that the deposition of solid particles, ''crystallisation'' is the opposite of the dissolution process. The difference in solute concentration between the bulk solution and the surrounding surface is the driving force for the crystallisation and dissolution processes, as described in Eq^n 2.17. The thickness of stagnant diffusion film, which reduces the diffusion and growth rates, can be significantly affected by flow turbulence. However, it has been found that the film thickness is not sufficient to explain the crystal growth, especially at a film of zero thickness. Also, in later investigations, it was demonstrated that the dissolution is faster than crystallisation and it is not the reverse of crystallisation.

Berthoud [104] and Valeton [105] have inserted considerable modifications on the diffusion theory that is then known as diffusion-reaction theory. They described the surface crystallisation in two successive steps; diffusion of scaling species from the bulk to the vicinity of the surface, and chemical reaction subsequently occurring between the scaling species to form the crystal lattice (Eq^n 2.17 and 2.19). The general equation of the crystal growth rate (m_d) based on the combination of the two steps is written below:

$$m_d = K_G(C_b - C_{sat})^n \qquad (2.23)$$

Where, C_b is the concentration of an ion in a bulk solution, and K_G is an overall crystal growth coefficient that is given by:

$$K_G = \frac{K_t\, k_r}{K_t + k_r} \qquad (2.24)$$

Where, K_t and k_r are the transport coefficient and reaction rate constant, respectively. The dependency of K_G on K_t and k_r varies based on the operating conditions. The diffusion-reaction theory of crystal growth becomes the most acceptable theory according to research findings.

2.1.5. Adhesion

When a uniform fouling crust is built on the heated surface, an interfacial area of crystal/substrate is created due to the adhesion phenomenon of individual crystals on the surface [70]. The adhesion of mineral crystals on the surface is a major challenge being faced in scale mitigation and cleaning processes. Researchers defined the adhesion force of two bodies as the maximum force required

for particle detachment, which is often brought about by hydrodynamic forces such as wall shear stress [106-109]. In the fouling process, the adhesion can be categorised into the nucleated crystals being diffused to the surface and precipitated crystals from the bulk.

The interfacial interactions in the crystal/ surface interface are classified as mechanical and molecular interactions. The mechanical interactions are surface topography related like micro-contours and roughness. Mechanical interactions have a pronounced impact on the adhesion strength since individual scale particle adheres preferentially to particular profile elements of the surface [62]. The Derjaguin-Landau-Verwey-Overbeek (DLVO) theory is often used to describe the mechanism of $CaCO_3$ adhesion on heat transfer surfaces [110]. The molecular links play a crucial role in the adhesion of deposits, such as Lifshitz-van der Waals forces (F_{vdW}), chemical bonding (F_{chem}), hydrogen bonding (F_H), electrostatic force (F_{el}), etc. [111, 112]. The following equation represents the adhesion force (F_{ad}) of scale particle on the solid surface.

$$F_{ad} = F_{vdW} + F_H + F_{chem} + F_{el} + \cdots \qquad (2.25)$$

Collins [112] presented a brief description of the principal interaction forces between the deposits and solid surfaces. The molecular interactions of adhesion are commonly described based on the fact that dispersive and polar Lifshitz-van der Waals forces are prevailing. As reported in the literature, the van der Waals forces are governed by chemical and physical properties as well as the geometry of the interacting bodies. The van der Waals force of attachment of scale spherical particle (Fig. 2.15a), of radius R, on planer surface, can be obtained as follows [113, 114]:

$$F_{ws} = \frac{A_H \, R}{6 \, x^2} \qquad (2.26)$$

For two plates (Figure 2.15b), the van der Waals force (F_{wp}) per unit area would be:

$$F_{wp} = \frac{A_H}{6 \, x^3} \qquad (2.27)$$

Where A_H is the Hamaker constant and x is the distance between the interacting bodies.
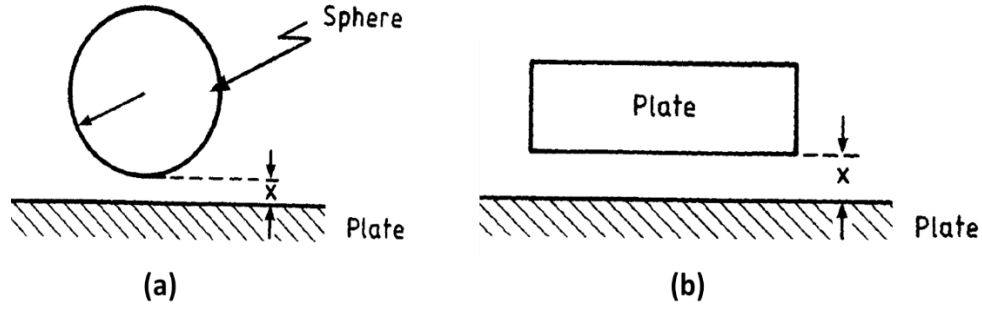
Figure 2.15. Two bodies in contact; (a) sphere-plate and (b) two plates [115].

Butt and Kappl [111] stated that the adhesion force (F_{ad}) between spherical crystal and plate is given as follow:

$$F_{ad} = -2\pi R E_{ad} \qquad (2.28)$$

The adhesive energy per surface area, E_{ad} can be obtained from the surface energy of each body and interfacial energy,γ_1 ,γ_2 and γ_{12}. The interfacial energy is defined as the reversible work required to create a unit interfacial area between the bodies.

$$E_{ad} = \gamma_1 + \gamma_2 - \gamma_{12} \qquad (2.29)$$

The influence of surface topography is considered in the calculation of adhesion force by as follows:

$$F_{ad} = \frac{A_H R}{6\,x^2}[(1 + \frac{32RK_1 r_{rms}}{d^2})^{-1} + (1 + \frac{K_1 r_{rms}}{D_0})^{-2}] \qquad (2.30)$$

Where, d is the average distance between asperities, r_{rms} is the root mean square roughness [116] and K_1 is the related proportionality factor ($K_1= 1.817$).

2.1.6. Removal

The adhered deposit crystal to the surrounding surface and even the small nuclei could be exposed to removal by the hydrodynamic load, crystal breaking up and dissolution [30]. There are two practical methods for scale removal from the surface: chemical methods and mechanical methods. In the chemical removal, an acid or a chelating agent such as hydrochloric acid and ethylene-diamine-tetraacetic acid (EDTA) can be used. The mechanical removal includes jet blasting,

milling and explosives. However, chemical removal is cheaper and causes less damage compared to mechanical methods [117, 118].

Crystallisation fouling rate can be minimised by enhancing the removal process of scale particles from the surface (Eq^n. 2.22*)*. The number of crystals leaving the surface per unit area per time is controlled by several parameters such as wall shear stress, adhesion force, crystal size and density [24, 41]. The most commonly used formula for mass removal rate $\dot{m}_r$, was that suggested by Kern [119] and Taborek [120], in which the removed mass is proportional to deposition rate (m_d) and the mean shear stress (F_τ):

$$m_r = \frac{K F_\tau m_d}{\psi}$$ (2.31)

Where, K and ψ are a proportionality constant and deposit strength, respectively. In the deposit mass balance, this expression predicts that the fouling mass exponentially approaches an asymptotic value. However, there is no clear method adopted for predicting what the depositing strength and proportionality constant are, and how it can be estimated.

The following model proposed by Förster [121] reveals that the removal rate of deposit mass could be estimated from a removal probability, flow shear force applied on crystal and the adhesion force:

$$m_r = \Gamma \left(\frac{F_\tau}{F_{ad}}\right) m_d$$ (2.32)

The removal probability (Γ) is a function of a ratio of wall shear stress to adhesion force. It can be obtained through a Weibull distribution [121]:

$$\Gamma = 1 - e^{-\left(\frac{\left(\frac{F_\tau}{F_{ad}}\right) - \chi_I}{\chi_{II}}\right)^{\chi_{III}}}$$ (2.33)

Where $\chi_I, \chi_{II},$ and χ_{III} are the Weibull parameters, the minerals growing on the heated substrate are exposed to shear stress, F_τ, by flowing solution and can be expressed as shown below:

$$F_\tau = C \rho v$$ (2.34)

Where C is a constant that depends on the flow Reynolds number, and v is the overall flow velocity.

2.2. Water chemistry

Both potable and surface water contain a variety of ionic species that contribute to the formation of different types of inorganic deposits in water distribution systems and domestic appliances [122]. Many industries find locations where close access to water sources are available such as rivers, lakes, etc. While the composition and quality of potable water vary based on geographic location [18], the heating of potable water is generally associated with the formation of various deposits with the most common being $CaCO_3$, $CaSO_4$, $Mg(OH)_2$, and $MgCO_3$ [91, 123, 124].

According to the data collected by Kemmer [46], the analysis of the water from some UK rivers is listed in Table 2.3. As can be observed from the table, a significant variation in the composition of water between the Dee River source and a point downstream is attributed to the "pick up" of salts from soil and rocks by flowing water. Also, the hardness of groundwater (wells water) can reach three times that of surface water [125]. Therefore, the tendency of scaling out of water relies on the water source. Figure 2.16 illustrates a map of water hardness across England and Wales. Water in around 60% of the UK regions is classified as hard to very hard, hence the domestic appliances and industrial heat exchangers in these areas are highly exposed to fouling.

The content of some fouling species in water may also determine the identity of the deposited salt. The presence of some mineral ions in water such as Ca^{2+}, Mg^{2+}, Na^+, Cl^-, HCO^- and SO_4^2 may contribute positively or negatively to the scale layer growth rate [12, 126]. For instance, when the content of SO_4^2 is considerable in water, the formation of $CaSO_4$ scale is potentially occurring, seawater desalination is an example [127-129]. However, in some cases, a composite fouling layer builds upon the heat transfer surface [51].

31

Table 2.3. Water composition in some UK rivers [42].

River	Tees	Tyne	Dee*	Dee**	Great Ouse	Severn
Constituent						
Calcium	74	77	8	78	357	136
Magnesium	30	33	1	21	25	45
Sodium	15	20	10	39	58	30
Total Electrolyte	119	130	19	138	440	211
Bicarbonate	77	80	3	62	242	71
Carbonate	0	0	0	0	0	0
Hydroxyl	0	0	0	0	0	0
Sulphate	24	32	2	38	144	70
Chloride	17	17	13	37	51	68
Nitrate	1	1	1	1	3	2
Alkalinity†	77	80	3	62	242	71
Carbon Dioxide	3	3	5	3	Nil	3
pH	7.6	7.5	6.3	7.7	8.1	7.7
Silica	4	-	1.5	8.0	-	5
Iron	0.5	0.6	0.6	0.5	0.1	Nil

Concentrations in *mg/l*

*   Head waters in Wales
**   Downstream
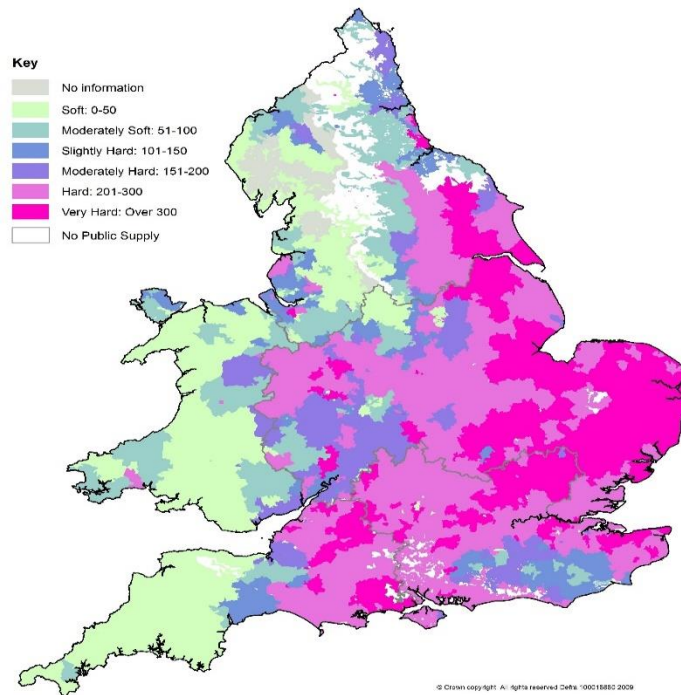
Figure 2.16. Map showing water hardness in England and Wales in mg/L $CaCO_3$ [130].

2.3. Deposited minerals

The severe operating conditions and variety of water composition result in the formation of different types of mineral salts in domestic and industrial heat transfer equipment [131]. Different mineral scales have different structures and physical properties. The density, thermal conductivity and porosity of the fouling layer varies with a prevailing mineral that composes the layer. Some minerals occasionally form due to special conditions. For instance, the content of zinc in tap and surface water normally does not exceed 1.1 mg/L that is relatively very low [132]. However, zinc deposits such as zinc carbonate might be found in some water treatment systems due to zinc ion release as a corrosion by-product.

2.3.1. Calcium carbonate

$CaCO_3$, the main constituent of limescale, is an inorganic mineral salt. It is commonly produced from dolomite or marble in different particle sizes to meet application requirements [133]. $CaCO_3$ is widely used for different purposes such as low-cost filler and pigment in various industries such as paint, cosmetics, plastics, papers, ink, pharmaceutics, asphalts, and nutritional supplements for animals [134, 135].

On the other hand, a $CaCO_3$ deposition is a widespread form of crystallisation fouling in a wide range of industrial processes which deals with water as a working fluid. Equipment like desalination evaporators, cooling towers, oil and gas pipes and heat exchangers, condensers, boilers, solar collectors as well as domestic appliances are commonly prone to crystallisation fouling [4, 136-138]. $CaCO_3$ fouling impedes heat transfer due to the insulating effect of the scale layer and resulting in an enormous increase in energy consumption, followed by increased carbon dioxide emissions and climate change problems [54, 139]. The formation of $CaCO_3$ is the most evident manifestation of fouling in tap water systems due to the abundance of calcium and bicarbonate in potable, surface and groundwater.

2.3.1.1. Polymorphic phases of CaCO$_3$

The dehydration of solute ions results in a phase transition of salt molecules at the interface between solid surface and solution [140]. Amorphous $CaCO_3$ (ACC) could be initially observed on the surface as a transient precursor phase. It appears to be metastable, the softest and highly water-soluble form of $CaCO_3$, which aggregate into bigger particles depending on surface temperature and characteristics. As the crystallisation fouling proceeds, the ACC particle grows in

the direction perpendicular to the heated surface; thereafter, it radially extends to a particular width yielding the first crystalline phase [141]. Du, et al. [142] found that at the early stages, the ACC particle diameter increases associated with Gibbs free energy decrease. The particle subsequently can transform into the crystal through solid-state transformation or dissolution-recrystallisation processes (Fig. 2.17). The shape of an amorphous particle on the surface could be an indicator of $CaCO_3$ crystal shape [141].
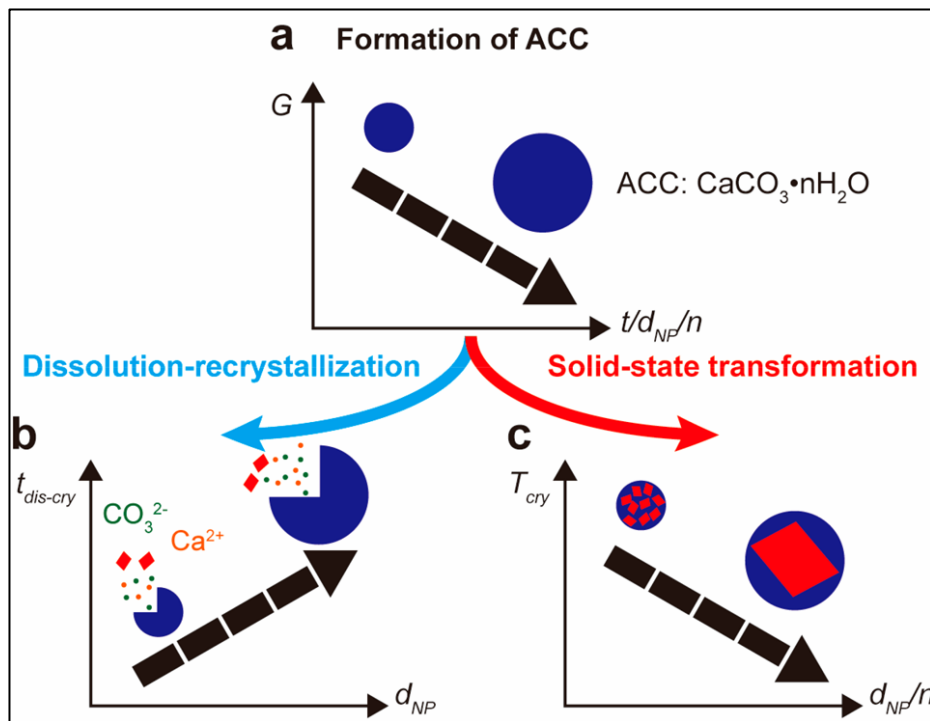
Figure 2.17. Schematic drawing of the growth of amorphous $CaCO_3$ particles and their transformation [142].

Besides the amorphous $CaCO_3$ phase, $CaCO_3$ forms commonly in three anhydrous crystalline polymorphic phases including calcite (Rhomboedric), aragonite (Needle-Like) and vaterite (Hexagonal) [123, 143, 144]. SEM morphology images of $CaCO_3$ polymorphs are displayed in figure 2.18. Among the forms, calcite is thermodynamically the only stable polymorphic phase at room temperature and pressure. Under similar conditions, aragonite and vaterite are metastable and converts to calcite based on the system temperature and pressure [145, 146]. The polymorphic phases have different solubility products relying on the system temperature [38]. Aragonite and

vaterite are both denser and higher in solubility than calcite at the same temperature [75]. Figure 2.19 illustrates the abundance of CaCO₃ crystalline forms as a function of temperature. Chakraborty, et al. [147] reported that the initial formed polymorphic phase is vaterite in most instances and then progressively transforms to calcite.
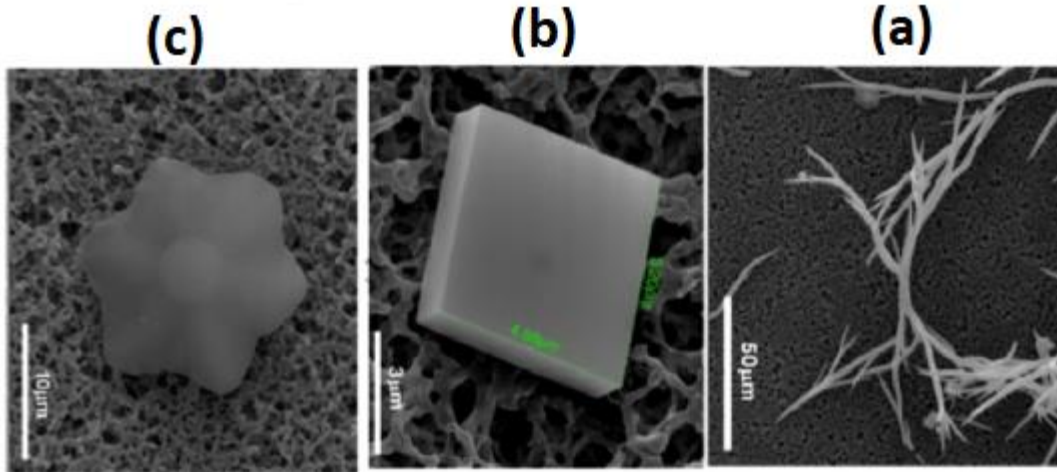
Figure 2.18. SEM morphology displaying the polymorphs of CaCO₃; (a) Aragonite, (b) Calcite and (c) Vaterite [148].
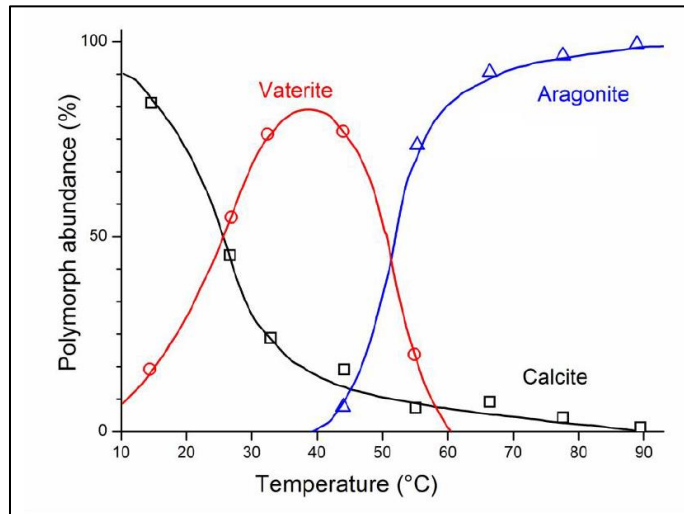
Figure 2.19. The abundance of CaCO₃ polymorphic phases as a function of temperature [149].

2.3.2. Calcium sulphate

Another inorganic salt is CaSO₄ that naturally occurs from seawater, groundwater and soil [150]. It is industrially produced from the desulphurization of flue gas and petroleum products [151].

CaSO$_4$ exists in three crystalline forms: anhydrate (CaSO$_4$), hemihydrate (CaSO$_4$·12H$_2$O) and gypsum (CaSO$_4$·2H$_2$O). Gypsum is the most stable phase, and anhydrate is the most abundant, while hemihydrate contains the highest water content. CaSO$_4$ fouling is a frequently encountered heat transfer problem in some systems such as seawater desalinators and boilers [127, 152]. The solubility of different CaSO$_4$ forms is high when compared with CaCO$_3$ and MgCO$_3$, however, it has higher thermal conductivity than that of CaCO$_3$ [42].

2.3.3. Magnesium Carbonate

MgCO$_3$ is an odourless white carbonate salt that occurs naturally as the crystalline form magnesite in rocks and groundwater. It is a major ore for elemental magnesium and is commonly used in fertilizers, food additives, pharmaceuticals, and as an antacid. It can be found in hydrated forms such as barringtonite (MgCO$_3$. 2H$_2$O), nesquehonite (MgCO$_3$. 3H$_2$O), and lansfordite (MgCO$_3$. 5H$_2$O) [153]. Magnesia incorporates with brucite (Mg(OH)$_2$) in MgO–CO$_2$–H$_2$O systems to form crystalline forms such as artinite (MgCO$_3$. Mg(OH)$_2$. 3H$_2$O), hydromagnesite (4MgCO$_3$. Mg(OH)$_2$. 4H$_2$O) and dypingite (4MgCO$_3$ ·Mg(OH)$_2$ ·5H$_2$O) [39].

The precipitation of magnesia can be found in different systems such as evaporators and boilers [43, 124]. MgCO$_3$ deposits have lower thermal conductivity than CaCO$_3$ and CaSO$_4$ which may cause significant retardation of heat transfer efficiency when it precipitates in the system [154]. Figure 2.20 displays an SEM image of synthetic magnesia MgCO$_3$.
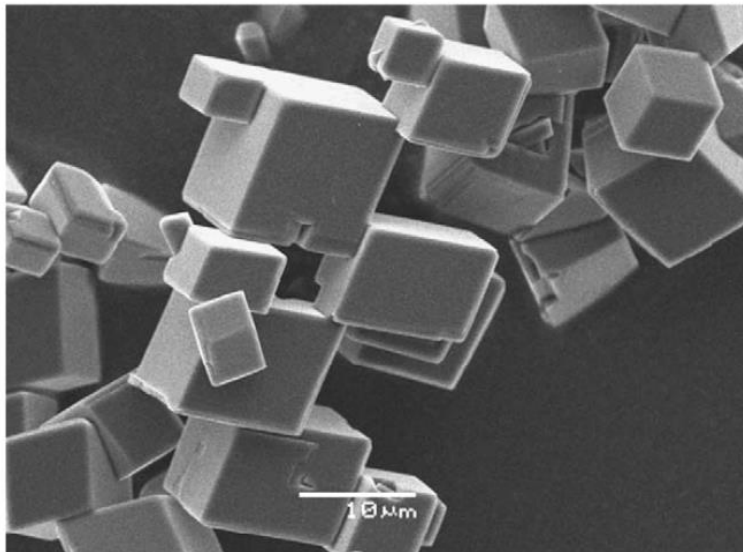
Figure 2.20. SEM image of synthetic magnesia MgCO$_3$ [39].

2.3.4. Other Minerals

Other inverse solubility minerals might be found in household and industrial heat transfer equipment based on operating conditions and water chemistry. Barium sulphate ($BaSO_4$), also known as barite, is commonly occurring in an enhanced oil recovery process under high temperature and high-pressure conditions [155]. In comparison to other sulphate and carbonate scales, BaSO4 has low solubility and a tenacious mineral scale. The precipitation of BaSO$_4$ takes place in crude oil wells when formation water (high in sulphate) and seawater (high in barium) are mixed [156]. The following equation describes the reaction of sulphate and barium ions:

$$Ba^{2+}_{(aq)} + SO_4^{2-}_{(aq)} \leftrightarrow BaSO_{4\ (s)} \tag{2.35}$$

Mg(OH)$_2$, also known as brucite, is an alkaline scale that mostly forms alongside the CaCO$_3$ scale in seawater evaporators and wastewater treatment plants [157, 158]. Some water-softening additives increase the concentration of hydroxide ions (OH$^-$) and the pH of water. This shifts the CO_2 - HCO_3^- - CO_3^{2-} equilibrium to the side that increases the deposition of CaCO$_3$. At the same time, at pH greater than 11, the OH$^-$ in water reacts with Mg^{2+} to form Mg(OH)$_2$ precipitate as given below:

$$Mg^{2+}_{(aq)} + 2\ OH^- \leftrightarrow Mg(OH)_{2\ (s)} \tag{2.36}$$
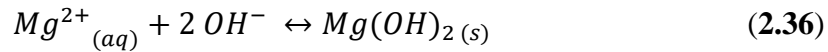
Mg(OH)$_2$ scale can be easily removed by acidifying the system or using chemical inhibitors [159].

2.4. Summary of Theory

In this chapter, the theory behind crystallisation fouling in heat transfer systems has been presented. It can be seen that the formation of scale, either on the heat transfer surface or in the bulk solution is a complex process that occurs through a series of steps. Each step can be affected by different parameters and conditions. The fouling process begins with solution supersaturation, in which the concentration of solute exceeds the solubility limit. Supersaturation is the thermodynamic driving force for the crystallisation of scale particles. When the solution is supersaturated, small nuclei form on the surrounding surface by heterogeneous nucleation or in the bulk solution by homogenous nucleation.

Nuclei then grow to visible crystals by one of the crystal growth mechanisms. The crystal growth process is prominently controlled by diffusion mass transfer, crystallisation reaction, or both. The

adhesion of scale crystal/ nucleus occurs alongside the nucleation and growth processes. However, in some cases, a mature crystal in the bulk solution transfers to a solid surface and adheres to it, however, the crystals that adhered to the surface are prone to removal by fluid flow. The process steps could be affected by the operating conditions, water chemistry and substrate nature.

In a system that uses portable, surface and groundwater as a working fluid, precipitation and/ or surface deposition of the composite scale is anticipated. The theory behind the formation of mineral salt includes the chemical equilibria and the presence of crystalline and non-crystalline forms. $CaCO_3$ is the most common scale type in domestic and industrial systems. However, other inorganic minerals such as $MgCO_3$, $CaSO_4$, and $Mg(OH)_2$ may also deposit depending on water composition and conditions. The composition of tap/ surface water varies following the geographical location. The theoretical data presented in this chapter is important for analysing and justifying the experimental findings.

Chapter 3: Literature Review

3.1. Overview of crystallisation fouling

Understanding the crystallisation fouling of industrial and domestic heat transfer systems is of great interest in the scientific community. Crystallisation fouling, the formation of unwanted inorganic deposits either on the heated surfaces in contact with the solution or in bulk fluid, occurs as a consequence of the supersaturation of salt. The formation of inorganic scale is thermodynamically possible when the aqueous solution is supersaturated with one of the sparingly soluble salts such as $CaCO_3$, sulphate salts of calcium, $Mg(OH)_2$, etc [2, 160]. Many studies, including numerical simulation and modelling, have investigated the inorganic scale formation process as well as scale morphology and structure [23, 64, 161, 162].

The work done includes assessing the kinetics and morphology of inorganic fouling under different operating conditions [28, 73, 163], substrate properties [25, 31, 164, 165], water chemistry [24, 126, 166] and chemical additives and inhibitors [167-171]. The investigations of the kinetics have focused on the bulk precipitation and surface deposition as the main two mechanisms of scale formation. Several researchers have examined different techniques to evaluate the impact of fouling on heat transfer. The experimental findings have been employed to develop a numerical approach to predict the rate and layer properties of fouling. In this chapter, a literature survey on crystallisation fouling has been conducted in line with the work experimental results.

3.2. Mechanisms of scale formation

3.2.1. Bulk precipitation

The formation of scale crystals in the bulk solution either by homogenous or heterogeneous nucleation is called ''bulk precipitation'' [172]. The formed particles may suspend in the bulk solution or sediment and adhere to the surrounding surface. Besides the effect of precipitates on the heat transfer efficiency and fluid flow, it also affects the quality of the produced water such as taste and colour [17]. For instance, the suspended solids in the boiled water produced from coffee machines, kettles or instant water boilers may affect the taste of coffee, tea, and the like. The precipitation of mineral salts in the bulk fluid can be assessed by visual examination, turbidity measurements, pH, conductivity and foulants concentration in the solution.

The bulk precipitation of inorganic scale has been considered in numerous studies [5, 35, 43, 167, 173, 174]. Söhnel and Mullin [5] studied the precipitation of $CaCO_3$ for different initial solution supersaturation. They determined the induction period experimentally in presence of various trace impurities such as Mg^{2+}, Br^-, and Mn^{2+}. However, the numerical procedure was used to determine some parameters such as nucleation rate, growth rate, crystal number and size based on the measurements of supersaturation. Koutsoukos and Kontoyannis [173] investigated the precipitation of $CaCO_3$ in an aqueous solution using the seeded-growth technique. They pointed out that the growth rate and the number of crystals rapidly increase at the initial stage of crystallisation. At the later stages, the crystal growth continues with no increase in the crystal number.

In the work of Pokrovsky [43], the unseeded precipitation of $CaCO_3$ and $MgCO_3$ was investigated in the CaO-MgO-CO_2-H_2O system. It was observed that the induction time of precipitate formation is independent of the dissolved inorganic carbon (DIC) and the content of Mg^{2+} in the solution. Magnesium combines with $CaCO_3$ crystals to form different deposits such as Mg-calcite and Mg-aragonite. The incorporation rate of Mg^{2+} into the Ca-Mg carbonate form is determined by the $MgCO_3$ supersaturation.

Case, et al. [153] reported the influence of temperature, solution chemistry and the presence of a solid surface on the precipitation of $MgCO_3$ in an aqueous solution using a batch glass reactor. They illustrated that the increase in temperature resulted in rapid precipitation of $MgCO_3$ crystals, but with less thermodynamic stability. The precipitation was found sensitive to supersaturation with respect to $MgCO_3$ which is highly affected by the chemical equilibria. Also, contamination of solution with forsterite substrate has no impact on the precipitation rate.

3.2.2. Surface deposition

Surface deposition of inorganic minerals occurs when the crystallisation reaction of the fouling species takes place on a solid surface yielding a solid phase of mineral salt. The deposits form on the surface primarily by heterogeneous crystallisation directly on the heat transfer surface, however, under some conditions, fouling particles are created in the bulk fluid, then transport and adhere to the surface [175]. In both situations, surface deposition causes a reduction in heat transfer efficiency, increasing the power consumption and blockage of flowlines in heat transfer devices subjected to fouling [10, 36, 176, 177]. It has been revealed that surface temperature, solution

composition, flow rate and substrate nature play a role in the kinetics, adhesion and morphology of deposited scale [22, 28, 178-180].

As the surface properties affect the adhesion and deposition rate, a non-metal silicon carbide (SiC) was used by Al-Janabi and Malayeri [31] as a heat transfer surface to test the scaling tendency of $CaSO_4$. The deposition rate and fouling resistance of deposits have been lowered by four-folds when compared with stainless steel. The deposition rate of inverse solubility salts is sensitive to surface roughness, surface energy, wettability and thermal properties [181-183]. However, there is no agreement yet regarding the influence of surface parameters on the deposition process. Zhao, et al. [184] reported that deposition rate increases with total surface energy, while Al-Janabi and Malayeri [185] found there is no explicit relationship between surface deposition and surface energy.

Surface crystallisation is prominently determined by diffusional mass transfer, crystallisation reaction, or both [30, 74]. It is often suggested that the crystallisation reaction controls the surface deposition as the flow rate increases [91, 186]. However, at low flow rates and constant surface temperature, the deposition process is controlled by the diffusion of foulants from the bulk solution to the vicinity of the surface [88, 187]. According to the study of Hasson, et al. [87], the determining step of scale deposition of $CaCO_3$ on the heated surface is the mass transfer of the ionic species.

Surface deposition demands less supersaturation (i.e. lower energy barrier) when compared with bulk precipitation that occurs by homogenous crystallisation. Eroini, et al. [188] emphasised that there is a significant difference between kinetics and mechanisms of surface deposition and bulk precipitation of $CaCO_3$. However, the crystallisation rate of both processes is physically interlinked but with different reaction constants [189]. Chen, et al. [137] found that the morphology of scale particles formed in the bulk solution differs from that formed on the heated surface, as displayed in figure 3.1. The average size of the surface crystal is greater than the precipitated one which is attributed to the heterogeneous crystallisation process.
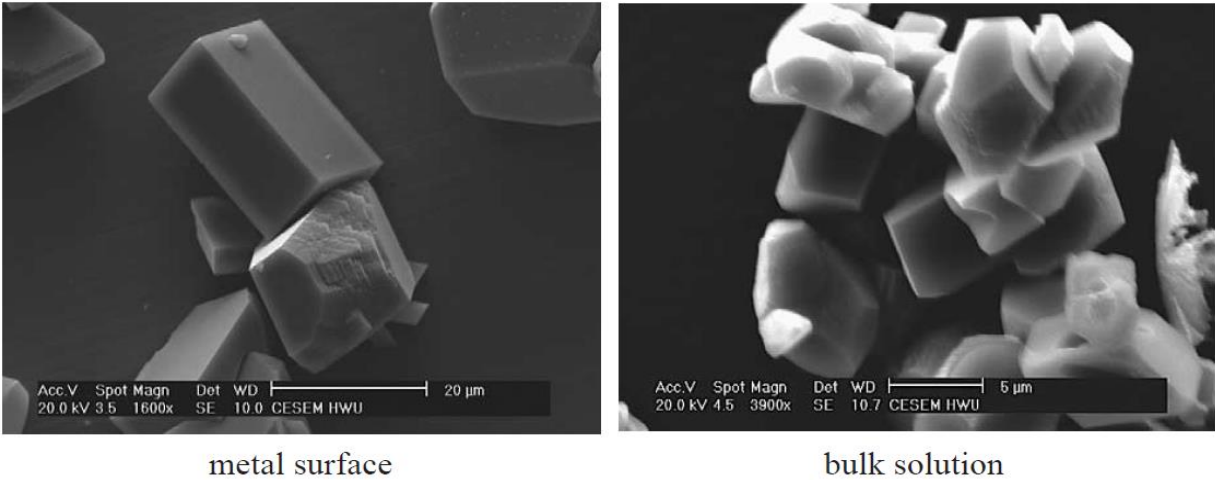
Figure 3.1. Scale morphology of scale crystals formed in the bulk solution and on the metal surface [137].

3.3. Formation of calcium carbonate scale

Calcium and bicarbonate are specifically abundant in natural waters as a result of the decomposition of geological calcareous minerals which makes $CaCO_3$ salt the most common type of scale formed from potable, surface, and groundwater. Many researchers have investigated the morphology and kinetics of $CaCO_3$ formation in heat transfer equipment under different conditions and using different techniques [10, 12, 190, 191]. Understanding different aspects of $CaCO_3$ fouling on heat transfer surfaces is important to predict and therefore mitigate the impact of scale on heat transfer efficiency. The studies were distributed over kinetics assessment, morphological structure, adhesion investigations and removal techniques.

3.3.1. Kinetics of CaCO₃ fouling

The experimental investigations of $CaCO_3$ formation kinetics led to developing numerous models which represent the inorganic scaling process [192-194]. The fouling resistance is introduced in the design of heat exchangers to consider the potential impact of fouling. Most surface fouling models have been established according to the Kern and Seaton [195] model (Eq[n] 3.1) which states that the difference of deposition rate and removal rate is known as fouling rate. These models combine mass transfer term and surface crystallisation term as well as the relevant physical properties of the fluid and deposits. The Kern and Seaton [195] model can also be expressed in terms of fouling resistance (R_f) with time (t):

$$m_f = m_d - m_r = \frac{dR_f}{dt}\, \rho_f\, \lambda_f \qquad\qquad (3.1)$$

ρ_f and λ_f denote the fouling layer density and thermal conductivity, respectively. Eq^n 3.1 is integrated with respect to R_f. The deposition rate (m_d) is assumed to be proportional to the bulk concentration of solute (C_b) and fluid velocity (u), while the removal rate (m_r) is simplified through its dependency on fouling layer thickness and wall shear stress (τ_w), as written below:

$$R_f = \frac{K_3\, C_b\, u\, (1 - e^{-K_4\, \tau_w\, t})}{K_4\, \tau_w\, \lambda_f} = R_f^* \,(1 - e^{-K_4\, \tau_w\, t}) \qquad\qquad (3.2)$$

Where, K_3 and K_4 are constants that could be estimated from the fouling resistance curve and R_f^* is known as the asymptotic fouling resistance in which the rates of removal and deposition are equal [42].

Konak [192] proposed a novel model for the surface reaction-controlled growth of crystals. He distinguished the growth process by the following steps: (1) ions transport from the bulk to the vicinity of formed crystal either by molecular diffusion or eddy; (2) ions adsorption on the crystal surface; (3) displacement of surface ions to the kinks; (4) Dehydration of ions and water diffusion to the bulk; and (5) integration of dehydrated ions into the crystal lattice. The model provides a detailed description of both mass transfer and surface reaction mechanisms.

The fouling process is numerically studied using a CFD code in the study of Brahim, et al. [66]. Based on models of Krause [26] for fouling rate calculations, CaSO$_4$ scale formation on heat transfer surfaces was predicted. The local values of the density of the scale layer were determined as a function of the distance from the heated surface and time-dependent layer thickness. Under favourable fouling conditions, the scale layer forms in inhomogeneous sub-layers (Fig. 3.2). The growing of the fouling layer results in new, porous and fewer coherence sub-crusts [67]. They consequently concluded that the mass deposition rate decreases with the layer thickness, while the removal rate increases due to weak adhesion of crystals on the top sub-layer. As the scale layer becomes highly porous, the local density of the fouling layer decreases with thickness increase.
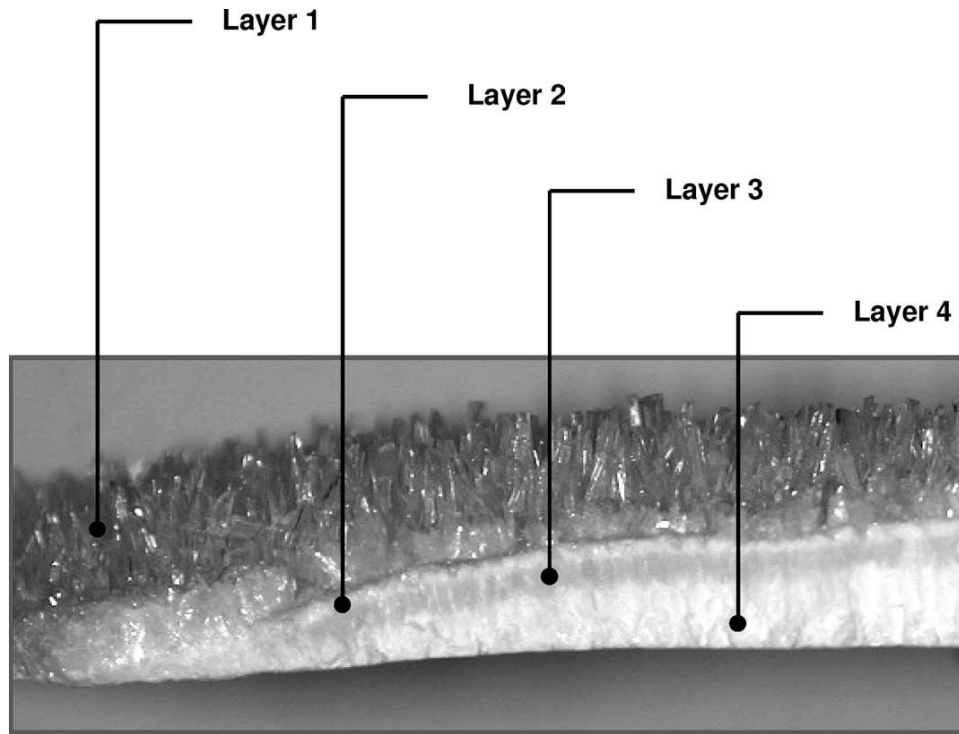
Figure 3.2. The profile of the fouling layer [58].

Pääkkönen, et al. [89] conducted a modelling study of crystallisation fouling of $CaCO_3$ on the heat transfer surface by defining the characteristics of the scale layer. The obtained data of deposition rates were utilised in regression analysis to estimate the kinetic parameters of various fouling models. The fluid velocity effect was included in the model using the time scaling factor. The researchers examined fouling models namely, surface integration, integration-diffusion, integration-velocity and integration-diffusion-velocity models. Based on these models, the effects of surface temperature, fluid velocity and heat flux on the mass deposition rate were investigated.

Regarding the practical predictive tools and procedures, Bahadori, et al. [196] presented a novel predictive procedure to estimate the formation of $CaCO_3$ precipitation in CO_2-saturated solution as a function of system pH, scale ions concentration, CO_2 concentration and temperature. The method predictions were compared with reported findings in the literature and achieved good agreement. In the same line, Eseosa and Atubokiki [197] built an easy-to-use tool for predicting the scaling tendency of formation water. The Visual Basic Software estimates the propensity of scale formation based on the Stiff Davis model, Langelier's saturation index and general saturation

index. The predicted scale index is calculated for different operating conditions including temperature, pressure, CO_2 mole fraction and ionic strength.

The scaling tendency can be predicted by different models and indices for various conditions and systems. The common indices for that purpose are the Langelier Saturation Index (LSI) and the Ryznar Stability Index (RSI). Langelier Saturation Index (LSI) is a qualitative index pointing out whether the solution is supersaturated or undersaturated with respect to $CaCO_3$. The Langelier Saturation Index (LSI) is expressed as:

$$LSI = pH - pHs \qquad\qquad (3.3)$$

Where *pHs* is the pH value of $CaCO_3$ saturation that obtained by:

$$pHs = pK_2 - pKsp + pTA + p[Ca^{2+}] \qquad\qquad (3.4)$$

Where, K_2, K_{sp} and TA are the second dissociation constant of carbonic acid, the solubility product, and the total alkalinity, respectively. If the LSI has a positive value, the solution is supersaturated and has the potential to form mineral deposits. Conversely, if water LSI is negative, it is likely to be corrosive and is undersaturated. However, the LSI does not show if the supersaturation degree is enough to commence the crystallisation process. RYZNER [198] proposed the Ryznar Stability Index (RSI) which links between water saturation degree and the probability of scale formation.

3.3.2. Morphology of $CaCO_3$

As mentioned in the previous chapter, $CaCO_3$ deposits exist as amorphous and in three crystalline forms: calcite, aragonite and vaterite. The habit of the scale crystals may differ based on water composition, operating conditions, and the presence of additives [149, 199-203]. The morphology of crystalline $CaCO_3$ is found sensitive to the presence of some ionic species in water such as magnesium. Interestingly, Mg^{2+} plays a vital role in the transformation process of the polymorphic phases by retarding the dehydration of the precursor phase [201]. Figure 3.3 shows the morphologies of first crystallites at different concentrations of Mg^{2+} in a solution. It has also been found that sulphate SO_4^{2-} has a weak inhibitory effect on scale formation. However, at concentrations above 0.01 M, the transformation of calcite to aragonite is favourable. Sulphate ions preferably bind to calcite rather than aragonite [204, 205].
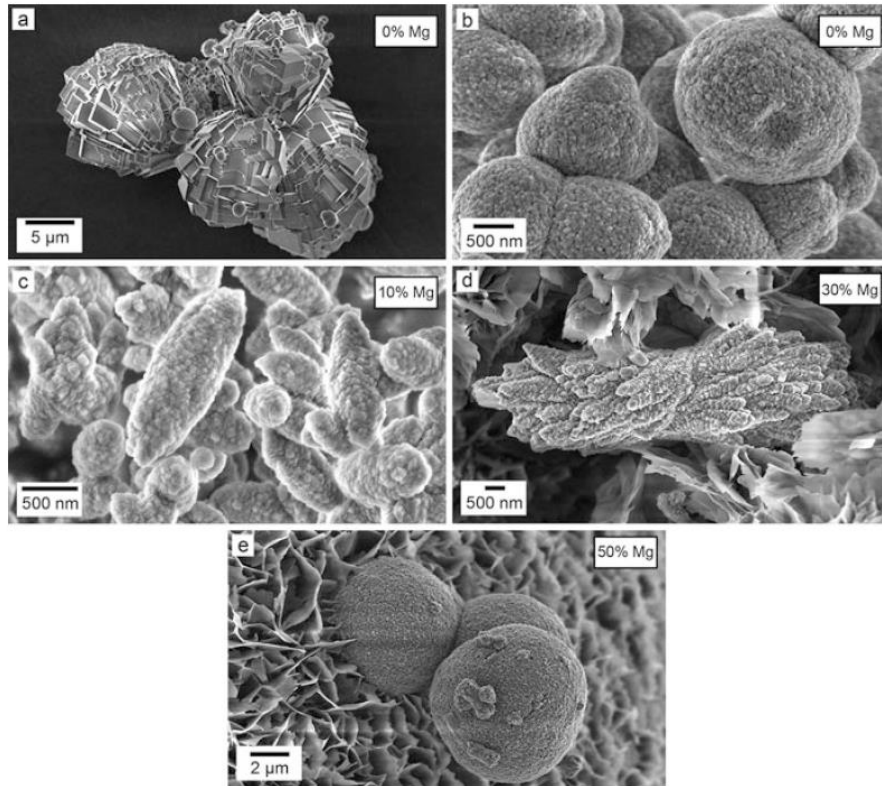
Figure 3.3.The morphologies of first spherulitic crystallites at different concentrations of Mg^{2+} [73].

Another influential parameter is antiscalants or scale inhibitors. Inhibitors retard the scaling by three mechanisms; chelating the scale species, retarding the nucleation and growth rates by blocking the energetically favourable growth sites of the scale matrix, and weakening the crystalline structure [10, 160]. Yu, et al. [206] concluded that the carboxylic group in the polyacrylic acid (PAA) incorporates with CaCO$_3$ crystal leading to suppress the growth, which also results in a change of the size and morphology of the crystals. In their study, Setta and Neville [170] demonstrated the effect of four antiscalants on the morphology of CaCO$_3$ on the stainless steel surface. Using PolyphosphinoCarboxylic acid (PPCA), Polymaleic Acid (PMA) and Polyaspartate (PA) promote the transformation from calcite to aragonite crystal, while CarboxyMethyl Inulin (CMI) leads to the formation of vaterite crystals (Fig. 3.4).
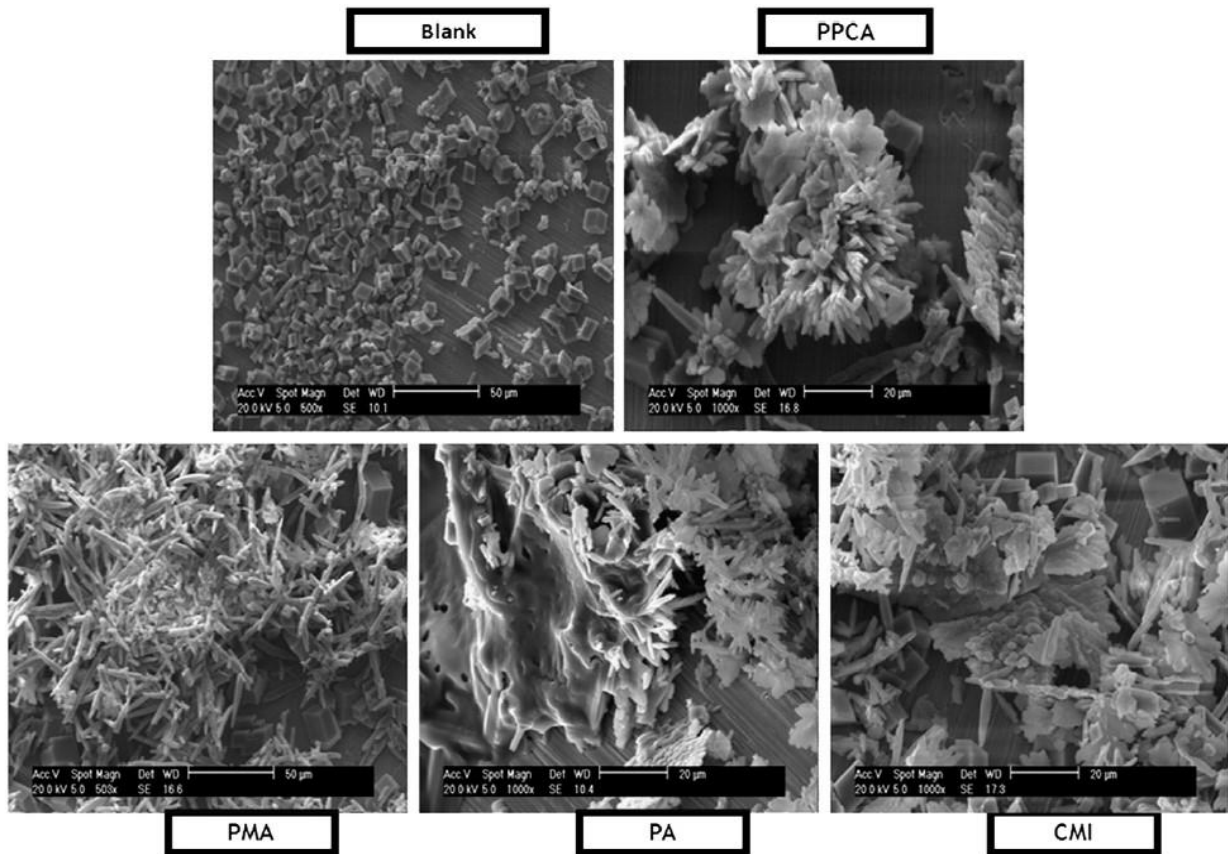
Figure 3.4. The influence of different scale inhibitors on the morphology of CaCO$_3$ [170].

Wang, et al. [207] compared the effects of Al$_2$O$_3$ nanoparticles and the scale inhibitor 2-phosphonobutane-1,2,4-tricarboxylic acid (PBTCA) on the morphology of CaCO$_3$ deposits (Fig. 3.5). The addition of 1 g/L of Al$_2$O$_3$ nanoparticles leads to transform of rhombohedral and smooth calcite to rod-shaped crystals with small particles. However, rough, and spherical crystals of CaCO$_3$ were formed when PBTCA is added to the solution with a concentration of 4 mg/L. In the test solution containing 1 g/L of Al$_2$O$_3$ nanoparticles and 4 mg/L of PBTCA yields rod-shaped crystals with small particles same as when only Al$_2$O$_3$ nanoparticles were added, which implies that the Al$_2$O$_3$ nanoparticles were more influential than the scale inhibitor concerning the morphology.
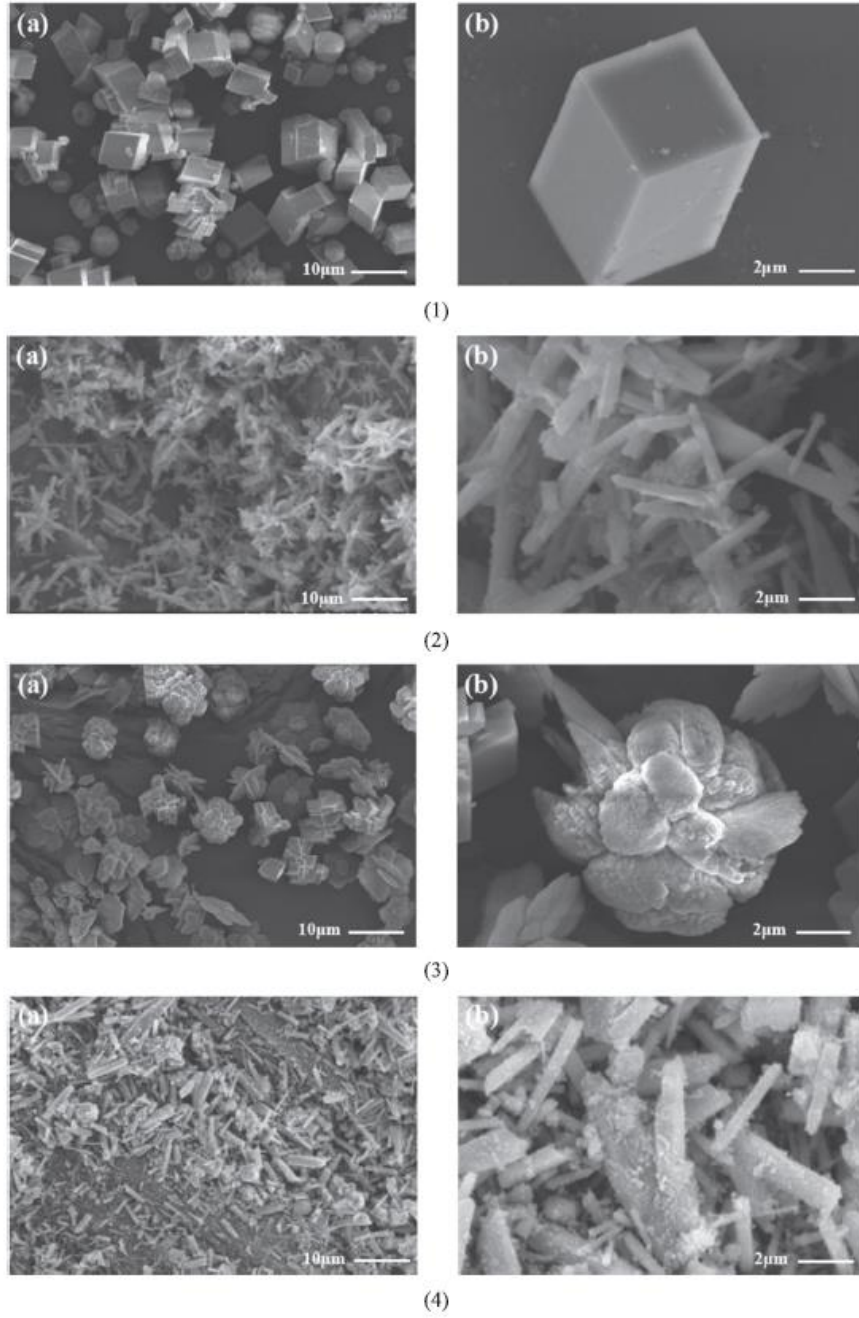
Figure 3.5. SEM observations of CaCO$_3$ scale; (1) base case, (2) 1 g/L Al$_2$O$_3$ nanoparticles, (3) 4 g/L PBTCA and (4) 1 g/L Al$_2$O$_3$ nanoparticles and 4 g/L PBTCA [207].

3.4. Factors impacting crystallisation fouling

The operating parameters including flow velocity, temperature, and system pressure significantly affect the fouling process [24, 89, 208, 209]. The solution chemistry such as salt concentration, dissolved CO_2 concentration, the presence of additives, impurities and pH is also able to influence the fouling process [27, 40, 50, 166]. Finally, surface properties like roughness, topography, surface energy and substrate metal could be utilised to accelerate or hinder the fouling process [162, 178, 210].

3.4.1. Influence of temperature

Temperature is one of the decisive crystallisation parameters which can manipulate both supersaturation and crystallisation reaction kinetics [191]. Overall, temperature controls the fouling rate as well as deposits morphology. The saturation concentration on the vicinity of the surface decreases with system temperature increase due to lowering solubility and hence increasing the supersaturation ratio. At the earlier stages of the crystallisation fouling process, the kinetics of solvated ions can be enhanced by the bulk temperature rising which leads to more ions transfer to the surface [75, 211].

Amor, et al. [212] studied the effect of surface temperature on the nucleation rate of $CaCO_3$ on metallic and plastic materials. They found that the concentration of calcium ions in the bulk solution decreases when the surface temperature increases from 30 ºC to 50 ºC. Moreover, the temperature increases the supersaturation of the solution resulting in reducing the theoretical time of nucleation [35], as follows:

$$\log T_{Nucleation} = A + \frac{B}{(\log \sigma)^2} \tag{3.5}$$

Where *A* and *B* are constants, *B* is inversely proportional to temperature. Nucleation rate reversibly changes with nucleation time $\left(J \propto \frac{1}{T_{Nucleation}} \right)$. So, nucleation time is reduced due to increasing temperature, thus increasing the number of nuclei formed per unit time.

Pääkkönen, et al. [22] carried out $CaCO_3$ deposition experiments on stainless steel (AISI 316L) in a flat plate heat exchanger. The influence of scale on heat flow from an electrical heater to the flowing solution is characterised by measuring the fouling resistance over the experiment time. They reported that fouling resistance increases with increasing heat flux applied to the surface at

a constant inlet temperature of 30 ℃ and flow Reynolds number of 6900. Higher surface temperature caused by increasing heat flux develops the fouling rate due to the temperature influence on supersaturation and surface integration reaction.

Yang, et al. [25] investigated the effect of wall temperature on the deposition process of $CaCO_3$ crystals on copper-modified heat transfer surfaces with low surface energy. Two types of coated surfaces: Cu-DSA (copper- DocoSanoic Acid) and Ni-P-PTFE are used in a cooling water system. The value of fouling resistance increased from 2.1E-6 m^2 ℃. kW^{-1} to 15 E-6 m^2 ℃. kW^{-1} when the wall temperature of Cu-DSA changed from 70.8 ℃ to 82.8 ℃ at a fixed flow velocity and bulk temperature.

The morphology of $CaCO_3$ is affected as well by system temperatures. At temperatures > 25 ℃, calcite forms as a metastable phase, while at a temperature between 40 ℃ and 60℃, the formation of aragonite is favourable and becomes the predominant polymorph until 70 ℃. Above 70 ℃, aragonite transforms to calcite which is the thermodynamically stable phase of $CaCO_3$ in most instances. Vaterite is often the dominant phase at temperatures under 40 ℃. Once the temperature increase over 40 ℃, the relative abundance of vaterite diminishes through conversion to aragonite and calcite [149, 213-215].

3.4.2. Influence of pressure

Another critical parameter in domestic and industrial systems is the pressure that may affect the fouling process alongside the temperature. Studies have investigated the relationship between the system pressure and the formation of scale in the upstream oil and gas industry [216-218]. Pressure in the household appliances reaches up to 12 bars due to the generation of steam. The pressure range in these systems is undoubtedly much lower than that in the oil industry.

Dyer and Graham [218] carried out dynamic tube blocking tests to examine the role of pressure and temperature on the fouling of $CaCO_3$ and $BaSO_4$. It was determined that the pressure reduces the fouling rate of both $CaCO_3$ and $BaSO_4$. However, the impact of temperature is more pronounced in comparison with pressure. In oil and gas fields, the scaling of $CaCO_3$ increases with the reduction in reservoir pressure and release of dissolved CO_2 in solution which shifts pH to higher values [219]. An increase in pressure reduces the release of carbon dioxide from the solution. This shifts the equilibrium to the left-hand side, hence reducing the formation of $CaCO_3$

and $MgCO_3$ scale (Eq^n 3.6 and 3.7). Therefore, the effect of pressure on the scaling tendency of $CaCO_3$ is relatively insignificant.

$$Ca_{(aq)}^{2+} + 2HCO_{3\ (aq)}^{-} \leftrightarrow CaCO_{3\ (s)} + CO_{2\ (g)} + H_2O_{(l)} \qquad \textbf{(3.6)}$$

$$Mg_{(aq)}^{2+} + 2HCO_{3\ (aq)}^{-} \leftrightarrow MgCO_{3\ (s)} + CO_{2\ (g)} + H_2O_{(l)} \qquad \textbf{(3.7)}$$
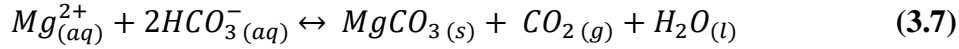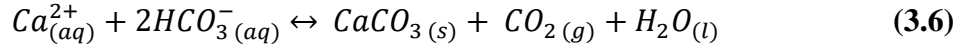
According to Peyvandi, et al. [220] work, which was done using the electrochemical technique, the surface coverage of $CaCO_3$ and $BaSO_4$ declines as the pressure increased (Fig. 3.6). They also found that increase in pressure results in the formation of less and smaller scale particles. Besides pressure impact on the kinetics of scale formation, it may control the dominant crystalline form. Pressure drop during crude oil production leads to deposition of calcite through minimizing salt solubility [221, 222].
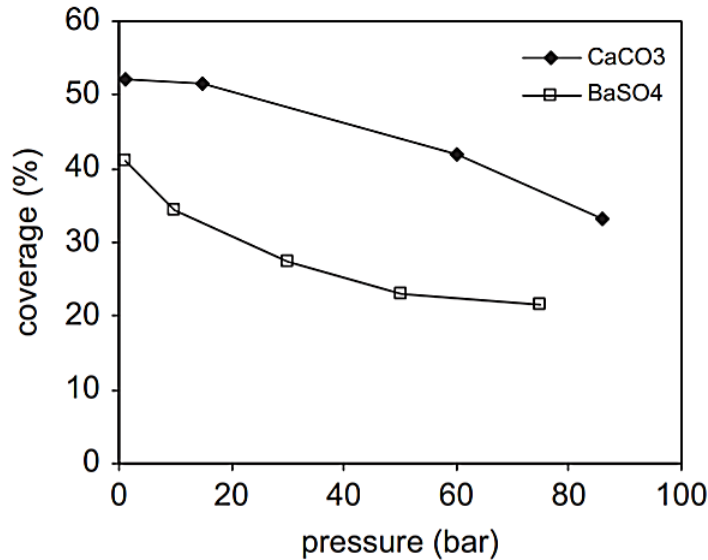
Figure 3.6. Surface coverage of CaCO$_3$ and BaSO$_4$ as a function of pressure [220].

3.4.3. Effects of fluid flow and hydrodynamic conditions

Not a few numbers of studies have reported that the flow velocity and turbulence in open systems significantly impact the fouling rate on the solid surface as well as the morphology of the deposits [22, 87, 223-225]. However, the researchers expressed adverse outcomes regarding the trend of

flow velocity influence on the deposition rate of inorganic scale. In the work of Watkinson and Martinez [223], the heat transfer coefficient is calculated based on the measurement of the wall temperature of the copper tube for different flow velocities at a fixed bulk temperature and water chemistry. The heat efficiency was enhanced by increasing the flow velocity. Furthermore, the flow Reynolds number is increased at fixed velocity by increasing the tube diameter. In contrary to flow velocity, tube diameter lowers the heat transfer coefficient, precisely after 20 h of the experiment.

In the same line, Wang, et al. [73] implemented fouling resistance experiments in the laboratory-scale setup of stainless steel (AISI 316L) double pipe heat exchanger. The influence of flow velocity of the artificially hardened solution on the characteristics of $CaCO_3$ fouling is tested. The Reynolds number changes over a range of 618 (laminar flow) to 9406 (turbulent flow) passing through the transitional flow zone. The study showed that the velocity poses different effects on the fouling process depending on the flow regime. When the flow is laminar or transitional, the scaling rate increases expeditiously with increasing velocity, and the fouling process might be controlled by ions mass transfer. However, in turbulence flow, surface integration reaction controls the deposition rate and flow shear stress increases to important values. As the shear stress improved on the scale particles, the increasing removal rate diminishes the overall fouling rate. Velocity does not only reduce the asymptotic fouling resistance but enhances the heat transfer at the induction period. The results of Wang, et al. [73] confirmed the outcomes of Bohnet [30] work, in which the velocity effect has been investigated with insufficient attention.

However, the geometry of the flow domain may manipulate the velocity impact in the laminar flow regime as reported by Mayer, et al. [28]. They examined the characteristics of crystallisation fouling in the microscale heat exchanger comprising stainless steel channels. $CaCO_3$ scale has a reduced influence on the heat transfer and pressure drop at higher flow rates within the laminar flow region. As flow Reynolds number increases from 66 to 264 the pressure drop decreases by 58 times and the heat transfer coefficient increases by seven times over 200 minutes of the experiment.

Förster, et al. [54] adopted a fouling mitigation strategy through amendment of the flow velocity using a pulsation technique. A pulsator is employed to produce an oscillating flow at an adjustable frequency (Fig. 3.7). The results showed that for the pulsating flow, an improvement of heat

transfer, which appeared as a negative fouling resistance, was observed over the total test time. To achieve the optimum operation conditions, a set of experiments were run for different oscillation delay times. It was found that the fouling layer is growing faster at a longer delay time.
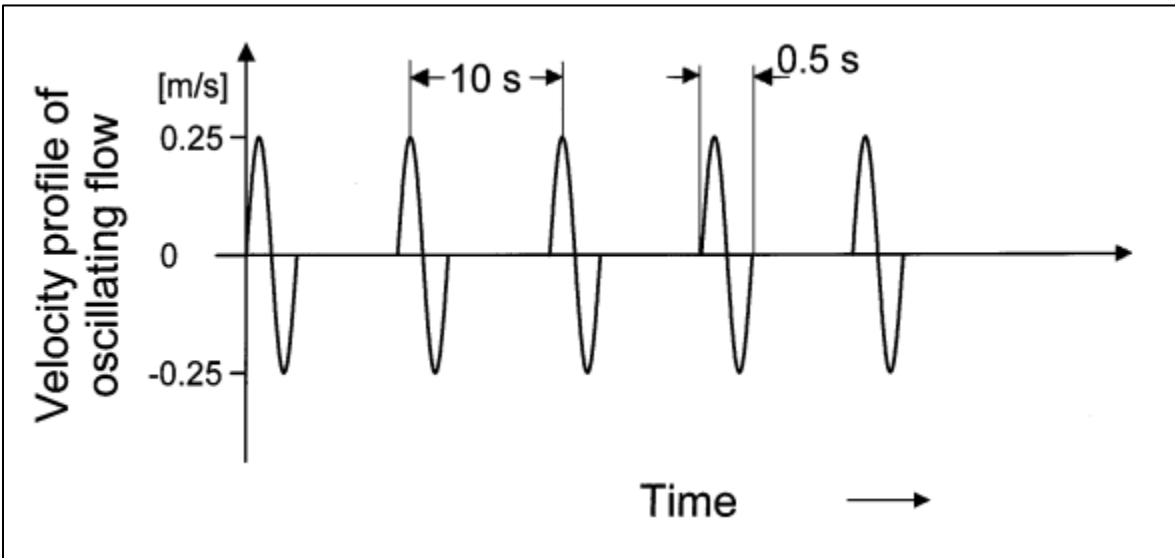
Figure 3.7. Pulsating flow profile [54].

According to the work of Najibi, et al. [187], the Reynolds number enhances the fouling rate on heat transfer surfaces during subcooled flow boiling. They justified this effect in terms of the thickness of the boundary layer which forms next to the heated surface. The increasing flow velocity diminishes the molecular diffusion by reducing the boundary layer thickness, which implies the scale formation is more controlled by the crystallisation reaction on the surface. Moreover, the surface reaction mechanism can dominate over the ions transport due to growing vapour bubbles that cover the surface.

3.4.4. Influence of substrate nature

The substrate material and surface, in particular, have a marked effect on the crystallisation fouling process [56, 226, 227]. Much research consequently has been performed for amending the surface properties by ion sputtering, ion implantation, coating, and finishing techniques. The substrate

characteristics which may affect the deposition rate, adhesion and morphology, are roughness, surface energy, surface chemistry, thermal conductivity and wettability [228].

3.4.4.1. Surface wettability

The scaling tendency of mineral salts on hydrophobic and hydrophilic is not identical. Wetting is described by static contact angle which depends on surface finishing, surface roughness and cleanness conditions [229, 230]. The effect of surface wettability on the adhesion and heterogeneous nucleation has been investigated [183, 231]. The wetting behaviour of the surface is changed from hydrophobic to hydrophilic by using UV-ozone treatment. The rate of nucleation increases with increasing hydrophilicity and reducing the contact angle. Moreover, the surface hydrophilicity inhibits the formation of vaterite form allowing calcite to dominate. Similarly, Yamanaka, et al. [141] mentioned that the absorption of hydrated sodium ions on the hydrophilic surface is the potential reason for the retardation of heterogeneous nucleation.

Dash, et al. [165] proposed a strategy to enhance heat transfer performance and mitigate crystallisation fouling during the pool boiling. The strategy includes using hybrid hydrophilic-hydrophobic surfaces to avoid heat transfer deterioration due to surface fouling. This hybrid surface increases the nucleation sites and the departure frequency of vapour bubbles, as shown in figure 3.8.
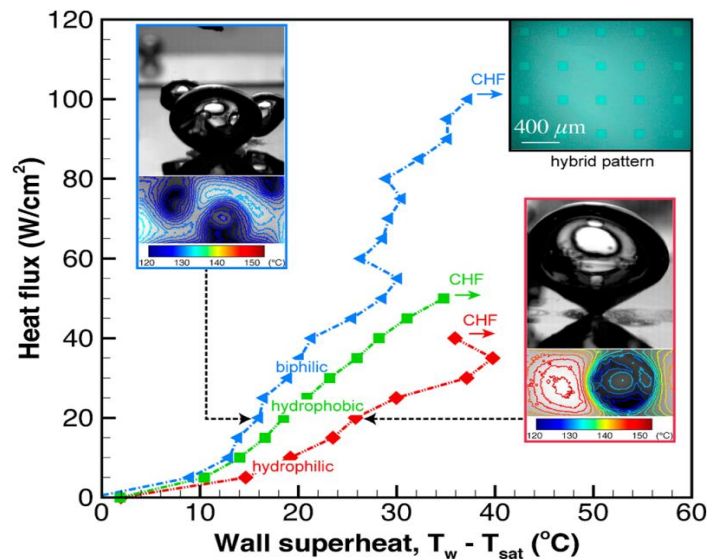
Figure 3.8. . Boiling curves for a hydrophobic surface, a hydrophilic surface and a hybrid surface [165].

3.4.4.2. Surface roughness

The roughness can be defined as a measure to depict the unevenness of a surface [10]. The surface roughness was determined to exert a noticeable impact on the tenacity of the mineral deposits. The early research of the roughness effect on the deposit morphology has been reviewed by [161, 232]. Keysar, et al. [162] examined the surface roughness on the morphology and adhesion of calcite deposits on the mild steel coupon. The stress required to detach the calcite crystals binding to the rough surface (Ra= 18-24 μm) was estimated to be as much as 30 times greater than that for a smoother surface (Ra=0.1-0.15 μm). The researchers justified these outcomes that the roughness provides increased hooking sites and large contact area, hence promoting adhesion strength. The results also revealed that the porosity of the fouling layer formed on the smooth surface was three times higher than that on the rougher one. Finally, surface roughness enhances wettability and reduce contact angle, thus improving the nucleation rate.

In the work of Bohnet [62], the fouling behaviour and adhesion on substrates with different surface topographies were studied. The dimensions of the profile element of PTFE and stainless steel were compared in figure 3.9. It can be seen that the width and depth of the profile element of PTFE are the largest, thus, there is an increased probability that minerals bind to the surface. On stainless steel, by increasing the mean roughness depth 16 times, the induction time of the fouling resistance is minimised by eight times. They depicted the profile element of the surface as valley and hill. The deeper valleys act as a shelter for crystals against flow shear, while hills could be the scale hooking sites.
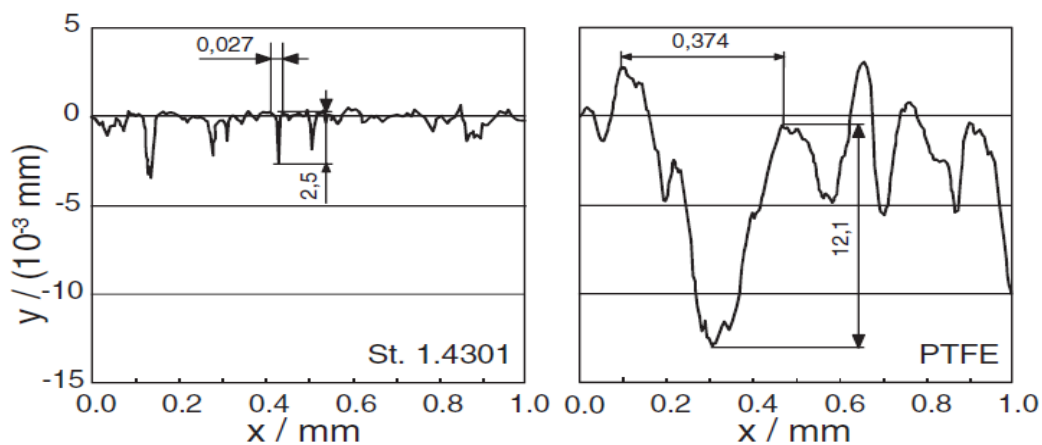
Figure 3.9. Surface contours of PTFE and stainless steel surfaces [62].

Cheong, et al. [33] supported Bohnet [62] findings by examining the effect of the asperity height on the crystals adhesion. They pointed out that the sharp tops of asperities promote heterogonous nucleation by acting as sites for crystallisation initiation. The formed crystal lies on the top of nano-/micro-structures with greater adhesion force than on the smoother one once it attains a noticeable size.

3.4.4.3. Surface Energy

Surface free energy is often defined as the excess energy associated with the surface presence. It may be expressed regarding either Helmholtz *F* or Gibbs *G* free energies, per unit area [180]. The property of surface energy is usually considered fundamental to an understanding of scale adhesion and the formation of adhesive links. It is commonly determined as interfacial energy γ_{Sv} of solid and vapour phase boundaries in contact according to Young's equation [109]:

$$\gamma_{SV} = \gamma_{Sl} + \gamma_{lv} \cos \theta \qquad (3.8)$$

Where, θ is the dynamic contact angle of the liquid on the surface and *v, l,* and *s,* denote system phases, vapour, liquid and solid, respectively. The total interfacial energy between solid and liquid phases can be divided into a permanent polar part and fluctuating dispersive part [53]. The higher the contact angle the lower the surface energy and the greater the nucleation energy barrier. According to the reported literature, it can be concluded that surface energy plays an important role in mitigating scale formation in the early stages of the fouling process. Expressing differently, the surface energy influences nucleation rate and the work of adhesion [54, 233]. The free surface energy can be changed through one of the following: surface coating, surface finishing, ion sputtering and ion implantation.

The ion implantation method includes bombarding the surface layer with ions such as F, C, Si, etc. in the KeV to MeV energy range [234]. This process lowers the number of free electrons on the surface; hence surface energy will be decreased. By applying the ion implantation as a fouling mitigation strategy, the implantation of SiF_2^+ on the stainless steel surface significantly diminishes the crystallisation fouling [235]. While ion sputtering involves the ejection of the atom from the surface and replacing it with coating atoms [236].

The surface coating is the typical way to modify the surface energy. However, a coating of the surface may produce some disadvantages like adding thermal resistance, cost and complicated coating process. An experiment of crystallisation fouling on the fluorinated diamond-like-carbon (DLC) coated surface showed that almost no scale was found [237]. Separately, the formation of inorganic depositions on heat exchanger surfaces coated with a polymer (SAKAPHEN Si57E), has been effectively inhibited [238]. In the work of Yang, et al. [25], $CaCO_3$ fouling behaviour on copper, Ni-P-PTFE and Cu-DSA molecular self-assembled monolayer surfaces have been experimentally studied. The findings revealed that the deposition rates on the coated surfaces were higher than that for Cu in the presence of air bubbles, but lower when no bubbles were on the surface. The weak fouling-surface interaction on the modified surfaces results in small grains in the first layer of the fouling, hence higher irregularity of the $CaCO_3$ fouling.

However, Bohnet [62] emphasised that there is no correlation between surface free energy and fouling behaviour. He studied the effect of the surface energy of ten different surfaces on the induction time. Figure 3.10 displays that DLC coated surface has the most extended induction period although it has a medium surface energy value among the tested surfaces.
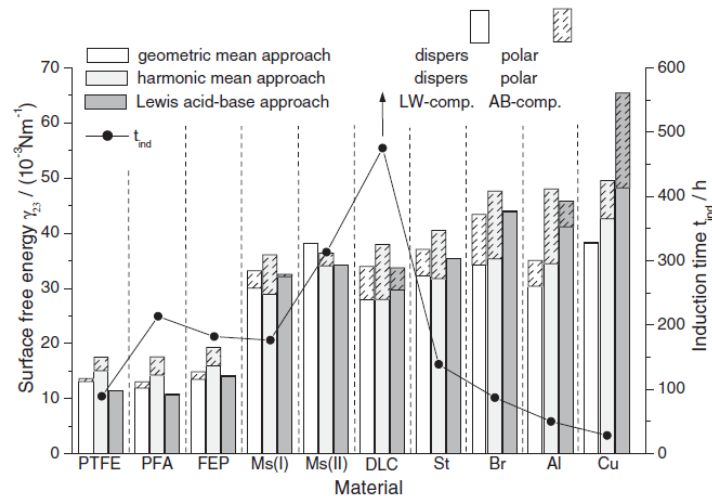
Figure 3.10. Surface energies and scale induction time [62].

3.4.5. Influence of water chemistry

The degree of supersaturation, which is the driving force of the formation of inorganic scale, links directly to the composition of the ionic species in water. Divalent metal cations like calcium and

magnesium are responsible for the hardness in water. It has been found that the relationship is linear between the concentration of $CaCO_3$ in water and scale precipitation potential, where the latter increases three times when the amount of $CaCO_3$ increases from 100 mg.l^{-1} to 300 mg.l^{-1} [12]. Teng, et al. [178] studied the effects of water hardness on the formation of $CaCO_3$ deposits. They observed that the higher the hardness of $CaCO_3$ the higher the fouling resistance and the shorter the induction period. Regarding the deposition rate of minerals, Parsiegla and Katz [239] pointed out that the crystallisation reaction for calcite was second order with respect to calcium at low calcium level and first order at high concentration.

3.4.5.1. Ionic species

The presence of simple metal ions or complex ions in the water may pose an inhibitory impact on the nucleation and growth process of scale crystals. At very low concentrations, cationic additives like magnesium, copper, zinc, lead, manganese, nickel and iron could absorb onto the active growth positions on the precipitate particles [204]. Reddy and Wang [240] reported that magnesium ion (>0.001 M) significantly reduced the crystallisation rate. They demonstrated that the absorption of magnesium at the growth sites of the crystal results in decreasing growth rate constant, hence crystal formation. In the work reported by Chen, et al. [167], the kinetics of $CaCO_3$ surface deposition and bulk precipitation were investigated for different concentrations of magnesium ions using a rotating disk crystalliser (RDC). The results showed that Mg^{2+} has an inhibiting effect on the surface deposition and bulk precipitation as well as $CaCO_3$ polymorphic phases (Fig. 3.11). The inhibition mechanism includes absorbing the ion on the surface of calcite causing crystals distortion. The ratio of calcite to vaterite noticeably increases with the increasing concentration of Mg^{2+}.
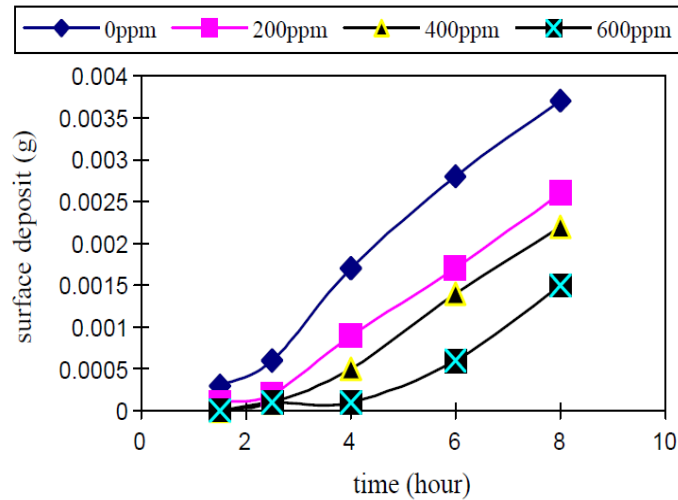
Figure 3.11. Scale mass gain on the surface for different Mg^{2+} levels [167].

The inhibition efficiency of either simple or complex ions of iron is highly strong [204]. Copper ion diminishes the nucleation rate of CaCO$_3$ crystals in moderate water hardness with a restricted concentration range, while Zn reacts with carbonate forming ZnCO$_3$ crystals which enhance the heterogeneous nucleation [241, 242]. Cations like silver, manganese and sodium have no mitigation effects on the scale formation [243-245].

It has been demonstrated by Tai and Chien [244] that the presence of sodium ions slightly influences the induction time of CaCO$_3$ formation in a semi-batch crystalliser. Similarly, it has been found that some monovalent cations such as silver and manganese have little influence on fouling kinetics [243, 245, 246]. However, it is difficult to exclude Cl$^-$ from test solutions to investigate the effect of Na$^+$ alone. It has long been known that chloride ions are aggressive towards many pipe materials by enhancing the corrosion rate [247]. The presence of Cl$^-$ in potable water as a biocide may also potentially diminish the effectiveness of scale control additives such as poly-maleic acid that leads to a totally different response from these additives [138, 248].

Wada, et al. [245] pointed out how the scaling process was affected in presence of Ag$^+$, Al^{3+}, and Cr^{3+} in scale-forming solutions. By using a double diffusion technique, it was found that Al^{3+} ions formed Ag$_2$CO$_3$ crystals which acted as nucleation sites for CaCO$_3$ crystals. Chromium and aluminium have a moderate influence on the growth rate and morphology (Fig. 3.12). The complex ions in water could hinder scale particle growth based on the absorption and poisoning mechanism.

59

The addition of orthophosphate (PO_4^{3-}), arsenate AsO_3^{-4}, and sulphate (SO_4) ions reduced the inorganic scale formation by 80%, 50%, and 20%, respectively at different concentrations [204]. A few studies concerning the effect of SO_4^{2-} have focused on bulk precipitation. It has been found that the presence of SO_4^{2-} has a weak inhibitory effect on scale formation. However, at concentrations above 0.01 M, the transformation of calcite to aragonite is favourable as sulphate ions preferably bind to calcite rather than aragonite [204, 205]. Waly, et al. [179] reported that the induction time of the $CaCO_3$ formation in seawater reverse osmosis system has been increased by 11 times when adding 0.025 mol/L of SO_4^{2-}.
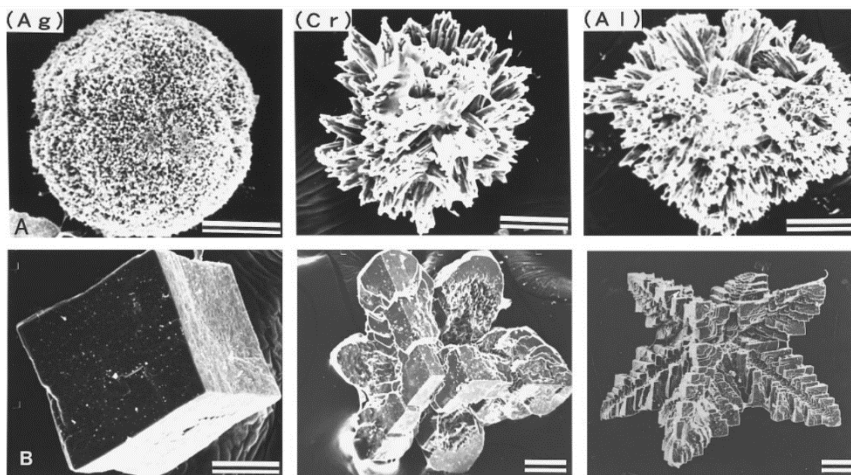
Figure 3.12. Aragonite (top) and calcite (bottom) morphologies in the presence of Ag^+, Al^{+3}, and Cr^{+3} [245].

Dalvi, et al. [248] performed experimental work to determine the role of chemical species (Fe^{3+}, $Fe(OH)_2$, Mo^+, Fe_2O_3, Cr^{3+} and Ni^{2+}) on the scale inhibitors in multistage flash desalination plants. The scaling threshold was indicated by measuring the total alkalinity in the solution. The efficiency of polyphosphonate-based PPN inhibitor was reduced to about 88% and Polymaleic acid-based PMA to 81% at 0.5 ppm of Fe^{3+}. In the presence of 2 ppm of iron (II) hydroxide, the performance of PPN and PMA were retarded to 40% and 32%, respectively. Cr^{3+} at 1 ppm minimises the efficiency of PMA to 88% and PPN to 93%. Finally, nickel and molybdenum have no adverse effect on scale inhibitors performance.

The role of mineral ions in the anti-scaling process varies from inefficient to extremely effective based on ambiguous factors. Tap water contains a range of cations and anions which are presenting

different concentrations. These constituents make the study of the crystallisation fouling process a pronounced challenge.

3.4.5.2. Organic molecules

Natural organics exist in water from various sources. They are complex molecules that affect colour, odour, taste and cause serious health issues. The predominant type of natural organic material is known as humic substances which are classified into humin, fulvic acids and humic acids [249, 250]. The solubility of humic acids, which is pH-dependent, raises the content of total organic carbon (TOC) in potable water. The typical molecular structure of humic acid is shown in figure 3.13 [251]. The presence of TOC in water can inhibit the formation of inorganic scale [252, 253].
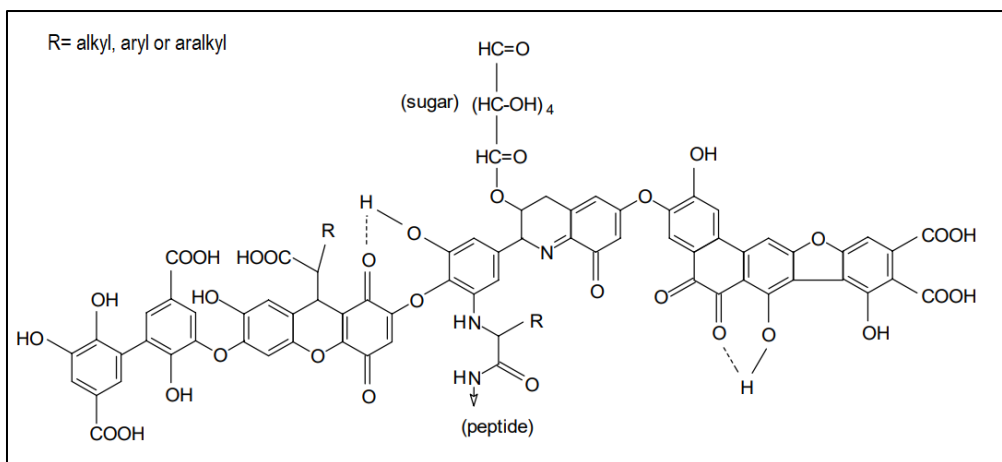
Figure 3.13. Model structure of the humic acid molecule according to Stevenson [254].

Hoch, et al. [255] carried out seeded precipitation of calcite in a sealed reactor at the fixed condition to examine the effect of humic substances insolated as hydrophobic organic acids from the Florida Everglades and as a fulvic acid from Lake Fryxell, Antarctica. The findings showed that hydrophobic acids have a higher inhibitory effect on the growth of calcite than fulvic acid. The inhibitory impact of the organic molecules highly depends on the heteroatom content, aromaticity and molecular weight. However, carboxyl content and aliphatic C–C chain content were found to play a less crucial role in the inhibition process. The concentration of Dissolved Organic Matter (DOM) enhances the inhibition of calcite growth. The increase in DOM concentration reduces the consumption of calcium in the bulk solution (Fig. 3.14).
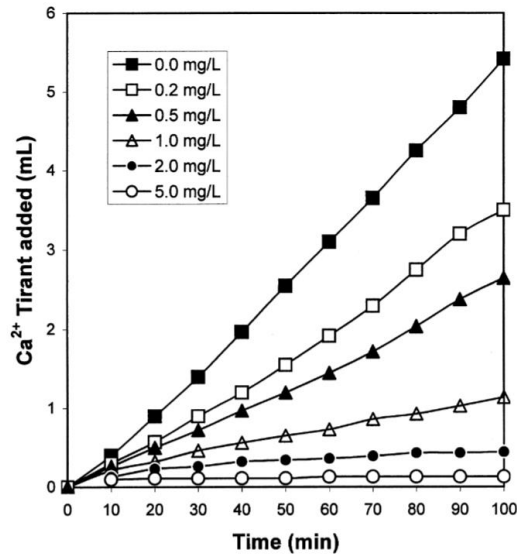
Figure 3.14. Effect of concentration of DOM on the concentration of calcium in the solution [255].

Fan, et al. [256] studied the relationship between the fractional components of Natural Organic Matter (NOM) and the fouling of hydrophobic and hydrophilic microfiltration membranes. The fouling influence is relatively significant in the hydrophobic membrane when the high molecular weight fraction of NOM is added. The aromaticity of the NOM determines flux decline, the higher the aromaticity the lower the solution flux.

3.4.6. Influence of impurities

Scale formation can be strongly influenced by the presence of foreign particles or mineral salts in water [257-259]. The presence of suspended particulates is frequent in the working fluid of many industries. There is a prevailing belief that these solids make the fouling layer weaker and less coherent. In contrast, the scaling tendency of minerals rises when foreign particles are suspended in the solution [260, 261].

Webb and Li [262] mentioned that the presence of solid particulates (iron silicate, silica, and copper oxide) in the water contributes to producing a soft and "fluffy" crust of minerals that could be easily detached by a primitive mechanical method. In the work of Andritsos and Karabelas [27], the effects of added solid particles on the $CaCO_3$ fouling has been examined for three various types of particulate matter (aragonite, calcite, and TiO_2). The addition of aragonite particles results in the highest relative pressure drop in the plate heat exchanger at a fixed pH value of 9, while calcite, in

62

similar conditions, has an insignificant impact on the pressure drop. However, the deposits layer which formed in the presence of aragonite was softer and less coherent than other cases and could be removed by flow shear stress.

3.4.7. Influence of pH

The crystallisation fouling is significantly dependent on solution pH, even more than temperature. As solution pH is increased, the reaction equilibrium shifts to the right-hand side, hence producing more carbonates and bicarbonates, followed by the potential formation of $CaCO_3$ [49, 50, 263]. Augustin and Bohnet [264] presented the effect of the pH on the full range of corrosion and the $CaCO_3$ fouling (Fig. 3.15). Concerning the influence on fouling, they measured the fouling resistance of scale on stainless steel tube in the double pipe heat exchanger for a pH range of 6.2 to 10 at a constant temperature of 42ºC. The surface temperature increased by about 6 ºC due to the scale layer insulation effect for a mentioned range of pH.
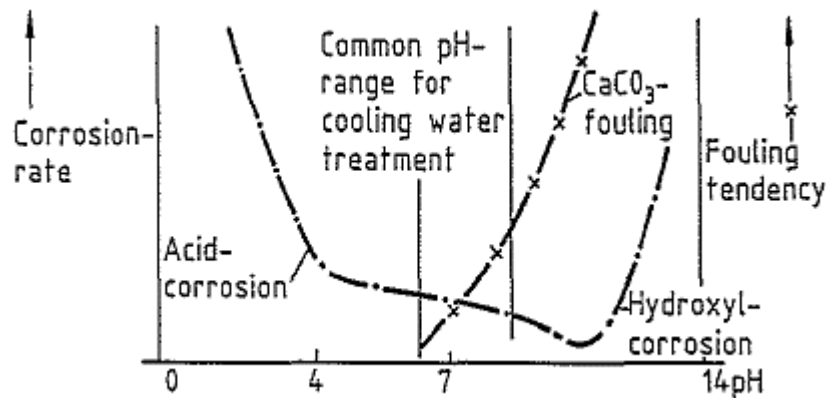
Figure 3.15. The effect of pH on the scale fouling and corrosion [264].

Andritsos and Karabelas [265] studied the bulk precipitation from tap water in the tubular test section for various values of pH. The authors reported that the amount of scale formed on the sample area increased from 2 mg. cm^{-2} to 12 mg. cm^{-2} when pH increase from 8.8 to 10 after two hours of the experiment. Dawson [209] performed a comparison of the influence of pH and temperature on the supersaturation degree. Increasing pH by three units had a much greater influence than temperature when the later increased to 80 ºC. As pH increased from 7 to 8, the supersaturation ratio rises from 3 to 15. As the pH increases the supersaturation of the solution,

the nucleation rate increases leading to the formation of a higher number of crystals. This influence implies the pH change can affect the morphology of $CaCO_3$ deposits as well as the deposition rate as determined by Chen, et al. [266].

Sano and Nakashima [126] recently carried out a series of experiments for studying the effect of acid electrolysed water on the suppression of scale formation. The mineral deposition was examined in a copper millimetre-sized channel in which the surface is heated by hot water. A collection of thermocouples is used to measure the fouling resistance and total heat transfer. Acid electrolysed water controls the pH of the solution, and they found the scale raked on the surface was largely mitigated at pH 6.9 or below. Increasing the pH to 8.1 promotes scale formation around the entrance of a channel causing a significant pressure drop in the system after only 15 minutes of the starting time.

3.5. Fouling monitoring and evaluation techniques

3.5.1. Surface deposition

3.5.1.1. Fouling resistance

Inorganic fouling on the heat transfer surface retards heat transfer to the solution due to the insulation characteristics of scale. The fouling resistance is a measure of heat transfer retardation introduced by scale deposits [131, 223, 267]. In other words, the reciprocal of the overall heat transfer coefficient, as expressed below:

$$R_f = \frac{1}{U_f} - \frac{1}{U_o} \qquad\qquad (3.9)$$

Where, U_f and U_o are the overall heat transfer coefficient of fouled and clean surfaces, respectively. At constant heat flux Q, with surface temperature, T_s, and solution bulk temperature T_b are measured by thermocouples, the U_f and U_o can be calculated by the following general formula:

$$U = \frac{Q}{T_s - T_b} \qquad\qquad (3.10)$$

The fouling resistance is a time-dependent parameter that is most likely found to change according to the trend in figure 3.16. At the early stage of scaling, extremely low and even negative values

of the fouling resistance in some systems may be measured. This can be explained by an increase in the convective heat transfer as a result of turbulent flow over a rougher scale layer.
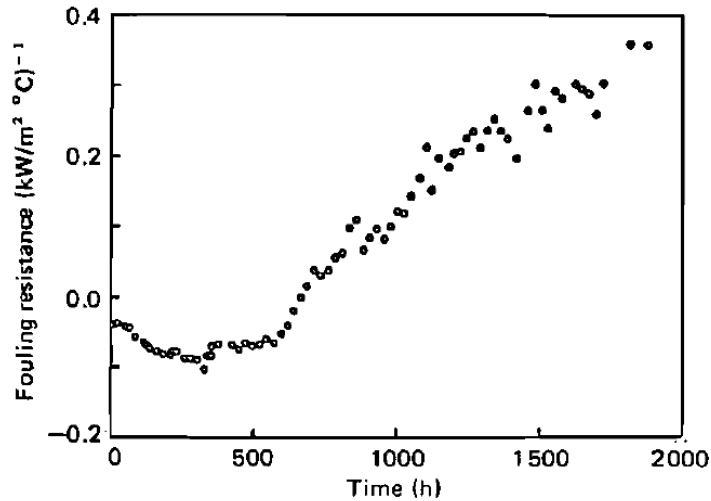
Figure 3.16. Thermal resistance curve for the fouling from geothermal water [29].

The thermal resistance due to fouling can also be estimated from the deposits mass m_d and thickness x_f for known properties of the porous fouling layer [268]:

$$R_f = \frac{m_d}{\rho_f \, \lambda_f} \tag{3.11}$$

$$R_f = \frac{x_f}{\lambda_f} \tag{3.12}$$

Where, $\rho_f \; and \; \lambda_f$ are the density and the thermal conductivity of the porous fouling layer.

3.5.1.2. Surface visualisation

The concentration of foulant ions reduced with time due to deposits formation and this does not reflect what happens in real processes. For achieving a full understanding, once-through in-situ flow visualisation setups were used in some studies [6, 175, 269, 270]. The scale particles on the surface can be observed using a high-performance camera that takes a surface image at an adjustable time step. Figure 3.17 shows the build-up of deposits on the heat transfer surface as

detected by the charged couple device (CCD) video camera. The analysis of the images includes a quantitative assessment of surface deposition by a programming approach in which a set of algorithms improves the image quality and minimises the noise as well as extracting scale-related information such as surface coverage, number of crystals and crystal size distribution [188].
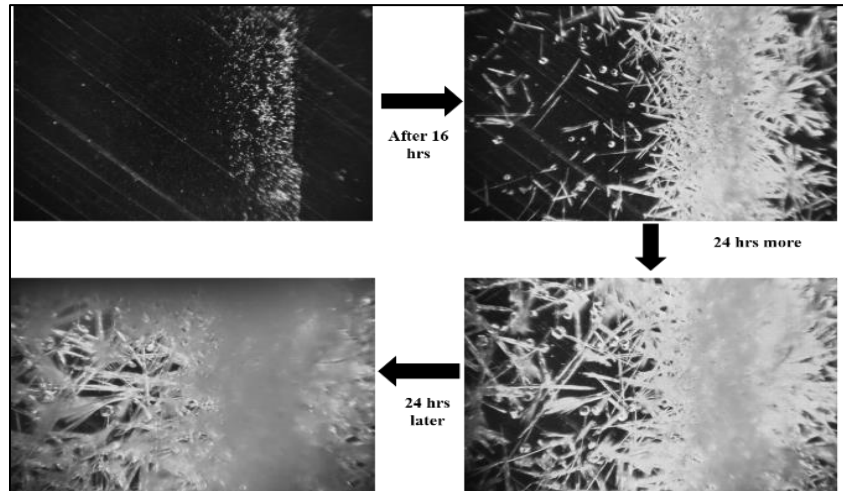
Figure 3.17. Camera images of scale development on the surface.

3.5.1.3. Tube blocking test

Besides the reduction in heat transfer, scale builds up a crust that minimises the flow area or even completely blocks small diameter pipes. This drawback is employed to determine how long the scale need to form in the tube. The flow of supersaturated solution in a capillary metallic tube allows the deposits to form leading to high differential pressure [126, 271, 272]. Zhang, et al. [189] reported that the carbonate scale thickness was non-uniform along the millimetre-sized tube. The thickness decreases with the distance from the entrance of the tube due to the solution supersaturation decrease (Fig. 3.18). The tube blocking technique indicates the induction time of the system with a non-heated surface.
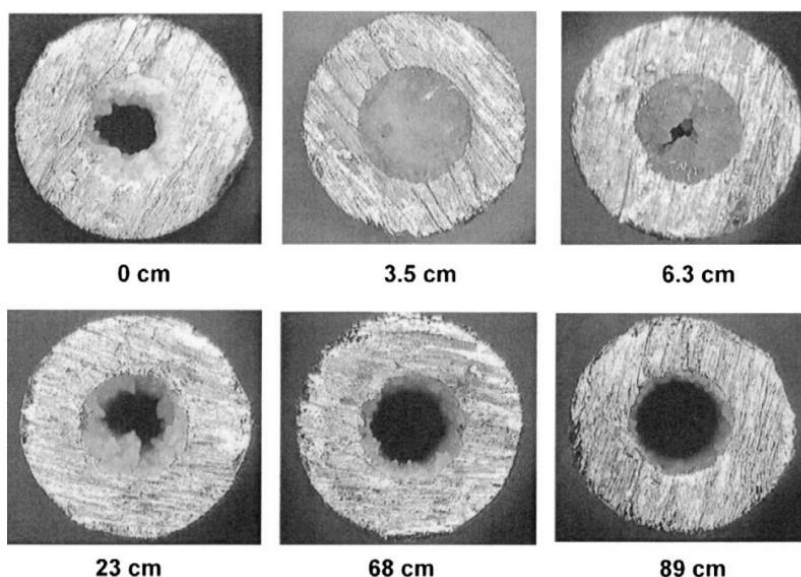
Figure 3.18. Photographs of tube blockage at a different distance from the entrance [272].

3.5.1.4. Electrochemical methods

Once the nucleation and growth of scale crystal take place on the surface, oxygen reduction to hydroxide occurs in parallel. The produced hydroxide ions induce the transformation of bicarbonate to carbonate by bringing about an increase in pH [52, 137, 273]. The analysis of oxygen reduction rate can be used to estimate the scale deposition rate on the surface. Under potentiostatic control, Neville, et al. [274] used a rotating disk electrode (RDE) surface to study the surface scaling, in which cell, two electrodes are connected to Potentiostat; working and resentence electrode. The purpose of the rotating disk is to mix the supersaturated solution. This allows the mass transfer of the scale species to a metallic surface to be well achieved.

3.5.2. Study of bulk precipitation

3.5.2.1. Turbidity measurement

The homogeneous and heterogeneous nucleation in the bulk fluid leads to scale crystals formation. The formed crystals are suspended in the solution, which may reduce the solution transparency. The measure of the solution cloudiness is known as turbidity. The solution turbidity can be determined using a turbidity probe which applies a light beam of a certain wavelength through a solution [5]. The intensity of scattered light by the suspended scale particles is correlated in a turbidity meter with other constants (Eq^n. 3.13$)$. The turbidity measurement can provide important

information about the scaling system such as an induction period and crystals size distribution [173, 275].

$$t_\lambda = \frac{1}{l} \log\left(\frac{I_0}{I_L}\right) \tag{3.13}$$

Where, l is the optical path length and I_0 and I_L are the intensity of the incident and transmitted rays, respectively.

3.5.2.2. Ionic species concentration measurement

The rate of crystallisation reaction can be assessed by determining the concentration of ionic species in the solution which represents the unreacted foulants. Various methods are used to measure the concentration of Ca^{2+}, Mg^{2+}, HCO^-_3 and SO^{2-}_4; namely, a simple titration, electrical conductivity, atomic absorption spectroscopy (AAS), spectrophotometry, radiotracer, and inductively coupled plasma mass spectrometry (ICP-MS) [170, 212, 241, 276-278]. The measurement of the consumption rate of foulant allows understanding of how fast the reaction is, induction time, and reaction rate at different conditions.

3.5.2.3. Evaluation of solution pH

As fouling is a pH-dependent process, it was used to monitor the crystallisation reaction and process termination [49, 279]. At the initial stages of the $CaCO_3$ formation, solution pH increases due to bicarbonate transformation to carbonate and hydroxide ions releases (an alkaline mechanism) [40, 280]. Once the reaction of carbonates and calcium starts, the pH decrease can be noticed as a result of carbonates consumption (Fig. 3.19). The crystallisation reaction is assumed to have finished when no further decrease in the pH values are recorded. However, the measurement of pH is unable to provide a full understanding of the scaling process for different conditions compared with turbidity measurements.
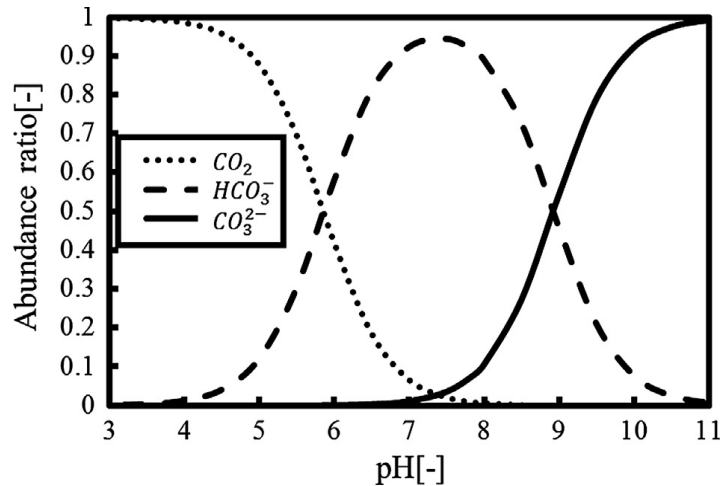
Figure 3.19. The abundance of inorganic carbon compounds as a function of solution pH [52].

3.6. The State of Art

Understanding of crystallisation fouling of industrial and domestic heat transfer systems is of great interest in the scientific community. Inorganic fouling is recognised as one of the serious problems in heat transfer equipment, therefore, so much effort is being made to mitigate and prevent the deposition of minerals. Various aspects of the fouling process have been extensively investigated using different techniques. The researchers have focused on the influence of operating conditions, heat transfer surface properties and using additives on the kinetics of fouling and morphological structure. However, the effect of water chemistry and key operating conditions on surface fouling and bulk precipitation is still not fully understood.

According to the survey presented in this chapter, inorganic scale forms through two mechanisms; surface deposition and bulk precipitation which both proceeds in a complex series of processes. Researchers have investigated the formation of kinetics and scale morphology that are produced by the two mechanisms. As $CaCO_3$ is the most common type of scale, it has been examined in the majority of studies. The kinetics of $CaCO_3$ scaling has been predicted using numerous models. The morphology of $CaCO_3$ is important to the research of crystal growth, adhesion and removal of deposits. Therefore, the effects of different parameters on the morphology of $CaCO_3$ have been highlighted.

The fouling process is affected by operating conditions, water chemistry and surface properties. The operating parameters including flow velocity, temperature, and system pressure significantly

69

affect the fouling process. The solution chemistry such as salt concentration, dissolved CO_2 concentration, the presence of additives, impurities and pH are also able to influence the fouling process. Finally, surface properties like roughness, topography, surface energy and substrate metal could be utilised to accelerate or hinder the fouling process.

The type and quantity of impact made by each parameter are not the same. For instance, temperature, supersaturation, and pH have a strong impact on fouling kinetics. Besides the kinetics, some additives play an important role in distorting the habit of the scale crystals. Conflicting findings have been reported from different experimental studies regarding the effect of some parameters such as flow velocity and surface energy. However, other factors such as pressure and surface roughness pose a secondary impact on scale formation tendency. The impact of fouling on heat transfer efficiency and equipment performance can be evaluated by different techniques.

Despite the investigations done to understand the fouling process, the kinetics and morphology of crystallisation in domestic systems from potable water, surface water and groundwater have received little attention. Inorganic scale formed in domestic appliances is mostly coupled with boiling or subcooled boiling conditions. Due to complex water chemistry and severe temperature and pressure, the kinetics, morphology and adhesion of deposits on household devices are all needed to carefully be considered.

Chapter 4: Development of Rigs

4.1. Introduction

The present study uses four experimental setups/ apparatuses to cover the objectives assigned at the beginning. These setups each serve a particular purpose and come with features and limitations. The boiling static setup was adopted to perform the bulk precipitations experiments. While the other three rigs were used for evaluating the influence of different factors on the surface crystallisation from potable water. The effect of scale formation on heat transfer was assessed using qualitative and quantitative techniques. In this chapter, the development of the experimental rigs used in the investigation including the purpose, design and materials of the rig is described.

4.2. Boiling static setup

4.2.1. Setup purpose

The boiling static setup was built to study the precipitation of inorganic scale from potable water in a closed system. It was a batch crystalliser in which the precipitated scale particles in the bulk fluid and on the surface can be evaluated. The studies of mineral scaling in batch systems have been reported for various operating conditions and assessment techniques [86, 137, 281-283]. For bulk precipitation kinetics, the turbidity of solution and concentration of ionic species were quantitatively determined. The solution content of ionic constituents such as Ca^{2+}, Mg^{2+}, Zn^{2+}, and SO^{2-}_4 was measured as a function of time following an accurate sampling procedure. The precipitation of deposits on the surface takes place on cylindrical samples fixed by a metallic holder.

The effects of bulk temperature, surface roughness, surface material, water chemistry, heating rate and cooling rate on the kinetics and morphology of both bulk and surface precipitations, in absence of fluid flow, were investigated using this setup. As a result of high bulk temperature (> 85 ^{o}C) under atmospheric pressure, the transition pool boiling was the dominant boiling mode. The saturation ratio with respect to mineral salts reduced with time in such a closed system. This unique setup was developed for mimicking a batch evaporation process in domestic and industrial systems. Figure 4.1 illustrates the schematic of scale precipitation during pool boiling in the boiling static setup.
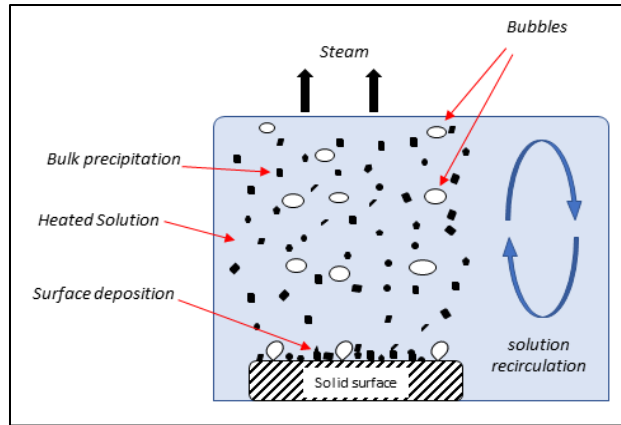
Figure 4.1. Representation of scale precipitation in the boiling static setup.

4.2.2. Setup design

The setup consists of a borosilicate glass beaker, hot plate, thermocouple, sample holder, and identical metallic samples. The sample holder was constructed of stainless steel 316L (SS31603) for minimizing the potential of corrosion products formation. The temperature probe (ThermoScientific, UK) was connected to a laboratory hot plate (Radleys, UK) to control the temperature in a 1000 ml borosilicate glass vessel. The power consumed by the hot plane was ranging from 1748 to 2139 W for the tested temperatures. The schematic drawing of the sample and sample holder as well as the setup are presented in figure 4.2.

Eight cylindrical samples of each copper C12200, aluminium 1050A and stainless steel SS31603 were made with similar heights and diameters of 10 ± 0.05 mm. The composition of metal alloys used in the present work is presented in table 4.1. The metals selected are the most common materials used in constructing pipes and pools in domestic appliances. The samples were fabricated with a hollowed bottom with a depth of 8 ± 0.05 mm to be established on the sample's holder vertical fines. Samples and samples' holders were designed using solid modelling computer-aided design SolidWorks (*v 2018*) and fabricated in the fabrication workshop at the University of Leeds.
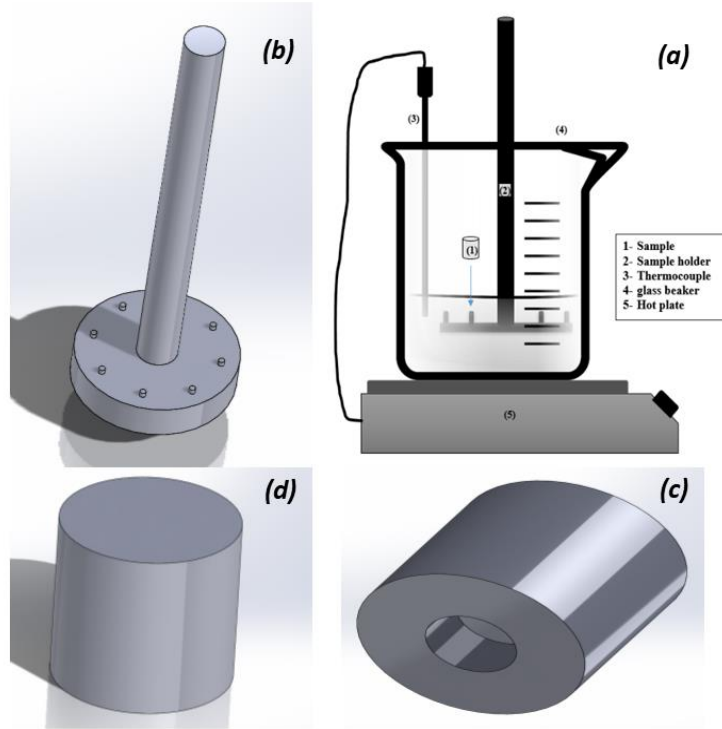
Figure 4.2. Boiling static setup; (A) the entire setup, (B) samples' holder, (C) sample bottom and (D) sample top.

Table 4.1. Composition of metal alloys used in the study.

Stainless steel SS31603		Aluminium 1050A		Copper C12200	
Ingredients	Weight %	Ingredients	Weight %	Ingredients	Weight %
Carbon	0.03	Manganese	0 - 0.05	Phosphorus	0.015 - 0.04
Manganese	2.00	Iron	0 - 0.40	Copper	Balance
Silicon	1	Copper	0 - 0.05		
Chromium	16-18	Magnesium	0 - 0.05		
Nickel	10-14	Silicon	0 - 0.25		
Phosphorus	0.045	Zinc	0 - 0.07		
Sulphur	0.03	Titanium	0 - 0.05		
Molybdenum	2-3	Other	0 - 0.03		
Nitrogen	0.1	Aluminium	Balance		
Iron	Balance				

Experiments of heating and cooling rates were carried out in two different setups; namely, a lab-scale closed system and a commercially available electric kettle. The first setup consists of a 250 ml borosilicate vessel placed on a hot plate to provide the required heating. This simple setup is mimicking the heating process in some appliances such as kettles and uncomplicated coffee makers with a lower heating rate. To enhance the heating rate and to get to the boiling temperature in a shorter period, a silicone beaker heater with a power density of 0.008 W/mm^2 (BriskHeat, USA) was used. The second apparatus is a kitchen electric kettle that has a capacity of 1700 ml and power of 3000 W. The heat was provided through a flat heating element in the bottom of the kettle.

4.3. Once-through flow visualization rig

4.3.1. Purpose of rig

Convective heat transfer and subcooled boiling can be found over a significant area of heat transfer surface in domestic and industrial systems during the convective boiling heat transfer. In such a condition, steam bubbles form and develop on the heated surface with a temperature higher than the saturation temperature. Bubbles then detach from the surface and condense in the bulk solution which is below the saturation temperature [23, 187, 284, 285]. Figure 4.3 shows the convective boiling heat transfer regimes including subcooled boiling conditions. To achieve this condition in the laboratory, the once-through flow visualization rig was employed in which deposition processes can be visualised and followed.
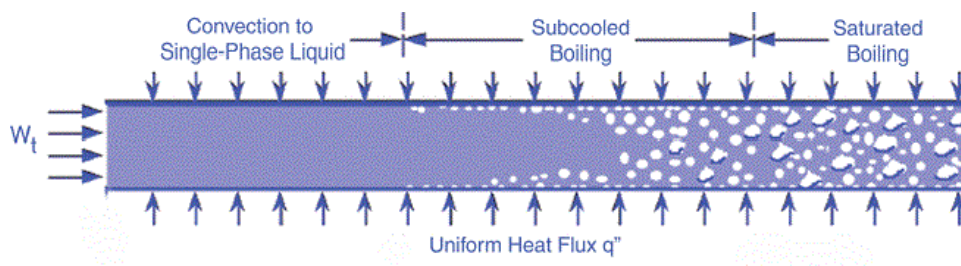
Figure 4.3.Convective and convective boiling heat transfer regimes [286].

The test surface was heated by an electric heater; hence the reaction of inorganic mineral crystallisation occurred on the surface. The fouling of the heat transfer surface can quantitively be assessed by the real-time visualization of scale crystal formation and growth. The visualization

system in the rig was able to collect high-quality images for the surface at different time steps. These images can later be analysed to identify key scale characteristics. Post-experiment, the amount of scale deposits on the surface would be evaluated. The scale structure was also subject to morphological analysis as a qualitative assessment.

The purpose of this experimental setup was to evaluate the influence of different parameters on the scale quantity and structure during convective heat transfer. This includes the study of surface scaling associated with steam bubble formation and fluid flow. The flow was once-through to avoid a decrease in saturation degree with time which may result from fluid circulation [287].

4.3.2. Rig design and modifications

This rig was originally built by Erioni [270] and used later by Sanni [269] and Bukuaghangin [288] to investigate the bulk precipitation of $CaCO_3$ and $BaSO_4$ on the surface. The formation of scale began, based on solution supersaturation, when two brine solutions (formation water and seawater) were mixed inside the visualization cell, the scale particles subsequently precipitated on the test specimen. The precipitation in the bulk fluid and on the surface was evaluated using turbidity measurements and surface imaging, respectively. The surface images obtained from the camera were processed using set of algorithms to estimate the number of crystals, size of crystal and surface coverage.

To study surface deposition, the rig flow lines, and sample geometry was modified. As the scale primarily forms on the heat transfer surface rather than the bulk fluid, the turbidity probe was removed. This study focuses on the surface crystallisation of mineral salts from potable water. One potable water feed pipe was therefore introduced to the flow cell instead of two feed pipes and mixing point. Also, the potable water was fed to the cell at ambient temperature, thus no need for the water bath.

Alternatively, the heating system consists of a stainless-steel cartridge heater (L: 25 mm, OD: 6.5 mm and power: 120W), proportional–integral–derivative (PID) temperature controller (CAL 9900, UK) with an accuracy of ± 1 ℃ and two mineral-insulated thermocouple sensors. The thermocouples were used; one for the controller feedback signal and the second to make sure the surface temperature is the desired value. The apparatus mainly consists of a feed tank, peristaltic digital pump, flow cell, surface heating system, surface imaging system and waste tank. The schematic diagram of the experimental setup is shown in figure 4.4.
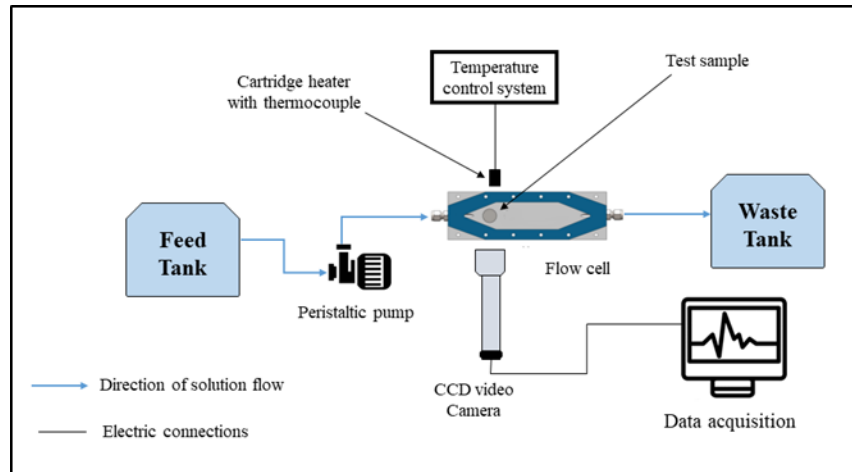
Figure 4.4. Configuration of the experimental setup.

In terms of test sample modification, three cylindrical metallic samples (copper C12200, aluminium 1050A and stainless steel SS31603) with the same surface finish and dimensions of 24 mm (height) and 10 mm (outer diameter) were used. The sample geometry was a one-sided hollow cylinder with an inner diameter of 6.7 mm (Fig. 4.5). The cavity enabled the position of a cartridge heater for heating the sample. The cartridge heater was tightly positioned inside the sample using a heat sink compound to eliminate any gap. A 0.5 mm deep channel was made in the internal wall to install the temperature sensor between the heater and sample.
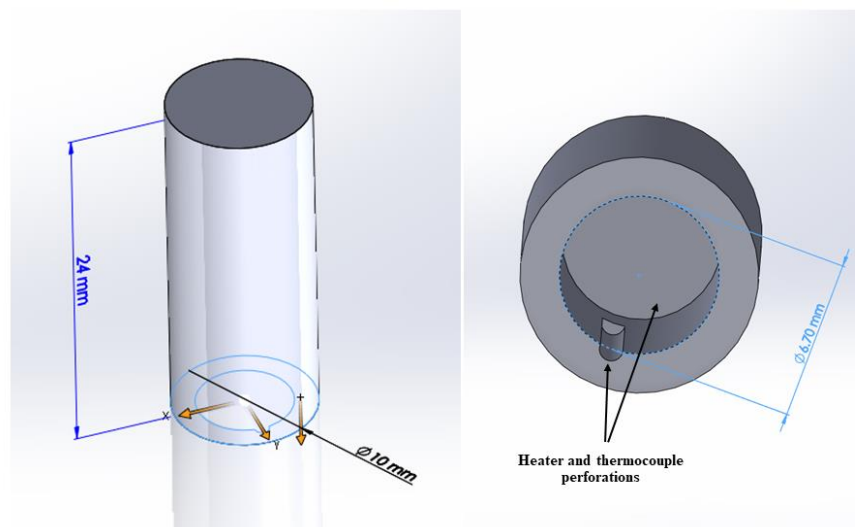
Figure 4.5. The geometry of a sample used in the boiling static setup.

The flow cell (cell volume of 15 ml), where the surface scale forms, was designed to work under atmospheric pressure (Fig. 4.6). It is built of two polymethylmethacrylate plates (230 mm in length and 70 mm wide) separated by a Teflon sheet with a well-defined channel in the middle. The surface deposition was simultaneously monitored through the transparent channel by a digital imaging machine.

A high-performance monochrome digital (charged couple device) CCD video camera with 50 frames per second and 1 mega-pixel resolution was connected to a computer to automatically store the surface images at specific time steps for image analysis. To reduce the noise and improve the focus, each frame after lens adjustment has a size of 1mm x 1mm. A mercury lamp was adopted to enhance the quality of the surface image as well as an optic system to magnify the images. On the computer, the surface imaging and camera settings are controlled using a user-defined software developed by the LabVIEW platform. Figure 4.7 shows a photograph of a once-through visualization rig including the software interface.
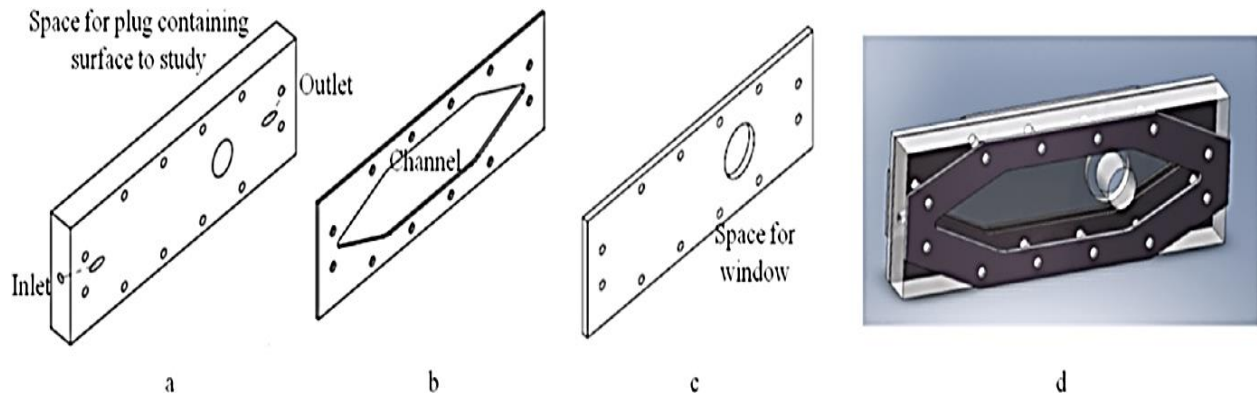
Figure 4.6. The flow cell is composed of (a) PMMA back plate, (b) Teflon plate, (c) PMMA front plate. (d) The entire body of the cell [289].
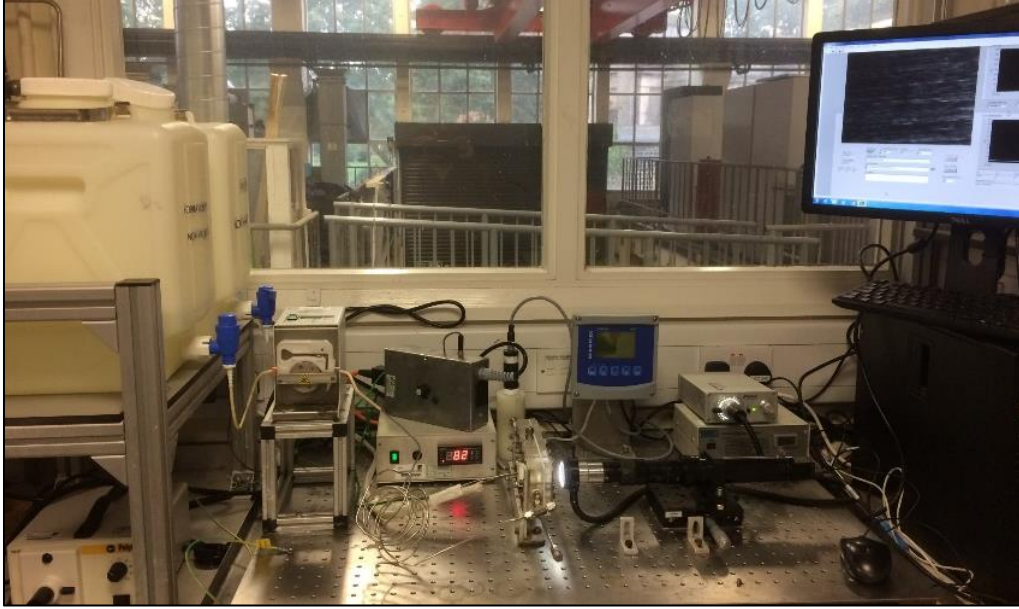
Figure 4.7. Photograph of once-through visualisation rig including the software interface.

4.4. Flow-Evaporation Scaling Cell

4.4.1. Purpose of setup

In the Flow-Evaporation Scaling Cell (FESC), the inorganic fouling of heat transfer surface associated with partial water evaporation was studied during pool boiling. This setup was an open system where a once-through flow was adopted. As mentioned in the Theory chapter, water boils and evaporates during the heating process in household appliances. For instance, an Espresso machine provides hot water and steam from two different outlets. In the FESC, the test fluid flows in 5 mm depth over the test heated surface in a laminar flow regime. The steam bubbles generate on the surface, detach from the metal, and then depart the solution to the atmosphere.

Figure 4.8 illustrates the schematic of surface deposition under the conditions used in the FESC. The heat transfer condition in the FESC differs from that in the visualization rig. The steam bubbles generated on the heated surface depart to the atmosphere through the open window at the top of the cell mimicking the process in steaming equipment. The presence of bubbles either on the surface or in the solution affect the heat and mass transfer phenomena [23, 187, 290, 291].
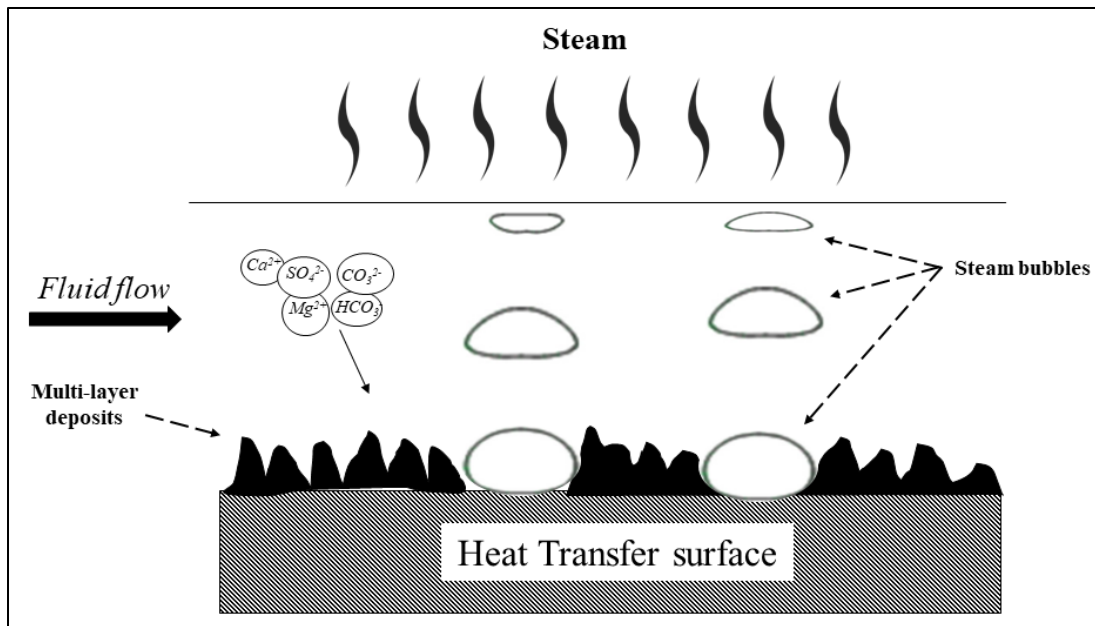
Figure 4.8. Schematic of surface deposition in the FESC.

4.4.2. Design of the setup

The schematic view of the experimental apparatus is shown in figure 4.9. It consists of a solution tank, peristaltic pump, test flow cell, sample heating system, data acquisition system and waste tank. This once-through flow system was adopted to avoid any reduction in the saturation state which may result from solution re-circulation. The flow cell (cell volume of 400 ml), where surface scale deposits, was designed to work under atmospheric pressure with an open top window (Fig. 4.10). The outer body part was made of nylon 6 (130 mm length, 50 mm wide and 55 mm height) with 10 mm wall thickness. In the middle, a metal sample was fixed by a sample holder made of nylon 6. The cell had three inlets and six outlets positioned at different height levels from the base to regulate or change the level of solutions in the cell when required. The flow level and flooding potential for flow Reynolds number of 5000 were simulated using ANSYS-FLUENT (V18.1), as shown in figure 4.11.
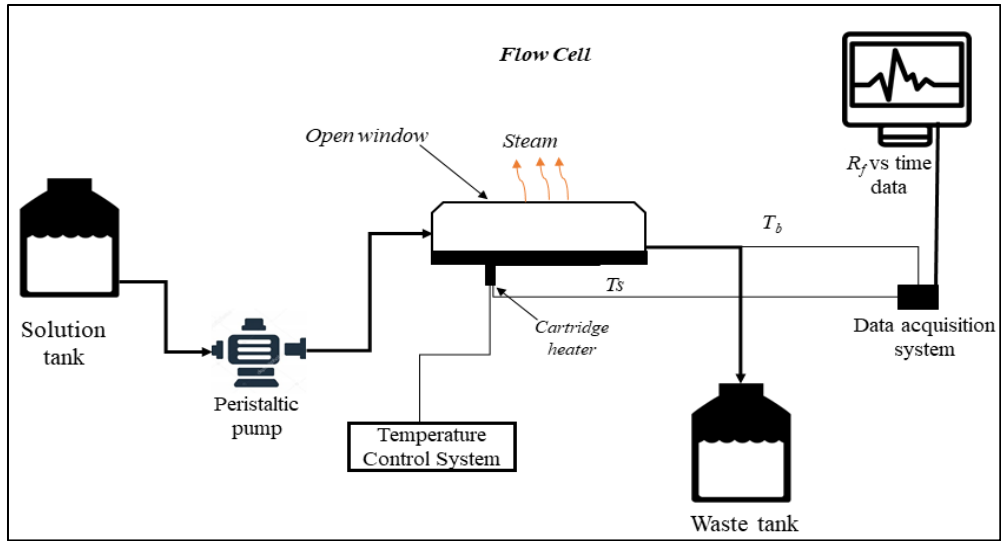
Figure 4.9. Configuration of the FESC apparatus.
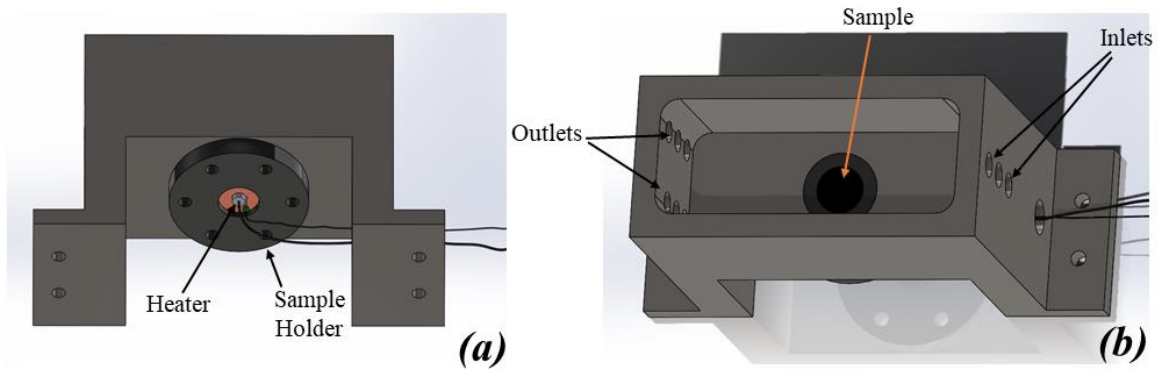
Figure 4.10. The flow cell; (a) bottom view and (b) top view.
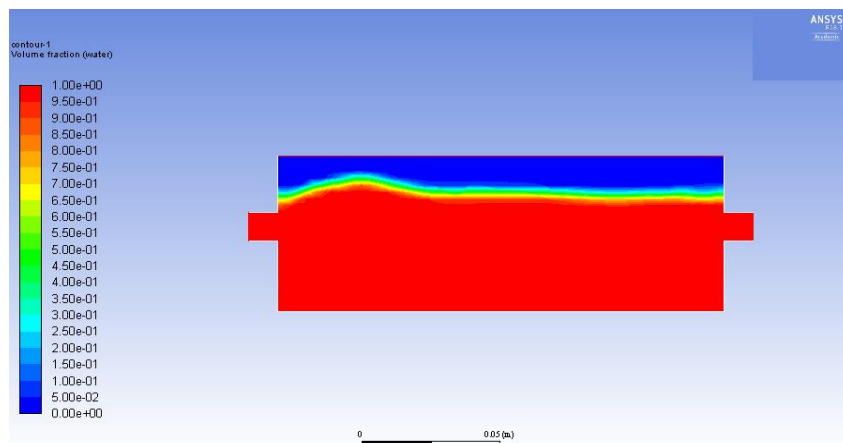
Figure 4.11. Test solution flow dynamics in the FESC.

80

Aluminium alloy 1050A (Al ≥ 99.5%) was used to fabricate test cylindrical specimens (22 mm height and 20 mm diameter). Aluminium alloy was chosen as it is one of the most common materials used in constructing heat transfer surfaces in household appliances. The specimen was fabricated into a one-sided hollow cylinder with an inner diameter of 6.7 mm and a depth of 19 mm (Fig. 4.12). A bore enables to firmly position a cartridge heater for heating the surface. A 3 mm depth channel was perforated in an internal wall to fit a K type temperature thermocouple between heater and specimen. The test specimen surface, which is the exposed surface to the solution, was grounded with silicon carbide paper (1200 grit) and then polished with diamond suspension (0.5 μm).
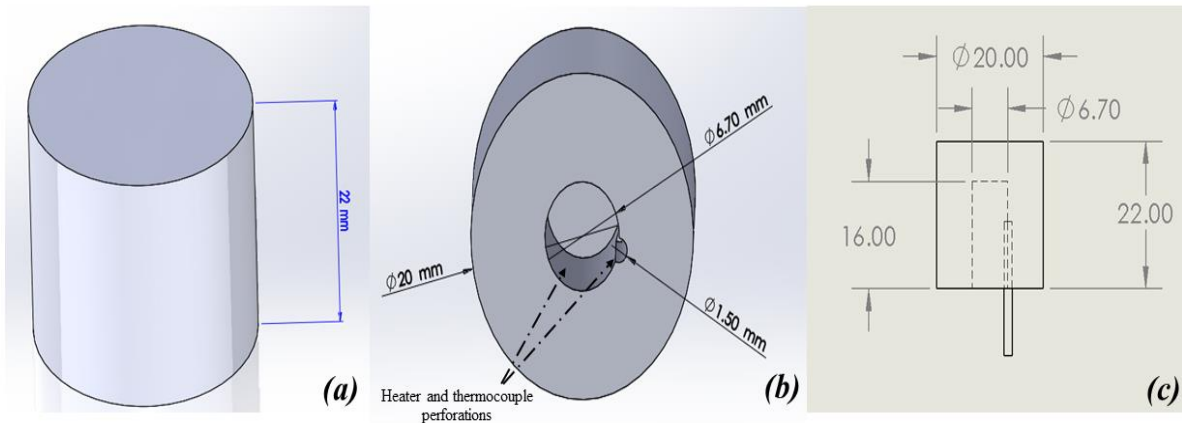
Figure 4.12.The FESC test sample; (a) top view, (b) bottom view and (c) 2D side view of an assembly of thermocouple and sample (all dimensions in mm).

The heating system used in this setup to heat the surface and control the temperature was the same one used in the visualization rig, except there were four thermocouples attached to the system. Three mineral-insulated K type thermocouple sensors (TC Direct, UK) were adopted to measure the surface and bulk temperatures. It was complicated to measure the bulk temperature at a certain point within the cell, as such, the average value of the inlet and outlet temperatures was considered. These thermocouples were linked to a data acquisition system from which the numeric data of temperature were extracted to determine the fouling resistance. The fourth temperature thermocouple was placed in the channel between the heater and specimen to send feedback to the heating system which controls the temperature with an accuracy of ± 1 ℃.

4.4.3. Data acquisition system

The data acquisition system (NI USB-6009 multifunction I/O, UK) is a device in which the analogue signals are converted into digital numeric values. The multifunction I/O device was connected to Quad K-type analog thermocouple amplifier 10 V (Playing with Fusion, USA) and other components to build the multi-channel thermocouple data logger box (Fig. 4.13). The system was able to process the signal from four K-type thermocouples. The numeric values of temperature as a function of time are sent to a computer via USB cable. Figure 4.14 represents a schematic of the data acquisition system.

Figure 4.13. Photograph of the multi-channel thermocouple data logger.

The number of measurement samples, rate of sampling and time step size can be inputted using a user-defined software developed by the LabVIEW platform. Besides controlling the data acquisition, the software displays curves of the temperatures that change with time. At the end of the total measurement time, the temperature and time values from two thermocouples were stored in an Excel spreadsheet on a computer. The temperature data and heat flux of the heater was used later to calculate the fouling resistance due to surface fouling. The heat flux was measured using a plug-in power monitor (Brennenstuhl, Germany).
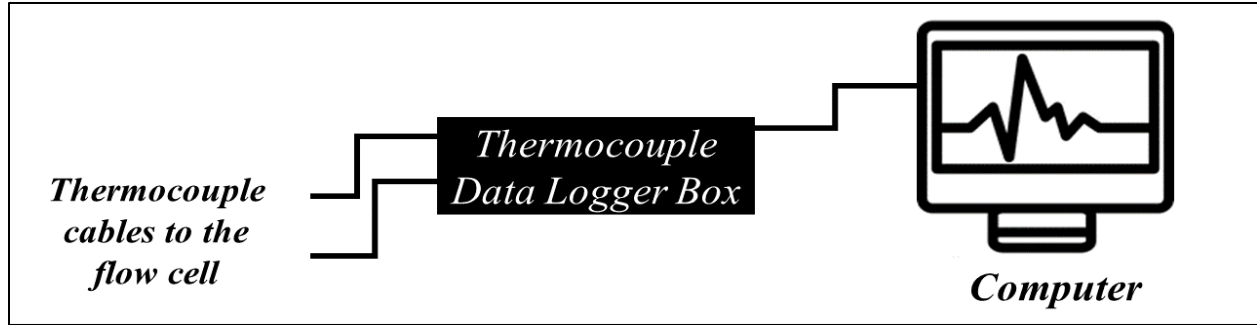
Figure 4.14. Representation of the data acquisition system.

4.4.4. Fouling evaluation technique

The influence of the resistive fouling layer on the heat transfer was evaluated using fouling resistance. The formation of salt deposits on the heat transfer surface raised the surface temperature and subsequently reduced the bulk temperature. The fouling resistance was a measure of heat transfer retardation introduced by scale deposits. Fouling resistance was estimated using the following analytical expressions for convection heat transfer [26]:

$$R_f = \frac{1}{U_f} - \frac{1}{U_c} \qquad (4.1)$$

$$R_f = \left(\frac{T_s - T_b}{Q}\right)_f - \left(\frac{T_s - T_b}{Q}\right)_c \qquad (4.2)$$

$$R_f = \frac{T_s^f - T_s^c - T_b^f + T_b^c}{Q} \qquad (4.3)$$

Where, U_f is the overall heat transfer coefficient for the fouled surface, U_c is the overall heat transfer coefficient for the clean surface, Q is the heat flux, T_s is the surface temperature, T_b is the bulk temperature, superscript f is for fouled surface and c is for a clean surface.

4.5. Pressurised Flow-Evaporation Scaling Cell

4.5.1. Purpose of cell

The pressurised flow-evaporation scaling cell (PFESC) was developed to assess the influence of system pressure on the crystallisation fouling on the heat transfer surface. Studies investigated the relationship between the system pressure and the formation of scale in the upstream oil and gas

industry [216-218]. In this cell, the test solution completely evaporates and leaves the cell as steam which is similar to the process in some household devices such as steam iron and electric steamer. The sequestration of steam inside the cell raises the pressure. Thermodynamically, pressure increases the water boiling point until reaching the equilibrium state. The surface temperature to boiling water at the desired pressure was estimated using the integrated form of the Clausius-Clapeyron equation (Eq^n 4.4) [292].

$$\ln \frac{P_1}{P_2} = \frac{\Delta H_{vap}}{R} \left[\frac{1}{T_2} - \frac{1}{T_1} \right]$$ (**4.4**)

Where, T_2 and T_1 are the boiling point of water at P_2 and P_1, respectively, ΔH_{vap} is the molar heat of vaporization and R is the gas constant. The fouling impact on the heat transfer was evaluated using fouling resistance by the same procedure mentioned previously.

4.5.2. Design of the setup

The Flow-Evaporation Scaling Cell was modified to create a pressurised atmosphere in the cell. The steaming process inside the cell generated a pressure higher than the atmospheric pressure. A 3D diagram of the modified pressurised flow cell is shown in figure 4.15. The body wall thickness of the primary cell was increased to 20 mm of Nylon 6 as a constructing material. The number of inlets and outlets was reduced to one each. The upper window was covered with a Nylon 6 lid (150 mm length, 70 mm wide and 10 mm height) which was attached to the body of the cell with stainless steel screws. A gasket made of rubber was placed between the lid and the cell to prevent potential leakage. No modifications were inserted on the specimen, specimen holder and heating system.

The experimental setup for pressure tests (Fig. 4.16) is different when compared with the configuration of the primary setup of FESC presented previously in figure 4.9. For the pressure test, the test solution flowed by the peristaltic pump to the cell in which the solution evaporated, and the formed steam generated pressure inside the cell. The pressure was measured using an analogue positive pressure gauge (RS components, UK). A pressure relief valve with a variable maximum set pressure was used to control the pressure. The solution flowing in the cell transformed completely to steam and batched through the relief valve, and liquid effluent was excluded. The exiting steam is condensed in a plastic tube and flows to a waste tank. Temperature measurements were acquired and processed in the same procedure as the FESC experiments. The

experimental apparatus described herein mimics, to some extent, the steaming process in some domestic appliances, such as steam irons and boilers.
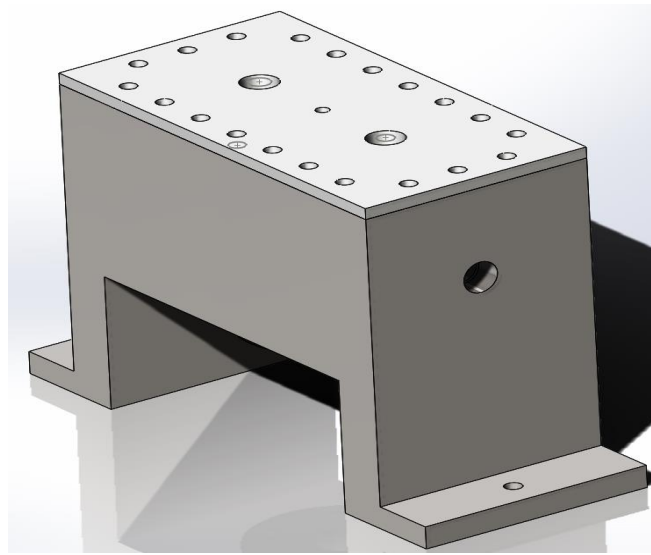
Figure 4.15. Pressurised flow cell.
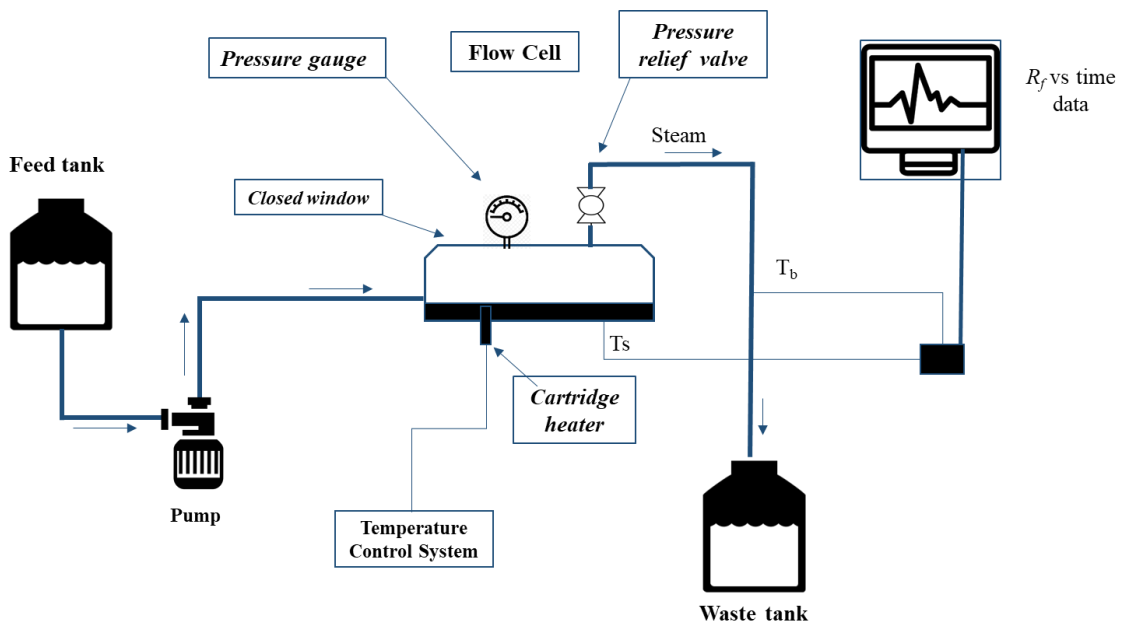
Figure 4.16. Configuration of the experimental setup for pressure tests.

4.6. Summary of rigs development

In this chapter, the development of experimental setups used in the work has been presented. The development description includes the purpose of setup, design of setup and assessment methods. The phenomena of fluid flow, heat transfer and scale formation have also been described. The results collected from these experimental rigs allow achieving the project aim and objectives. The goal of fabricating four experimental setups is to study the key parameters which affect the scaling kinetics and microstructure from potable water in domestic appliances. The following aspects were considered:

- Scale formation in bulk solution and on heat transfer surface.

- Different boiling conditions; saturated pool boiling and subcooled boiling.

- Once-through flow system and closed system.

- Quantitative and qualitative measurements.

The flow cells, samples, samples' holder and essential components were designed using solid modelling computer-aided tool SolidWorks (V 2018) and fabricated in the fabrication workshop at the University of Leeds.

Chapter 5: Research Methodology

5.1. Introduction

The experimental methodology including the materials, conditions, preparation of test solutions and sample preparation for each experimental rig is presented in this chapter. The materials and conditions for each experiment set are selected based on the real application in domestic appliances and water distribution systems. Besides the experimental methodology, the development and calculation procedure of the in-house saturation ratio/index calculator is described. The surface and bulk solution characterisation techniques used in the present work are discussed in terms of working principle, the purpose of measurement, conditions of measurement. A full description of the research methodology allows researchers to develop an understanding of the process that occurs in each setup. First, the chemical reagents used in the preparation of test solutions, and the preparation procedure of the test surface are discussed.

5.1.1. Chemical reagents

The main test solution used in experiments is commercially-available bottled water with a pH of 7.2. It has been chosen for its hardness of 307 ppm of $CaCO_3$, which is almost the same as potable water hardness in some areas of the south UK. Different grades of reagent salt are used in the preparation of the other test solutions, as listed in Table 5.1. The NaOH and HCl solutions in different dilutions were used for surface cleaning and pH adjustment purposes.

Table 5.1. Chemical reagents were used in the experiments.

Name	Formula	Assay	Manufacturer
Calcium chloride hexahydrate	$CaCl_2.6H_2O$	97 to 100%	Honeywell Fluka
Sodium sulfate	Na_2SO_4	Min. 99%	VWR Chemicals
Magnesium chloride hexahydrate	$MgCl_2.6H_2O$	100%	VWR Chemicals
Sodium bicarbonate	$NaHCO_3$	99.5%	ACROS Organics
Sodium chloride	NaCl	Min. 99%	Honeywell Fluka
Humic acid	$C_{187}H_{186}O_{89}N_9S$	100%	Sigma Aldrich
Sodium nitrate	$NaNO_3$	Min. 99.5 %	VWR Chemicals
Zinc sulfate monohydrate	$ZnSO_4.H_2O$	Min. 99.9%	Sigma Aldrich
Hydrochloric acid	HCl	36.5-38.0 %	Sigma Aldrich
Sodium hydroxide	NaOH	98.5-100.5%	VWR Chemicals
Potassium chloride	KCl	99.5-100.5%	Honeywell Fluka
polyvinyl sulfonate	-	-	Clariant AG

5.1.2. Sample preparation

The metallic specimens employed in the experimental investigations were cleaned and prepared according to the initial surface finishing. The top surface of the sample, which is the tested surface, was grinded with silicon carbide paper (1200 grit) and then polished with diamond suspension (0.5 μm) by a mechanical polishing method. It was subsequently rinsed with acetone, distilled water, and dried at 37 ºC for 24 hours. Prior to an experiment, the roughness of the top surface of the dried sample was examined using the 3D optical profiler NPFlex (Bruker, USA). The arithmetic average of the absolute values of the surface roughness (Ra) was kept within the desired value for all tests. Figure 5.1 displays the topography of the sample surface using 3D optical profiler NPFlex.
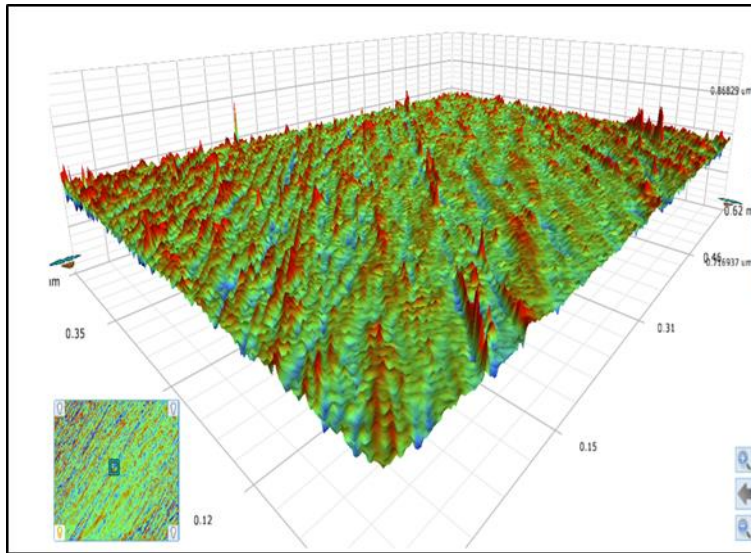
Figure 5.1. Microstructure of aluminium surface of Ra= 20 nm in NPFlex optical profiler.

5.2. Boiling static setup

5.2.1. Materials and brine solutions

The experimental setup consists of a 1000 ml borosilicate glass beaker, hot plate, thermocouple, sample holder, and identical metallic samples. The sample holder is constructed of stainless steel 316L (SS31603) for minimising the potential of corrosion products formation. Eight cylindrical samples of each copper C12200, aluminium 1050A and stainless steel SS31603 have been made with the same surface finish and dimensions. The metals/alloys selected are the most common materials used in constructing pipes and pools in domestic appliances.

The main solution used (solution A) in the experiments is commercially available bottled water. It has been chosen rather than tap water, for its hardness of 307 mg/L of $CaCO_3$ and pH of 7.2. Solution A was used as a test solution in experiments, bulk temperature, surface material, surface roughness, evaporation rate, heating rate and cooling rate. Table 5.2 shows the composition of the solutions. The composition of solution A has been taken from the bottled label. However, the same batch has been analysed using the inductively coupled plasma atomic emission spectroscopy (ICP-OES). The analysis showed variation in some element's concentrations such as calcium 94 mg/L, magnesium 30.8 mg/L and sulphate 10.4 mg/L.

Table 5.2. Solution compositions.

Ions (mg/L)	Brine solutions											
	A	B	C	D	E	F	G	H	I	J	K	L
Ca^{2+}	80	200	-	80	80	80	80	80	80	80	80	80
Mg^{2+}	26	-	26	88	150	26	26	26	26	26	26	26
Na^+	6.5	183	130	6.5	6.5	6.5	6.5	6.5	136	136	25.3	43.6
K^+	1	-	-	1	1	1	1	1	1	1	1	1
Si^{4+}	15	-	-	15	15	15	15	15	15	15	15	15
HCO_3^{-}	360	-	360	360	360	360	360	360	360	360	360	360
SO_4^{2-}	14	400	-	14	14	21.3	28.7	36	14	14	14	14
Cl^-	10	350	84	177	361	10	10	10	216	216	10	10
NO_3^{-}	3.8	-	-	3.8	3.8	3.8	3.8	3.8	3.8	3.8	54	104
Zn^{2+}	-	-	-	-	-	5	10	15	-	-	-	-
TOC	-	-	-	-	-	-	-	-	2	4	-	-
Initial SR of $CaCO_3$	0.19	-	-	0.19	0.19	0.19	0.19	0.19	0.19	0.19	0.19	0.19
Initial SR of $CaSO_4$	0.007	0.52	-	0.007	0.007	0.007	0.007	0.007	0.007	0.007	0.007	0.007

The eleven other brines (B-L) have been prepared to investigate the effect of water composition on the precipitation process. The highest concentrations of SO_4^{2-}, Mg^{2+}, NO_3^{-}, Zn^{2+} and Total Organic Carbon (TOC) have been chosen based on the drinking water quality report of the World Health Organization (WHO) [18]. Solutions B and C are to study the precipitation of $CaSO_4$ and $MgCO_3$, respectively, from potable water at the test conditions. Solutions A, D and E were used

to compare the effect of Mg^{2+} concentration on the precipitation of inorganic scale. The effect of Zn^{2+} concentration was examined using solutions F, G and H. The influence of Total Organic Carbon (TOC) on scaling was evaluated from solutions A, I and J. Finally, solutions A, K and L were employed for studying NO^{3-} concentration.

Solution B is prepared by mixing 1.09 g/L of $CaCl_2.6H_2O$ and 0.59 g/L of Na_2SO_4 into deionised water. Solution C is made by mixing $MgCl_2.6H_2O$ and $NaHCO_3$ into deionised water. Finally, solutions D and E are prepared by adding $MgCl_2.6H_2O$ to solution A to obtain the magnesium content to 88 and 150 mg/L, respectively. Solutions E, F and G are made by adding 0.013, 0.027 and 0.041 g/L of zinc sulphate monohydrate to solution A, respectively. In the preparation of brines K and L, 0.068 and 0.137 g/L of sodium nitrate was dissolved in solution A.

The humic acid solubility is pH-dependent, as such, the pH of deionized water was raised to 12 by adding 3 ml of NaOH solution (50 wt. %) to each litre of water. 26 and 9.75 mg/L of humic acid was dissolved using a magnetic stir bar at a rate of 600 rpm to obtain a TOC concentration in solutions J and I, respectively. As the inorganic carbonate formation is favoured at high pH values, the pH of the humic acid solution was lowered to 7 using 2.5 ml of HCl (20 vol. %) solution. Based on the corrected volume of the humic acid solution, salts $CaCl_2.6H_2O$, Na_2SO_4, $NaHCO_3$ and $MgCl_2.6H_2O$ were dissolved at the same mixing rate to achieve almost the same composition of solution A.

The salts used in the preparation of brine solution were weighed using a digital laboratory balance (Oxford GM2505D) with an accuracy of $\pm$ 1.5 mg. The salts then were dissolved using a magnetic stir bar at a rate between 600 - 900 rpm at room temperature. All these solutions were filtered using 20-25 μm filter paper to exclude the effect of impurities, and then a sample from each solution is taken to measure the initial value of pH and ion content. The Saturation Ratio of $CaCO_3$ and $CaSO_4$ has been calculated for each solution based on the initial concentrations of scale species at a temperature of 25 ºC using the in-house spreadsheet-based calculator.

5.2.2. Conditions

The experimental conditions of the tests carried out in this setup have been adopted based on the conditions in some potable water heating closed systems. Table 5.3 displays the tested parameters, their values, and other fixed conditions.

Table 5.3. Experimental conditions.

Tested parameter	Values	Other fixed parameters
Bulk temperature	85, 95 and 105 ℃	Pressure: 1 bar, Surface: stainless steel, Solution: A, Roughness (*Ra*): 8-24.6 nm Evaporation rate: 4.6 ml/ min
Surface material	Copper, Aluminium and Stainless Steel	Pressure: 1 bar, Bulk temperature: 95 ℃, Roughness (*Ra*): 8-24.6 nm Solution: A, Evaporation rate: 4.6 ml/ min
Surface roughness	10, 106, and 182 nm	Pressure: 1 bar, Bulk temperature: 95 ℃, Surface: Stainless steel Solution: A, Evaporation rate: 4.6 ml/ min
Evaporation area	3.3, 4.6 and 5.7 ml/ min	Pressure: 1 bar, Bulk temperature: 95 ℃, Roughness (*Ra*): 8-24.6 nm Solution: A, Surface: Stainless steel

		Pressure: 1 bar,
Magnesium content	26, 88 and 150 mg/L	Bulk temperature: 95 ºC, Roughness (Ra): 8-24.6 nm Evaporation rate: 4.6 ml/ min, Surface: Stainless steel
Zinc content	0, 5, 10 and 15 mg/L	Pressure: 1 bar, Bulk temperature: 95 ºC, Roughness (Ra): 8-24.6 nm Evaporation rate: 4.6 ml/ min, Surface: Stainless steel
TOC content	0, 2 and 4 mg/L	Pressure: 1 bar, Bulk temperature: 95 ºC, Roughness (Ra): 8-24.6 nm Evaporation rate: 4.6 ml/ min, Surface: Stainless steel
Nitrate content	3.8, 54 and 104 mg/L	Pressure: 1 bar, Bulk temperature: 95 ºC, Roughness (Ra): 8-24.6 nm Evaporation rate: 4.6 ml/ min, Surface: Stainless steel

To achieve different evaporation areas, three reaction vessels were used: tall-form beaker, low-form beaker, and wide-form vessel. The conditions of heating and cooling rate experiments are

listed in tables 5.4 and 5.5. The different heating rates (Table 5.4) were achieved using the original beaker for the slow heating, the wrapped beaker for the medium heating, and finally the electric kettle to get the rapid heating. The heating rates were determined by the linear progression of the initial rising period of temperature (approximately between room temperature and 90 ºC). Once attaining the boiling temperature, the heat source is switched off and the cooling rate investigations start. Table 5.5 shows the experimental configurations for the cooling rate experiments and temperature reduction rates. In the forced cooling experiment, the solution has been cooled in one litre jacketed vessel. Fresh tap water at room temperature is used as a coolant with no flow velocity. All tests of determining the effects of the heating and cooling rate are performed using solution A.

Table 5.4. Experimental setup for each heating rate.

Experimental configuration	Heating regime	Time to reach 100 ºC	Heating rate (ºC / min)
Uncovered beaker	Slow	39 min	3.19
Heating band-wrapped beaker	Medium	16 min	6.35
Electrical kettle	Rapid	2.34 min	30.6

Table 5.5. Experimental setup for each cooling rate.

Experimental configuration	Heating regime	Cooling rate (ºC/ min)
Natural cooling	Slow	-0.9
Forced cooling	Rapid	-7.39

5.2.3. Experimental procedure

The experimental procedure of the temperature, material, roughness, and evaporation area tests (set 1) slightly differs from that of magnesium, zinc, TOC, nitrate content, and heating and cooling rates (set 2). For set 1, solution A is heated to the boiling point ($\approx$ 100 °C), then for every 100 ml

of the evaporated water, a metallic sample and 1 ml of solution were taken from the test vessel. The solution level in the test vessel decreases with time as shown in figure 5.2. The solution volume was mixed with 9 ml of a quenching (KCl/polyvinyl sulfonate) solution to prevent further precipitation. Quenching solution was prepared by dissolving 1 gm of polyvinyl sulfonate (PVS) scale inhibitor and 5.71 gm of potassium chloride (KCl) in 1000 ml of distilled water, then the pH was adjusted to a value between 8 – 8.5. The weight of the metallic sample was evaluated, and the surface deposits were characterised. While the 10 ml solution sample is used to assess the bulk concentration of cations (i.e., calcium, magnesium) by atomic absorption spectrophotometer (AAS) (Agilent Technologies, USA).

Fixed heat flux
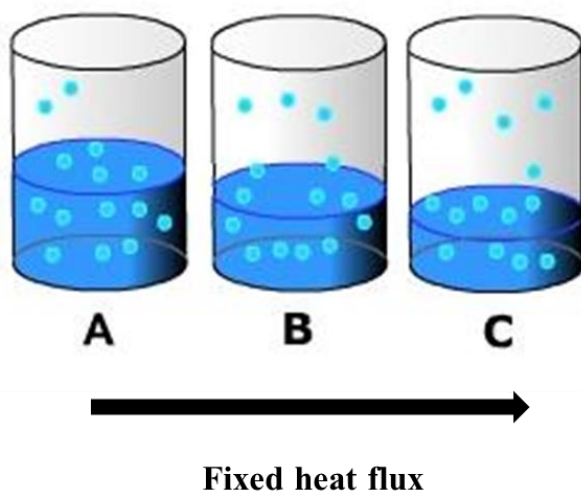
Figure 5.2. Solution evaporation as a function of time.

The procedure of set 2 includes heating one of the solutions to its boiling temperature under atmospheric pressure. Once the heat source is switched on, solution sampling is regularly undertaken. By using a pipette, 1 ml of the solution sample is mixed with 9 ml of a quenching solution. The first portion of the solution sample is used to measure the bulk concentration of cations by AAS. Other portions of the sample are also used to determine the solution pH and turbidity.

5.2.4. Surface deposition characterization

Prior to the experiment, surface roughness parameters were evaluated prior to the experiments using the 3D optical profiler NPFlex (Bruker, USA). A digital laboratory balance (Oxford GM2505D, UK) with an accuracy of ± 1.5 mg is used to determine the initial and final weight of dried samples. The deposit morphology was examined using a Philips X'Pert X-ray diffractometer (XRD) (X'Pert MPD, Cu anode x-ray source, Netherlands) with the 2 theta between 5 to 70º for 35 minutes at a step size of 0.033 degrees and Scanning Electron Microscope (SEM) (Carl Zeiss EVO MA15). Elemental analysis of the deposits was carried out using an Energy-dispersive X-ray (EDX) (Oxford Instruments AZtecEnergy) with an accelerating voltage of 15 kV and a working distance between 9.2 to 10 mm.

5.2.5. Bulk precipitation analysis

Prior to an experiment, the pH and ionic content of the solution were evaluated using a pH-meter (HI 8014 Hanna, UK) and atomic absorption spectrophotometer (AAS), respectively. The concentration of total organic carbon (TOC) was measured by Hach-Lange IL550 analyzer (Hach Lange Ltd, UK). During the test, the measurements of pH and turbidity of the solution are done using a HI 8014 Hanna pH-meter and DR-890 Colorimeter (CAMLAB, UK), respectively. The content of sulphate SO_4^{2-} in solution has been analysed using a spectrophotometer (DR3900, HACH, Lange, UK) with sulphate cuvette test. The bulk concentration of cations namely, Ca^{2+}, Mg^{2+} and Zn^{2+} by AAS as a function of time.

5.3. Once-through flow visualization rig

5.3.1. Materials and solutions

Three cylindrical metallic samples (copper C12200, aluminium 1050A and stainless steel SS31603) with the same surface finish and dimensions of 24 mm (height) and 10 mm (outer diameter) are used. A commercially available bottled water has been used as the fouling test fluid in all experiments carried out in the flow visualization rig. Table 5.6 shows the specified composition of test water.

5.3.2. Conditions

The effect of operating conditions and surface material and roughness was studied in this setup during subcooled flow conditions. One test fluid with fixed composition was used for all

experiments. The fluid inlet temperature is maintained constant during the experiments at 23 ± 1 ℃. The tested parameters, their values and other fixed conditions are stated in table 5.7. The effect of steam bubbles presence on the heated surface was monitored using the high-performance camera under all conditions.

Table 5.6. Composition of the test solution.

Ion	mg/L
Ca^{2+}	80
Mg^{2+}	26
Na^+	6.5
K^+	1
Si^{4+}	15
HCO^{3-}	360
SO_4^{2-}	14
Cl^-	10
NO^{3-}	3.8
Dry residue at 180 ℃	345
SR to aragonite $CaCO_3$ at 25 ℃	0.92

Table 5.7. Experimental conditions for flow visualization rig.

Tested parameter	Values	Other fixed parameters
Surface temperature	80, 90 and 100 ℃	Pressure: 1 bar, Surface: copper, aluminium, and stainless steel, Roughness (*Ra*): 23-37.3 nm Flow rate: 4 ml/ min Experimental time: 72 hours
Surface material	Copper, Aluminium and Stainless Steel	Pressure: 1 bar, Surface temperature: 90 ℃,

		Roughness (*Ra*): 13-27 nm
		Flow rate: 4 ml/ min
		Experimental time: 72 hours
Surface roughness	31, 96, 181, and 384 nm	Pressure: 1 bar, Surface temperature: 90 ℃, Surface: stainless steel, Flow rate: 4 ml/ min Experimental time: 72 hours
Flow rate	0.65, 1.5, 2.4, 4 and 6.23 ml/ min	Pressure: 1 bar, Surface temperature: 90 ℃, Surface: stainless steel, Roughness (Ra): 10 - 18.6 nm Experimental time: 72 hours
Experimental time	48, 72, 96 and 120 hr.	Pressure: 1 bar, Surface temperature: 90 ℃, Surface: stainless steel, Roughness (Ra): 10 - 18.6 nm Flow rate: 4 ml/ min

The bulk and cell wall temperatures were measured using a digital K-Type thermocouple thermometer (Comark KM330, UK). However, the variation in the bulk and wall temperatures was insignificant. Investigation of the effects of temperature was carried out based on surface temperatures rather than the temperature of the heater. Table 5.8 lists the temperatures of the heater, surface, cell wall and bulk solution for stainless steel.

Table 5.8. Temperature data from the flow visualization cell

Heater temperature (ºC)	Surface temperature (ºC)	Cell wall temperature (ºC)	Bulk temperature (ºC)
86.7	80	44.5	68
98.2	90	52.5	75.5
116.5	100	57	86.5

5.3.3. Experimental procedure and imaging process

The apparatus mainly consists of a feed tank, peristaltic digital pump, flow cell, surface heating system, surface imaging system and waste tank. The test solution is pumped using the peristaltic pump from the feed tank through a plastic tube to the flow cell. A thermocouple is attached to the feed tube to measure the inlet temperature. Inside the cell, the solution flows over the heated surface in the laminar flow regime toward the cell outlet. The exiting solution then flows to a waste tank. The imaging system collects images of the surface at a specified time interval. A high-performance monochrome digital (charged couple device) CCD video camera with 50 frames per second and 1 mega-pixel resolution is connected to a computer to automatically store the surface images at specific time steps for image analysis. On the computer, the surface imaging and camera settings are controlled using a user-defined software developed by the LabVIEW platform.

5.4. Flow-Evaporation Scaling Cell (FESC)

5.4.1. Materials and solutions

Three types of sample material were adopted in the investigation of surface substrate effect: copper C12200, aluminium 1050A and stainless steel SS31603. For other tests, aluminium alloy 1050A (Al $\geq$ 99.5%) was used as a surface material. Aluminium was chosen as it is one of the most common materials used in constructing heat transfer surfaces in household appliances.

The composition of solutions used in the present experiments is given in table 5.9. Solution A is the commercially-available bottled water. Solutions B was prepared by dissolving 0.437 g/L $CaCl_2.6H_2O$, 0.21 g/L $MgCl_2.6H_2O$, 0.495 g/L $NaHCO_3$ and 0.02 g/L Na_2SO_4 in deionized water. 167 mg of sodium chloride NaCl was dissolved in solution B to increase the concentrations of chloride to 315 mg/L and sodium to 202 mg/L in solution C. Different amounts of $MgCl_2.6H_2O$

were added to solution B to obtain Mg^{2+} concentration of 0, 52, 104 and 150 in solutions D, E, F and G, respectively. Ca-CO$_3$ and Mg-CO$_3$ systems were achieved in solutions H, I and J.

The concentration of SO_4^{2-} was varied in solution B by adding 0.026, 0.186 and 0 g/L of Na_2SO_4 to produce K, L and M. To examine the effect of zinc concentration, solutions N, O and P were prepared by adding $ZnSO_4.H_2O$ to solution A. The TOC solutions (Q and R) were prepared according to the procedure described in the Static Boiling Setup section. The salts used in the preparation of brine solution were weighed using a digital laboratory balance (Oxford GM2505D) with an accuracy of ± 1.5 mg. The salts then were dissolved using a magnetic stir bar at a rate between 600 - 900 rpm at room temperature. All these solutions were filtered using 20-25 µm filter paper to exclude the effect of impurities, and then a sample from each solution is taken to measure the initial value of pH and ion content.

Table 5.9. Solution compositions for FESC experiments.

Elements, mg/L	[Ca^{2+}]	[Mg^{2+}]	[HCO$_3^-$]	[SO$_4^{2-}$]	[Cl$^-$]	[Na$^+$]	[Zn^{2+}]	TOC
Solution A	80	26	360	14	10	6.5	-	-
Solution B	80	26	360	14	216	136	-	-
Solution C	80	26	360	14	315	202	-	-
Solution D	80	0	360	14	140	136	-	-
Solution E	80	52	360	14	292	136	-	-
Solution F	80	104	360	14	443	136	-	-
Solution G	80	150	360	14	577	136	-	-
Solution H	80	0	360	0	140	130	-	-
Solution I	0	26	360	0	75	130	-	-
Solution J	0	80	360	0	233	130	-	-
Solution K	80	26	360	42	216	149	-	-
Solution L	80	26	360	126	216	188	-	-
Solution M	80	26	360	0	216	130	-	-
Solution N	80	26	360	21.3	10	6.5	5	-
Solution O	80	26	360	28.7	10	6.5	10	-
Solution P	80	26	360	36	10	6.5	15	-
Solution Q	80	26	360	14	10	6.5	-	2

Solution R	80	26	360	14	10	6.5	-	4

5.4.2. Conditions

The tested parameters, their values, and other fixed conditions in the FESC are stated in table 5.10. The influence of operating conditions, surface properties and water chemistry on surface crystallisation of inorganic scale were assessed during saturated pool boiling conditions. The fluid inlet temperature is kept constant in all experiments over a range of $23.1\pm1 – 24.6\pm1$ ºC. The bulk fluid temperature increases as surface temperature increased. In all experiments of mineral scaling conducted on the aluminium surface at temperatures between 80 to 110 ºC, the formation of thin passivation film of aluminium oxide was investigated.

Table 5.10. Experimental conditions for Flow-Evaporation Scaling Cell setup.

Tested parameter	Values	Other fixed parameters
Surface temperature	90, 100 and 110 ºC	Pressure: 1 bar, Surface: aluminium, Roughness (*Ra*): 21.7-44.9 nm Flow rate: 8 ml/ min Experimental time: 24 hours Solution: A
Surface material	Copper, Aluminium and Stainless Steel	Pressure: 1 bar, Surface temperature: 100 ºC, Roughness (*Ra*): 26.8-40 nm Flow rate: 8 ml/ min Experimental time: 24 hours Solution: A
Surface roughness	0.2, 1.18, 1.48, and 1.91 µm	Pressure: 1 bar,

		Surface temperature: 90 ℃,
		Surface: aluminium,
		Flow rate: 8 ml/ min
		Experimental time: 24 hours
		Solution: A
Flow rate	1.54, 8 and 13 ml/ min	Pressure: 1 bar, Surface temperature: 100 ℃, Surface: aluminium, Roughness (Ra): 19 - 32.4 nm Experimental time: 24 hours Solution: A
Experimental time	2, 5, 16 and 24 hr.	Pressure: 1 bar, Surface temperature: 100 ℃, Surface: aluminium, Roughness (Ra): 28.9 - 34.1 nm, Flow rate: 8 ml/ min, Solution: A
Mg content	0, 26, 52, 104 and 150 mg/L	Pressure: 1 bar, Surface temperature: 100 ℃, Surface: aluminium, Roughness (Ra): 28.9 - 34.1 nm, Flow rate: 8 ml/ min,

		Experimental time: 24 hours, Solutions: A, D, E, F and G
Sulphate content	0, 14, 42 and 126	Pressure: 1 bar, Surface temperature: 100 ℃, Surface: aluminium, Roughness (Ra): 28.9 - 34.1 nm Flow rate: 8 ml/ min Experimental time: 24 hours Solutions: A, M, K and L
Na and Cl content	[Cl$^-$]: 10, 216, 315 mg/L [Na$^+$]: 6.5, 136, 202 mg/L	Pressure: 1 bar, Surface temperature: 100 ℃, Surface: aluminium, Roughness (Ra): 10 - 35 nm Flow rate: 8 ml/ min Experimental time: 24 hours Solutions: A, B and C
TOC content	0, 2 and 4 mg/L	Pressure: 1 bar, Surface temperature: 100 ℃, Surface: aluminium, Roughness (Ra): 17 – 26.4 nm, Flow rate: 8 ml/ min, Experimental time: 24 hours,

		Solutions: A, Q and R
Zinc content	0, 5, 10 and 15 mg/L	Pressure: 1 bar, Surface temperature: 100 ºC, Surface: aluminium, Roughness (Ra): 22.4 – 31.2 nm, Flow rate: 8 ml/ min, Experimental time: 24 hours, Solutions: A, N, O and P

5.4.3. Experimental procedure

The test solution is placed in the feed tank at room temperature. The solution is fed to the flow cell using a peristaltic digital pump (MS-2/12 Reglo, Ismatec, Germany) at a controlled flow rate. The solution flows with a laminar profile over the heated aluminium surface without fluid recirculation. The heating system provides the required heat to the test specimen. As the experiments were performed at surface temperatures between 90-110 ºC, the test solution partially evaporates. The generated steam leaves the cell through the top window, while the remaining liquid discharges to the waste tank. The real-time measurements of temperature allow the fouling resistance to be calculated after being stored on a computer.

5.4.4. Solution and surface characterization

Prior to an experiment, the pH and ionic content of the solution were evaluated using a pH-meter (HI 8014 Hanna, UK) and atomic absorption spectrophotometer (AAS), respectively. The arithmetic average of the absolute values of the surface roughness (Ra) was measured using the 3D optical profiler NPFlex. A digital laboratory balance (Oxford GM2505D, UK) with an accuracy of ±1.5 mg was utilised to weigh the specimen before and after a test.

For the post-experiment analysis, the fouled aluminium surface was rinsed with deionised water and later dried for 24 hours at 37 ºC in an oven. Scanning Electron Microscope (SEM) (Carl Zeiss EVO MA15) and a Field Emission Scanning Electron Microscopes (FE-SEM) (Hitachi SU8230)

were used to examine the habit of the scale crystals. Elemental analysis of the deposit crystals was performed using an Energy-dispersive X-ray (EDX) (Oxford Instruments AZtecEnergy) with an accelerating voltage of 15 kV and a working distance between 9.2 to 10 mm. The X-ray diffraction (XRD) patterns for the scale layer were measured using a Philips X'Pert X-ray diffractometer (X'Pert MPD, Cu anode x-ray source, Netherlands) with the 2 theta between 5 to 70º for 35 minutes at a step size of 0.033 degrees.

5.5. Pressurized Flow-Evaporation Scaling Cell (PFESC)

5.5.1. Materials and solutions

The purpose of the PFESC is to evaluate the effect of system pressure on the fouling kinetics and morphology during saturated boiling conditions. Aluminium alloy 1050A (Al $\geq$ 99.5%) was adopted as a surface substrate for pressure tests. Regarding the test solution, the commercially-available bottled water with a pH of 7.2 was used. The composition of the test solution is previously listed in table 5.6.

5.5.2. Conditions

As mentioned earlier, aluminium is the test substrate at a variable initial temperature which was set to achieve the desired pressure. The influence of three absolute pressures were examined in the PFESC: 100, 170 and 250 kPa at a surface temperature of 100, 122 and 135 ºC, respectively. The tested samples have a mean roughness value (R_a) over a range of 10-35 nm. The flow rate was reduced to 0.8 ml.min^{-1} in comparison with the FESC experiments to avoid the high-pressure drop inside the cell. Also, pumping a lower amount of solution to the cell demands lower heating to evaporate the liquid. The time of pressure experiments was 250 minutes. The characterizations of solution and surface were similar to those in the FESC setup.

5.5.3. Experimental procedure

The scale-forming solution flows by a peristaltic pump to the cell in which the solution evaporates and the formed steam generates pressure inside the cell. The pressure was measured using an analogue positive pressure gauge (RS components, UK). A pressure relief valve with a variable maximum set pressure was used to control the pressure. The solution flowing in the cell transforms completely to steam and batches through the relief valve, and liquid effluent is excluded. The exiting steam condenses in a plastic tube and flows to a waste tank. Temperature measurements were acquired and processed in the same procedure as the FESC experiments. The experimental

procedure described herein mimics, to some extent, the steaming process in some domestic appliances, such as steam irons and boilers.

5.6. Saturation ratio calculation approach

As it is essential to assess the kinetics of scale formation, solution supersaturation was determined using the in-house spreadsheet-based calculator. This calculator was developed to cope with limitations that lead to unrealistic outcomes in the commercially-available calculators. Some of these tools are only suitable for a specific system such as scaling in the oil and gas industry, and the inability to predict the saturation state as a function of time. The concentration of Cl^- affects the salinity of solution, thus the equilibrium between HCO_3^- and CO_3^{2-}. The content of Cl^- is estimated by a commercial calculator based on Ca^{2+} concentration obtained from $CaCl_2$ as present in artificially-hardened solutions. However, the present tool comes with the following features which adopt the potable water scaling system:

- Calculating the saturation ratio of solution concerning different mineral salts and polymorphs.

- CO_2 partial pressure is includable but it's not mandatory to proceed with the calculations.

- Capable of predicting the concentration of HCO_3^- and CO_3^{2-} for known Ca^{2+}, hence change in supersaturation as a function of time, temperature, and solution volume.

- The concentration of Cl^- can be specified by the user, and not estimated by the calculator based on Ca^{2+} content.

Two assumptions are made in the current calculation of saturation ratio (SR); no atmospheric CO_2 dissolves in the solution, and salinity is estimated based on chloride content. The input parameters required to calculate the SR are temperature, scale species concentration, solution pH and CO_2 partial pressure resultant from bubbling. Saturation index (SI) is the logarithm of SR that can be expressed as follows [293]:

$$SI = \log SR \tag{5.1}$$

$$SI = log[Ca^{2+}] + log[HCO_3^-] + logK_2 - logK_{sp} + pH \tag{5.2}$$

Where, k_{sp} is the solubility product constant and k_2 is the second ionization constant of bicarbonate that represents the CO_3^{2-} - HCO_3^- equilibrium:

$$HCO_3^- \leftrightarrow CO_3^{2-} + H^+ \tag{5.3}$$

$$k_2 = \frac{[H^+][CO_3^{2-}]}{[HCO_3^-]} \tag{5.4}$$

K_2 can be estimated based on solution temperature (T) and salinity (S) [294]:

$$pK_2 = 17.0001 - 0.01259S - 7.9334*10^{-5}S^2 + \frac{936.291}{T} - 1.87354\ln(T) - \frac{2.61471S}{T} + \frac{0.07479S^2}{T} \tag{5.5}$$

The solubility product constant, k_{sp}, is an independent parameter on temperature. The k_{sp} correlation of each polymorphic phase of CaCO₃, CaSO₄ as anhydrite and MgCO₃ as magnesite are listed in table 5.11.

Table 5.11.Solubility product constant correlations (T in K).

Mineral salt	K_{sp} correlation	Reference
CaCO₃ (aragonite)	$\log K_{sp} = -171.9773 - 0.077993T + \frac{2903.293}{T} + 71.595\log T$	[38]
CaCO₃ (calcite)	$\log K_{sp} = -171.9065 - 0.077993T + \frac{2839.319}{T} + 71.595\log T$	[38]
CaCO₃ (vaterite)	$\log K_{sp} = -172.1295 - 0.077993T + \frac{3074.688}{T} + 71.595\log T$	[38]
CaSO₄ (anhydrite)	$\log K_{sp} = -215.509 - 0.070707T + \frac{6075.2}{T} + 85.685\log T$	[47]
MgCO₃ (magnesite)	$\log K_{sp} = 7.267 - \frac{1476.604}{T} - 0.033918T$	[39]

The effect of CO₂ on the supersaturation of the test solution is included in the calculation approach. The bubbling of CO₂ with certain pressure dissolves partially in the solution and converts to HCO_3^- according to the following equilibrium reaction:

$$CO_2 + H_2O \leftrightarrow H^+ + HCO_3^- \tag{5.6}$$
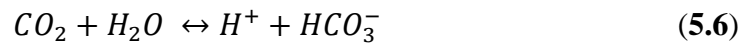
To estimate the contribution of CO_2 to the bicarbonate content in water, the dissolution constant and the molar concentration of CO_2 is needed. The solubility of CO_2 is evaluated by estimating Henry's law coefficient (K_H) of CO_2 in the brine solution, as given below:

$$K_H = \frac{[CO_2]}{PCO_2} \qquad (5.7)$$

PCO_2 refers to the partial pressure in the bar. K_H is expressed as a function of temperature [38]:

$$\log K_H = 108.3865 + 0.01985076\,T - \frac{6919.53}{T} - 40.45154\log T + \frac{669365}{T^2} \qquad (5.8)$$

The first ionisation constant of the carbonic acid, k_1, expresses the equilibrium between dissolved CO_2 and HCO_3^- as stated below:

$$k_1 = \frac{[H^+]\,[HCO_3^-]}{[CO_2]} \qquad (5.9)$$

Similar to the second ionization constant, k_1 is determined from Eq^n. 5.10 based on temperature and salinity [294]:

$$pk_1 = -8.712 - 9.46 * 10^{-3}S + 8.56 * 10^{-5}S^2 + \frac{1355.1}{T} + 1.7976\ln(T) \qquad (5.10)$$

The equations mentioned above were incorporated in one Excel (2016) spreadsheet with different tabs for different calculation options, as presented in figure 5.10.

Figure 5.3. Screenshot of spreadsheet-based supersaturation calculator.

5.7. Summary

The research methodology including materials, solutions, experimental procedure, and conditions for each experimental setup is presented in this chapter. The sample materials and their composition are described. The preparation of brine solutions and the reagents used in the preparation are displayed. The main test solution is commercially available bottled water. For each apparatus, the full operating conditions, specimen material and properties are mentioned. The typical procedure of experiments in each rig is fully described. Finally, the characterisation of surface and solution prior to and post the experiment is also presented.

The main techniques used in the characterisation are also described including the purpose of technique, working principle and analysis settings. For surface analysis, NPFlex, SEM-EDX, XRD and contact angle measurement are the techniques used in this research. The bulk solution examination includes AAS, turbidity measurement and spectrophotometry. Other measurements, which have been mentioned in each rig section, are the gravimetric measurement of mass gain and pH measurement. As the solution supersaturation is crucial in fouling kinetics analysis, a saturation ratio/ index spreadsheet-based calculator was developed to overcome the limitations in the known commercial calculators. The calculation procedure including the mathematical correlations and models is presented in the current chapter.

Chapter 6: Crystallisation Fouling in Batch Systems

6.1. Introduction

Formation of mineral scale, particularly $CaCO_3$, has long been a concern in domestic appliances such as boilers, steamers and washing machines. It is an extremely common and complex problem in industrial and domestic systems where potable water is a working fluid [2, 137]. Potable water used in domestic or industrial applications generally contains a variety of ions prone to precipitate over a range of concentrations depending on water quality and its geographic location. The precipitated layer of inorganic salt, therefore, comprises $CaCO_3$, $CaSO_4$, $Mg(OH)_2$, etc., generated by a chemical reaction of cations and anions in a solution.

Fouling of heat transfer surfaces in domestic appliances results in environmental and economic impact. The power consumption of electric boilers, steam irons, washing machines, dishwashers and coffee makers is significantly increasing due to the retarded thermal conductivity of the fouling layer [51]. It is estimated that the heat transfer efficiency of gas water-boilers will be reduced by 30% over a period of 15 years if no effective mitigation strategy is applied [295].

Dobersek and Goricanec [19] investigated the influence of mineral deposits on the consumption of electrical energy for domestic appliances. They found that scale layers of 2 mm thickness reduced the heat flow by 10% to 40%, depending on the composition of the scale. For the same scale thickness, the power consumption of an electric boiler is two times higher than that for a washing machine. Moreover, the precipitation of salts in the bulk solution also affects the quality of the produced water such as taste and colour [17].

Investigations into crystallisation fouling have largely focused on the surface deposition in the industrial systems using solutions supersaturated with calcium and carbonate ions. The supersaturation of similar solutions at constant temperature decreases with time due to the consumption of ions in the crystallisation reaction. The water heating in household devices mostly includes water evaporation. Aspects of the mechanism of the scaling process from tap water in domestic appliances under evaporation conditions are still not fully understood. Evaporation of test solution, besides Ca^{2+} and CO_3^{2-} consumption, affects solution supersaturation.

When the water temperature rises from room temperature up to its boiling point, the solubility of inverse solubility salts decreases. This reduction in solubility along with an increase in salinity due to water loss through evaporation during the heating process contributes to an increase in the thermodynamic driving force for the crystallisation reactions prompting the precipitation of salts out of solution [296]. Figure 6.1 describes the process of salt precipitation as a function of time and temperature while figure 6.2 shows how the solubility product of $CaCO_3$ as calcite, $MgCO_3$ and $CaSO_4$ changes with temperature, respectively as derived from experimental studies [38, 39].
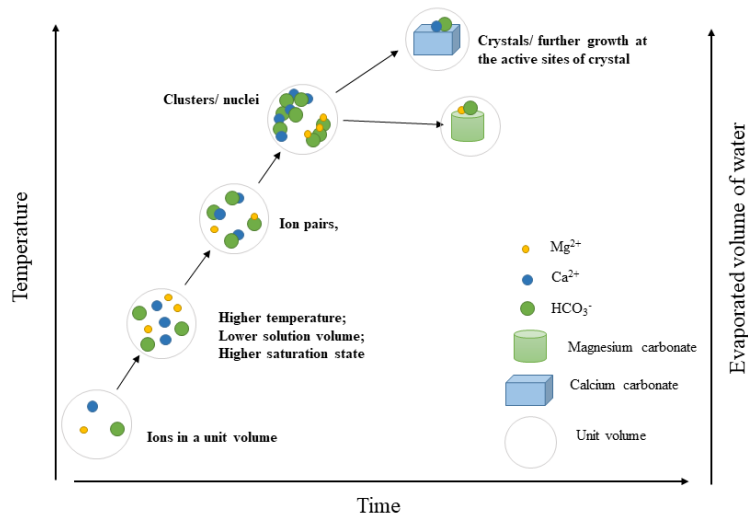
Figure 6.1. Schematic drawing of composite precipitates formation from potable water.
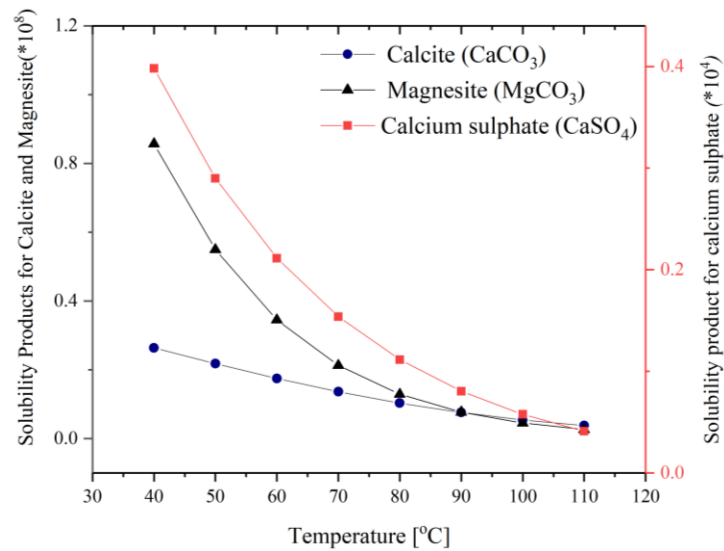
Figure 6.2. The solubility of CaCO₃ forms and MgCO₃ as a function of temperature.

In the present chapter, the scale formation from potable water has been investigated to improve the understanding of fouling mechanisms in domestic systems. The scaling kinetics and morphology have been examined by subjecting potable water to different solution temperatures, surface roughness, surface material, evaporation area, heating rate, cooling rate and water composition. These experiments were carried out in the Boiling Static Setup according to the conditions and procedure mentioned in the Methodology section.

6.2. Effect of bulk temperature

The rate of evaporation of water increases with water temperature due to an increase in the kinetic energy of molecules (Fig. 6.3). Figure 6.4 shows the amount of scale precipitated on the stainless steel surface increases with the evaporated water volume and the bulk temperature. Temperature increase from 30 to 90 ℃ reduces the solubility of $CaCO_3$ from 220 to 40 mg/L and hence increases the supersaturation and scaling tendency at a constant concentration of foulant [5]. The consumption of calcium ions in water by crystallisation reaction increases with the volume of evaporated water at 95 ℃ (Fig. 6.5). It can be seen from the exponential decay of calcium ions, the consumption rate of calcium in the solution is faster than the water evaporation rate, as such saturation ratio decreases with time, as presented in figure 6.4.
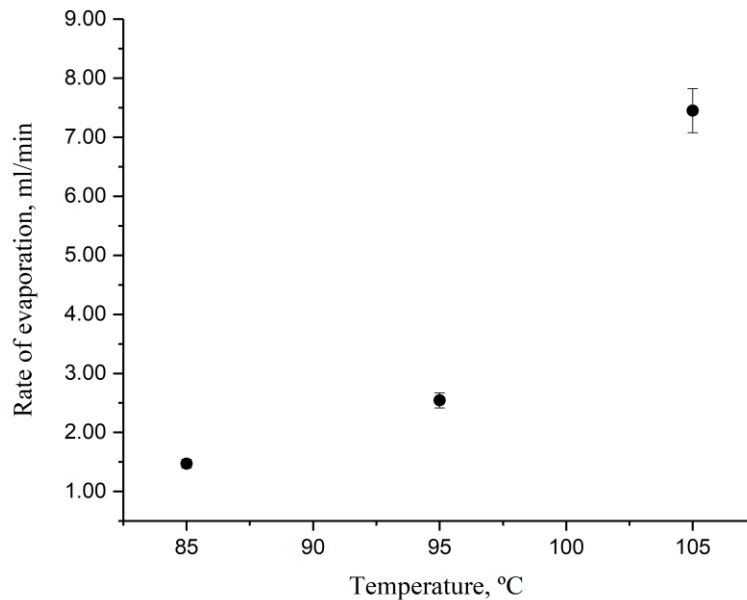
Figure 6.3. The evaporation rate of solution at different bulk temperatures.

112
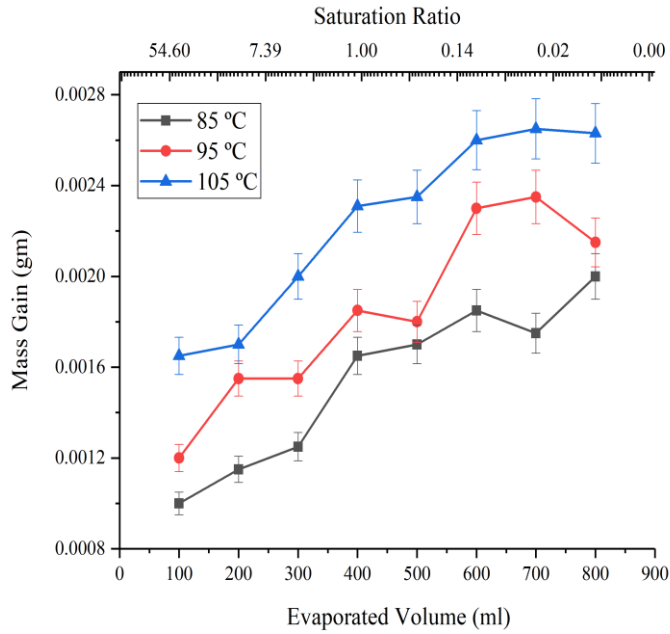
Figure 6.4. Effect of temperature on the scale formation of stainless steel.
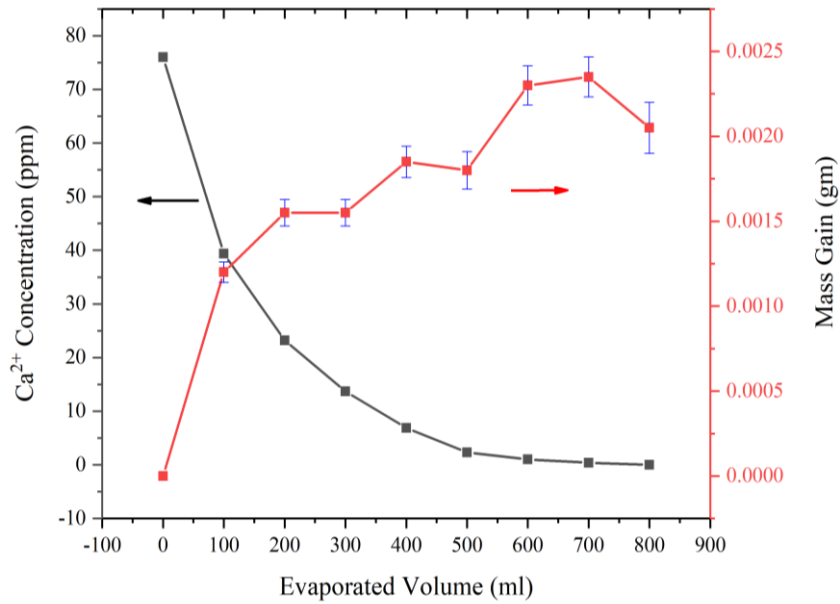
Figure 6.5. Effect of water evaporation on Ca²⁺ concentration at 95 ⁰C.

The SEM observations in figure 6.6 show that the needle-like aragonite crystals are the dominant form of $CaCO_3$ at the tested temperatures. The elemental analysis by EDX shows that magnesium content in the flake-like particulate is slightly higher than that in aragonite particles (Spectrums 6 and 7 in Fig. 6.7). However, magnesium may have an inhibitory effect on the morphological transformation of crystalline particles [297-299].
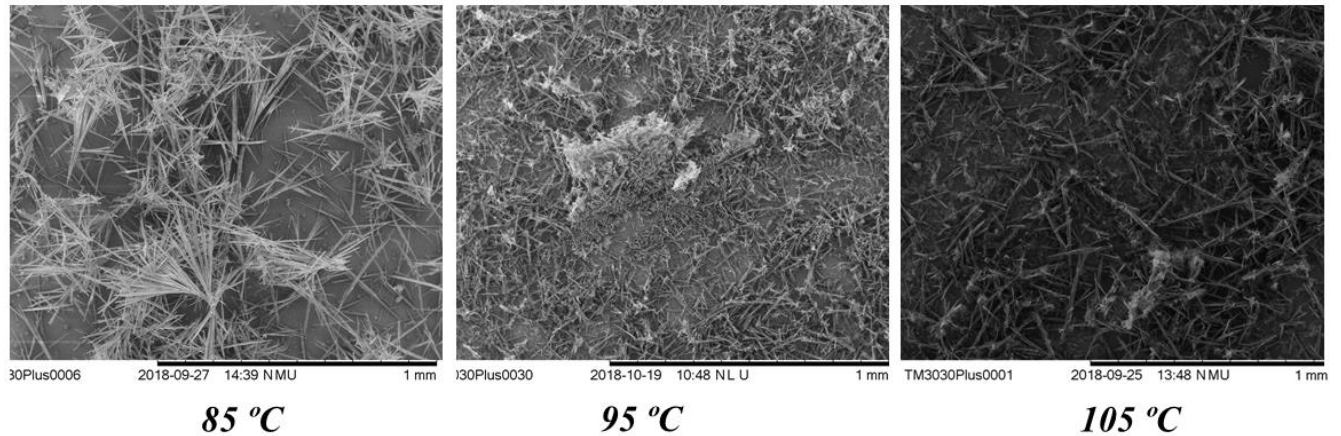
Figure 6.6. SEM observations of scale crystals for a different solution temperature.
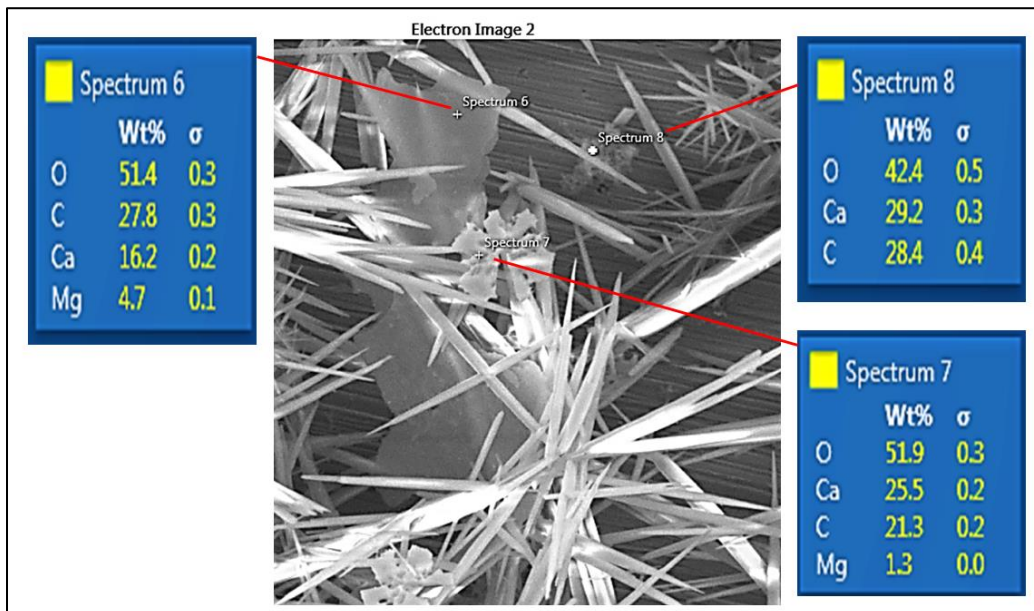
Figure 6.7. EDX elemental analysis for different forms of $CaCO_3$ deposits.

The XRD analysis of scale deposited on the surface illustrates that the aragonite is the prevailing polymorph $CaCO_3$ for all temperatures (Fig. 6.8). The solution temperature promotes the morphological transformation on the surface from vaterite and calcite to aragonite. In the XRD for precipitates in the bulk, a few changes have been spotted: namely, the transformation of aragonite to calcite, and the presence of $CaSO_4$ as anhydrite at temperatures of 95 and 105 ºC (Fig. 6.9).
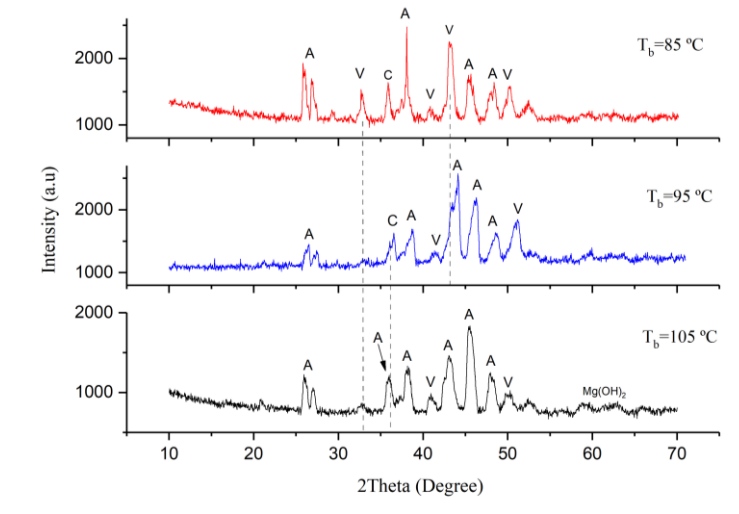
Figure 6.8. XRD analysis of the scale crystalline species on the surface (A: Aragonite, C: Calcite, and V: Vaterite).
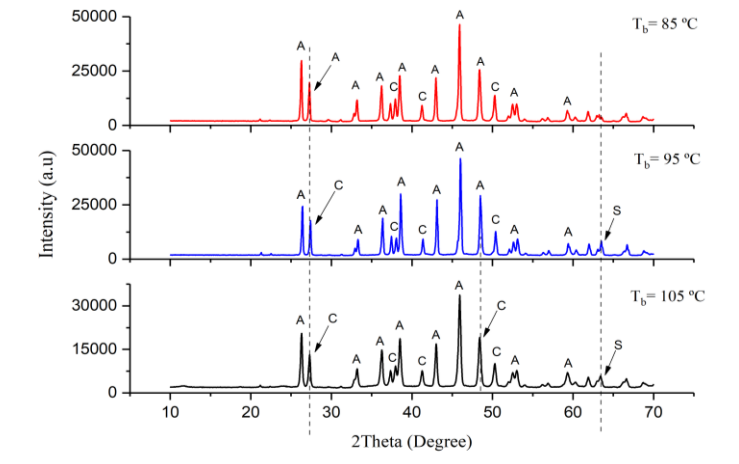
Figure 6.9. XRD analysis of the bulk precipitation (A: Aragonite, C: Calcite, and S: CaSO$_4$ as anhydrite).

115

6.3. Effect of surface material

The visual observations show that the aluminium sample was coated by a black layer. According to the SEM-EDX analysis, this porous black crust comprises Al and O, and this strongly suggests the formation of the aluminium oxide (Al_2O_3) layer (Fig. 6.10). No significant variation in the amount of the precipitated scale among the tested surfaces has been observed (Fig. 6.11). The mass gain on aluminium is a mixture of oxide layer and mineral deposits. As crystal forms in the bulk solution by the homogeneous nucleation, the surface may not affect the nucleation and growth process. The surface nature nevertheless can influence the adhesion with the precipitated crystal [111].

The common denominator among the morphology of the deposits on the different surfaces is the presence of flake-like particles which occupy a large area of the copper surface compared to the other metals (Fig. 6.12). The copper ions yielded as a corrosion product may inhibit the transformation from amorphous to crystalline form [300]. Al^{3+} also may behave similarly on the aluminium substrate but with lower inhibitory efficiency as a consequence of the consumption of ions in the oxidation reaction. It seems furthermore that the population of scale crystals on aluminium is relatively low, and the oxide layer may provide a weaker adhesive strength. Regarding the scale structure on stainless steel, the secondary growth of the flake-like particulates might heterogeneously commence after the aragonite binding on the surface.
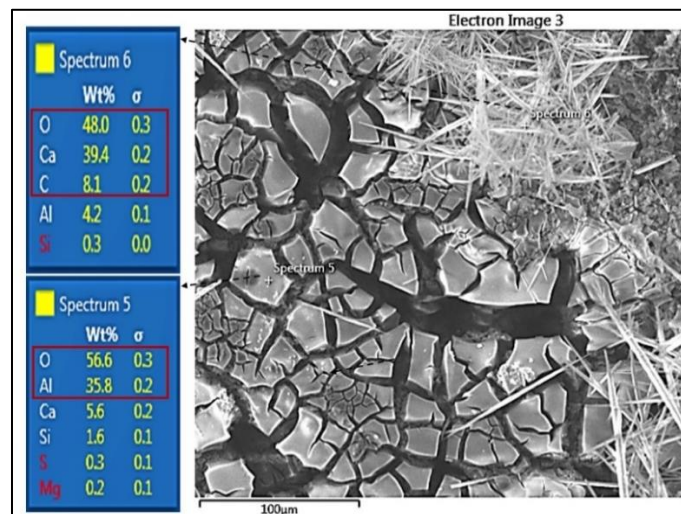
Figure 6.10. EDX analysis for oxide layer and scale crystals on the aluminium surface.
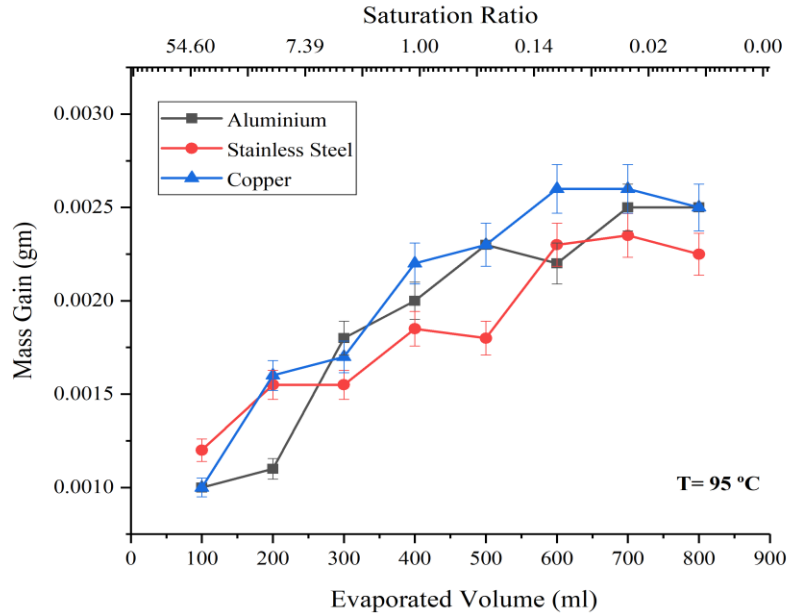
Figure 6.11. Effect of surface material on scale deposition.
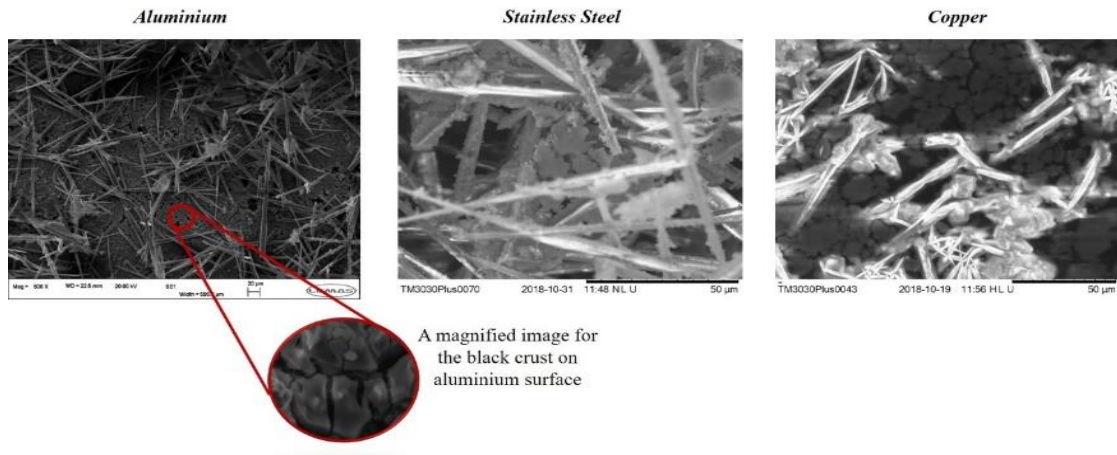
Figure 6.12. SEM images of scale particles on different surface materials.

The XRD analysis shows differentiated findings in terms of the crystallographic structure and the abundance of the crystalline phase, (Fig. 6.13). The $CaCO_3$ vaterite on copper is higher than that on the other materials. The absence of ionic species such as Al^{3+} and Cu^+ may allow the transformation to aragonite form. Crystals of γ-alumina (γ-Al_2O_3) have been detected on aluminium, which confirms that the dark porous crust underneath the deposits is built of aluminium oxide.

117
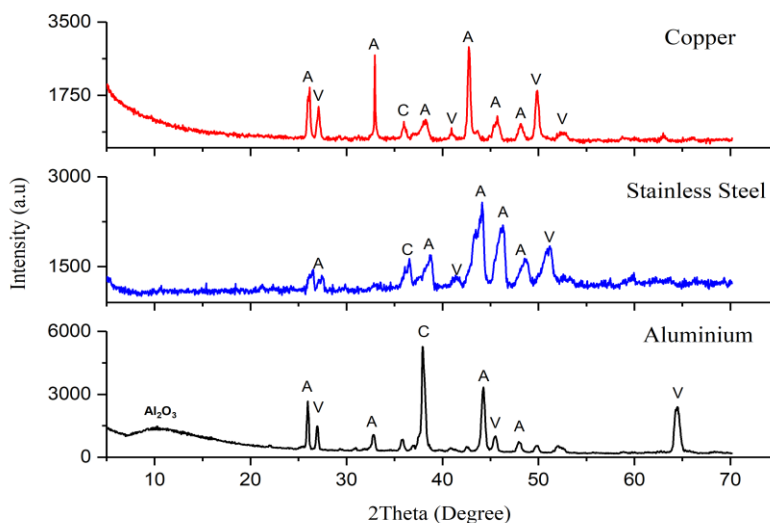
Figure 6.13. XRD analysis of scale crystalline species on different surface materials (A: Aragonite, C: Calcite, and V: Vaterite).

6.4. Effect of surface roughness

Figure 6.14 shows that the precipitated mass on all surfaces is very similar, particularly in the earlier stages of evaporation. It seems that it is hard to remove the scale particles from the rougher surface by the turbulent bubble circulation at the later stages of evaporation, where the water level is low. As the crystals are formed by homogenous crystallisation, the influence of roughness concentrates on the aspects of particle-surface adhesion. The SEM observations in Figure 6.15 show that the amount of deposit flakes increases with the roughness. It also illustrates that the flowers of aragonite formed underneath the scaly coat. However, the presence of these flakes may affect the accuracy of the XRD analysis. Many differences can be observed in the XRD measurements related to peaks intensity and position, and the detected polymorphs (Fig. 6.16). The significant morphological transformation paths include calcite on the smooth surface to aragonite on the moderately rough surface (R_a= 106 nm) which in turn transforms sequentially to vaterite particles on the rougher surface (R_a= 182 nm).
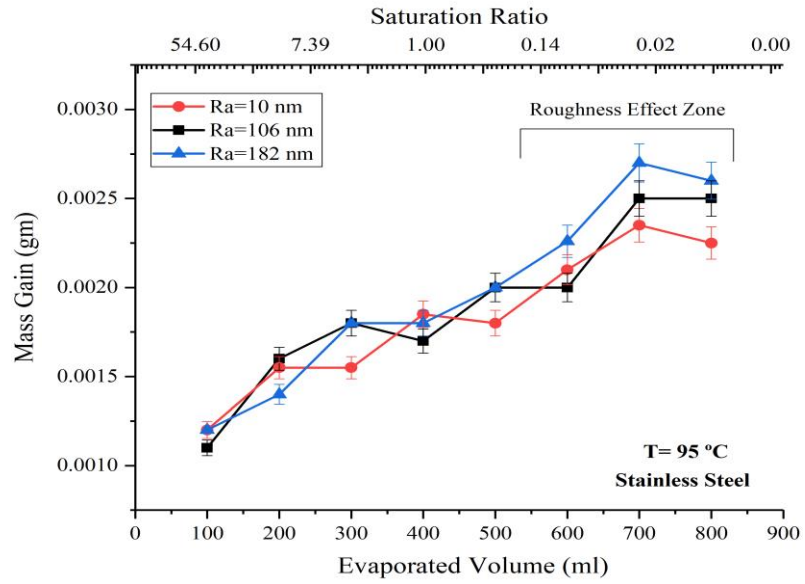
Figure 6.14. Effect of surface roughness on scale deposition

R_a=10 nm   *R_a=106 nm*   *R_a=182 nm*
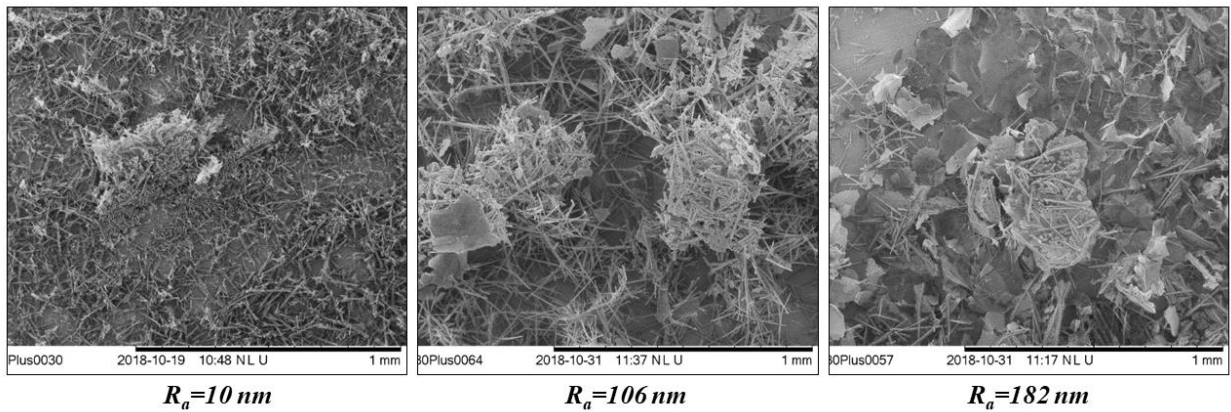
Figure 6.15. SEM images of scale deposits on surfaces with different roughness.

119
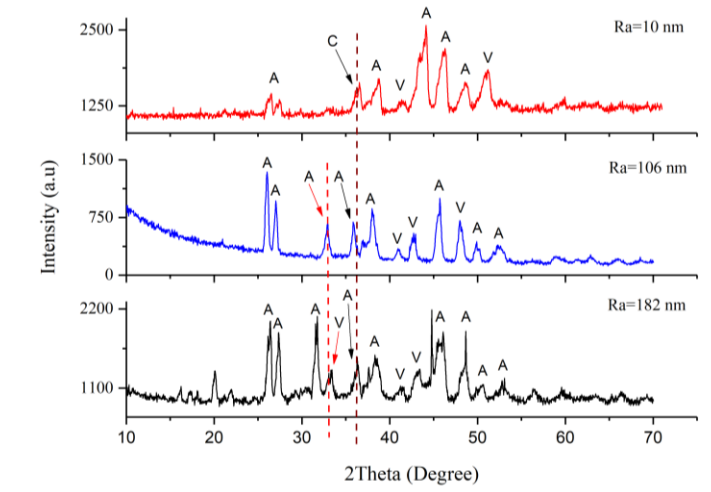
Figure 6.16. XRD analysis of the scale crystalline species on different roughness surfaces (A: Aragonite, C: Calcite, and V: Vaterite).

6.5. Effect of evaporation area

Changing the area of evaporation leads to altering the evaporation rate due to an increase in the number of liquid molecules in contact with air. The evaporation rate was measured as a function of the liquid-air contact area, as presented in figure 6.17a. The measurement of total deposition on stainless steel specimen shows that the increase in the evaporation area (i.e. evaporation rate) reduces the amount of deposited scale (Fig. 6.17b). The crystallisation reaction is a time-dependent process [301]. The faster the evaporation rate the shorter the experiment time which allow less amount of deposits to form.
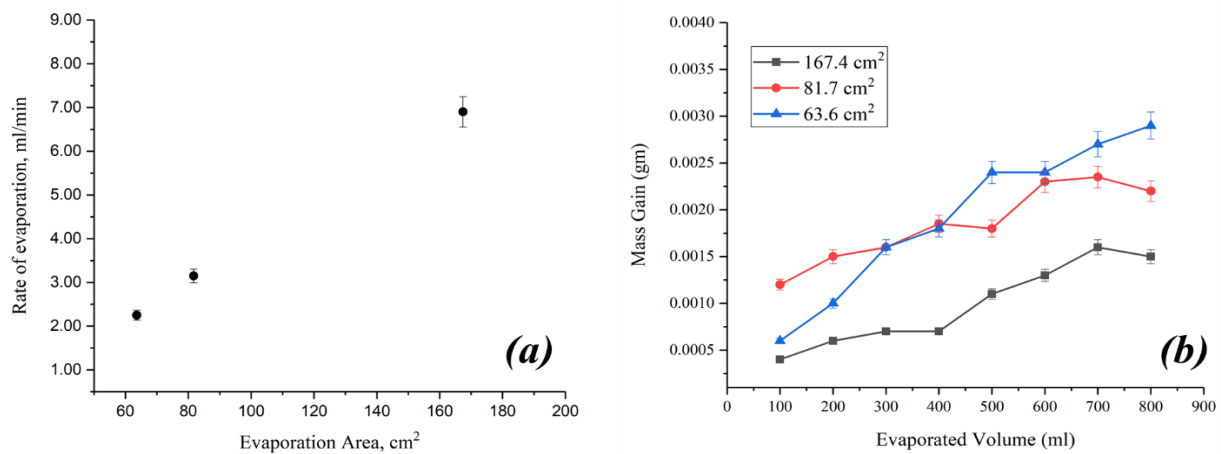
Figure 6.17. (a) Relationship between the evaporation rate and evaporation area and (b) scale mass change with evaporated water for different evaporation areas.

120

The analysis of crystal habit demonstrates that the crystals formed at the lower evaporation rate are larger than that at the ones with a higher evaporation rate. In all cases, the needle-like aragonite is the predominant form of $CaCO_3$. However, SEM images show also flake-like particles maintained on the aragonite needles, as illustrated in figure 6.18. The elemental analysis of the mineral deposits by EDX shows that the Mg content in the flake-like particles is relatively high (Fig. 6.19). These flakes may form as a result of Mg^{2+} interaction with scale crystal during the growth stage.
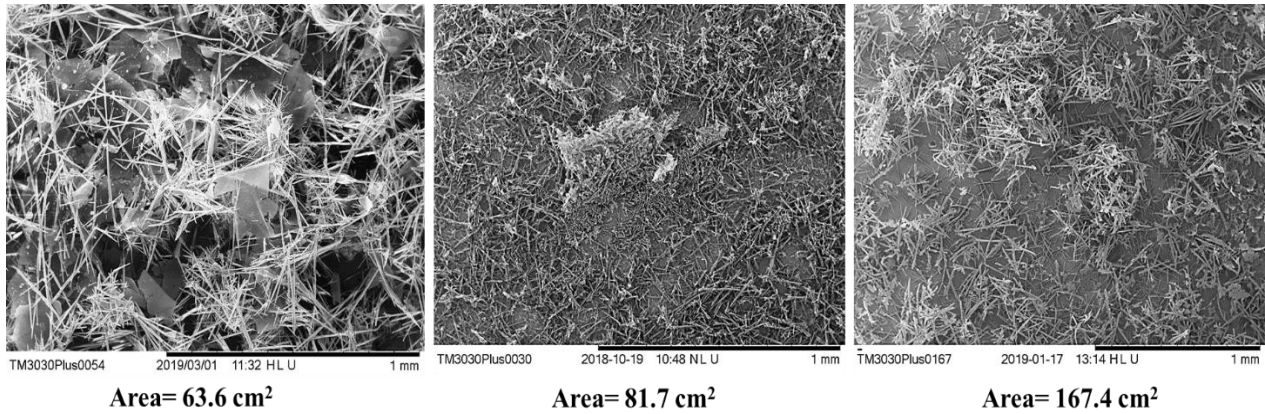
Figure 6.18. SEM observations of scale layer on stainless steel surface for different evaporation areas.
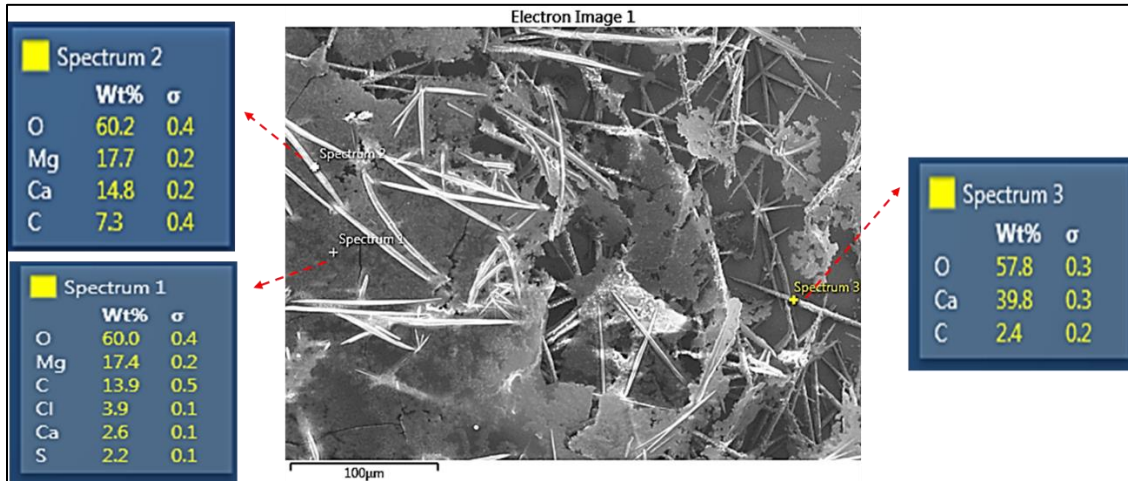
Figure 6.19. EDX analysis of scale particles formed from evaporation area experiments.

6.6. Effect of water composition

It has been reported that the major fouling species in potable water are calcium and bicarbonate which crystallise to form different crystalline phases of $CaCO_3$ [302, 303]. The other constituents

in water play different roles in terms of fouling kinetics and morphology [248]. The present work investigates the effect of the common ionic species, namely, Mg^{2+}, SO^{2-}_4, NO_3^-, Zn^{2+} and total organic carbon (TOC) based on the drinking water quality standards. The formation of the secondary inorganic minerals such as $CaSO_4$, $MgCO_3$ and $ZnCO_3$ from these ions is also studied using a batch crystallisation system.

6.6.1. Effect of magnesium

The presence of magnesium in water may contribute to the formation of different types of deposits such as MgO, $Mg(OH)_2$, and $MgCO_3$ based on the operating conditions and composition [158, 304]. Figure 6.20a shows how the content of magnesium changes in two different solutions. In solution C, no change in the magnesium content has been observed when the solution temperature is between about 25 and 60 °C. Then, as the temperature exceeded 60 °C, the content of magnesium starts to increase due to water evaporation. Upon reaching a critical saturation concentration, $MgCO_3$ deposits form, the concentration of magnesium decreases due to the scaling reaction. For this water composition, the critical temperature for the magnesium scale to be formed is around 94 °C at a fixed heating rate. It can be seen that the consumption rate of Mg^{2+} in solution A is slower than in solution C. The consumption rates of Mg^{2+} and Ca^{2+} in drinking water have been compared in figure 6.20b. The reduction in the concentration of Ca^{2+} is larger than Mg^{2+}, which illustrates that the calcium reaction rate is higher even at lower temperatures due to the low solubility of $CaCO_3$.
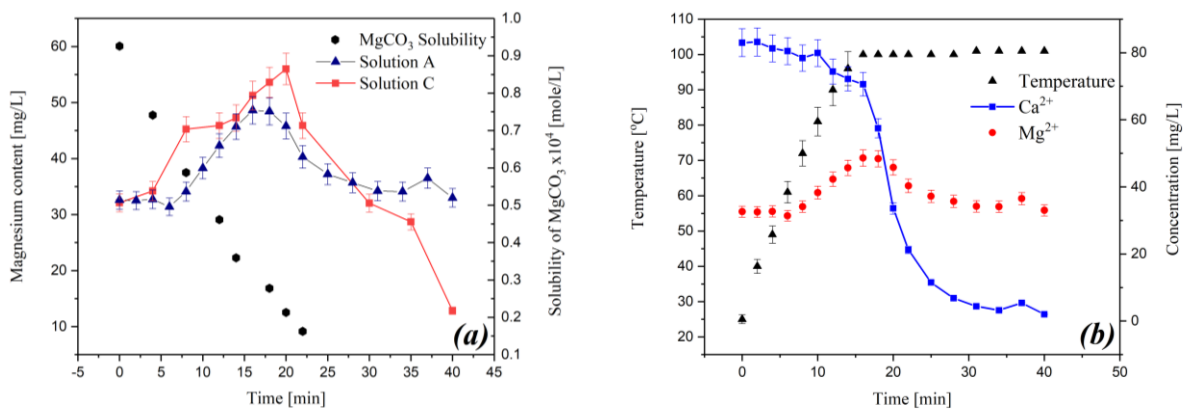
Figure 6.20. (a) Change of $MgCO_3$ solubility with temperature, and magnesium content in different solutions, (b) the consumption rates of Mg^{2+} and Ca^{2+} in solution A, under the medium heating rate.

122

Figure 6.21a displays the effect of magnesium content on the calcium precipitation rate as a function of temperature. The lower the content of magnesium in the potable water the steeper the decrease of calcium at the same range of temperature and bicarbonate content. The concentration of calcium in commercially bottled water (solution A) is not identical. When it was measured by AAS, the initial concertation of calcium in solution A was ranging between 78 and 80.6 mg/L. The magnesium competes with calcium to form $MgCO_3$. This is confirmed by the ratio of magnesium to calcium concentrations, as displayed in figure 6.21b. The higher the initial concentration of magnesium the higher the consumption rate, and the lessened the carbonates to react with calcium.
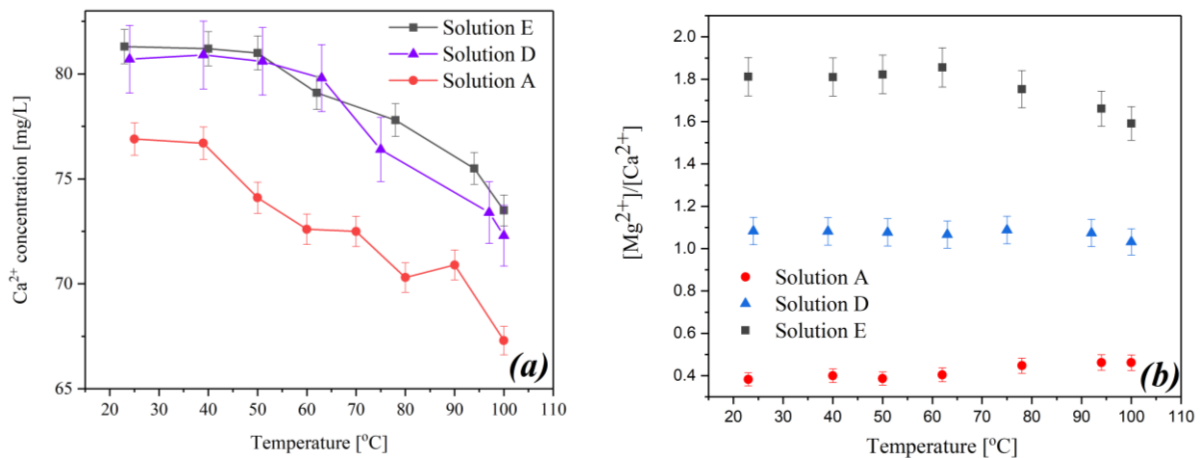
Figure 6.21. (a) Calcium concentration change, (b) magnesium concentration change, with the temperature at the different magnesium contents.

6.6.2. Effect of sulphate

No $CaSO_4$ deposits are observed from the tested drinking water either on the solid surface or in the bulk solution. The possibility of $CaSO_4$ scale formation in a potable water system was examined using the maximum recommended content of SO_4^{2-} in drinking water which is 400 mg/L. The change of calcium and sulphate ions has been examined as shown in figure 6.22. As such, there is no reduction in the concentration of Ca^{2+} and SO_4^{2-} occurring during the process of heating to 100 °C, no formation of $CaSO_4$ scale takes place. On the contrary, the content of the ions increases with time due to water evaporation. As the solubility constant of $CaSO_4$ is higher than that of $CaCO_3$, the reaction is not favourable at similar composition and temperature [47]. No precipitation has been noticed, even though the increase of temperature and concentrations of both

ions which increases the saturation ratio from 0.3 to 7.9. This makes the formation of $CaSO_4$ in similar systems and conditions unlikely to occur.
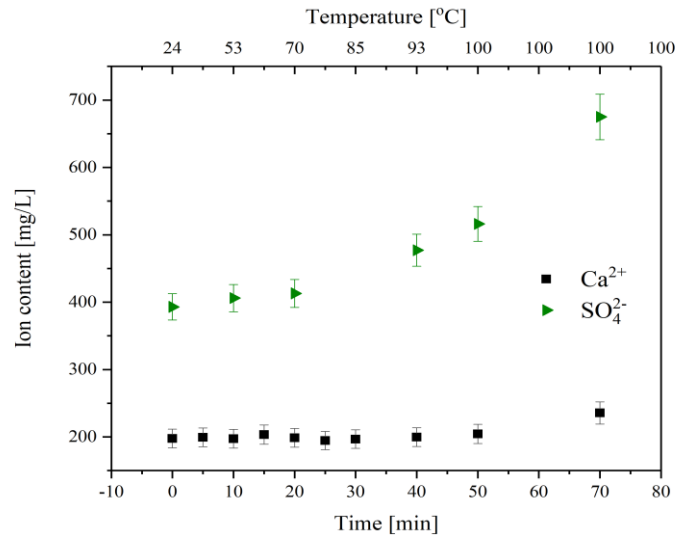
Figure 6.22. Change of ion concentration in solution B during the heating process.

6.6.3. Effect of zinc

The effect of Zn^{2+} on the bulk crystallisation of inorganic minerals from potable was studied. Figure 6.23a displays the profile of Ca^{2+} concentration during heating of zinc-containing potable water from room temperature to boiling under atmospheric pressure. In the zinc-free solution, the content of Ca^{2+} decreases at a temperature of about 57 °C after 5 minutes of heating. The time taken for Ca^{2+} (induction time) to reduce is prolonged as the Zn^{2+} content increased. On contrary, the concentration of Ca^{2+} increases due to water evaporation with temperature increase. However, it decreases when attaining the required supersaturation for the scale to precipitate. The Zn^{2+} in solution complexes with fouling species boost the energy barrier of the crystallisation reaction [305-307]. Also, it has been reported that zinc may react with CO_3^- resulting in the formation of stable $ZnCO_3$ and competing Ca^{2+} [241].

The sharp reduction in the Ca^{2+} concentration for cases with Zn^{2+} indicates that zinc inhibition has ended. The AAS analysis in figure 6.23b shows that Zn^{2+} concentration in the solution decreases with temperature and time. The higher the concentration of Zn^{2+} the faster the consumption. Forming a complex with HCO_3^-, CO_3^- and Ca^{2+} might be the case in the first period of heating (<

124

85 °C) [305]. However, for steeper depletion in Zn^{2+} (>85 °C), the crystallisation of $ZnCO_3$ occurs [308].
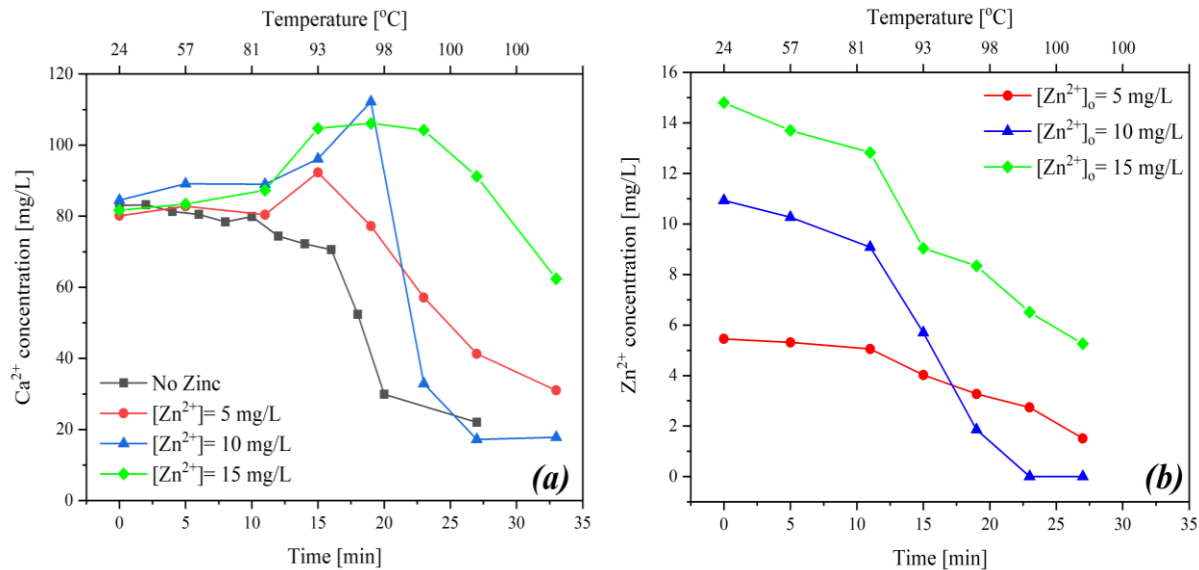
Figure 6.23. (a) calcium ion concentration profile and (b) zinc concentration profile, during water heating for different zinc content.

The results of Ca^{2+} profile at different zinc concentration was interpreted into the crystallisation induction time, as shown in figure 6.24a. The time taken to appear of first visible crystal in the bulk solution, induction time, increases exponentially with zinc content in water. This confirms that zinc during the initial period of heating forms a complex with the fouling species preventing crystallisation reaction [309]. Figure 6.24b illustrates the solution turbidity as a function of time for various concentrations of Zn^{2+}. The solution turbidity increases with time for all solutions. However, the turbidity of the high Zn^{2+} solutions (10 and 15 mg/L) is the lowest at the later stages of heating. The turbidity measurement indicates the solution cloudiness caused by the suspended particles of scale. As the density of the $ZnCO_3$ is two times that of $CaCO_3$, the $ZnCO_3$ crystals tend to precipitate faster than $CaCO_3$ or $MgCO_3$ [310] resulting in less turbidity.
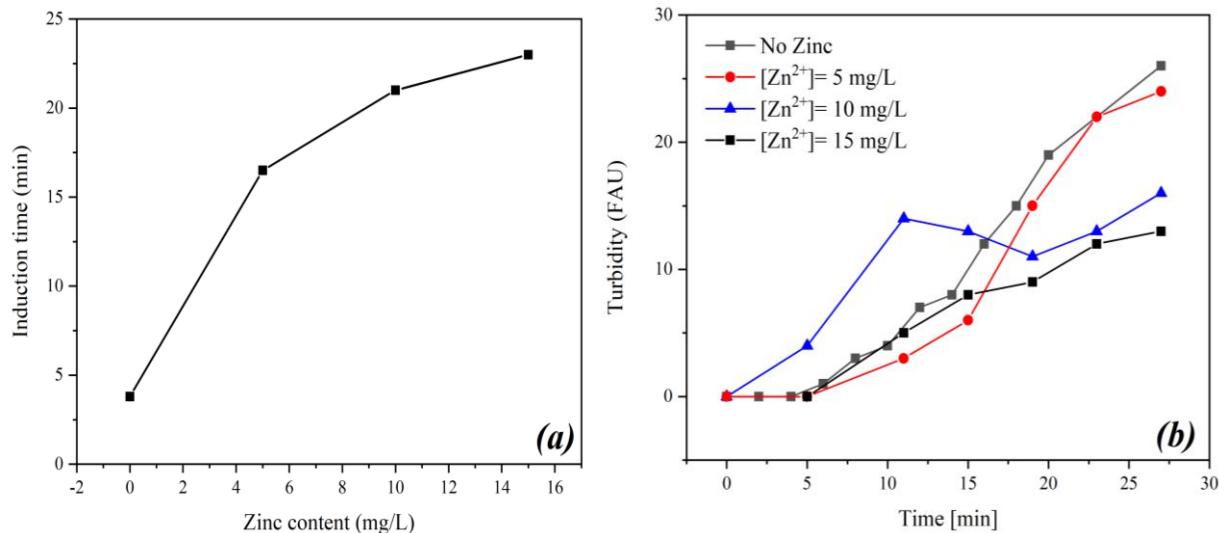
Figure 6.24. (a) Crystallisation induction time and (b) solution turbidity, for different zinc content.

The effect of Zn^{2+} on the scale morphology is presented in SEM and XRD analysis in figures 6.25 and 6.26. The SEM observations in figure 6.25 show that the deposits with no zinc mostly comprises needle-like aragonite. However, at 15 mg/L structure of mineral deposits transforms into lumpy crystals which are attributed to the precipitation of $ZnCO_3$. The presence of $ZnCO_3$ as a Smithsonite was confirmed by XRD analysis as shown in figure 6.26. A small peak corresponding to zinc oxide is also observed.
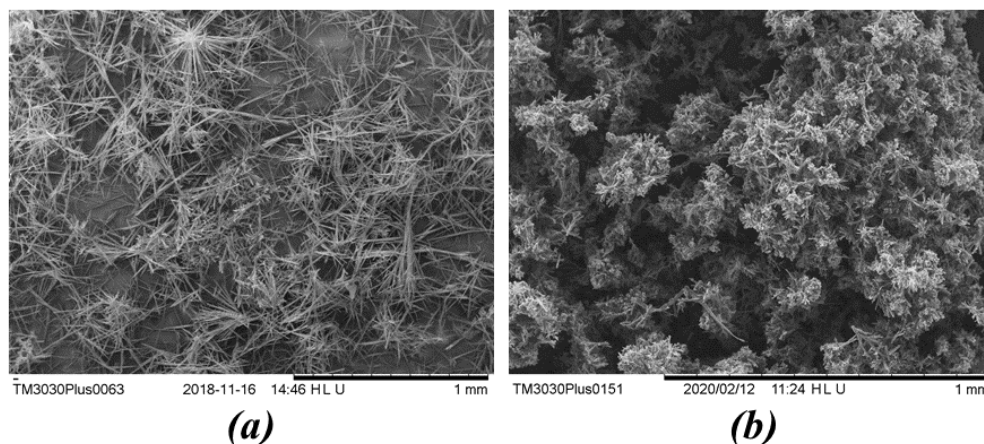
Figure 6.25. SEM images of the precipitated scale (a) with no zinc in water and (b) with 15 mg/L zinc.
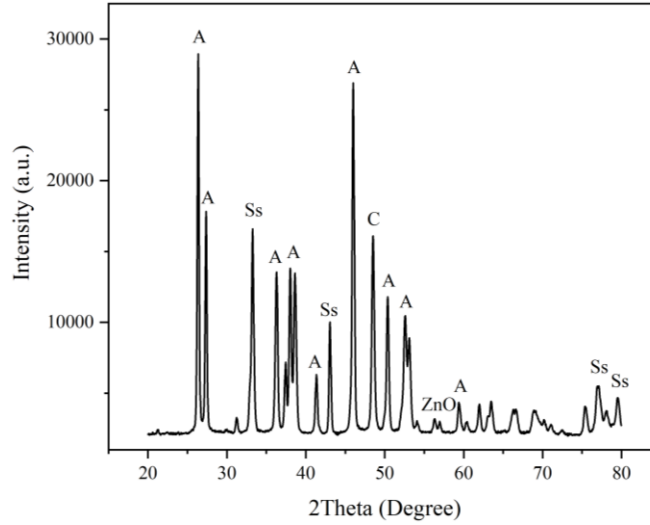
Figure 6.26. XRD pattern of bulk precipitate in presence of 15 mg/L zinc (A: aragonite, C: calcite, and Ss: Smithsonite).

6.6.4. Effect of nitrate

Nitrate (NO_3^-) is a monovalent complex anion that is present in drinking or surface water. The effect of nitrate ions on the bulk precipitation in potable water systems was examined. Figure 6.27 depicts Ca^{2+} profile at different concentrations of nitrate. From the graph, there is no significant difference in the concentration of Ca^{2+} during the heating process when different concentrations of nitrate are added. Similar to the kinetics investigations, no changes in the scale morphology were observed at 104 mg/L of NO_3^-, as shown in figure 6.28.
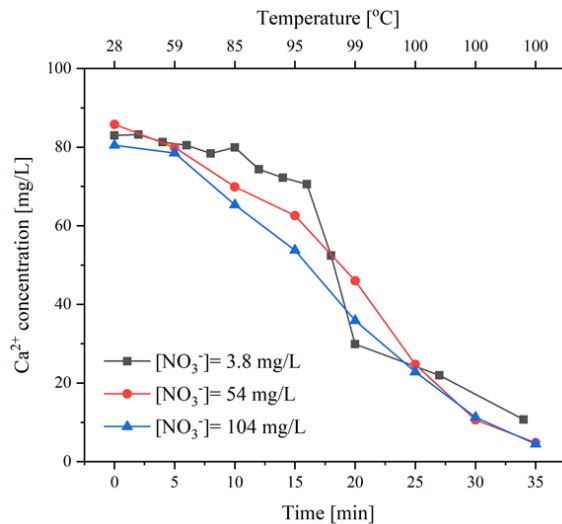
Figure 6.27. Calcium ion concentration profile during water heating for different nitrate content.
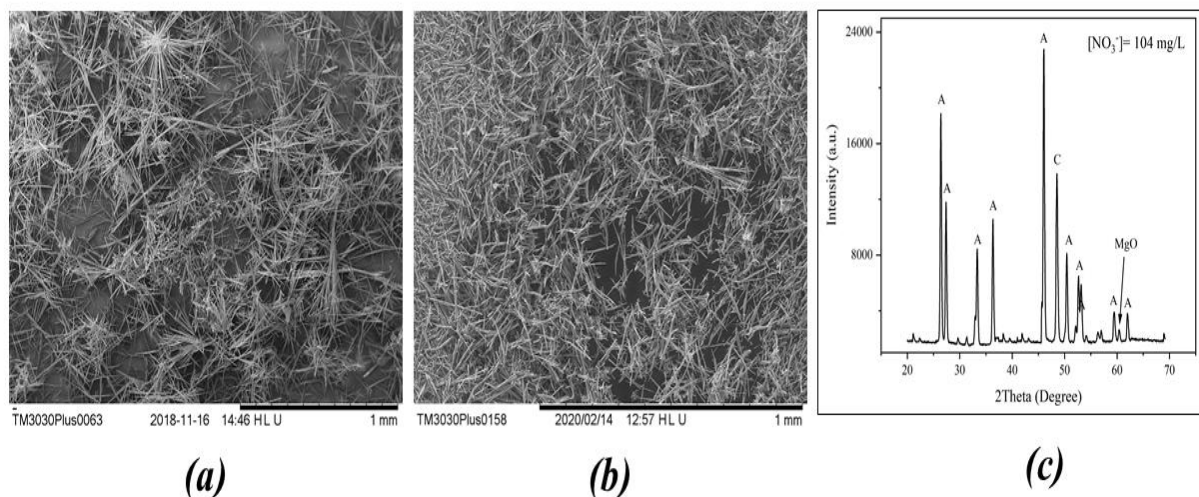
Figure 6.28. SEM images of deposits with (a) 3.8 mg/ L nitrate (b) 104 mg/ L nitrate and (c) XRD patterns for scale layer at 104 mg/ L nitrate.

6.6.5. Effect of Total Organic Carbon (TOC)

Figure 6.29 shows the effect of TOC on the concentration of Ca^{2+} during the heating process. TOC content reduces the consumption of Ca^{2+}, hence fewer calcium deposits form. The increasing TOC concentration also prolongs the induction time of crystallisation. Increasing the content of TOC to 4 mg/ L minimises the consumption of Ca^{2+} by about three times during a fixed heating period. The molecule of humic acid, the humic substance used to raise the TOC content, is relatively large (high molecular weight). It has been proposed by Hoch, et al. [255] that the substances with high molecular weight generate a great reduction in growth rate. These molecules form a colloid/complex with Ca^{2+} and Mg^{2+} which lowers the saturation state and inhibits the growth of the crystal. The cations complexation is likely to occur by carboxylic acid and phenolic functional groups [256].

128
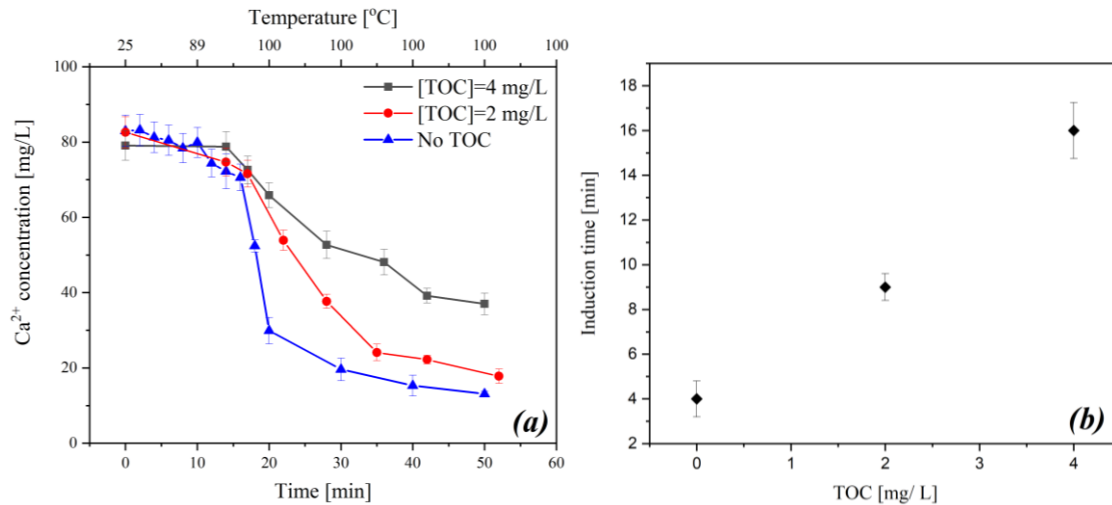
Figure 6.29. (a) Calcium ion concentration profile and (b) crystallisation induction time, during water heating for different TOC content.

6.7. Effect of heating rate

The temperature measurements in figure 6.30a show the time required to achieve water boiling temperature (100°C) under atmospheric pressure. The solution pH is simultaneously measured. At all heating rates, the pH increases as time and temperature increase. It gives an indication of bicarbonate conversion to carbonate as well as the release of carbon dioxide as the temperature increases. The release of carbon dioxide from the evaporating solution influences the equilibrium of HCO_3^- and CO_3^{2-} ions by shifting the pH to higher values (Eq^n 6.1). Hence, the formation of alkaline scales such as $CaCO_3$, $MgCO_3$ and $Mg(OH)_2$ is more likely to occur [40]. Moreover, the temperature increases the dissociation constant of bicarbonate at constant water salinity [311]. The salinity can be determined by chloride ion concentration. It may also enhance the bicarbonate dissociation constant, thus the formation of carbonate species [312]. The chloride (Cl^-) ion content and the salinity increase with the temperature and volume of evaporated water.

$$2HCO_3^- \leftrightarrow CO_2 + CO_3^{2-} + H_2O \qquad (6.1)$$
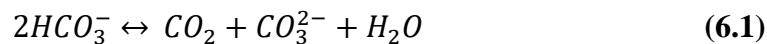
In the same period of heating, the calcium content in the solution has been reported in figure 6.30b. The findings show that the higher the heating rate the lower the amount of calcium consumed in the crystallisation reaction. The analysis of calcium ions concentration has been stopped when the bulk temperature reaches 100 °C. The solution contains 8.7, 52.4, and 66.1 mg/L of calcium in the slow, medium and rapid heating, respectively.

129
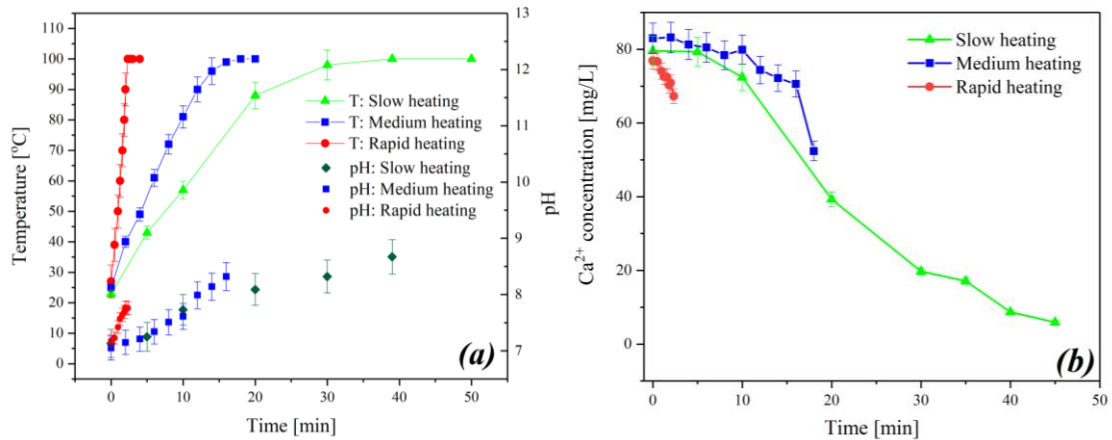
Figure 6.30. (a) Profile of bulk temperature and pH, (b) profile of calcium concentration, for different heating rates.

Figure 6.31a displays the change of calcium concentration as a function of temperature in the heating process for different heating rates. Solution A was used as a test solution in the investigation of the effect of the heating rate. The highest concentration of Ca^{2+} at the boiling point is achieved by rapid heating, while the lowest one is achieved by slow heating. This implies more precipitation is formed when the solution is slowly heated. The solution turbidity has been determined with temperature increase as shown in figure 6.31b. The solution becomes more turbid at the boiling point when water is slowly heated. This confirms that the calcium undergoes a crystallisation reaction with carbonate. The slow heating of potable water from room temperature to boiling temperature allows the solid deposits to form. In other words, the longer heating time leads to a higher amount of inorganic scale.
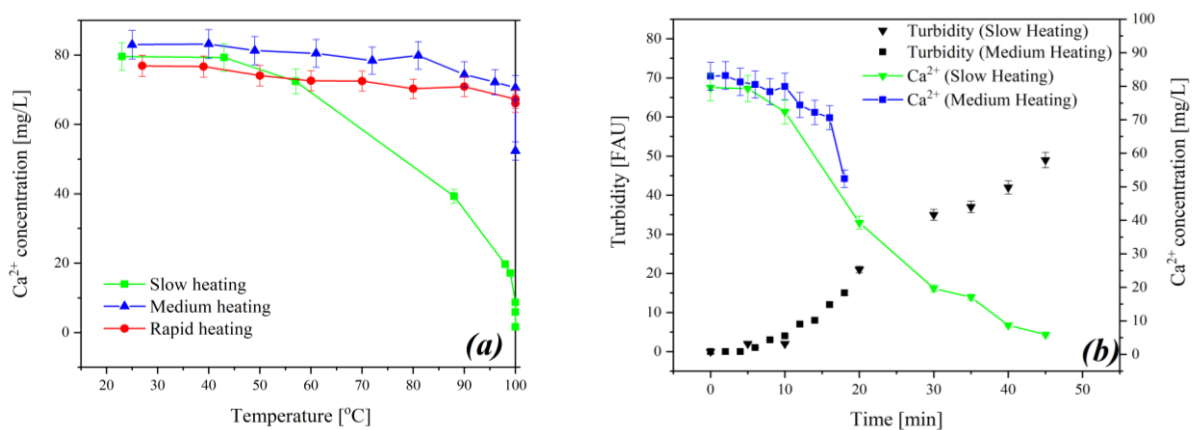
Figure 6.31. (a) Change of calcium concentration with temperature, (b) change of solution turbidity with time.

130

The effect of heating rate on the rate of calcium ion consumption in the solution is summarised in figure 6.32. The rate of temperature change is obtained by the linear fitting of the rising rate period in the (temperature-time) curve in figure 6.30a. A higher rate of temperature change leads to a faster reaction rate of calcium precipitation. However, although the reaction rate is slower at the lower heating rate, a longer time is required to achieve the boiling point leading to a greater amount of precipitated salt. The temperature influences the crystallisation reaction constant and rate of carbonate formation from bicarbonate, hence the overall reaction rate [42].
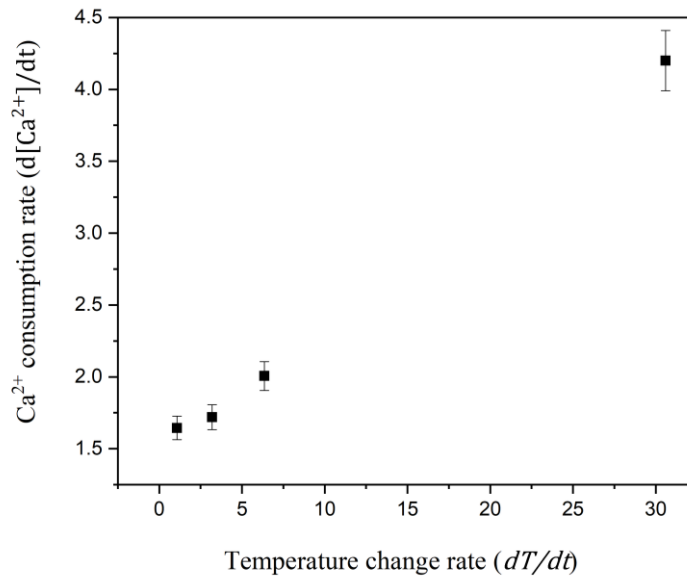
Figure 6.32. Change of calcium reaction rate with heating rate.

6.8. Effect of cooling rate

The formation of inorganic deposits is not only expected in the heating period but also after cutting the heat source and leaving the solution to cool. The drop of temperature from 100 °C to about 45 °C due to heat loss to the surroundings is the second phase for the scale formation. The cooling rate affects the consumption rate of calcium and final content at 45 °C, as shown in figure 6.33a. Longer residence time at the temperature range where the crystallisation reaction is favourable results in a higher amount of precipitate. The mechanism of bulk precipitation during the cooling stage is different from that during the heating stage as it is affected by the solution temperature and the pre-existing scale crystals. The particles that formed in the heating stage can act as nucleation sites and promote heterogeneous nucleation [27].

The results in figure 6.33b illustrate how the Ca^{2+} content at slow cooling is lower than that at quick cooling for the same solution temperature. The solution pH for both cooling rates rises as the temperature decreases with little dependence on the cooling rate. Figure 6.34a and figure 6.34b distinguish between the decay rates of calcium during the rapid heating and natural cooling for the commercially available electric kettle. The data has been linearly fitted to determine the rate of calcium consumption as a function of temperature in the heating and cooling cycles, respectively. It can be seen that the calcium ions are largely consumed in the cooling stage rather than that in the heating stage. In other words, the scale that forms when water is cooling is greater than heating as the time in the latter is much shorter.
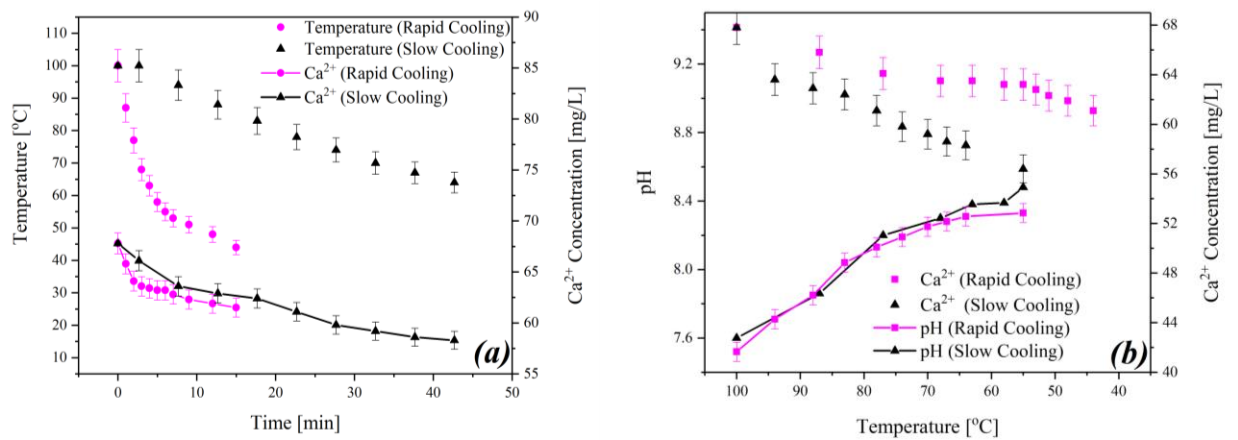
Figure 6.33. (a) Change of temperature and calcium concentration with time, (b) change of pH and concentration with the temperature at different cooling rates.
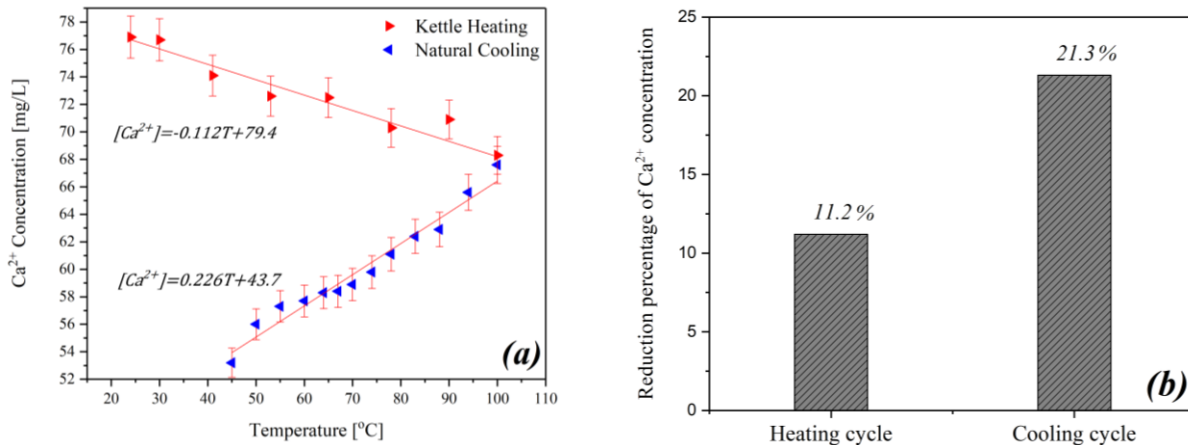
Figure 6.34. (a) Change of calcium content with temperature, (b) the reduction percentage of calcium during the heating and cooling cycles.

132

The mass of the CaCO₃ scale during heating and cooling cycles was theoretically estimated based on the precipitation rate model (Eqⁿ 6.2) proposed by Morse [93]. Two assumptions were made in the calculations; concentrations of calcium and carbonate are kept constant during the process, and the precipitated crystals are calcite. The temperature profile used in the calculations is adopted from the heating and cooling experiments. These calculations aim to estimate the scale amount if the scaling process is solely crystallisation reaction-controlled. In other words, the increase in the solution temperature enhances the solution saturation and hence the thermodynamic driving force of the scaling. Figure 6.35a shows that the scale mass formed in the cooling cycle is greater than that in the heating cycle which supports the present findings. Both the time and supersaturation of solution in the cooling stage are higher than those in the heating stage. The ratios of CaCO₃ precipitated in the cooling cycle to the heating cycle from the experiments and theoretical calculations were compared. It can be seen in figure 6.35b that the theoretical ratio is greater than the experimental ratio because in the experiments the concentration of fouling species are consumed as a function of time. The consumption rate of calcium in the experimental cooling cycle is higher than that in the cooling cycle.

$$G = K\,(S - 1)^n \qquad\qquad (6.2)$$

Where G is the precipitation rate, S is the saturation ratio, K is a rate constant and n is the order of reaction ($n=2$), as proposed by Opdyke and Wilkinson [90].
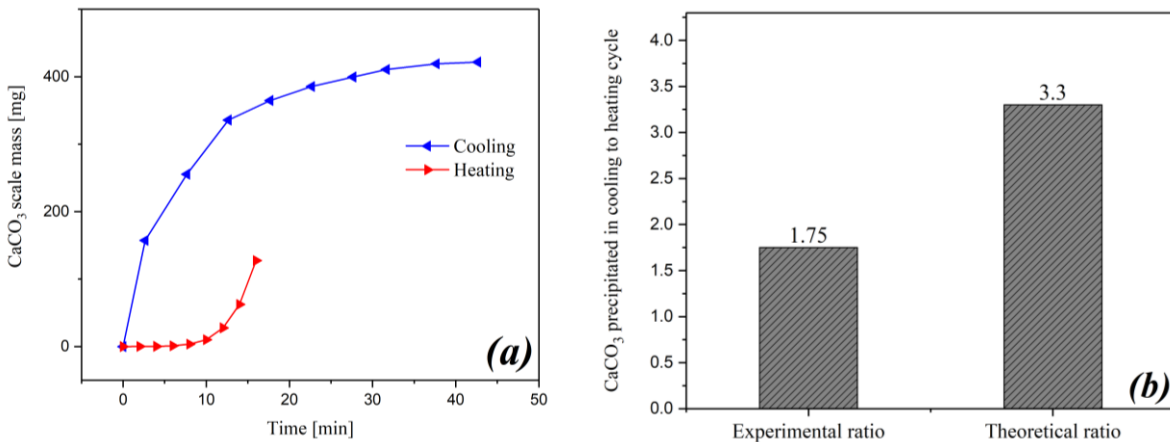
Figure 6.35. (a) The theoretical profile of scale formation during the heating and cooling cycles, (b) experimental and theoretical cooling to heating scale ratios.

133

6.9. Summary

This chapter has presented the investigations of bulk precipitation and surface deposition in closed systems. The effect of solution temperature, surface material, surface roughness, evaporation area, water composition, heating rate and cooling on the scaling kinetics and morphology were discussed. Water composition study includes the influence of magnesium, sulphate, zinc, nitrate, and total organic carbon. The comparison of cooling and heating rates effect included theoretical validation to emphasise that the scaling rate during the cooling period is greater than that in the heating period.

The deposited mass predominantly increases with the volume of evaporated water, while Ca^{2+} solution content simultaneously decreases according to an exponential decay relationship. The solution temperature promotes the bulk precipitation and the polymorphic transformation from both calcite and vaterite to aragonite. It is found that flake-like particles were formed above the crystalline particles.

The amount of flake-like deposits increases with temperature, and it consists of about 4% by weight of Mg. At high temperatures, Mg^{2+} in water may interact with growing crystals and inhibits further growth to aragonite. Similarly, the scale structure on aluminium and copper surfaces might be affected by the presence of Cu^{2+} and Al^{3+} which are released as corrosion products.

The effects of the surface substrate and roughness were found to be secondary on the precipitated scale. As the crystal forms in the bulk solution by the homogeneous nucleation, a surface may not control the nucleation and growth process. The surface nature nevertheless can affect the adhesion force with the precipitated crystal. The morphology analysis showed that calcite on the smooth surface turns into aragonite on the surface with moderate roughness and aragonite to vaterite on the rough surface. The evaporation rate is proportional to the evaporation area. The increase in the evaporation area reduces the amount of deposits scale in the solid surface. The analysis of crystal habit demonstrates that the crystals formed at the lower evaporation rate are larger than that at the ones with a higher evaporation rate. The flake-like crystals contain about 17% by weight of Mg, while no Mg was observed in needle-like particles.

A series of experiments have been carried out to simulate the heating of tap water to boiling temperature followed by the normal cooling to ambient temperature. The effect of the composition of water has also been studied. The concentration profile of magnesium, under the medium heating

regime, is different when compared to the calcium profile. No change in the magnesium content has been observed when the solution temperature is between 25 and 60 ºC. Then, as the temperature exceeded 60 ºC, the content of magnesium starts to increase due to water evaporation. Finally, it decreases as soon as saturation concentration is achieved, and it is thermodynamically sufficient for magnesium precipitate to form. The depletion rate of calcium is found to be affected by the content of magnesium for the same amount of carbonate. The concentration of calcium steeply decreases with initial magnesium concentration decrease.

To check the probability of formation of $CaSO_4$ deposits under identical conditions, a solution of calcium and sulphate has been tested. The results showed that the solution content of calcium and sulphate increases with time and temperature as a consequence of water evaporation. As no reduction in the content of both species occurs even after 25 minutes at the boiling temperature, the formation of $CaSO_4$ is concluded to be unfavourable.

The presence of Zn^{2+} reduces the consumption rate of Ca^{2+} during potable water heating. The induction time of $CaCO_3$ crystallisation is prolonged as the content of Zn^{2+} increased. Analysis of Zn^{2+} concentration as a function of time refers to Zn^{2+} consumption either in complexation with other foulants or in crystallisation reaction to $ZaCO_3$. The presence of $ZnCO_3$ as a Smithsonite was confirmed by XRD analysis. Zn^{2+} in scaling potable water also affects the morphology of the precipitates.

It has been shown that the presence of NO_3^- at different permissible concentrations does not affect the precipitation kinetics nor the morphology. On contrary, the Total Organic Carbon (TOC) in water provided by humic acid has a significant inhibitory effect on the kinetics of scaling. The TOC decreases the induction time as well as the precipitation rate.

This chapter has presented the precipitation kinetics of various types of inorganic scales during the heating and cooling processes relevant to the water in domestic appliances. The heating rate increases the rate of change of calcium consumption in a solution with time. However, the calcium concentration in solution when 100 ºC is attained at a rapid heating rate is higher than that at the same temperature at slow heating; a greater amount of scale is formed when the solution is slowly heated. For the cooling stage, the faster the cooling rate the lower the rate of the calcium reduction in crystallisation reaction. $CaCO_3$ formed in the cooling period was greater than in the heating period.

Chapter 7: Crystallisation Fouling During Convective Heat Transfer

7.1. Introduction

The convective heat transfer is common in domestic and industrial equipment that uses potable/ surface water as a working fluid. The kinetics and structure of crystallisation fouling on different heat transfer surfaces are affected by the operating conditions in open systems as well as the water chemistry. The flow of the scaling solution keeps the local supersaturation constant with time, in contrast to the batch systems. Also, the role of flow rate on the kinetics of fouling is still not fully understood in light of the complexity of potable water composition. Both potable and surface water contain a variety of ionic species that contribute to the formation of different types of inorganic deposits in water distribution systems and domestic appliances [122]. Many industries find locations where close access to water sources are available such as rivers, lakes, etc.

Heat transfer surfaces come with a tendency to corrode in high-temperature conditions [313]. The release of by-product ions such as the cupric ion (Cu^{2+}) in water from copper surfaces may lead to the formation of new types of solid deposits. The formed scales consequently have various morphologies, physical properties and adhesion characteristics. This can make scaling prevention and removal very challenging. Figure 7.1 presents a schematic of mineral scaling on the heat transfer surface from a reaction between water ionic constituents and/or surface ions. Figure 7.1 also shows two mechanisms of mineral deposition: transfer of ionic constituents from the bulk solution to the vicinity of the surface, and integration of scale particles on the surface.

In this chapter, the kinetics and morphology of fouling crystallisation on the heated surface during the convective heat transfer were examined using the Flow-Visualisation Rig. The camera observation of the surface and the scale mass gain evaluation determine the effect of surface temperature, surface material, surface roughness, flow rate and presence of vapour bubbles on the surface.
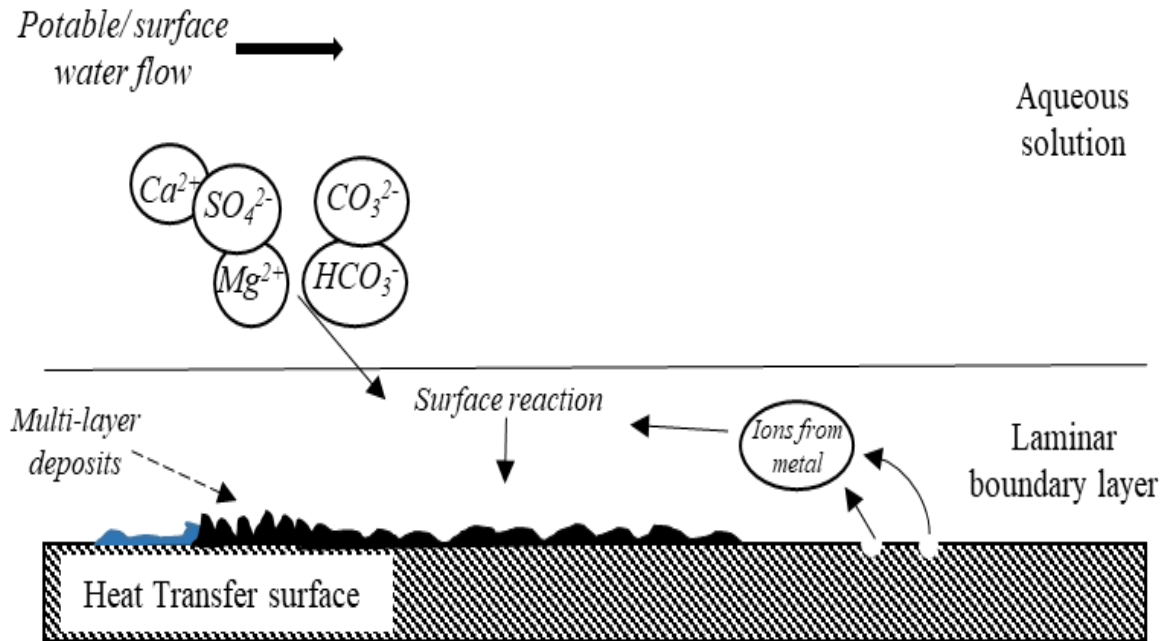
Figure 7.1. Schematic of surface scaling process from potable water.

7.2. Effect of surface temperature

The temperature of the heater was maintained constant during the deposition experiment. However, the temperature of the surface-solution interface depends on the conductive heat transfer through the sample. Figure 7.2 shows mineral deposits on the stainless-steel surface after 24 hours under different surface temperature (T_s) conditions. It can be seen that surface coverage and crystal size increase with the temperature of the surface and time. It can be seen that flower-like aragonite and rhombohedral calcite polymorphs are present on the surface. The number of crystals per unit area of a sample increases with the surface temperature. In the test of 100 °C, and after 8 hours from the beginning, a vertical bar of the tiny crystals formed in a path of the vapour bubble, then it developed to larger aragonite particles.

Figure 7.3 compares the total deposition on different substrates namely, stainless steel, aluminium, and copper. It is confirmed that the fouling rate increases with surface temperature for all metals as expected. The temperature enhances surface deposition by reducing the solubility of minerals that potentially form from potable water [314].
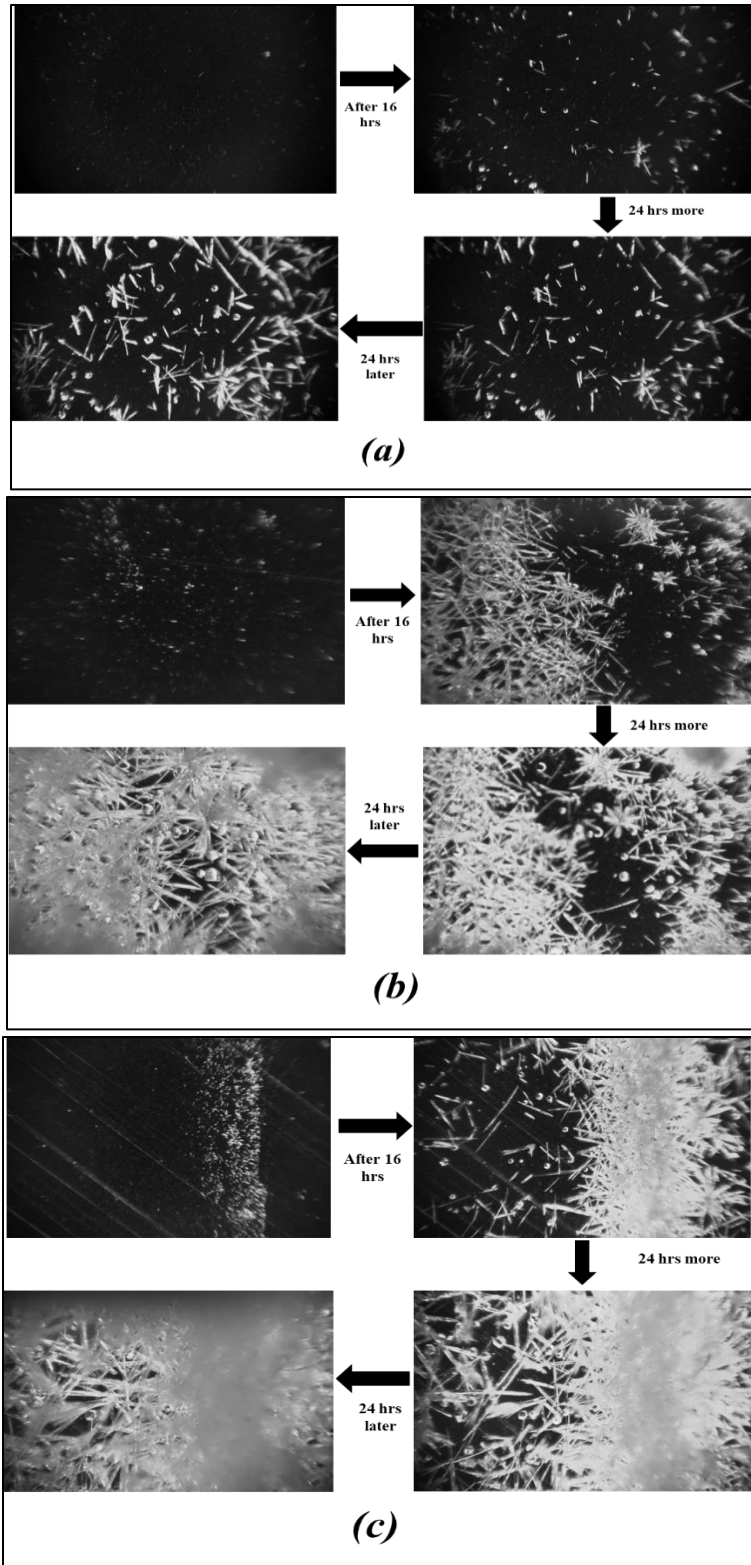
Figure 7.2. Camera images for scale formation at different stainless-steel surface temperatures: (a) T$_s$= 80 ºC; (b) T$_s$= 90 ºC; and (c) T$_s$= 100 ºC, t= 24 hr.
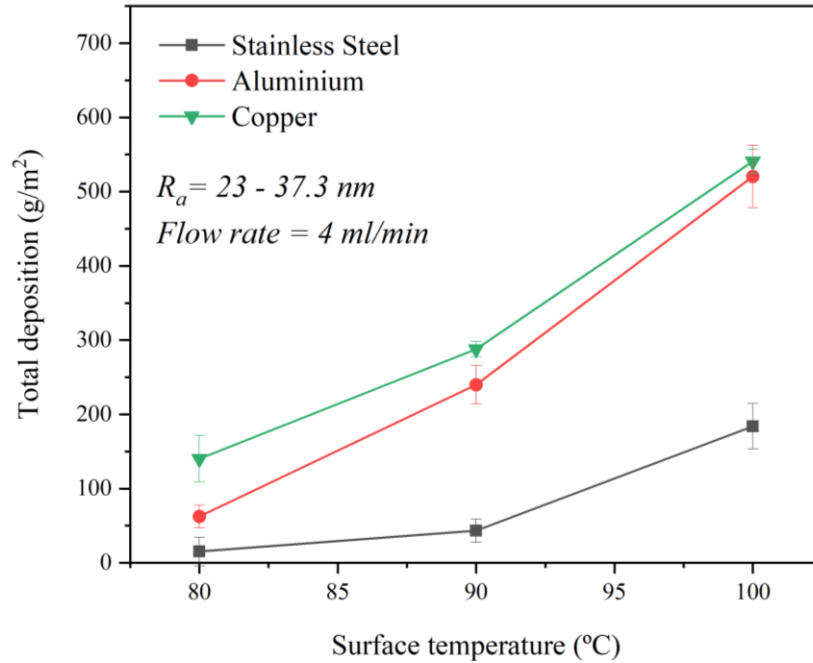
Figure 7.3. Total deposition on different surface materials under different surface temperatures.

The SEM observations show that the surface deposition at a surface temperature greater than 90 °C consists of two areas: a porous, rough layer and a smooth and flat layer (Fig. 7.4). It was found that the flat and smooth layer is the area underneath the vapour bubble and mainly comprises calcium, carbon, magnesium, and oxygen as analysed by the EDX technique (Spectra 3 and 4). The Mg^{2+} may inhibit the growth of $CaCO_3$ crystal through Mg-crystal incorporation, thereby preventing the morphological transformation to aragonite [298]. The elemental analysis for the rough layer (spectrum 5), which is under the effect of convective heat transfer, confirms that the deposited particles are $CaCO_3$.
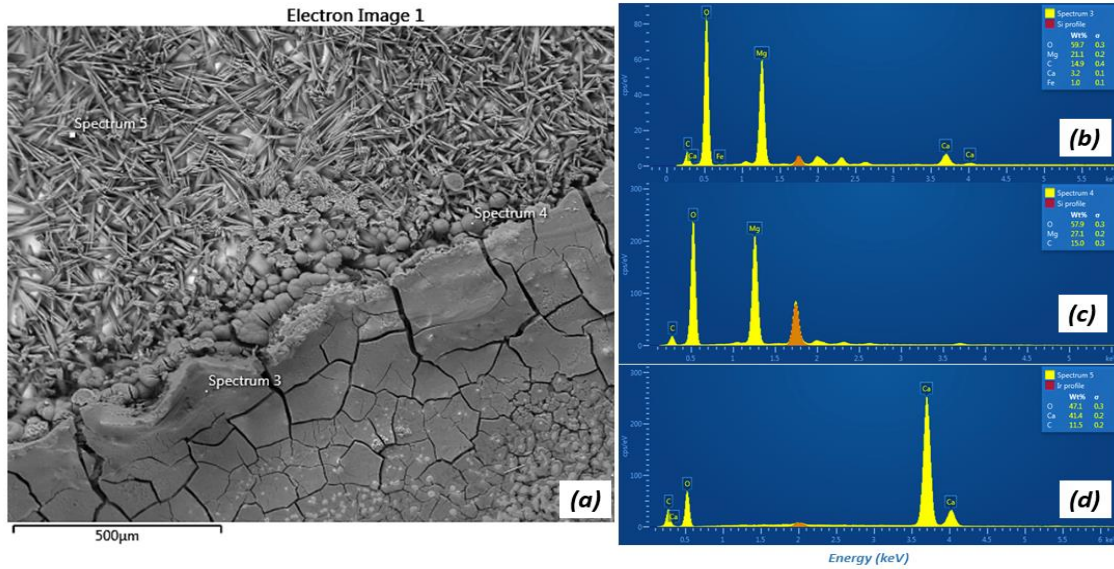
Figure 7.4. EDX elemental analysis of the deposits on stainless steel; (a) SEM image, (b) spectrum 3, (c) spectrum 4 and (d) spectrum 5.

The SEM images and the XRD patterns for the deposited materials show the polymorphic transformation from aragonite to calcite with increasing temperature (Fig. 7.5 and 7.6). Aragonite once more is the dominating form of $CaCO_3$ at the tested surface temperatures (Fig. 7.5) while no vaterite has been observed by XRD in figure 7.6 due to low stability at high temperatures [38].
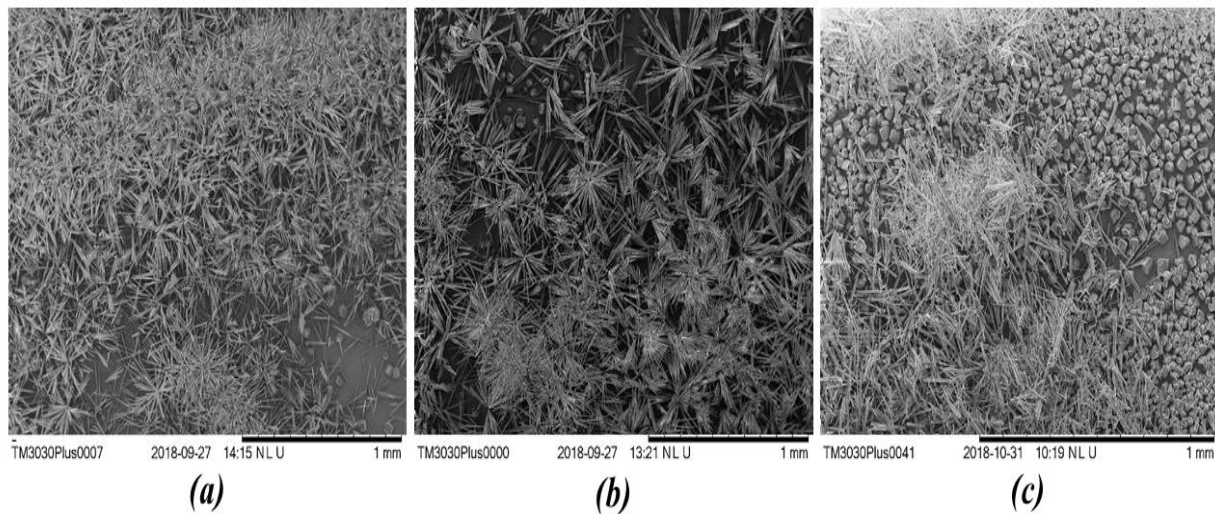
Figure 7.5. SEM images of scale on the surface with different surface temperatures: (a) T_s= 80 ºC; (b) T_s= 90 ºC; and (c) T_s= 100 ºC.

140
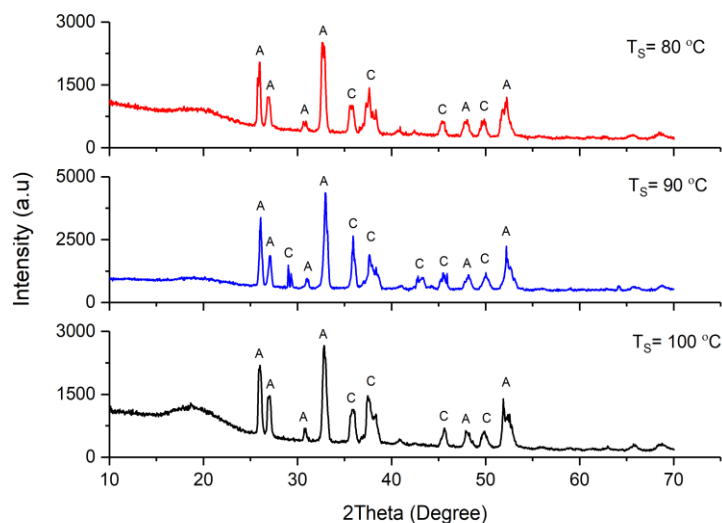
Figure 7.6. XRD data for the scale crystalline species (A: Aragonite and C: Calcite).

7.3. Effect of surface material

Figure 7.7 demonstrates the total mineral deposition on stainless steel, aluminium and copper at a heater temperature of 98.2 ℃ and initial surface temperature of 90 ℃. The thermal conductivity of each metal has been plotted against surface deposition to show how the fouling rate is consistent with the substrate's thermal conductivity. The amount of heat transferred by conduction from the heater and heater temperature is constant during the experiment. Therefore, surface temperature varies based on the material thermal conductivity, the higher the thermal conductivity, the lower the difference between the heater and surface temperatures. The temperature difference between the heater and surface is inversely proportional to thermal conductivity according to Fourier's law. Similar findings for the deposition of $CaSO_4$ on various heat transfer surface materials were obtained by Kazi, et al. [315]. Camera images as shown in figure 7.8 present the surface coverage after 24 hours of fouling experiment on the tested substrates. Copper is almost covered with scale particles, while few crystals are distributed on the stainless steel surface.
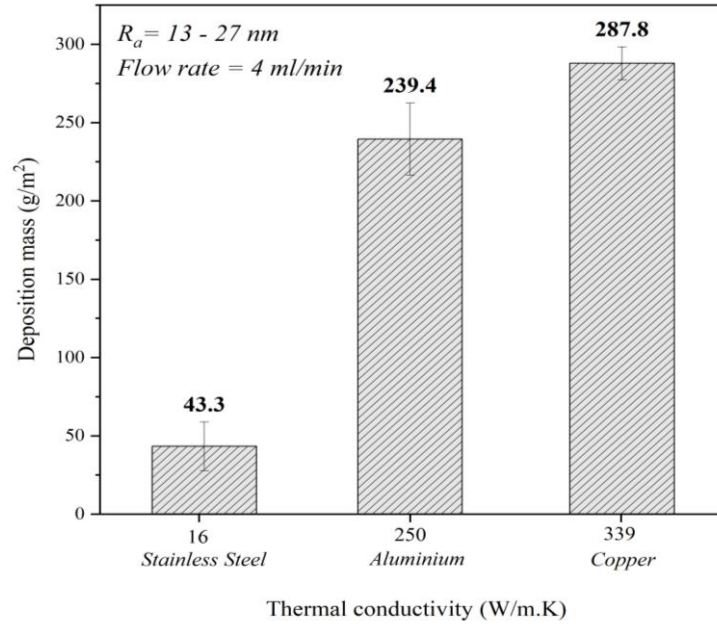
Figure 7.7. Surface deposition for thermal conductivity of different substrates at a heater temperature of 98.2 ºC.
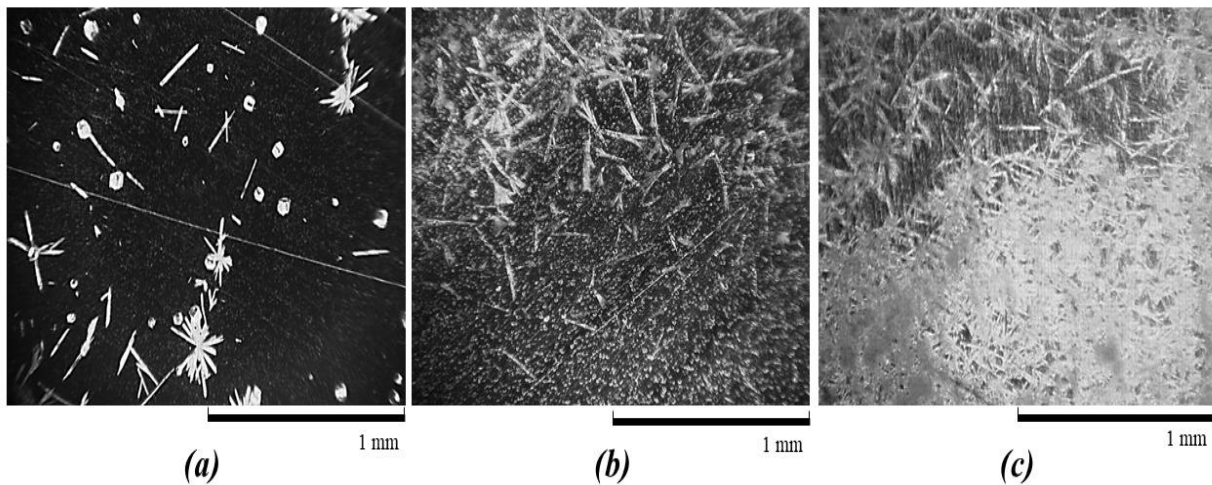
Figure 7.8. Camera images for scale formation on different substrates: (a) stainless steel; (b) aluminium; and (c) copper, t= 24 hr and T_h= 98.2 ºC.

The results of the EDX analysis of flat smooth deposits on the copper surface are presented in figure 7.9. The thin layers on the surface are rich in copper and oxygen (Spectra 7 and 8). It can be concluded that deposited layers are mainly made up of one form of copper oxide which is produced as a corrosion product from the heat transfer surface because the test water contains no

Cu ions. Hence, the surface temperature may promote the oxidation reaction. The second scenario is that Cu ions are absorbed into the growth sites of $CaCO_3$ crystal resulting in growth retardation [241]. The thicker layer mainly comprises calcium, carbon, magnesium, and oxygen (Spectrum 6).
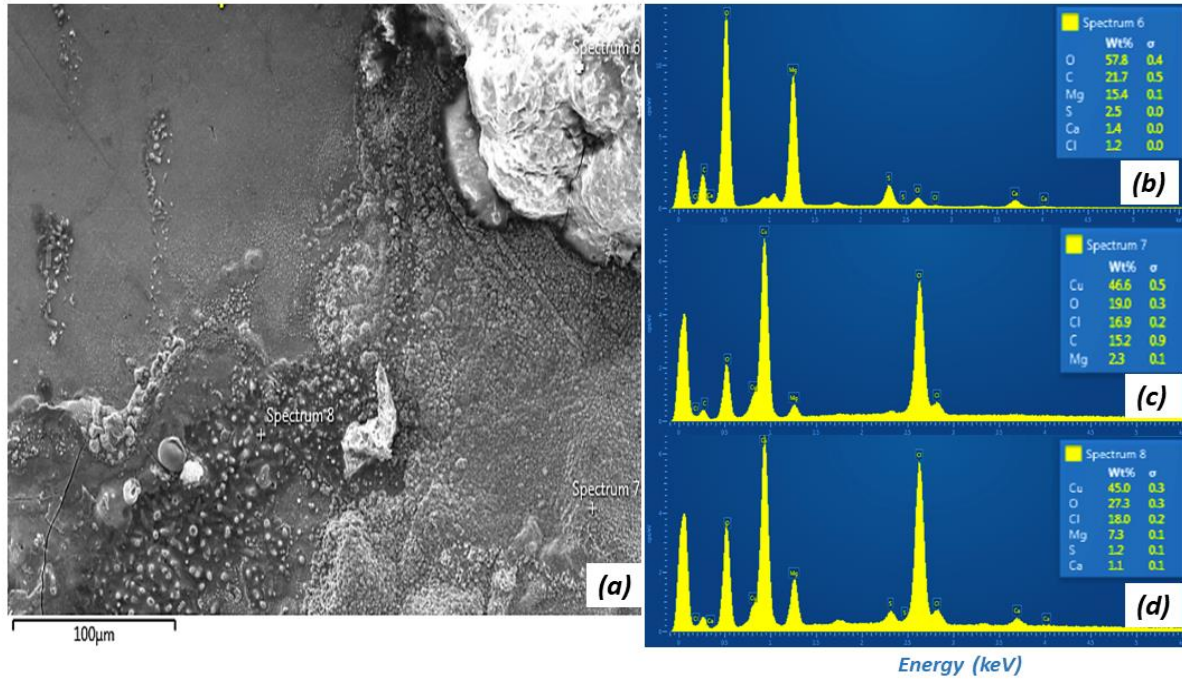
Figure 7.9. EDX elemental analysis of the mineral scale on copper; (a) SEM image, (b) spectrum 6, (c) spectrum 7 and (d) spectrum 8.

The SEM observations in figure 7.10 show the formation of two different phases of scale; porous, rough layer and flat smooth layer of deposits on the tested substrates with the rough part mainly consisting of needle-like aragonite. The X-ray diffraction data displayed in figure 7.11 displays that the crystalline phase of copper oxide (cuprous Cu_2O) might be formed on the copper substrate. The findings illustrate that aragonite is the prevailing polymorph of $CaCO_3$ for the tested substrates and the presence of $CaSO_4$ as anhydrite is also detected on the copper substrate.
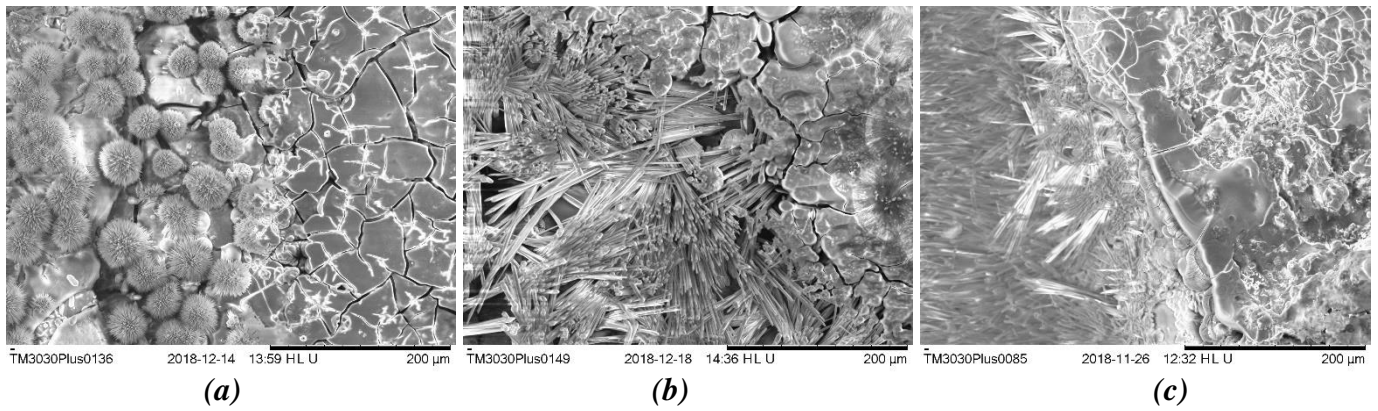
Figure 7.10. SEM images for scale formation on various heat transfer surfaces: (a) stainless steel; (b) aluminium; and (c) copper.
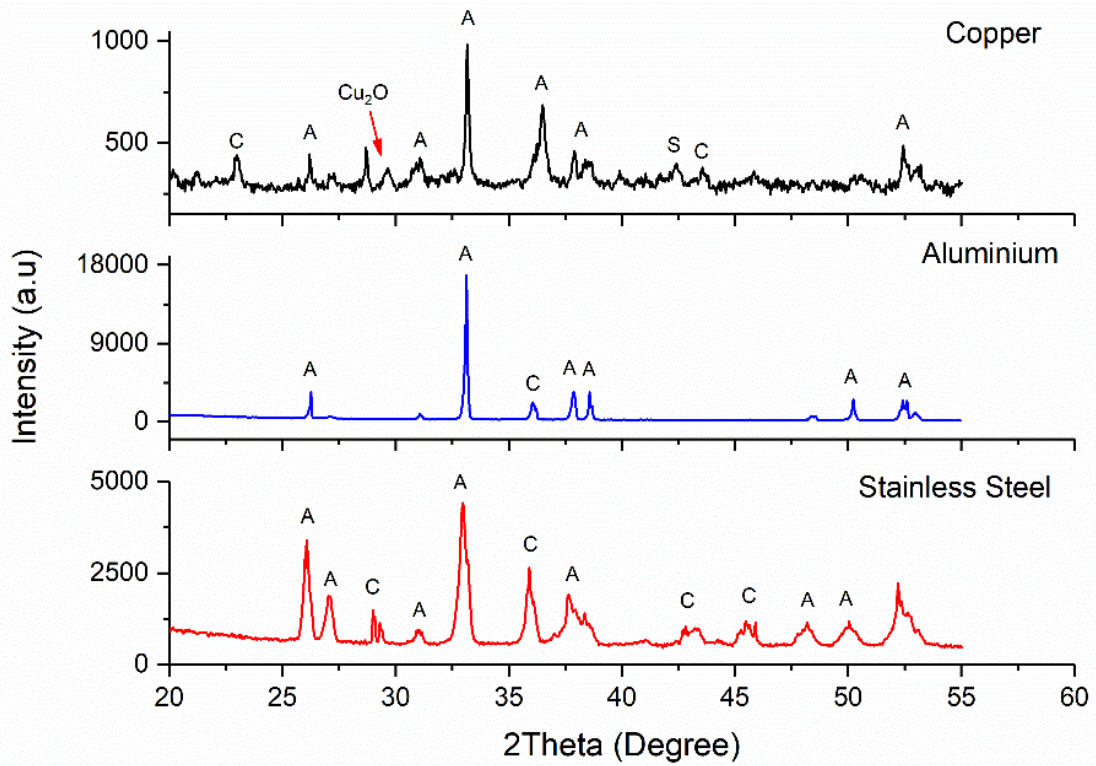
Figure 7.11. XRD data for the deposited materials on different substrates (A: Aragonite; C: Calcite; and S: Anhydrite calcium sulphate).

144

7.4. Effect of surface roughness

Four stainless steel surfaces with different average roughness values (Ra) have been chosen to understand the roughness role in the scaling process. The amount of mineral deposits somewhat linearly increases with a surface roughness (Fig. 7.12). This phenomenon can be explained by the following mechanisms: (1) The peaks on the surface may act as effective nucleation sites and as hooking sites, hence improving the nucleation rate and interlocking adhesion effect [162]. (2) The mechanical finishing may produce a clean surface, thus a high reactivity [316]. (3) The larger contact area of the rough surface leads to higher adhesion strength [317]. (4) Surface wettability is improved by roughness, hence enhancing the adhesive strength [318].
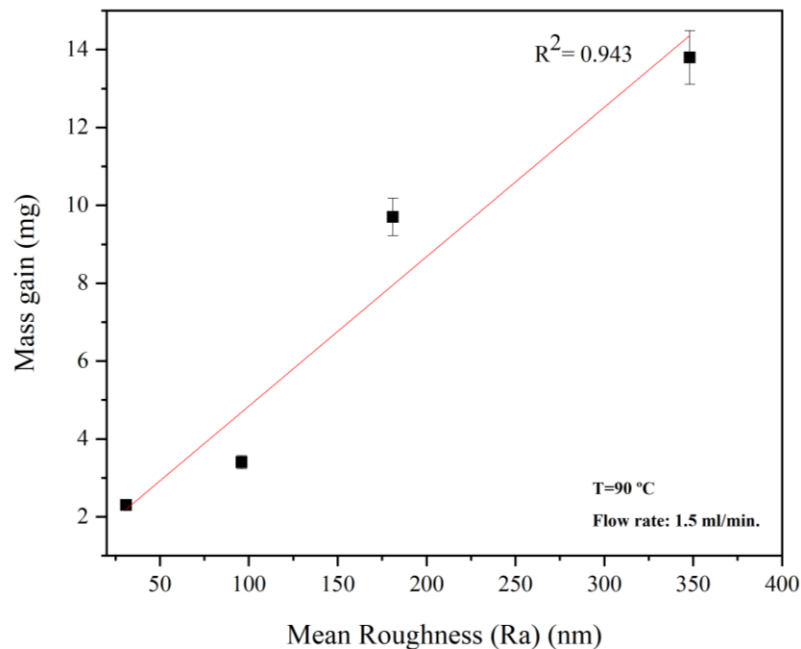
Figure 7.12. The scale mass gain on stainless steel with different roughness.

It seems that the rough surface prefers the aragonite polymorphic phase over the other forms. The flake-like and needle-like scale particles are present as compact build-up on the rougher surface, whereas a porous layer of calcite and aragonite mixture can be observed on the smooth and the medium surface (Fig. 7.13). A consequence of numerous nucleation sites on the rough substrate is the formation of robust adhesive bonds between the crystallites. The micro-cavities was filled by the growing crystals resulting in promoting adhesive bonding. The polymorphic transformation from calcite on the smooth surface to aragonite on the rough one has been

approved by the XRD measurement (Fig. 7.14). The mechanism of the morphological transformation as a result of surface roughening is still far from being obviously understood.

Ra= 96 nm   Ra= 181 nm   Ra= 348 nm
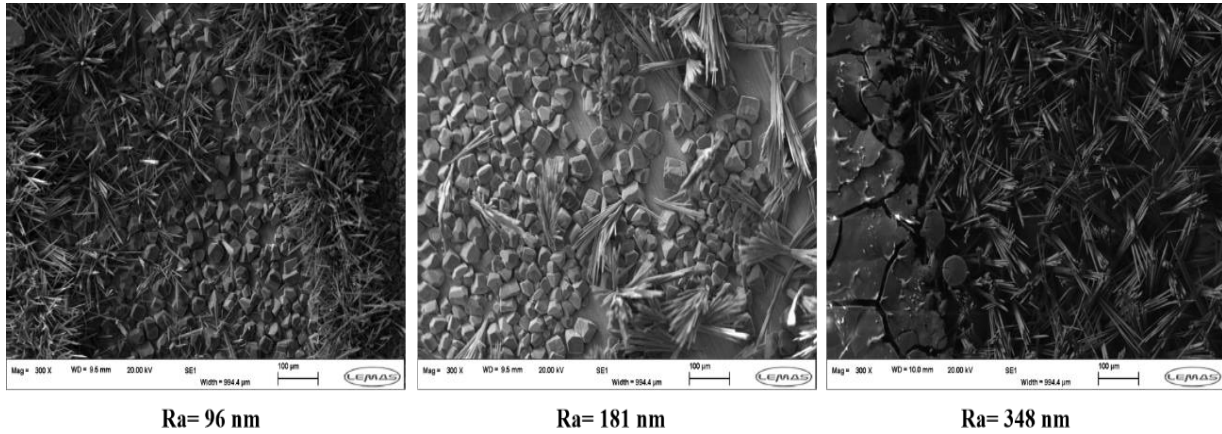
Figure 7.13. SEM images of scale on the surface with different roughness.
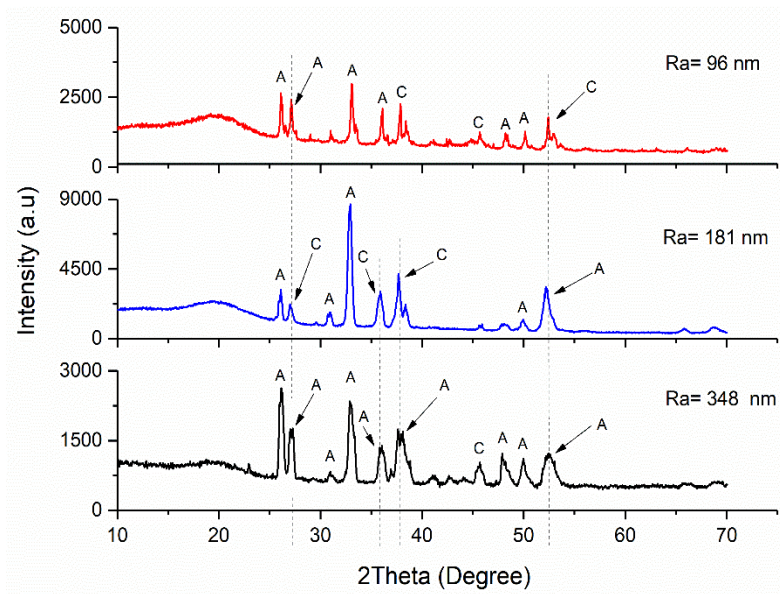
Figure 7.14. XRD analysis of the surface deposits on different roughness surfaces (A: Aragonite, C: Calcite, and V: Vaterite).

7.5. Effect of flow rate

The effect of flow rate on surface deposition has been studied using stainless steel substrate at a heater temperature of 98.2 ºC, tested flow rates in the range of 0.65 ml/min - 6.32 ml/min corresponding to laminar flow regime with Reynolds numbers 1.26 – 12.07 (Fig. 7.15). Solution

flow has a complicated role in crystallisation fouling. The increase in flow rate reduces the amount of scale formed on the heat transfer surface until it reaches the optimum point. The optimum point is the flow rate at which the lowest amount of mineral scale is deposited on the heated surface for particular surface characteristics and temperature. At the range below the optimum point, similar to findings obtained by Pääkkönen, et al. [22], flow rate reduces the surface temperature due to enhanced convective heat transfer, hence decreasing the crystallisation reaction rate and the total deposition. Above the optimum point, the total deposition increases with the flow rate. Flow velocity promotes the mass transfer of foulants from the bulk solution to react on the surface. According to the study by Hasson, et al. [87], the mass deposition rate is proportional to the mass transfer coefficient.
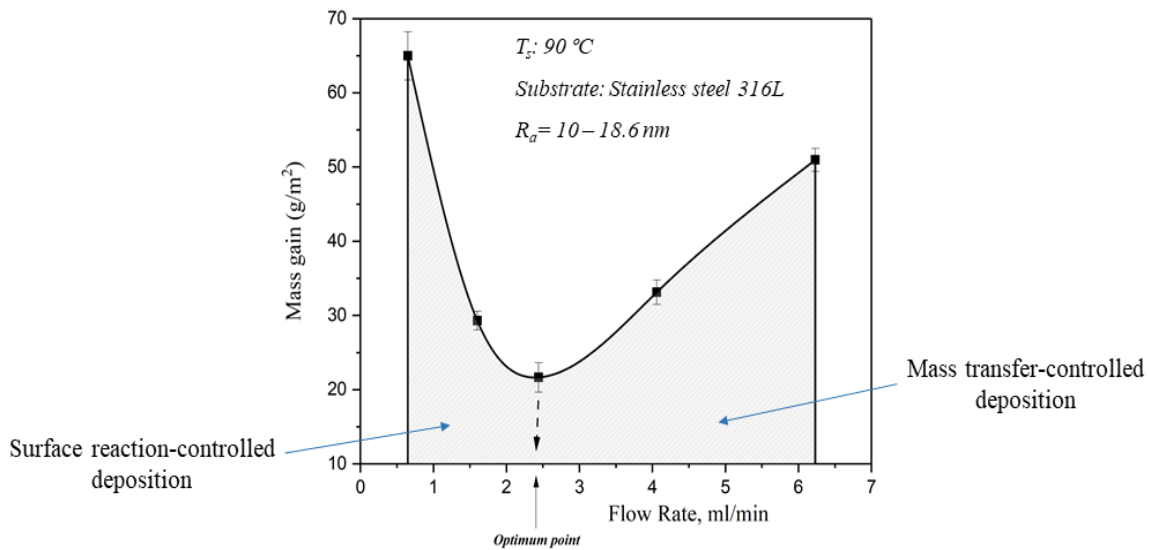
Figure 7.15. Effect of flow rate on the scale amount on the heat transfer surface.

At a lower flow rate, a mixture of needle-like and sunflower-like aragonite $CaCO_3$ was formed on the stainless steel with the absence of the smooth crystalline layer (Fig. 7.16). The flat smooth fouling layer can be seen in flow rate tests of 4 and 6.32 ml/min. Figure 7.17 displays the stages of morphological transformation for flower-like aragonite from twin-rosette aragonite, the tiny twin-rosette aragonite particles get taller with time (Fig. 7.17a and 7.17b). The bristles at the ends of the stick-like particle become longer and denser and start bending to approach those at the other end (Fig. 7.17c and 7.17d) until a complete flower-like particle forms and grows to larger flowers

(Fig. 7.17e and 7.17f). The above process allows the surface to be fully covered by a dense layer of flower-like aragonite which has a greater surface area than the twin-rosette.

The XRD data shows a morphological transformation of CaCO$_3$ crystallite from aragonite to calcite with an increase in flow rate (Fig. 7.18). Magnesium hydroxide, as brucite is detected on the surface under a water flow rate of 6.23 ml/min.

(b)   *(b)*   *(c)*
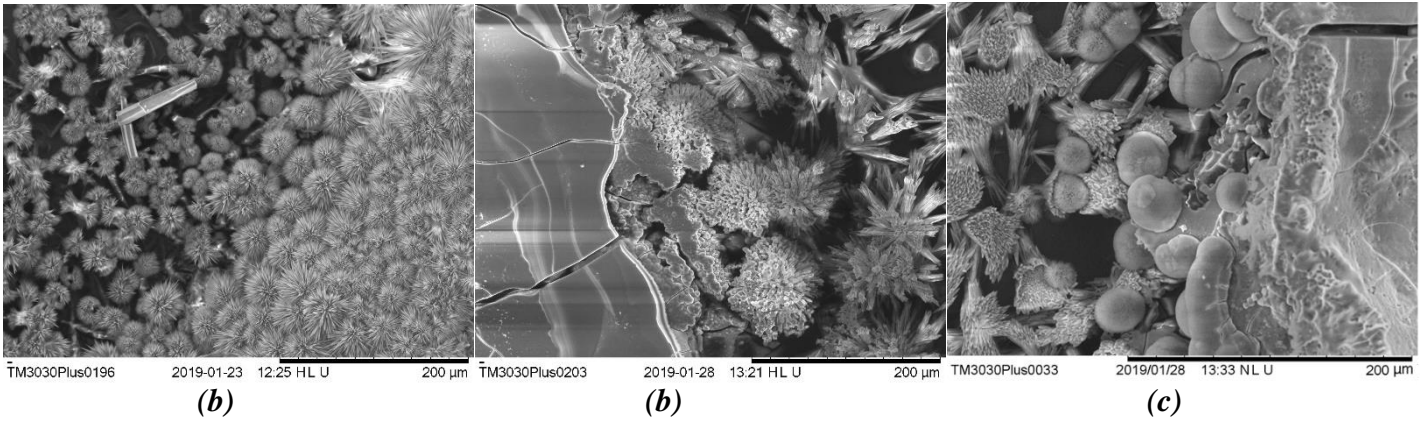
Figure 7.16. SEM images of scale particles under effect of various flow rate: (a) 0.65 ml.min^{-1}; (b) 4 ml.min^{-1}; and (c) 6.23 ml.min^{-1}.
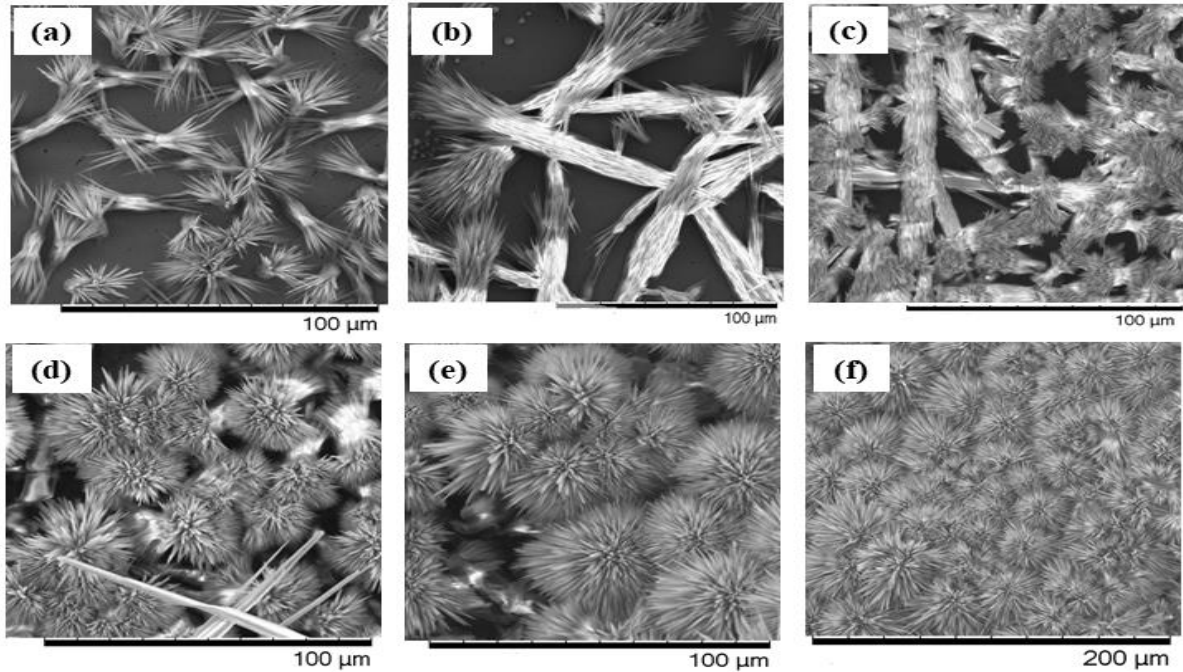
Figure 7.17. SEM observations of CaCO$_3$ morphology transformation on stainless steel with time under a flow rate of 0.65 ml.min^{-1}: (a-c) a twin-rosette aragonite at different growth stages; and (d-f) a flower-like aragonite.

148
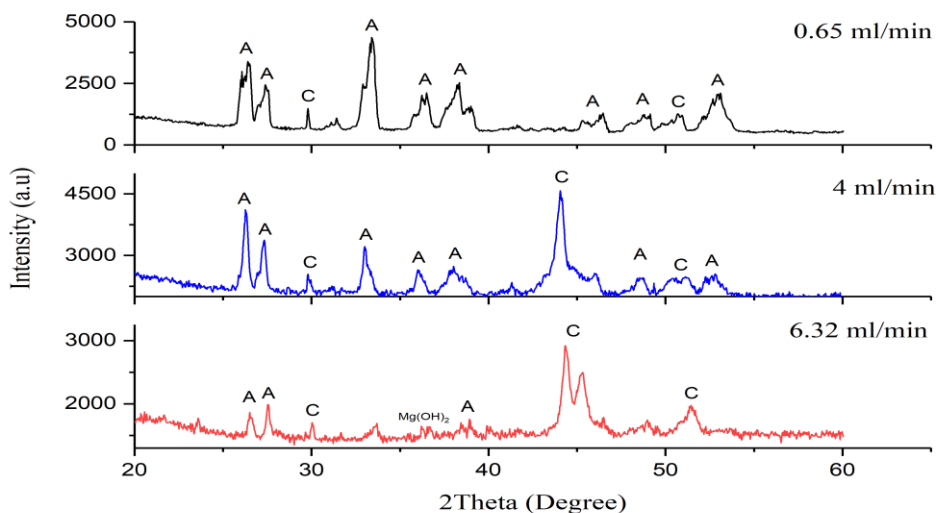
Figure 7.18. XRD data for the deposited minerals under the effect of different flow rates (A: Aragonite and C: Calcite).

7.6. Effect of vapour bubbles

As the surface temperature attaints the water boiling point, vapour bubbles form and distribute on the test surface with different sizes. The bubble departure diameter is small in the nucleation stage where no significant crystals are formed on the surface. The bubble departure diameter is the diameter at the point of the bubble leaving the hot surface. Once a uniform layer of scale covers most of the heat transfer surface, the departure diameter and residence time of bubbles increases due to the reduction of the crystal-solution interfacial temperature. In all experiments, a large vapour bubble covering around half of the fouled surface was visually observed. Figure 7.19 shows the small and medium size of steam bubbles formed on the surface. However, the camera was unable to detect the whole large bubble as it is out of the camera coverage.

The fouling process in the vicinity of developing vapour bubbles is crystallisation reaction controlled which is significantly affected by surface temperature [319]. These bubbles enhance the fluid turbulence near the surface, hence promoting the heat transfer and reaction rate. The vapour small bubbles formed on the heated surface promotes the heterogeneous nucleation rate, as illustrated in figure 7.20. The tiny nucleus formed underneath a bubble undergoes two scenarios based on the bubble's departure frequency. If a bubble develops to a large size (about 25% of the surface area), then departs the surface, the nuclei will grow to large crystals. The second scenario

is when a large bubble settles on the surface until the end of the experiment. Nuclei in between the bubble film and the surface will grow to a smooth crystalline layer.
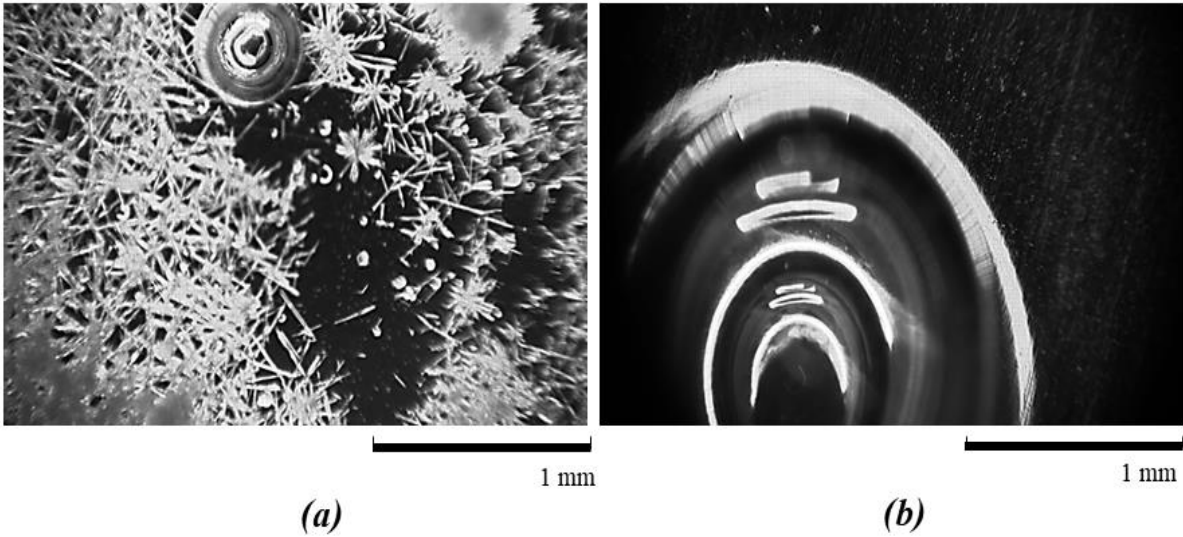
Figure 7.19. Camera images for (a) small size and (b) medium size of vapour bubbles.
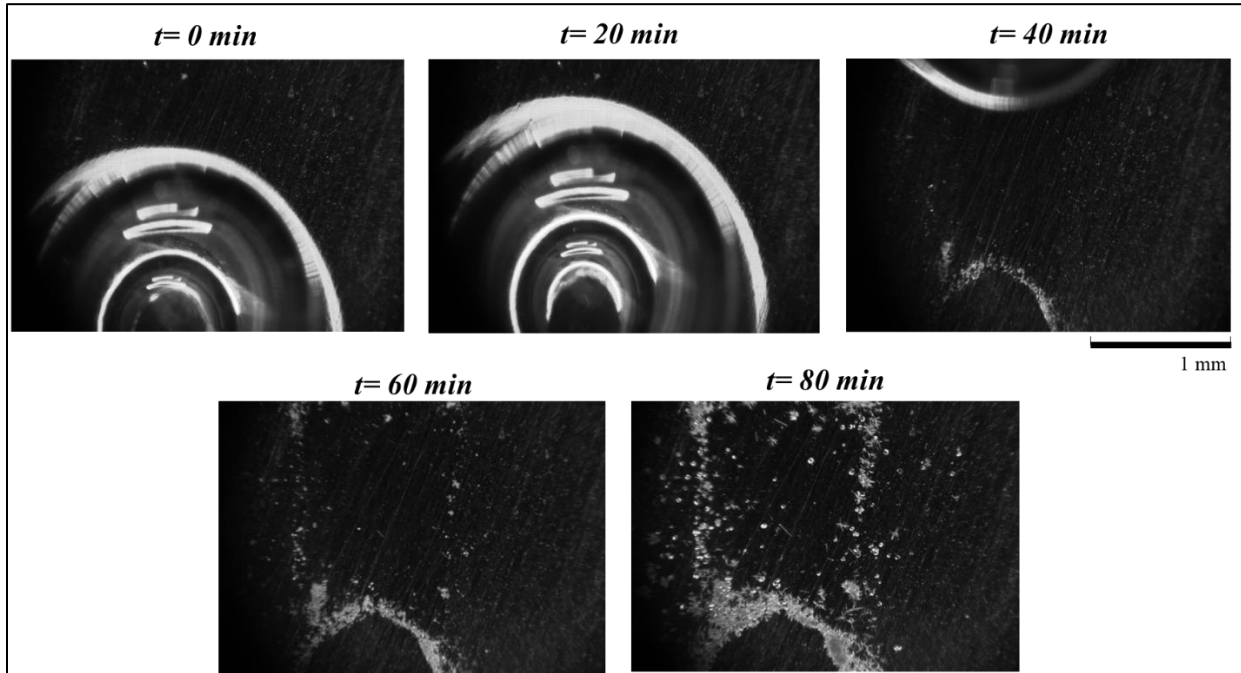
Figure 7.20. The effect of vapour bubble on the inorganic fouling on stainless steel, T_s=90 °C and flow rate = 1.5 ml. min^{-1} .

7.7. Summary

The convective heat transfer mechanism is the case in several domestic and industrial applications that uses potable water as a working fluid. The study of inorganic fouling kinetics on the heated surface during the convective heat transfer has been presented in this chapter. The experiments were carried out using a once-through flow visualisation setup. The formation of fouling particles and vapour bubbles on the heat transfer surface has been monitored using a high-performance camera. The effect of surface temperature, material, roughness, flow rate and vapour bubbles were investigated by measuring the scale mass gain as well as the camera observations. The impact of changing these parameters on morphology was also examined.

Surface temperature increases the amount of deposits that formed on all the tested substrates. The surface temperature increases the density of nucleating vapour bubbles on the surface leading to a higher nucleation rate due to an increase in the local supersaturation in the vicinity of the bubbles. Two distinct scale regions are observed on the surface under different temperatures, the first is the flat Mg-rich layer and the second is a rough scale layer of $CaCO_3$ The increase in temperature promotes the transformation of aragonite to calcite which is the most stable form under high temperatures. However, Aragonite is the dominating polymorphic phase of $CaCO_3$ at the tested surface temperatures.

Concerning the substrate effect, copper and stainless steel gained the largest and smallest amount of scale deposits, respectively, while the amount of scale formed on aluminium is closer to the amount on copper than stainless steel. Two distinct scale regions are observed on the surface under different temperatures, the first is the flat Mg-rich layer and the second is a rough scale layer of $CaCO_3$. However, copper and oxygen are observed as a thin deposited layer in some regions of the copper surface. The presence of copper oxide on the copper surface is confirmed by the XRD measurement.

The amount of mineral deposits somewhat linearly increases with surface roughness. The rough surface prefers the aragonite polymorphic phase over the other forms. The flake-like and needle-like scale particles are present as compact build-up on the rougher surface, whereas a porous layer of calcite and aragonite mixture can be observed on the smooth and the medium surface.

Fluid flow has a complicated role in the fouling rate. Flow rate reduces the amount of scale formed per unit area reaching the optimum point, at which the lowest scale mass is obtained. Above the

optimum point, the total deposition increases with the flow rate increase. In terms of scale morphology, aragonite is the dominating polymorphic phase of $CaCO_3$ under all test conditions.

The visual observations by the camera show the vapour bubbles influence the heterogeneous nucleation rate on the surface. This is attributed to the increasing supersaturation/ temperature in the vicinity and underneath the nucleating bubbles. The fouling process in the vicinity of developing vapour bubbles is crystallisation reaction controlled which is significantly affected by surface temperature.

Chapter 8: Crystallisation Fouling During Boiling Convective Heat Transfer

8.1. Introduction

The fouling crystallisation during boiling convective heat transfer was investigated using the aluminium surface. The experiments were conducted using the flow-evaporation scaling cell (FESC) and the pressurised flow-evaporation scaling cell (PFESC). The effect of surface temperature, surface roughness, system pressure and water chemistry has been examined. Aluminium is one common metal used in the fabrication of heat transfer surfaces in household devices and systems. It possesses the second-highest thermal conductivity after copper, but is less expensive, with fair resistance to corrosion in aqueous environments encountered in household devices [320]. There have been few significant attempts in terms of investigating fouling tendency on aluminium surfaces using potable water as the test fluid.

Water containing oxygen catalyses the corrosion reaction of aluminium metal. Oxygen in water bonds with aluminium forming a protective film of aluminium oxide which prevents further oxygen attack [321]. It has been reported that the thickness of aluminium oxide (Al_2O_3) film that forms in water is about twice that forms in the air [322]. The rate of oxygen attack on the metal increases with temperature. The oxidation of aluminium proceeds by the formation of an amorphous layer which subsequently develops into a crystalline oxide depending on temperature and time [323]. Aluminium oxide films forms in a porous structure consisting of discrete islands. As a result of the porous structure, the oxide layer is highly absorbent and thus prone to corrosion and fouling in aggressive conditions [324].

A variety of ionic species exist in potable water, such as Ca^{2+}, Mg^{2+}, Na^+, Cl^-, HCO^- and SO_4^{2-} and it is well known that some of these can contribute positively or negatively to the scale layer growth rate [12, 126]. Natural organics exist in water from various sources. They are complex molecules that affect colour, odour, taste and cause serious health issues. The predominant type of natural organic material is known as humic substances which are classified into humin, fulvic acids and humic acids [249, 250]. The solubility of humic acids, which is pH-dependent, raises the content of total organic carbon (TOC) in potable water. The typical molecular structure of humic acid is shown in figure 8.1 [251]. The presence of TOC in water can inhibit the formation of inorganic scale [252, 253].

Figure 8.1. Model structure of the humic acid molecule according to Stevenson [254].

The understanding of surface fouling from potable water in domestic appliances is a real challenge for the customers and manufacturers. For the better design of heat transfer surfaces, the effect of the key operating conditions and substrate needs to be studied. The present work is devoted to investigating the fouling process on the aluminium surface for different surface temperatures, roughness and process pressure. The fouling evaluations include qualitative analysis (morphology) and quantitative measurement (fouling resistance and mass of deposits). The structure and composition of the oxide film formed on aluminium during the heating process were also examined. Figure 8.2 illustrates the fouling process on a rough aluminium surface.

Figure 8.2. Schematic representation of the fouling process on a rough aluminium surface.

The presence of various ionic species in potable water complicates the understanding of fouling kinetics and deposit structure. The aim of this chapter, also, is to investigate the influence of

154

potable water constituents namely, Mg^{2+}, Na^+, Cl^-, SO_4^{2-}, Zn^{3+} and TOC on the scale formation kinetics at constant operating conditions. A study of the surface crystallisation of inorganic scale from different solutions was carried out in a rectangular open flow channel. The deposit morphology on the heat transfer surface was simultaneously discussed.

8.2. Aluminium oxide film

In all experiments of mineral scaling conducted on the aluminium surface at temperatures between 80 to 110 ℃, a thin passivation film of aluminium oxide fully covers the aluminium substrate (Fig. 8.3a). The scale crystals simultaneously grow through and on the aluminium oxide passive layer. Figure 8.3 shows SEM and FE-SEM images of the aluminium oxide film at different magnifications. The oxide film comprises porous discrete islands distributed on the surface. The XRD analysis of the oxide layer shows that β-Al_2O_3 (beta alumina) is the dominant form of aluminium oxide on the substrate (Fig. 8.4).

Beta alumina has much lower thermal conductivity than that of bare aluminium surface which causes additional resistance to heat transfer [325]. The growth rate and thickness of the aluminium-oxide film increase as a function of substrate temperature [326]. The contact angle (CA) measurements show that the CA of the water droplet is 96º and 24º on a bare substrate and the oxide film, respectively (Fig. 8.5). The formation of alumina film increases the hydrophilicity of the surface, essentially leading to a higher crystal/substrate contact area. The hydrophilic surfaces are known to reduce the energy barrier for crystallisation [327], hence a higher fouling rate is expected on the alumina coated substrate [328]. Fouling rate is the amount of inorganic deposit formed on unit area of surface per unit time.
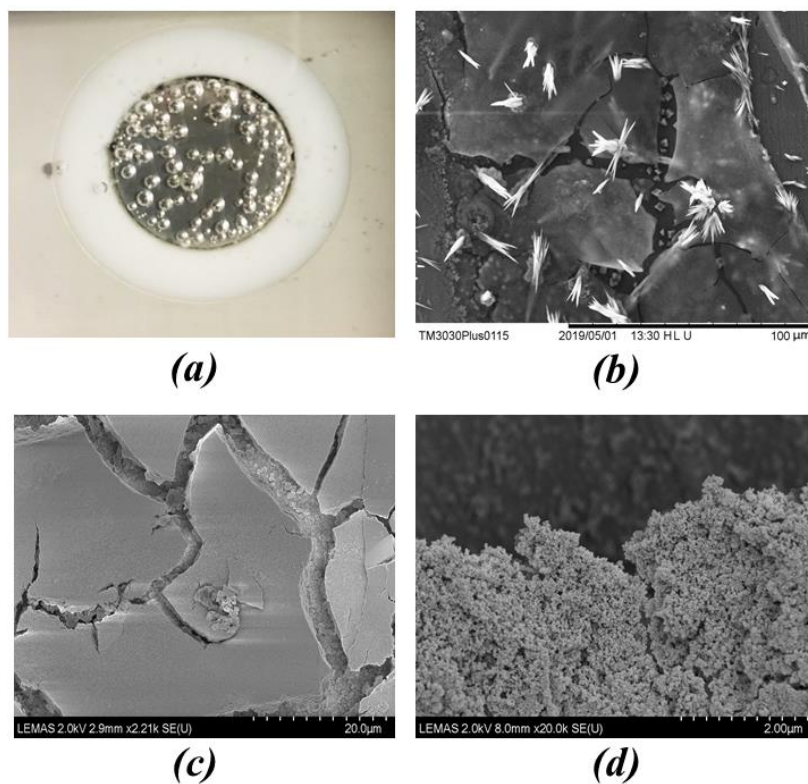
Figure 8.3. (a) Photo of aluminium surface coated with an aluminium oxide film, (b) SEM image of the oxide film segments with CaCO₃ crystals, (c) and (d) FE-SEM images of the oxide film with no scale crystals.
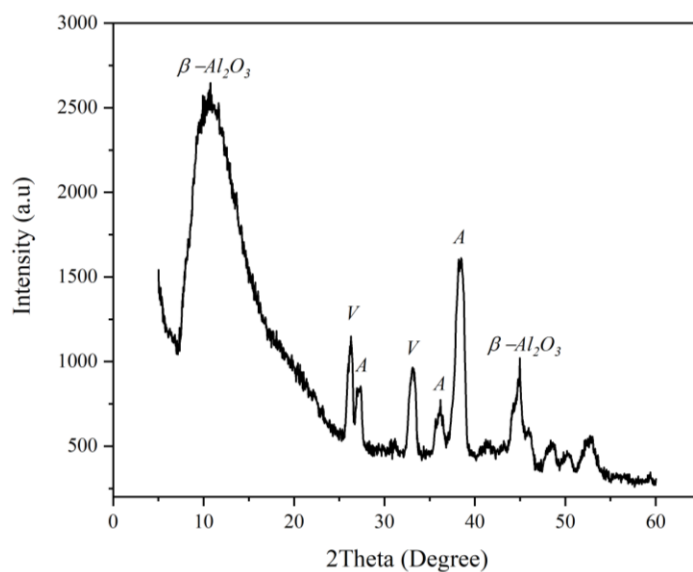
Figure 8.4. XRD pattern of the aluminium oxide layer in presence of CaCO₃ particles [A: aragonite and V: vaterite].

(a)   *(b)*
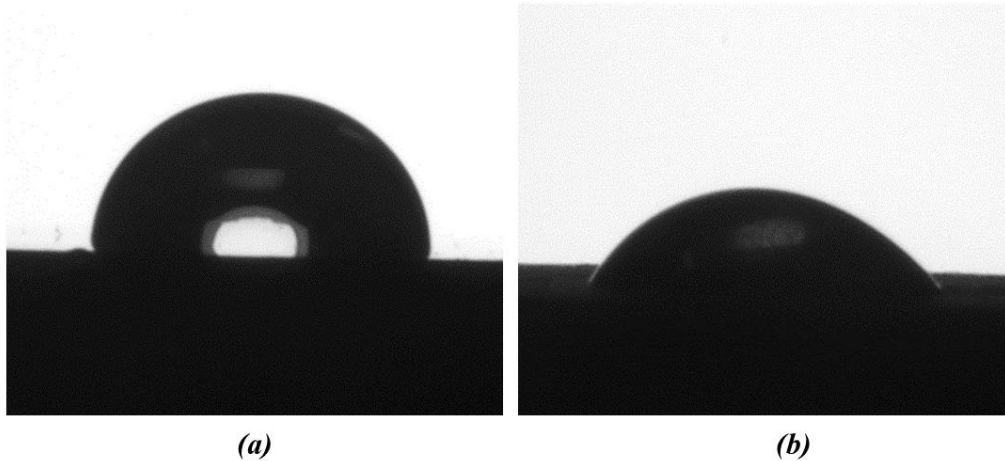
Figure 8.5. Contact angle measurement on (a) bare aluminium surface (96º) and (b) on aluminium oxide film (24º).

8.3. Effect of surface temperature

Figure 8.6a shows the effect of surface temperature on the fouling resistance of the scale layer; temperature reduces the fouling induction period. In all experiments, the heat transfer surface is fully covered with an inorganic fouling layer. The steady growth follows the induction period until reaches the asymptotic fouling resistance. The asymptotic fouling resistance increases with temperature increase (Fig. 8.6b). The asymptotic fouling resistance is attained when the deposition rate equals the removal rate. The surface temperature enhances the heterogeneous nucleation and growth rate of scale particles [22, 87]. The surface temperature reduces the local salt solubility at the vicinity of the surface and nucleating bubbles.

The increase of surface temperature also promotes the vapour bubbles nucleation rate leading to an increase in the interfacial concentration of fouling species. The fouling process in the vicinity of developing vapour bubbles is crystallisation reaction-controlled which is significantly affected by surface temperature [319]. These bubbles enhance the fluid turbulence near the surface, hence promoting the heat transfer and reaction rate. The reduction in solubility and increase in concentrations both enhance the local supersaturation, which is the deposition driving force. The scale mass and the scale layer properties affect fouling resistance to heat transfer [268]. Figure 8.6b demonstrates that the increase of fouling resistance is controlled by the mass of the deposit.

157
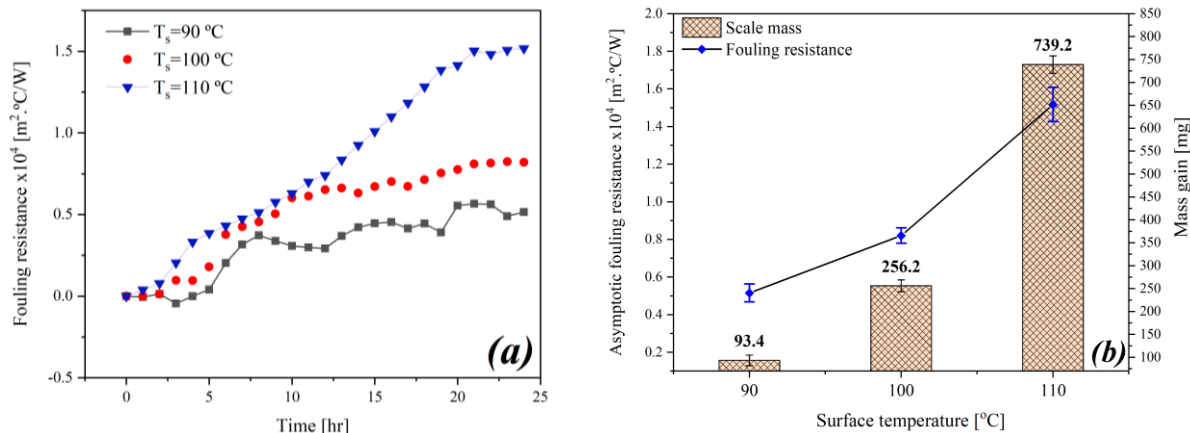
Figure 8.6. (a) Thermal resistance of fouling layer on the aluminium surface, (b) surface mass gain and asymptotic fouling resistance, for different surface temperatures.

In terms of scale morphology, no significant differences in the size and shape of the deposited particles have been observed with an increase in surface temperature (Fig. 8.7). The SEM image in figure 8.7a illustrates that the fouling layer at 90 ℃ is the most porous. The needle-like aragonite is the predominant polymorphic phase of $CaCO_3$ at all tested temperatures. However, aragonite was reported as a metastable form of $CaCO_3$ under similar temperatures [144]. The SEM images for the surface at the early stages of crystallisation show the different structures of the fouling layer (Fig. 8.8). The scale layer that formed in 2 hours of the experiment contains 14 wt.% of magnesium incorporated with $CaCO_3$ needles as shown by EDX analysis. These needles later grew to a few micrometres after 22 hours of the experiment.
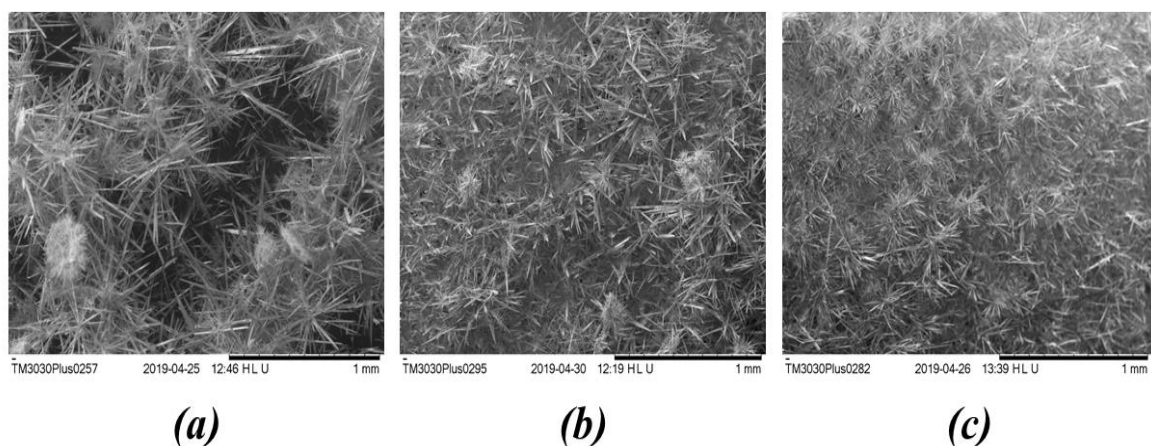
Figure 8.7. SEM images for deposits on the aluminium surface at different surface temperatures; (a) 90 ℃, (b) 100 ℃ and (c) 110 ℃.

158

Figure 8.8. Deposits on the aluminium surface at 100 °C; (a) SEM image and (b) EDX analysis.

8.4. Effect of pressure

Figure 8.9 displays the influence of pressure on the fouling resistance and the deposition rate. The pressure in the cell significantly minimises the fouling resistance as well as the amount of the deposits. Relieving the pressure in the cell and discharging steam results in inconstancy in the fouling resistance curve. This might be attributed to the leaving vapour bubbles from the surface which enhance the heat transfer coefficient [329]. An increase in pressure reduces the release of carbon dioxide from the solution. This shifts the equilibrium to the left-hand side, hence reducing the formation of $CaCO_3$ and $MgCO_3$ scale (Eq^n 8.1 and 8.2). Therefore, the effect of pressure on the scaling tendency of $CaCO_3$ is relatively significant [218].

$$Ca^{2+}_{(aq)} + 2HCO^-_{3\,(aq)} \leftrightarrow CaCO_{3\,(s)} + CO_{2\,(g)} + H_2O_{(l)} \qquad \textbf{(8.1)}$$

$$Mg^{2+}_{(aq)} + 2HCO^-_{3\,(aq)} \leftrightarrow MgCO_{3\,(s)} + CO_{2\,(g)} + H_2O_{(l)} \qquad \textbf{(8.2)}$$
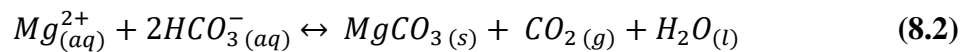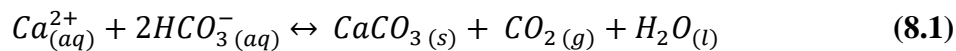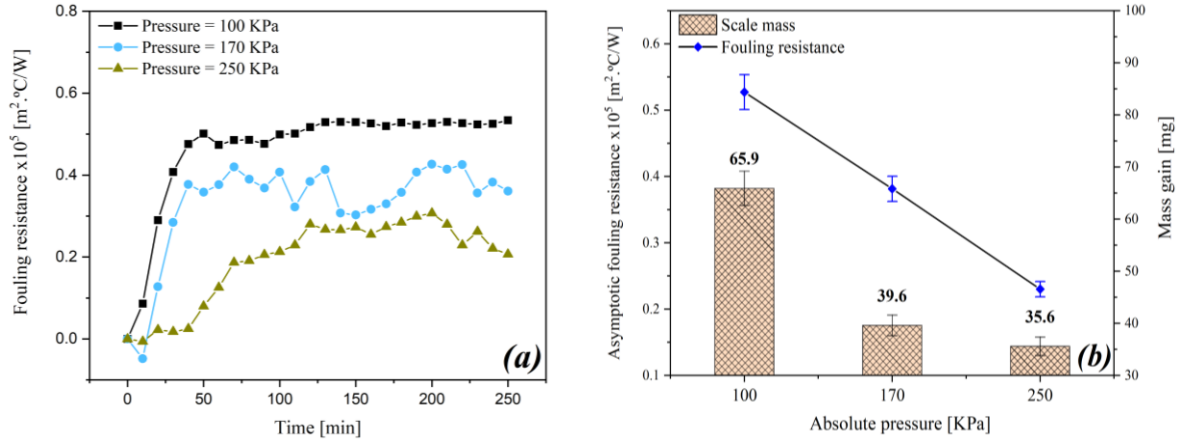
Figure 8.9. (a) Thermal resistance of fouling layer on the aluminium surface, (b) surface mass gain and asymptotic fouling resistance, for different absolute pressures.

Figure 8.10 shows SEM images of mineral deposits on the aluminium surface under different pressures. The salt particles aggregated in discrete colonies on the heat transfer surface. The salt crystals formed at a pressure of 100 kPa is a mixture of bouquet-like and dumbbell-like aragonite. As the pressure is increased to 170 kPa, more bouquet-like aragonite is formed with flake-like $MgCO_3$. Spherical crystals of $MgCO_3$ formed in aggregates with bouquet-like aragonite when the system is pressurised to 250 kPa. The presence of $MgCO_3$ in the fouling layer is suggested by EDX elemental measurement (Fig. 8.11). It is found that the crystals covered by spectrum A are $MgCO_3$ based on empirical formula estimation from the quantities of each element, while spectrum B covers needles of $CaCO_3$. As pressure is increased, the deposition of $MgCO_3$ is observed.
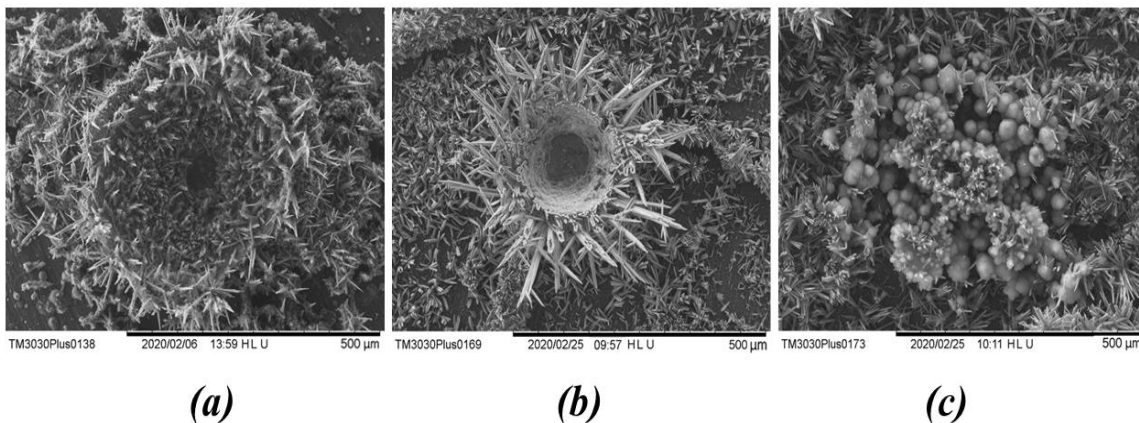
Figure 8.10. SEM images for deposits on the aluminium surface at different pressures; (a) 100 kPa, (b) 170 kPa and (c) 250 kPa.

160
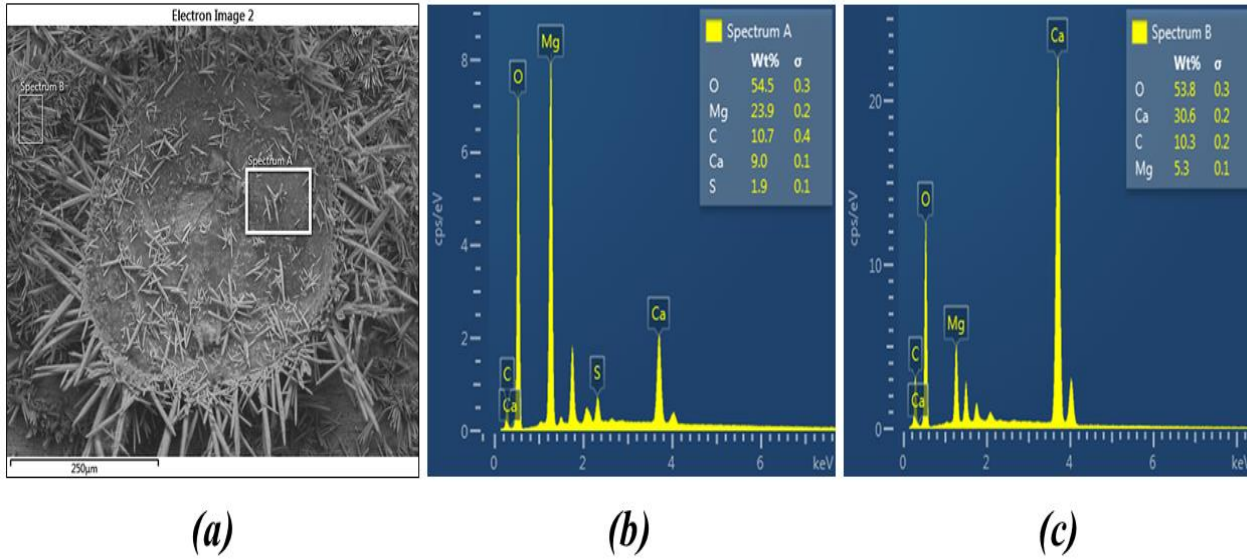
Figure 8.11. Deposits on the aluminium surface at 170 kPa; (a) SEM image, (b) Spectrum A and (c) Spectrum B, from EDX analysis.

8.5. Effect of surface roughness

The influence of surface roughness on the heat transfer resistance of the fouling layer is presented in figure 8.12. The fouling resistance increases with an increase in average surface roughness (R_a). Surface roughness exerts a noticeable impact on the rate of deposition. The profile element of the surface comprises asperities and valleys. The top sharp ends of asperities act as heterogonous nucleation sites which promote the scale particles formation [33] while the deep valleys protect the mineral deposition against the flow shear by acting as a shelter [62]. The unevenness of the rough surface provides a larger contact area developing the overall adhesion and tenacity of scale crystals [162]. For constant heat flux operation, an increase in roughness increases the surface heat transfer coefficient resulting in higher scale-solution interface temperature. In this case, the ageing rate decreases with a slower reduction in fouling resistance [330].

The amount of deposits increases with surface roughness increase (Fig. 8.12b). However, the amount of scale formed dropped from 403.3±15.8 mg to 396.4±17.6 mg when the roughness parameter increased from 1.18 to 1.48 μm. The reduction in the mass may owe to the change in the scale layer structure as the porosity of the fouling layer on a rough surface is relatively high [162]. The fouling layer comprises different sub-layers [66], therefore, SEM top view is not

161

adequately able to examine the salt layer porosity (Fig. 8.13). The SEM images in figure 8.13 show minor differences in the scale morphology on different surface roughness. The surface texture of domestic appliances is a controllable parameter. Smoothing the pipe and pool surfaces reduces the scaling tendency of the potable water.
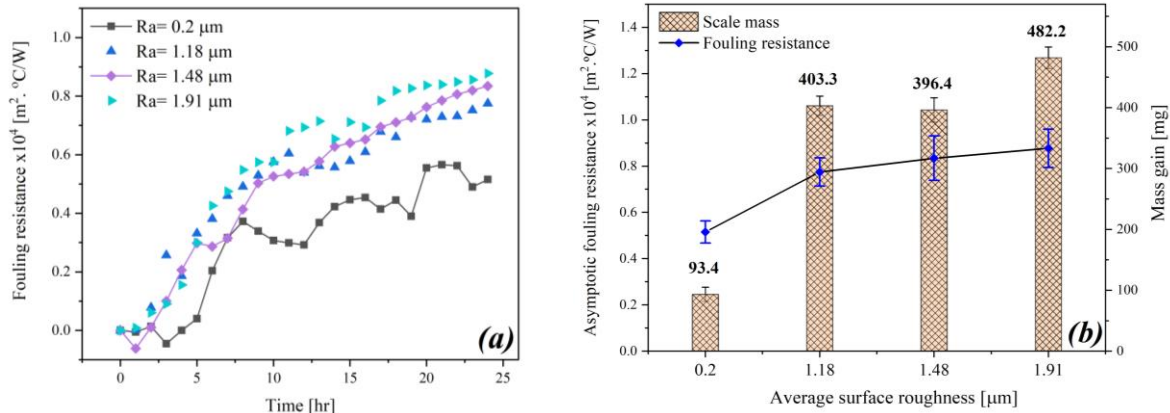
Figure 8.12. (a) Fouling resistance of scale on the aluminium surface, (b) surface mass gain and asymptotic fouling resistance, for different surface roughness.
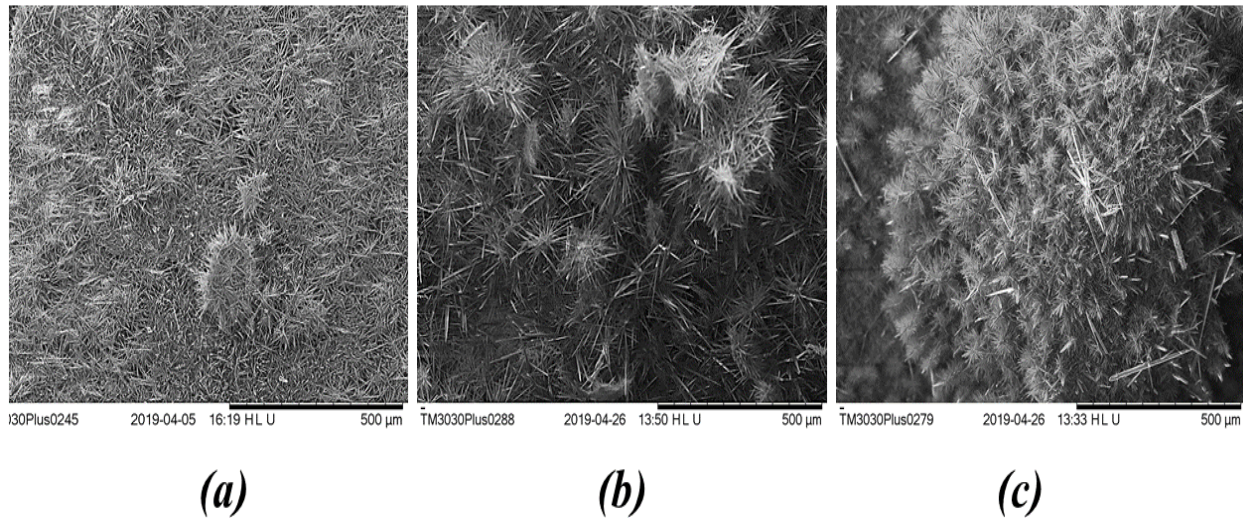
Figure 8.13. SEM images for deposits on the aluminium surface for different surface roughness; (a) R_a =1.18 μm, (b) R_a =1.48 μm and (c) R_a =1.91 μm.

162

8.6. Effect of sodium and chloride ions

The fouling resistance to heat transfer and the mass of scale formed from solutions with different contents of sodium and chloride are presented in figure 8.14a and 8.14b. It can be seen that the fouling resistance increases with the content of chloride and sodium ions. The kinetics of scale formation is enhanced as the concentrations of chloride and sodium ions increase. However, it has been reported that the sodium ion has no inhibitory effect on crystal growth or morphology [244]. The dissociation constant of bicarbonate HCO_3^- to carbonate CO_3^{2-} changes as a function of solution temperature and salinity [311, 312]. An increase in chloride ion (Cl^-) content enhances the solution salinity and the dissociation constant of bicarbonate ion, hence a higher amount of carbonate is produced and more $CaCO_3$ and $MgCO_3$ deposit on the surface.

In terms of deposit morphology, some changes have been observed as the concentration of chloride and sodium ions increase (Fig. 8.15). The needle-like aragonite is the dominant polymorphic phase in all tested solutions. However, it can be observed that the needles formed from solution A are larger when compared with those formed from solutions B and C. The composition of each solution is presented in table 5.9 in Chapter Five. The SEM image in figure 8.15b shows small holes distributed on the scale layer for the steam bubbles to leave the heated surface.
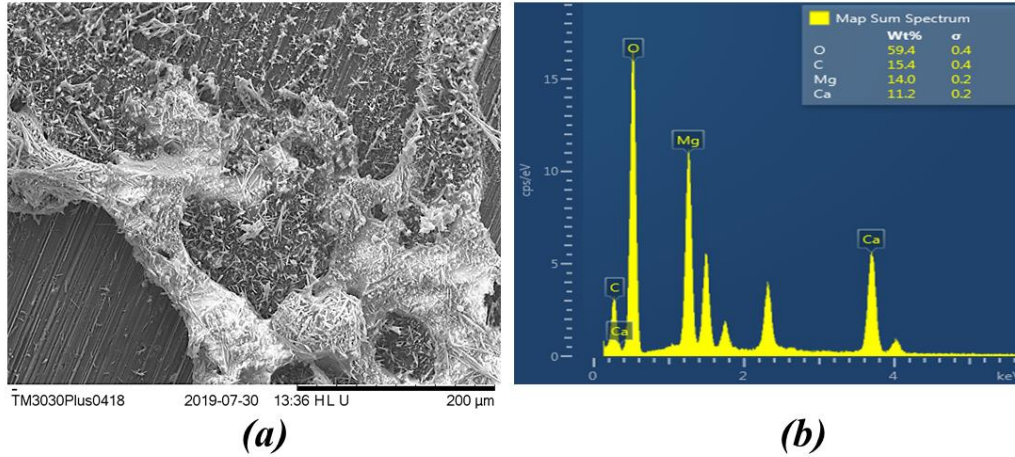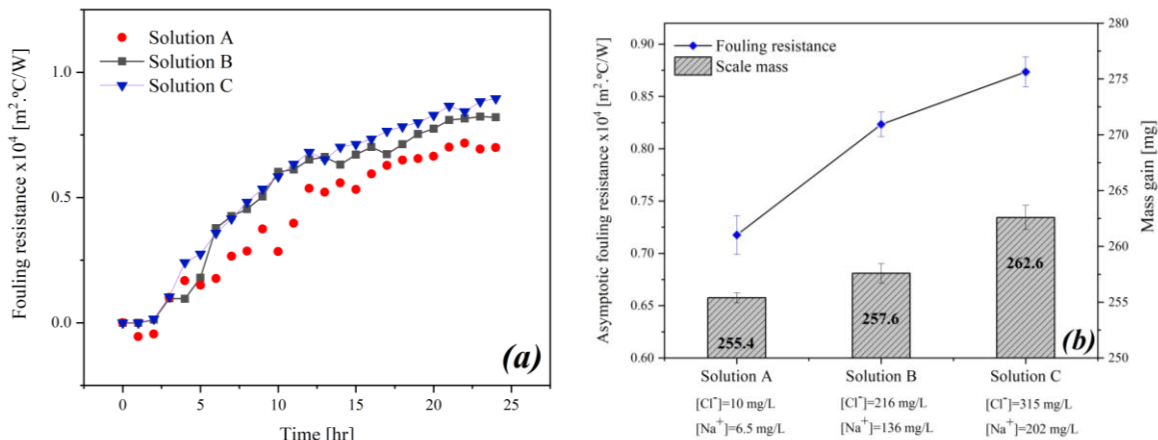

Figure 8.14. (a) Fouling resistance of scale on the aluminium surface, (b) surface mass gain and asymptotic fouling resistance, for different contents of chloride and sodium.
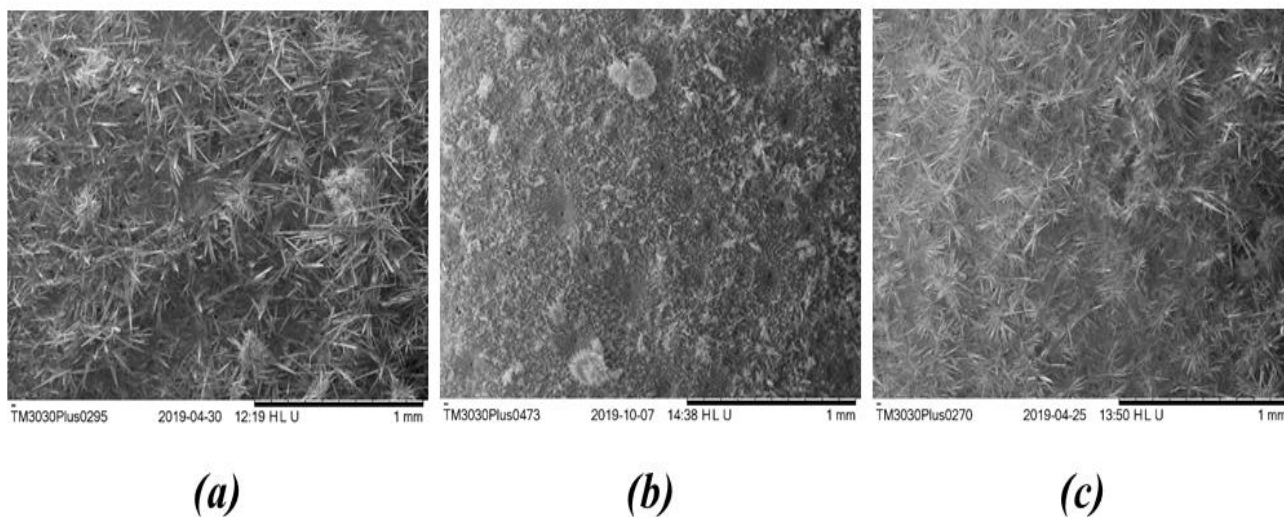
Figure 8.15. SEM image for deposits on the aluminium surface from different solutions; (a) [Cl⁻]=10 mg/L and [Na⁺]=6.5 mg/L, (b) [Cl⁻]=216 mg/L and [Na⁺]=136 mg/L, and (c) [Cl⁻]=315 mg/L and [Na⁺]=202 mg/L.

8.7. Effect of the magnesium ion

The effect of the concentration of magnesium ion on the fouling resistance is shown in figure 8.16a and b. The solution with no magnesium ion produces a fouling layer with the highest insulation effect. Increasing the content of the magnesium ions from 26 to 104 mg/L reduces the resistance to heat transfer by 3.5 times. The Mg^{2+} poses an inhibition influence on the formation of $CaCO_3$ which has been confirmed by Compton and Brown [297] and Tai and Chien [244]. It is found that the Mg^{2+} acted as an inhibitor by retarding the growth rate and/or incorporating it into a crystal.

The fouling resistance increases again when the concentration of magnesium ion is increased to 150 mg/L. The increase of the saturation ratio of $MgCO_3$ to about 60 provides enough driving force for the $MgCO_3$ scale to form. The formation of $MgCO_3$ besides $CaCO_3$ enhances the fouling resistance to heat transfer. However, the concentration of chloride ion in solution G, 577 mg/L is the highest for all the solutions which, could also account for the increase in the fouling resistance by producing more carbonate from bicarbonate. The SEM images in figure 8.17 show the changes that occurred when the concentration of Mg^{2+} increased to 150 mg/L. At a concentration of 52 mg/L, the scale particles are relatively small, and the overall layer is fluffy.

At 150 mg/L Mg^{2+}, a crust appears to cover the original aragonite crystal. This crust makes the needles in flower-like structures look thicker with a tapered end. The elemental analysis carried

164

out by EDX shows that the content of magnesium ions in these needles is high as 32.7 wt. % with a small amount of calcium (Fig. 8.18). The presence of $MgCO_3$ as magnesite and MgO as periclase is confirmed by the XRD analysis for the 150 mg/L Mg^{2+} samples. Aragonite is the only form of $CaCO_3$ that formed. Therefore, the formation of magnesium scales on the aragonite needles may increase the insulation capacity to the fouling layer.
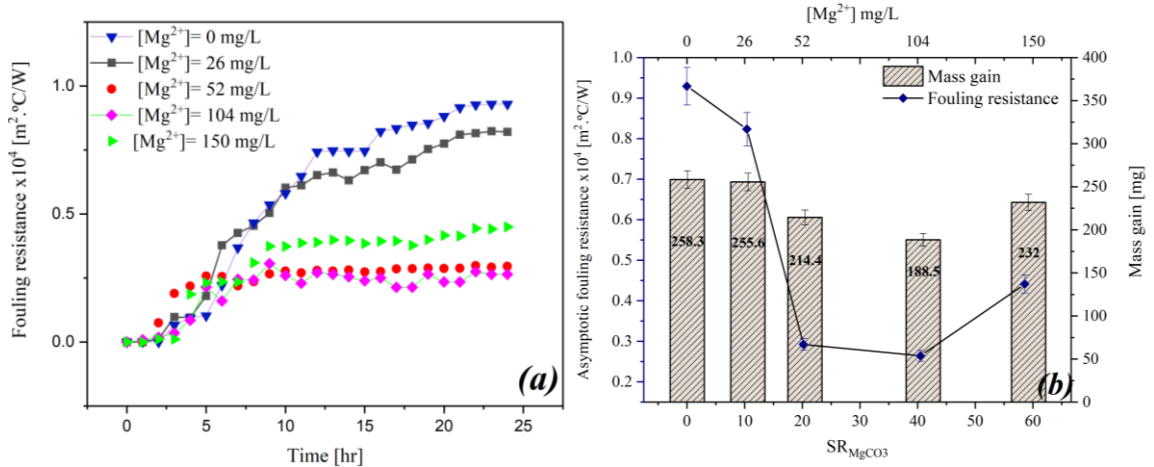
Figure 8.16. (a) Fouling resistance of scale on the aluminium surface, (b) surface mass gain and asymptotic fouling resistance, for different saturation ratios of MgCO₃.
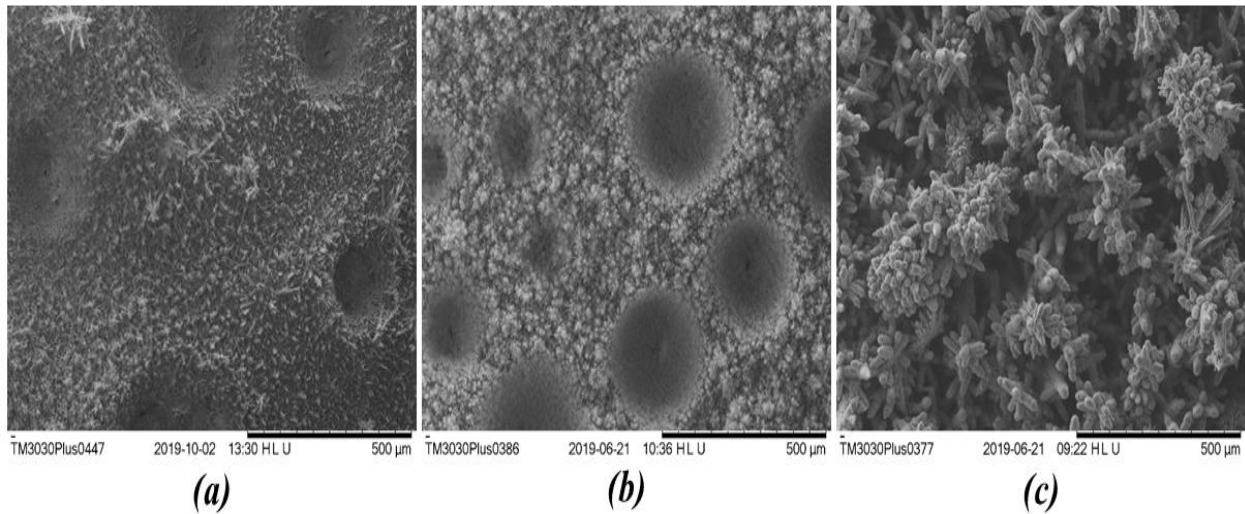
Figure 8.17. SEM image for deposits on the aluminium surface for different contents of magnesium; (a) no Mg²⁺, (b) [Mg²⁺] = 52 mg/L and (c) [Mg²⁺] = 150 mg/L.
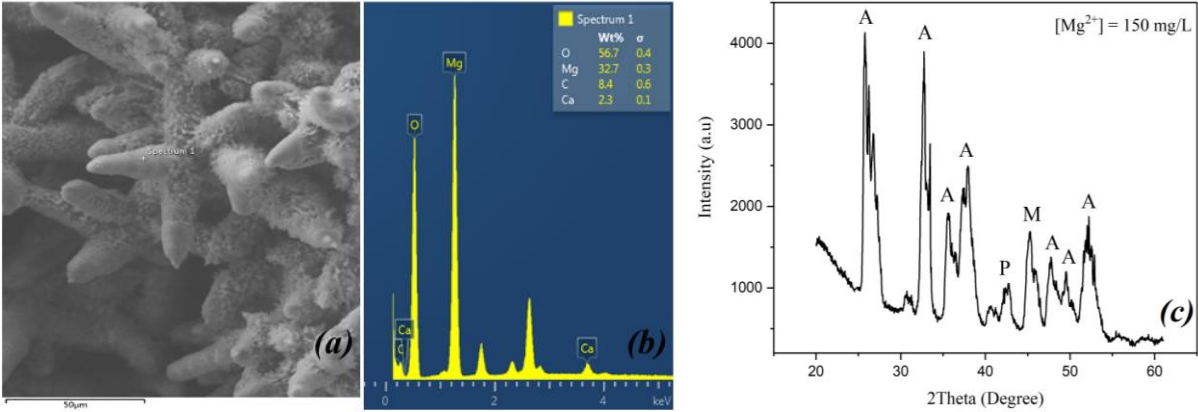
**Figure 8.18. EDX elemental analysis of the deposits on aluminium; (a) SEM image, (b) spectrum 1 and (c) XRD analysis of fouling layer at [Mg^{2+}] =150 mg/L, A for $CaCO_3$ as aragonite, M for magnesium carbonate as magnesite and P for MgO as periclase.**

The fouling reaction from different divalent cations with carbonate (CO_3^{2-}) systems has been examined as shown in figure 8.19. The scale layer formed from the Ca^{2+}-CO_3^{2-} system (solution H) has higher thermal resistance than that formed from Mg^{2+}-CO_3^{2-} equilibrium systems (solutions I and J). For the same concentration in solutions H and J, Ca^{2+} and Mg^{2+} react separately with 360 mg/L of HCO_3^-. The $CaCO_3$ deposits have a higher fouling resistance and a higher mass of 266.3 mg, while 72 mg for the $MgCO_3$ scale. Under similar conditions, the reaction rate of $CaCO_3$ is greater than that of $MgCO_3$. However, the solubilities of both salts are close under the test temperature.
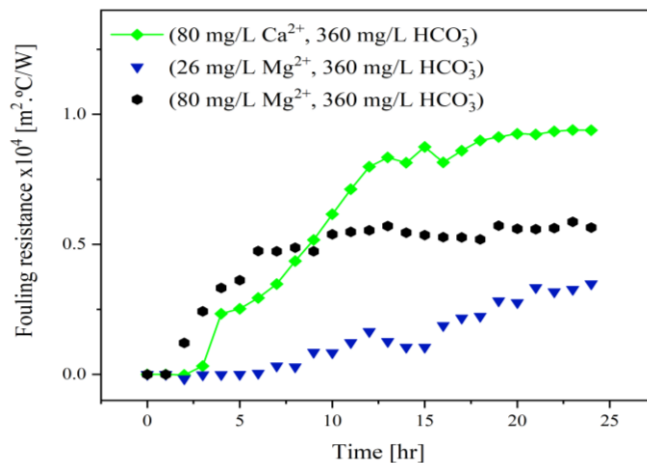
Figure 8.19. Fouling resistance of deposits on the aluminium surface for Mg^{2+}-CO_3^{2-} system (Solutions I and J) and Ca^{2+}-CO_3^{2-} systems (Solution H).

The SEM images in figure 8.20 show the scale structure from each solution. The $CaCO_3$ scale is a compact layer that consists mainly of aragonite needles (Fig.8.20a). However, it has been reported that aragonite is a thermodynamically unstable phase of $CaCO_3$ at a temperature of 100 ºC [149]. As the scale is multi-layered, the first layer next to the surface might be calcite and the following layers are aragonite as the interface temperature decreases with each layer forms. Using solution I as scaling fluid produces a loose layer of small spherical crystals. Good agreement has been obtained between the present structure and the one reported by Raza, et al. [331]. The increase of Mg^{2+} concentration to 80 mg/L generates a uniform crust of interlocking threads.
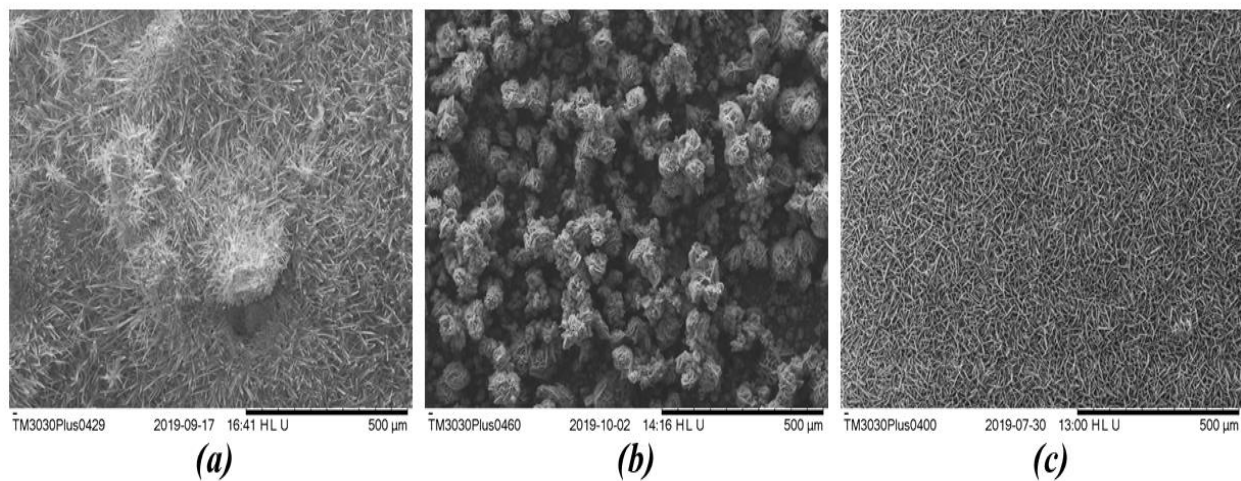
Figure 8.20. SEM image for deposits on the aluminium surface for Mg^{2+}- CO_3^{2-} and Ca^{2+}-CO_3^{2-} systems; (a) 80 mg/L Ca^{2+} - 360 mg/L HCO_3^-, (b) 26 mg/L Mg^{2+}- 360 mg/L HCO_3^- and (c) 80 mg/L Mg^{2+}- 360 mg/L HCO_3^-.

8.8. Effect of sulphate ion

Change in the concentration of sulphate ions in drinking water has no significant influence on the insulation of inorganic deposits. The increase of SO_4^{2-} content in water slightly reduces the fouling resistance (Fig. 8.21). It can be seen that there is no progress as the content of SO_4^{2-} increases from 42 to 126 mg/L. In accordance with the literature, the inhibitory efficiency of sulphate ions is relatively small [204]. As sulphate is one of the common fouling species, it is expected to support the fouling layer with $CaSO_4$ particles. However, neither the test temperature nor sulphate concentration is enough to supersaturate the solution. The solubility of $CaSO_4$ also is high in comparison with $CaCO_3$ and $MgCO_3$.
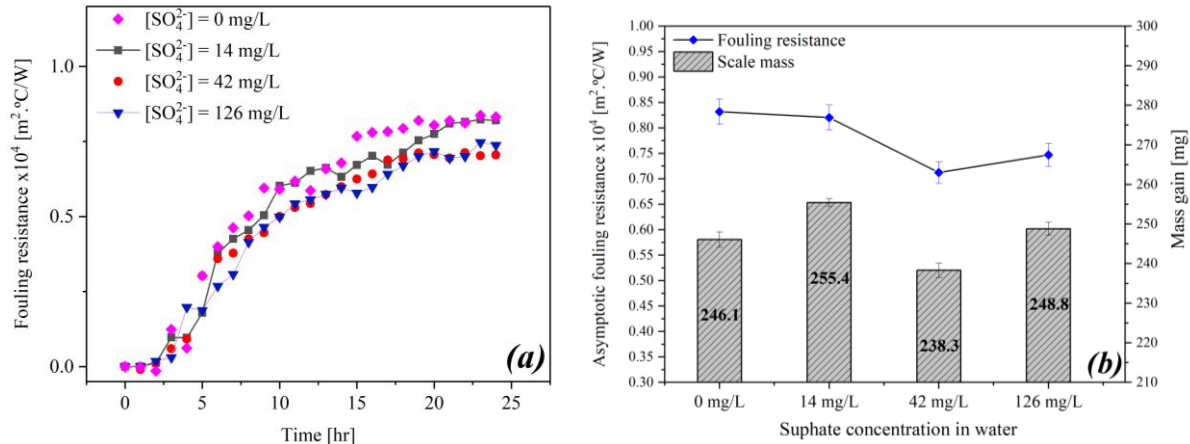
Figure 8.21. (a) Fouling resistance of scale on the aluminium surface, (b) surface mass gain and asymptotic fouling resistance, for different contents of sulphate in water.

In terms of the effect of sulphate ions on the morphology, SEM images are displayed in figure 8.22. The first image (Fig. 8.22a) shows the scale layer without the presence of sulphate ions in water. Fluffy soft deposits were formed when no SO_4^{2-} were added to the test solution. Then, it can be observed from the second image (Fig. 8.22b), when the SO_4^{2-} content is 42 mg/L, that fouling layer consists of obvious plateaus of flower-like aragonite. Increasing the SO_4^{2-} content to 126 mg/L produces a plane crust of needle-like aragonite as shown in figure 8.22b. The presence of sulphate ions in water contributes to forming one crystal type of aragonite with even growth in all directions.
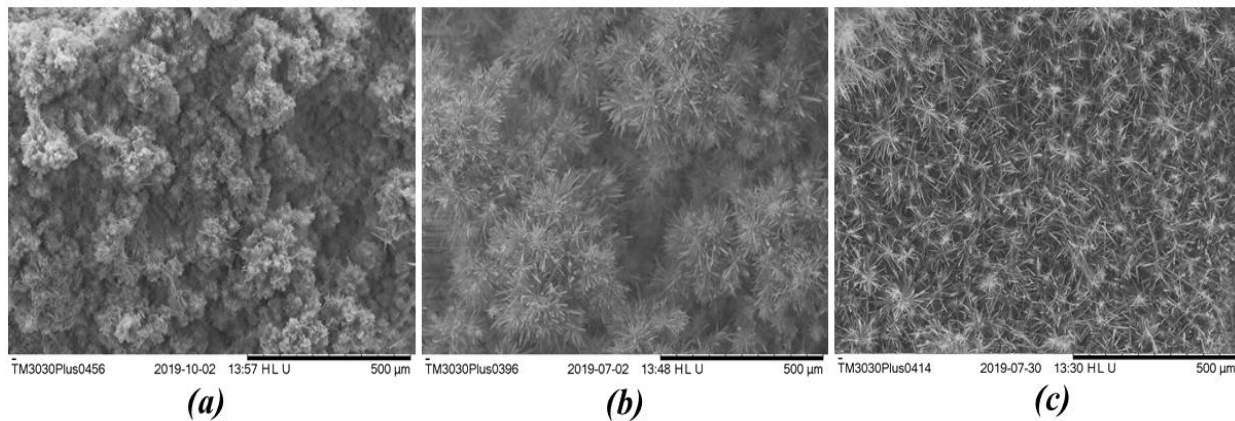
Figure 8.22. SEM image for deposits on aluminium surface for different concentrations of sulphate ion; (a) no sulphate, (b) $[SO_4^{2-}]$ = 42 mg/L and (c) $[SO_4^{2-}]$ = 126 mg/L.

168

8.9. Effect of Total Organic Carbon (TOC)

The change of fouling resistance as a function of time in the presence of organic carbon (OC) in the solution is shown in figure 8.23a. The fouling resistance has been reduced by about 4 times when the TOC content increased to 2 mg/L. However, a further increase of TOC under the same experimental conditions does not pose a difference in the scale insulation effect. The molecule of humic acid, the humic substance used to raise the TOC content, is relatively large (high molecular weight). It has been proposed by Hoch, et al. [255] that the substances with high molecular weight generate a great reduction in growth rate. These molecules form a colloid/complex with Ca^{2+} and Mg^{2+} which lowers the saturation state and inhibits the growth of the crystal. The cations complexation is likely to occur by carboxylic acid and phenolic functional groups [256].

The inhibition efficiencies of 31.3% and 47.9% are obtained for 2 and 4.3 mg/L of TOC, respectively (Eq^n 8.3). Evidently, at 2 mg/L TOC, the fouling resistance reduced much more than that at 4.3 mg/L. This might be explained as the TOC amount in water exceeds the amount required to inhibit the total surface deposition. Further increase in the amount of TOC accordingly does not contribute to a substantial reduction in scale formation. The amount of TOC needed to inhibit the fouling is subject to the operating conditions and water quality.

$$\% \text{ Inhibition efficiency} = \frac{M_a - M_p}{M_a} * 100 \qquad (8.3)$$

Where, $M_a \ and \ M_p$ are the amount of scale in the absence and presence of an inhibitor, respectively.
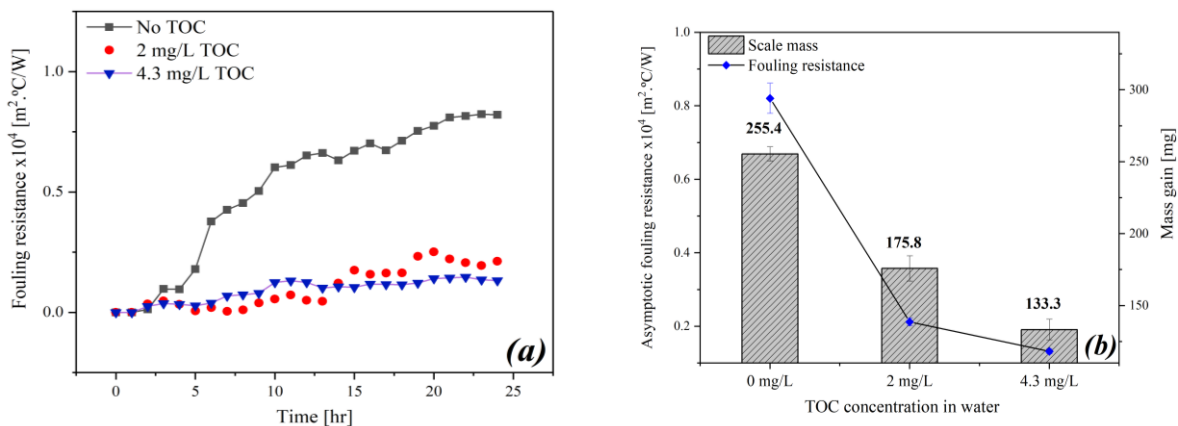
Figure 8.23. (a) Fouling resistance of scale on the aluminium surface and (b) surface mass gain and asymptotic fouling resistance, for different contents of TOC in water.

169

The inhibition role of the OC on the scale formation can be evaluated based on the morphology of the deposits. Figure 8.24 shows the effect of TOC content on the scale structure and morphology. The addition of 2 mg/L of TOC to the test solution produces a bumpy fouling layer with the non-uniform shape of crystals. By increasing the TOC content to 4.3 mg/L, the same structure is formed except for the appearance of some flat spots. Besides the formation of organics-Ca^{2+} complex, the aragonite crystals might be poisoned by OC in water yielding the presence scale layer. The TOC in the present experiments was high enough to react with all formed crystals. At the final stages of the fouling process, the removal and deposition rate become equal due to the weakness of the upper fouling sub-layer. Therefore, asymptotic fouling behaviour is observed in all fouling resistance graphs [63].

(a)   *(b)*   *(c)*
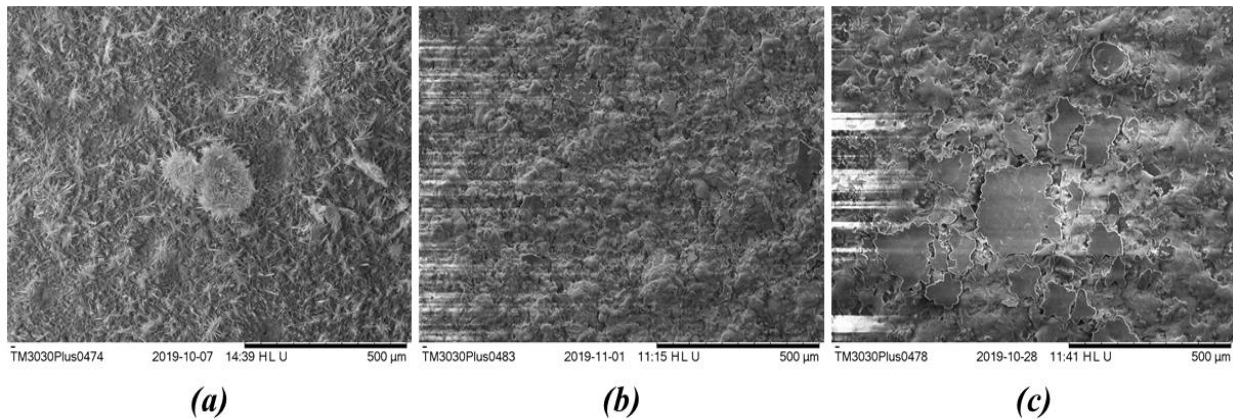
Figure 8.24. SEM image for deposits on aluminium surface for different concentrations of TOC; (a) no TOC, (b) [TOC] = 2 mg/L and (c) [TOC] = 4.3 mg/L.

8.10. Effect of zinc ion

The effect of the free zinc ion has been investigated on the composite crystallisation fouling from potable water. The findings show the fouling resistance drops as the concentration of Zn^{2+}, as shown in figure 8.25a. It also illustrates that Zn^{2+} concentration is also capable of affecting the induction time. The asymptotic fouling resistance was reduced by half when the Zn^{2+} concentration increased by 15 mg/L (Fig. 8.25b). The exponential decay of asymptotic fouling resistance refers to the decreasing inhibition efficiency of zinc. It has been reported that the nucleation of $CaCO_3$ is inhibited by Zn^{2+} with a concentration starting from 0.02 mg/L [332]. For the same range, the mass of deposits decreased by 25.3 mg.

170

Figure 8.26a shows an exponential growth relationship between the asymptotic fouling resistance and the scale mass. However, this relationship may indicate variation in the physical properties of the fouling crust such as density, thermal conductivity and porosity. As mentioned earlier, Zn^{2+} exhibits a pronounced impact on the induction period. The scaling induction time increased from 78 to 426 minutes when Zn^{2+} concentration raised from 0 to 15 mg/L, as displayed in figure 8.26b. The presence of Zn^{2+} in a solution suppresses the nucleation and growth of scale particles through the complexation with the foulants [305-307, 333]. Another inhibition mechanism, the high frequency of adsorption of Zn^{2+} at the nuclei sites may mitigate the nucleation rate [334].
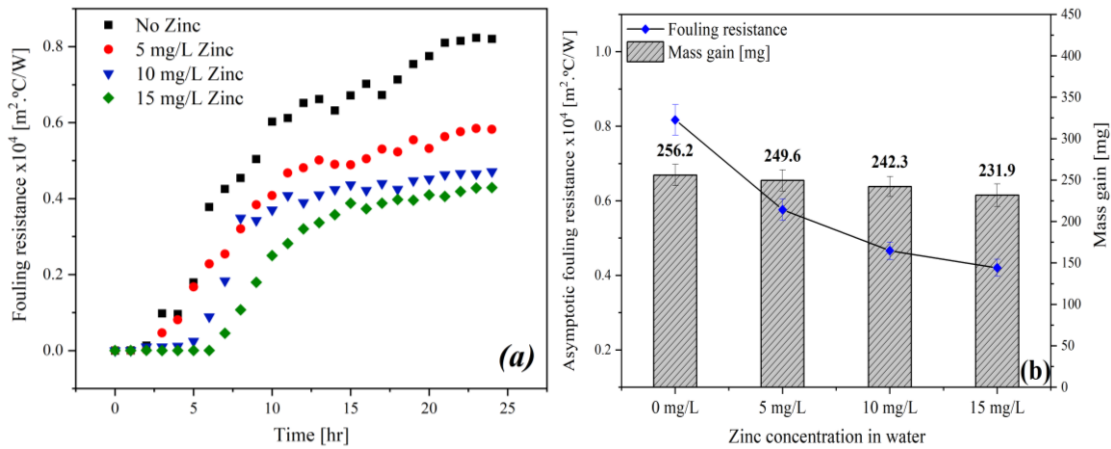
Figure 8.25. (a) Fouling resistance of scale on the aluminium surface and (b) surface mass gain and asymptotic fouling resistance, for different contents of zinc in water.
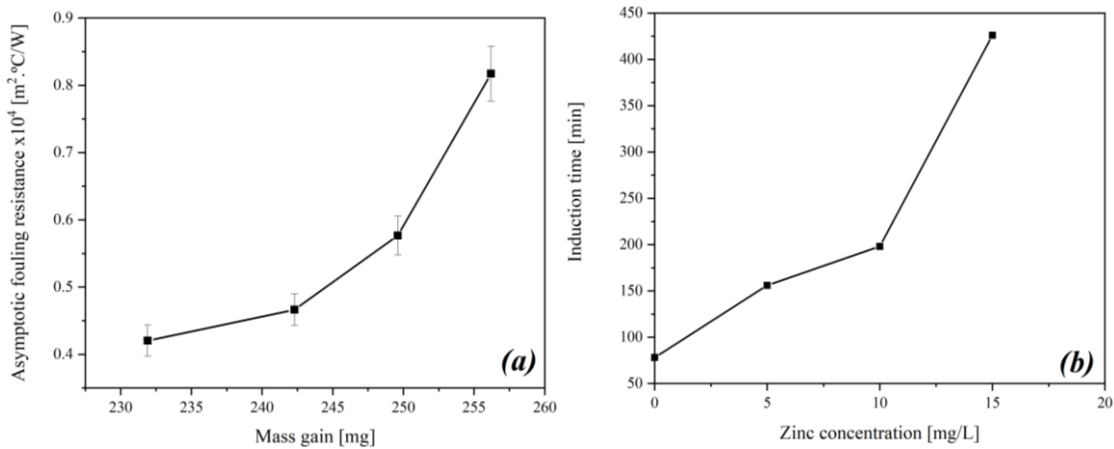
Figure 8.26. (a) Fouling resistance as a function of scale mass and (b) crystallisation fouling induction time for different concentrations of zinc in water.

On the other hand, the co-precipitation of zinc carbonate ($ZnCO_3$) and hydrozincite ($Zn_5(CO_3)_2(OH)_6$) crystals may occur at Zn^{2+} concentration greater than 6 mg/L [241, 242, 334]. The morphology investigations show that the Zn^{2+} has changed the structure of deposits, as displayed in the SEM images (Fig. 8.27). In the absence of zinc, the deposits from potable water comprise loose needle-like aragonite particles. However, smooth flat islands are found distributed on the flower-like aragonite when 10 mg/L is added to the test solution. At a concentration of 15 mg/L, the formed crystal structure completely changed. This morphology might be resulted from aragonite crystal poisoning with Zn^{2+} and/or co-precipitation of zinc deposits.

(a)   *(b)*   *(c)*
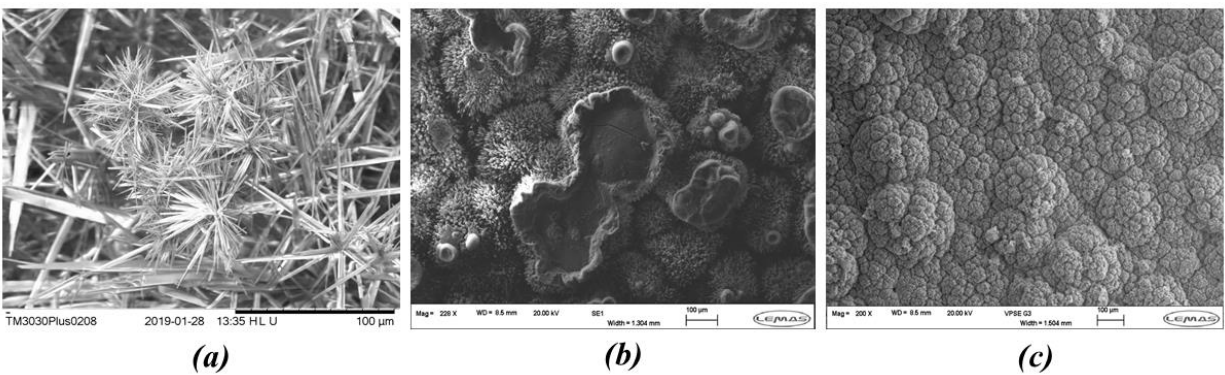
Figure 8.27. SEM image for deposits on aluminium surface for different concentrations of TOC; (a) no Zinc, (b) $[Zn^{2+}]$ = 10 mg/L and (c) $[Zn^{2+}]$ = 15 mg/L.

Figure 8.28 shows the elemental analysis (EDX) of the fouling layer for the three tested concentrations. The zinc content of deposits increases with Zn^{2+} concentration in a solution proving the interaction between Zn^{2+} and scale particles. It has been emphasised by Glasner and Weiss [242] that the carbonate-complex $[Zn(CO_3)_2]^{2-}$ acts as a nucleation site for $CaCO_3$ crystals. The affinity of Zn^{2+} to the carbonate ions is found greater than Ca^{2+}. Therefore, the combination between Zn^{2+} and CO_3^- is more likely at high concentrations of Zn^{2+} forming $[Zn(CO_3)_2]^{2-}$, $Zn_5(CO_3)_2(OH)_6$ or $ZnCO_3$ on the heat transfer surface.
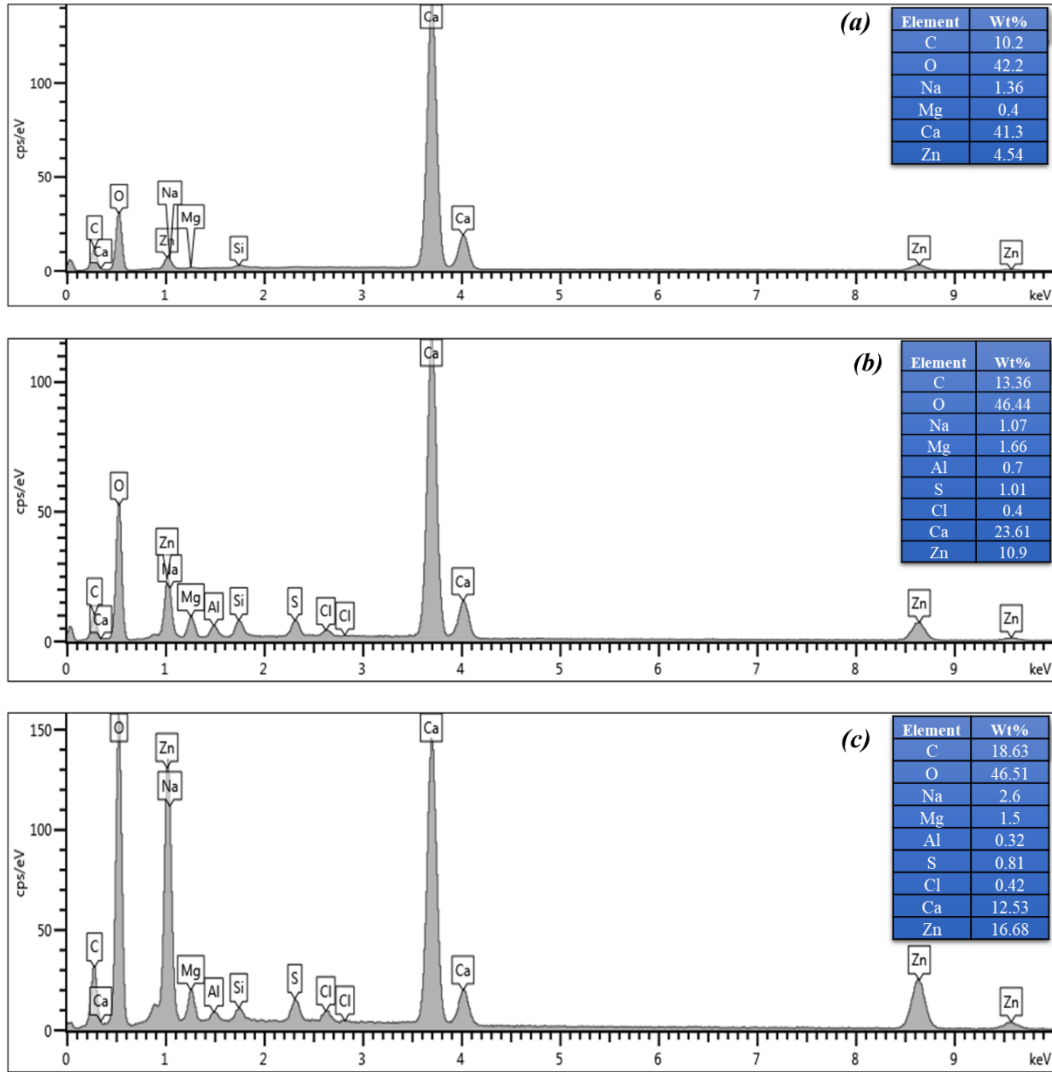
Figure 8.28. EDX elemental analysis of the deposits on aluminium; (a) [Zn^{2+}] = 5 mg/L, (b) [Zn^{2+}] = 10 mg/L and (c) [Zn^{2+}] = 15 mg/L.

8.11. Summary

The present chapter summarises the investigations of crystallisation fouling during the boiling convective heat transfer. The effect of surface temperature, surface roughness and the ionic species on the fouling kinetic and structure was evaluated using the flow-evaporation scaling cell (FESC). The water species examined include sodium, chloride, magnesium, sulphate, total organic carbon (TOC) and zinc. The effect of the system pressure has also been determined using the pressurised flow-evaporation scaling cell (PFESC). The structure and properties of the aluminium oxide film,

that forms on the aluminium substrate, were presented. The fouling resistance and scale mass approaches were used to assess the fouling kinetics. The SEM observations, XRD and EDX peaks were employed to determine the impact on the morphology.

During the water heating process using an aluminium substrate, a film of Al_2O_3 forms on the surface. The morphology analysis showed that the Al_2O_3 layer has a porous structure and good surface wettability. The XRD analysis of the oxide layer shows that β-Al_2O_3 (beta alumina) is the dominant form of aluminium oxide on the substrate.

The temperature increases the fouling resistance and the amount of the deposits. Also, the increase in temperature produces a less porous fouling layer. Needle-like aragonite is the prevailing deposition formed in all tested temperatures. In the early stages of surface scaling, magnesium-containing deposits were detected on the surface. The pressure in the cell significantly minimises the fouling resistance as well as the amount of the deposits. Pressure increase leads to the formation of separated colonies of $CaCO_3$ and $MgCO_3$ on the substrate. The pressure change affects the $CaCO_3$ equilibria and the size and departure frequency of the vapour bubbles. Surface roughness plays an important role in promoting the fouling rate. However, insignificant morphological changes were observed as a result of the roughness increase. The role of surface roughness in inorganic mineral formation was described according to different mechanisms.

The increase of chloride and sodium in potable water enhances the fouling rate and the deposited amount of scale on the heated surfaces. However, no remarkable change in the scale morphology has been marked as the content of chloride and sodium increase.

The presence of different concentrations of magnesium in water showed that there is no trend in the inhibition of scale formation. The increase of magnesium ion concentration from 26 to 104 mg/L reduces the resistance to heat transfer by about 3.5 times. However, increasing the $[Mg^{2+}]$ to 150 mg/L enhances the fouling resistance. The SEM images showed that the needle-like aragonite is the dominant form of $CaCO_3$, the fouling layer is nevertheless fluffier at $[Mg^{2+}]$ of 52 mg/L than that with no magnesium. At 150 mg/L Mg^{2+} what looks like a crust covers the original aragonite needle. The EDX findings showed that the content of magnesium in these coated needles is high as 32.7 wt. % with a low abundance of calcium.

SO_4^{2-} ions have a minor inhibiting effect on the surface deposition. The fouling resistance has insignificantly reduced when the content of sulphate ions increased from 42 to 126 mg/L. Adding sulphate ions to water produces a less fluffy and structured layer of aragonite. Another ionic constituent of potable water is Zn^{2+} and its role in the scaling process has been examined. The findings exhibit that Zn^{2+} reduces the fouling resistance and prolongs the induction time as a result of its inhibition capability. At concentrations greater than 6 mg/L, co-precipitation of zinc carbonate ($ZnCO_3$) and hydrozincite ($Zn_5(CO_3)_2(OH)_6$) crystal may occur.

Total organic carbon (TOC) at a concentration of 2 mg/L has reduced the fouling resistance to heat transfer by about 4 times. However, a further increase of TOC content does not pose a difference in the asymptotic fouling resistance which is owing to exceeding the TOC content the maximum concentration required to inhibit the entire surface deposition. The findings of morphology analysis illustrated that the presence of TOC poisons the scale crystals and deposits were transformed into a bumpy structure. These findings could be linked to the influence of the key operating conditions for a full understanding of the fouling process in household devices.

Chapter 9: Conclusions and Future Work

9.1. Conclusions summary

A summary of the outcomes arising from this work has been presented in this chapter. The mechanism, kinetics, and morphology of the inorganic fouling from potable water have been investigated under conditions similar to those in domestic appliances and systems. Besides the presentation and interpretation of the results, relevant theoretical background and literature review were provided. As a result of the variety of heat transfer mechanisms in the household appliances, three newly developed rig systems, as well as a modified experimental setup, were used for the experiments. The solution used in all experiments is commercially available bottled water with a pH of 7.2 and hardness of 3.07 mmol/L of $CaCO_3$, which is almost the same as tap water hardness in some regions in the south UK.

9.1.1. Crystallization fouling in batch systems

In this work, bulk precipitation and surface deposition in closed systems were investigated. The effect of solution temperature, surface material, surface roughness, evaporation area, water composition, heating rate and cooling on the scaling kinetics and morphology were discussed. Water composition study includes the influence of magnesium, sulphate, zinc, nitrate and total organic carbon. The comparison of cooling and heating rates effect included theoretical validation to emphasize that the scaling rate during the cooling period is greater than that in the heating period.

The solution temperature promotes the bulk precipitation and the polymorphic transformation from both calcite and vaterite to aragonite. It is found that flake-like particles were formed above the crystalline particles. The amount of flake-like deposits increases with temperature, and it consists of about 4% by weight of Mg. The scale structure on aluminium and copper surfaces might be affected by the presence of Cu^{2+} and Al^{3+} which are released as corrosion products. The effects of the surface substrate and roughness were found to be secondary on the precipitated scale. As the crystal forms in the bulk solution by the homogeneous nucleation, a surface may not control the nucleation and growth process.

The increase in the evaporation rate reduces the amount of deposits that scale on the solid surface. The analysis of crystal habit demonstrates that the crystals formed at the lower evaporation rate

are larger than that at the ones with a higher evaporation rate. The calcium concentration in the solution when 100 ℃ is attained at a rapid heating rate is higher than that at slow heating; a greater amount of scale is formed when the solution is slowly heated. For the cooling stage, the faster the cooling rate the lower the rate of the crystallisation rate. Calcium carbonate formed in the cooling period was greater than in the heating period.

In terms of water composition, the depletion rate of calcium is found to be affected by the content of magnesium for the same amount of carbonate. The concentration of calcium steeply decreases with lower initial magnesium concentration. The solution content of calcium and sulphate increases with time and temperature as a consequence of water evaporation and low supersaturation of $CaSO_4$. The presence of Zn^{2+} reduces the crystallization rate of $CaCO_3$ and prolongs the induction time. It has been shown that the NO_3^- at permissible concentrations does not affect the precipitation kinetics nor the morphology. On contrary, the TOC in water has a significant inhibitory effect on the kinetics of scaling.

9.1.2. Crystallization fouling during convective heat transfer

The kinetics and morphology of fouling crystallization on the heated surface during the convective heat transfer were examined using the Flow-Visualization Rig. The formation of fouling particles and vapour bubbles on the heat transfer surface has been monitored using a high-performance camera. The effect of surface temperature, material, roughness, flow rate and vapour bubbles were investigated by measuring the scale mass gain as well as the camera observations.

Surface temperature increases the amount of deposits that formed on all the tested substrates. The surface temperature increases the density of nucleating vapour bubbles on the surface leading to a higher nucleation rate due to an increase in the local supersaturation in the vicinity of the bubbles. Two distinct scale regions are observed on the surface under different temperatures, the first is the flat Mg-rich layer and the second is a rough scale layer of calcium carbonate. Concerning the substrate effect, copper and stainless steel gained the largest and smallest amount of scale deposits, respectively, while the amount of scale formed on aluminium is closer to the amount on copper than stainless steel.

The amount of mineral deposits somewhat linearly increases with surface roughness. The rough surface prefers the aragonite polymorphic phase over the other forms. The flake-like and needle-

like scale particles are present as compact build-up on the rougher surface, whereas a porous layer of calcite and aragonite mixture can be observed on the smooth and medium surface.

Fluid flow has a complicated role in the fouling rate. Flow rate reduces the amount of scale formed per unit area reaching the optimum point, at which the lowest scale mass is obtained. Above the optimum point, the total deposition increases with the flow rate increase. The visual observations by the camera show the vapour bubbles influence the heterogeneous nucleation rate on the surface. This is attributed to the increasing supersaturation/ temperature in the vicinity and underneath the nucleating bubbles.

9.1.3. Crystallization fouling during boiling convective heat transfer

The crystallization fouling during the boiling convective heat transfer was investigated using the flow-evaporation scaling cell (FESC) and the pressurized flow-evaporation scaling cell (PFESC). The effect of surface temperature, surface roughness, pressure, and ionic species on the fouling kinetic and structure was evaluated. The structure and properties of the aluminium oxide film, that forms on the aluminium substrate, were presented.

During the water heating process using an aluminium substrate, a film of Al_2O_3 forms on the surface. The morphology analysis showed that the Al_2O_3 layer has a porous structure and good surface wettability. The temperature increases the fouling resistance and the amount of the deposits. Also, the increase in temperature produces a less porous fouling layer. Needle-like aragonite is the prevailing deposition formed in all tested temperatures. In the early stages of surface scaling, magnesium-containing deposits were detected on the surface.

The pressure in the cell significantly minimizes the fouling resistance as well as the amount of the deposits. Pressure increase leads to the formation of separated colonies of $CaCO_3$ and $MgCO_3$ on the substrate. The pressure change affects the $CaCO_3$ equilibria and the size and departure frequency of the vapour bubbles. Surface roughness plays an important role in promoting the fouling rate. However, insignificant morphological changes were observed as a result of the roughness increase.

The presence of different concentrations of magnesium in water showed that there is no trend in the inhibition of scale formation. The increase of magnesium ion concentration from 26 to 104 mg/L reduces the resistance to heat transfer by about 3.5 times. However, increasing the $[Mg^{2+}]$ to

150 mg/L enhances the fouling resistance. The SEM images showed that the needle-like aragonite is the dominant form of $CaCO_3$, the fouling layer is nevertheless fluffier at $[Mg^{2+}]$ of 52 mg/L than that with no magnesium. At 150 mg/L Mg^{2+} looks like a crust that covers the original aragonite needle. The EDX findings showed that the content of magnesium in these coated needles is high as 32.7 wt. % with a low abundance of calcium.

The increase of chloride and sodium in potable water enhances the fouling rate and the deposited amount of scale on the heated surfaces. SO_4^{2-} ions have a minor inhibiting effect on the surface deposition. The fouling resistance has insignificantly reduced when the content of sulphate ions increased from 42 to 126 mg/L. Adding sulphate ions to water produces a less fluffy and structured layer of aragonite.

The TOC at a concentration of 2 mg/L has reduced the fouling resistance to heat transfer by about 4 times. However, a further increase of TOC content does not pose a difference in the asymptotic fouling resistance which is owing to exceeding the TOC content the maximum concentration required to inhibit the entire surface deposition. The findings of morphology analysis illustrated that the presence of TOC poisons the scale crystals and deposits was transformed into a bumpy structure.

9.2. Future work

9.2.1. Result analysis

The analysis of the study findings can go further to extract as much as possible of data related to the operation and design of the household appliances. The results of heat transfer measurements at different conditions can be linked and modelled to produce mathematical correlations. This allows predicting the tendency and influence of surface fouling and bulk precipitation based on the operating condition, surface material and water composition. However, time and effort, including research, are needed to carry out this work. The results presented in the present thesis consist of measurements of water composition, scale quantity, fouling resistance and fouling morphology.

The fouling resistance curves are used as an example to explain the information that can be obtained from the analysis. A mathematical relationship has emerged from curve fitting for fouling

resistance plots of the zinc ion effect investigation. Two main types of fitting models were used to achieve the best fitting, as shown in figure 9.1. The correlations of fouling resistance were used to estimate the power consumption as a function of time, as displayed in figure 9.2.

$$R_f = -2.46 * 10^{-5} + \frac{1.03 * 10^{-4}}{1 + 10^{(5.46-t)0.11}}$$

No zinc

Model	DoseResp
Equation	y = A1 + (A2-A1)/(1 + 10^((LOGx0-x)*p))
Plot	-2.46357E-5 ± 1.40994E-5
A1	7.88908E-5 ± 2.35789E-6
A2	5.46255 ± 1.13632
LOGx0	0.11648 ± 0.02143
p	0.97797
R-Square (COD)	

(a)

$$R_f = 4.43 * 10^{-5} - \frac{4.4 * 10^{-5}}{1 + \left(\frac{t}{7.24}\right)^{6.29}}$$

▼ [Zn^{2+}]=10 mg/L

Model	Logistic
Equation	y = 4.43147E-5 + (5.09612E-9-4.43147E-5)/(1 + (x/7.24445)^6.28951
Plot	10 mg/L Zn
A1	5.09612E-9 ± 1.00023E-6
A2	4.43147E-5 ± 6.69656E-7
x0	7.24445 ± 0.15654
p	6.28951 ± 0.73695
R-Square (COD)	0.98823

(b)

Figure 9.1. Fouling resistance curve fitting for (a) scaling solution with no zinc and (b) [Zn^{2+}]=10 mg/L.
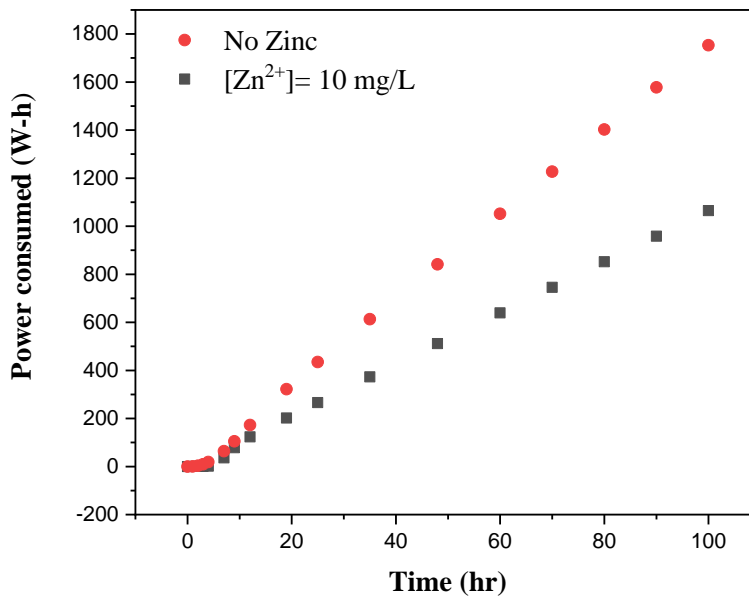
Figure 9.2. Power consumption of heat transfer equipment for two different content of zinc

180

9.2.2. Adhesion of deposits

Various water compositions and conditions produce various mineral scales and crystal polymorphs that differently adhere to a solid surface. Adhesion of scale crystal on a surface can be evaluated using the following methods [60, 180]:

- Surface energy measurements

- Atomic Force Microscope (AFM)

- Flow shear stress

The present study investigated the effect of different parameters on two mechanisms of crystallization fouling on the kinetics and morphology. However, for giving a clearer understanding of inorganic fouling in household appliances, the adhesion of different scale crystals on different heat transfer surfaces needs to be carefully considered.

Mineral scale particles of a certain composition adhere differently to the heat transfer surface. The effect of surface material and properties on the adhesion characteristics can be investigated. The test parameters include surface roughness, surface energy, microstructure and coating. A numerical approach can be adopted to carry out the modelling and simulation of single crystal attachments to the solid surface under different hydrodynamic conditions.

9.2.3. Green antiscalant

The fouling mitigation and prevention methods in domestic appliance and water treatment systems are relatively limited due to the health and environmental concerns coupled with the conventional fouling inhibitors. Frequently, the manufacturer of the appliances tends to modify/ change the heat transfer surface and/ or establish a water pre-treatment. These solutions come with some drawbacks such as high manufacturing and installation costs and reduction in heating efficiency. Recently, "natural" organic molecules were proposed as new green, environmentally friendly fouling inhibitors [171]. Plant extracts, such as soybean oil and Aloe Vera extract, are some of these green antiscalants which are more ecological than the commercial ones.

The proposed idea is to include a novel biodegradable and eco-friendly scale inhibitor in solid-state with a shelf life and dissolution rate. Figure 9.3 displays a schematic of a millimetre-sized chip of a natural inhibitor constructed by a polymer. Water flows through the chip channels causing

the inhibitor to dissolve in water reducing the scale formation. This porous chip can be installed in the pipelines perpendicular to the flow direction in the household appliances and water treatment systems. However, an intensive investigation might be required to study the factors that affect the lifetime and dissolution rate. A problem of pressure drop is expected in the system especially with turbulent flows. Therefore, an optimization of this antiscalant system including CFD simulations is necessary.
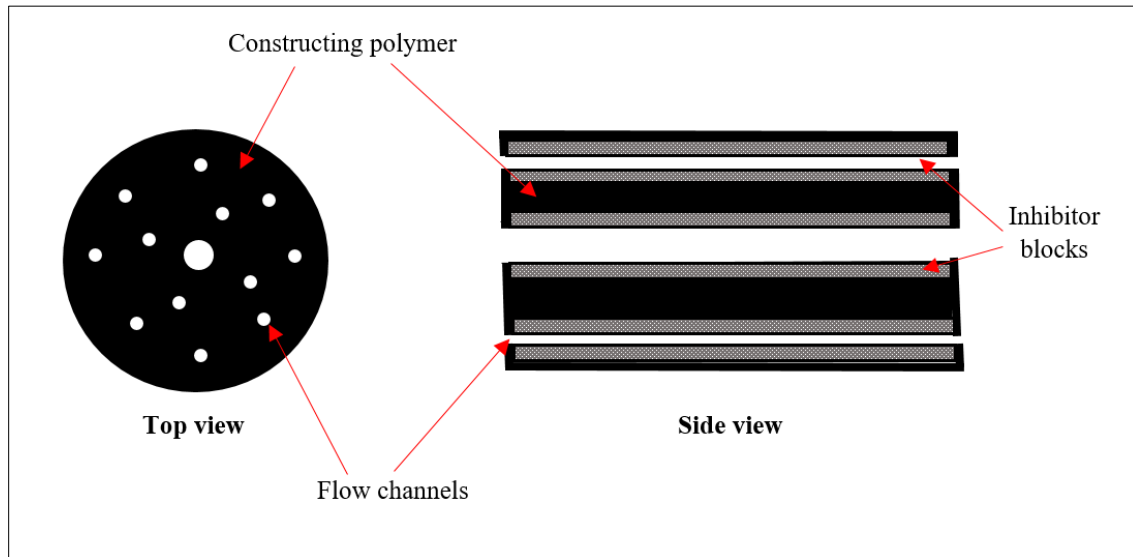
Figure 9.3. Schematic of porous inhibitor chip.

References

[1] K. D. Demadis, E. Mavredaki, A. Stathoulopoulou, E. Neofotistou, and C. Mantzaridis, "Industrial water systems: problems, challenges and solutions for the process industries," *Desalination,* vol. 213, no. 1-3, pp. 38-46, 2007.

[2] R. Steinhagen, H. Müller-Steinhagen, and K. Maani, "Problems and costs due to heat exchanger fouling in New Zealand industries," *Heat Transfer Eng.,* vol. 14, no. 1, pp. 19-30, 1993.

[3] A. Neville and A. Morizot, "A combined bulk chemistry/electrochemical approach to study the precipitation, deposition and inhibition of CaCO3," *Chem. Eng. Sci.,* vol. 55, no. 20, pp. 4737-4743, 2000.

[4] J. Nesta and C. Bennett, "Fouling mitigation by design," 2005.

[5] O. Söhnel and J. Mullin, "Precipitation of calcium carbonate," *J. Cryst. Growth,* vol. 60, no. 2, pp. 239-250, 1982.

[6] O. Bukuaghangin, O. Sanni, N. Kapur, M. Huggan, A. Neville, and T. Charpentier, "Kinetics study of barium sulphate surface scaling and inhibition with a once-through flow system," *J. PETROL. SCI. ENG.,* vol. 147, pp. 699-706, Nov. 2016. doi: https://doi.org/10.1016/j.petrol.2016.09.035.

[7] H. Müller-Steinhagen, M. R. Malayeri, and A. P. Watkinson, "Fouling of Heat Exchangers-New Approaches to Solve an Old Problem," *Heat Transfer Eng.,* vol. 26, no. 1, pp. 1-4, Jan. 2005. doi: https://doi.org/10.1080/01457630590889906.

[8] F. Schlüter, L. Schnöing, H. Zettler, W. Augustin, and S. Scholl, "Measuring Local Crystallization Fouling in a Double-Pipe Heat Exchanger," *Heat Transfer Eng.,* vol. 41, no. 2, pp. 149-159, Jan. 2020. doi: https://doi.org/10.1080/01457632.2018.1522084.

[9] A. Al-Gailani, T. V. Charpentier, O. Sanni, R. Crisp, J. H. Bruins, and A. Neville, "Inorganic Mineral Precipitation from Potable Water on Heat Transfer Surfaces," *J. Cryst. Growth,* p. 125621, Mar. 2020. doi: https://doi.org/10.1016/j.jcrysgro.2020.125621.

[10] J. Zhao, M. Wang, H. M. Lababidi, H. Al-Adwani, and K. K. Gleason, "A review of heterogeneous nucleation of calcium carbonate and control strategies for scale formation in multi-stage flash (MSF) desalination plants," *Desalination,* vol. 442, pp. 75-88, Sept. 2018. doi: https://doi.org/10.1016/j.desal.2018.05.008.

[11] E. Rammerstorfer, T. Karner, and M. Siebenhofer, "The kinetics and mechanisms of fouling in crude oil heat transfer," *Heat Transfer Eng.,* vol. 41, no. 8, pp. 691-707, Apr. 2020. doi: https://doi.org/10.1080/01457632.2018.1564202.

[12] J. MacAdam and S. A. Parsons, "Calcium carbonate scale formation and control," *Re/Views in Environmental Science & Bio/Technology,* vol. 3, no. 2, pp. 159-169, 2004.

[13] M. A. Kelland, "Effect of various cations on the formation of calcium carbonate and barium sulfate scale with and without scale inhibitors," *Industrial & Engineering Chemistry Research,* vol. 50, no. 9, pp. 5852-5861, 2011.

[14] A. Velloso Alves de Souza, F. Rosário, and J. Cajaiba, "Evaluation of Calcium Carbonate Inhibitors Using Sintered Metal Filter in a Pressurized Dynamic System," *Materials,* vol. 12, no. 11, p. 1849, 2019.

[15]   M. S. Kamal, I. Hussein, M. Mahmoud, A. S. Sultan, and M. A. Saad, "Oilfield scale formation and chemical removal: A review," *J. PETROL. SCI. ENG.,* vol. 171, pp. 127-139, 2018.

[16]   W. Q. R. F. (WQRF), "Softened Water Benefits Study (Energy and Detergent Savings)," *Lisle, IL: Water Quality Association.,* 2011.

[17]   A. J. Whelton, A. M. Dietrich, G. A. Burlingame, M. Schechs, and S. E. Duncan, "Minerals in drinking water: impacts on taste and importance to consumer health," *Water Sci. Technol.,* vol. 55, no. 5, pp. 283-291, 2007.

[18]   R. Khadsan and M. V. Kadu, "Drinking Water Quality Analysis of Some Bore-Wells Water of Chikhli Town, Maharashtra," *I Control Pollution,* vol. 20, no. 1, 1970.

[19]   D. Dobersek and D. Goricanec, "Influence of water scale on thermal flow losses of domestic appliances," *International journal of mathematical models and methods in applied sciences,* vol. 1, no. 2, pp. 55-61, 2007.

[20]   K. Y. Grinder, "How Does An HX Espresso Machine Work?," 2016.

[21]   C. S. Richards, F. Wang, W. C. Becker, and M. A. Edwards, "A 21st-Century Perspective on Calcium Carbonate Formation in Potable Water Systems," *Environmental Engineering Science,* vol. 35, no. 3, pp. 143-158, 2018.

[22]   T. Pääkkönen, M. Riihimäki, C. Simonson, E. Muurinen, and R. Keiski, "Crystallization fouling of $CaCO_3$ –Analysis of experimental thermal resistance and its uncertainty," *Int. J. Heat Mass Transfer,* vol. 55, no. 23-24, pp. 6927-6937, Nov. 2012. doi: https://doi.org/10.1016/j.ijheatmasstransfer.2012.07.006.

[23]   A. Vosough, S. M. Peyghambarzadeh, and M. R. Assari, "Influence of thermal shock on the mitigation of calcium sulfate crystallization fouling under subcooled flow boiling condition," *Appl. Therm. Eng.,* vol. 164, p. 114434, Jan. 2020. doi: https://doi.org/10.1016/j.applthermaleng.2019.114434.

[24]   A. Quddus and L. M. Al-Hadhrami, "Hydrodynamically deposited CaCO3 and CaSO4 scales," *Desalination,* vol. 246, no. 1-3, pp. 526-533, Sept. 2009. doi: https://doi.org/10.1016/j.desal.2008.11.005.

[25]   Q. Yang, J. Ding, and Z. Shen, "Investigation on fouling behaviors of low-energy surface and fouling fractal characteristics," *Chem. Eng. Sci.,* vol. 55, no. 4, pp. 797-805, Feb. 2000. doi: https://doi.org/10.1016/S0009-2509(99)00394-2.

[26]   S. Krause, "Fouling of heat-transfer surfaces by crystallization and sedimentation," *International Chemical Engineering (A Quarterly Journal of Translations from Russia, Eastern Europe and Asia);(United States),* vol. 33, no. 3, Jul. 1993.

[27]   N. Andritsos and A. Karabelas, "Calcium carbonate scaling in a plate heat exchanger in the presence of particles," *Int. J. Heat Mass Transfer,* vol. 46, no. 24, pp. 4613-4627, 2003. doi: https://doi.org/10.1016/S0017-9310(03)00308-9.

[28]   M. Mayer, J. Bucko, W. Benzinger, R. Dittmeyer, W. Augustin, and S. Scholl, "The impact of crystallization fouling on a microscale heat exchanger," *Exp. Therm Fluid Sci.,* vol. 40, pp. 126-131, Jul. 2012. doi: https://doi.org/10.1016/j.expthermflusci.2012.02.007.

[29]   T. R. Bott, "Aspects of crystallization fouling," *Exp. Therm Fluid Sci.,* vol. 14, no. 4, pp. 356-360, 1997/05/01/ 1997. doi: https://doi.org/10.1016/S0894-1777(96)00137-9.

[30]   M. Bohnet, "Fouling of heat transfer surfaces," *Chemical engineering & technology,* vol. 10, no. 1, pp. 113-125, 1987. doi: https://doi.org/10.1002/ceat.270100115.

[31] A. Al-Janabi and M. R. Malayeri, "Innovative non-metal heat transfer surfaces to mitigate crystallization fouling," *International Journal of Thermal Sciences,* vol. 138, pp. 384-392, 2019/04/01/ 2019. doi: https://doi.org/10.1016/j.ijthermalsci.2019.01.003.

[32] J. Gómez-Morales, J. Torrent-Burgués, A. López-Macipe, and R. Rodríguez-Clemente, "Precipitation of calcium carbonate from solutions with varying Ca2+carbonate ratios," *J. Cryst. Growth,* vol. 166, no. 1, pp. 1020-1026, 1996/09/01/ 1996. doi: https://doi.org/10.1016/0022-0248(96)00083-8.

[33] W. Cheong, P. Gaskell, and A. Neville, "Substrate effect on surface adhesion/crystallisation of calcium carbonate," *J. Cryst. Growth,* vol. 363, pp. 7-21, Jan. 2013. doi: https://doi.org/10.1016/j.jcrysgro.2012.09.025.

[34] Y. Lv, K. Lu, and Y. Ren, "Composite crystallization fouling characteristics of normal solubility salt in double-pipe heat exchanger," *Int. J. Heat Mass Transfer,* vol. 156, p. 119883, 2020/08/01/ 2020. doi: https://doi.org/10.1016/j.ijheatmasstransfer.2020.119883.

[35] O. Söhnel and J. Garside, *Precipitation: basic principles and industrial applications*. Butterworth-Heinemann, 1992.

[36] A. Al-Gailani, T. V. J. Charpentier, O. Sanni, R. Crisp, J. H. Bruins, and A. Neville, "Inorganic mineral precipitation from potable water on heat transfer surfaces," *Journal of Crystal Growth,* vol. 537, p. 125621, 2020/05/01/ 2020. doi: https://doi.org/10.1016/j.jcrysgro.2020.125621.

[37] C. Y. Tai and P. C. Chen, "Nucleation, agglomeration and crystal morphology of calcium carbonate," *AlChE J.,* vol. 41, no. 1, pp. 68-77, 1995.

[38] L. N. Plummer and E. Busenberg, "The solubilities of calcite, aragonite and vaterite in CO2-H2O solutions between 0 and 90 C, and an evaluation of the aqueous model for the system CaCO3-CO2-H2O," *Geochim. Cosmochim. Acta,* vol. 46, no. 6, pp. 1011-1040, Jun. 1982. doi: https://doi.org/10.1016/0016-7037(82)90056-4.

[39] P. Bénézeth, G. D. Saldi, J.-L. Dandurand, and J. Schott, "Experimental determination of the solubility product of magnesite at 50 to 200 C," *Chem. Geol.,* vol. 286, no. 1-2, pp. 21-31, 2011.

[40] A. E. Al-Rawajfeh, H. Glade, and J. Ulrich, "Scaling in multiple-effect distillers: the role of CO2 release," *Desalination,* vol. 182, no. 1-3, pp. 209-219, 2005.

[41] A. E. Al-Rawajfeh, "Influence of seawater composition on CO2 release and scaling in multi-stage flash (MSF) distillers from different arabian gulf intakes," *International Journal of Chemical Engineering and Applications,* vol. 1, no. 1, p. 43, 2010.

[42] T. R. Bott, *Fouling of heat exchangers*. Elsevier, 1995.

[43] O. S. Pokrovsky, "Precipitation of calcium and magnesium carbonates from homogeneous supersaturated solutions," *J. Cryst. Growth,* vol. 186, no. 1, pp. 233-239, 1998/03/01/ 1998. doi: https://doi.org/10.1016/S0022-0248(97)00462-4.

[44] D. Kralj, L. Brečević, and J. Kontrec, "Vaterite growth and dissolution in aqueous solution III. Kinetics of transformation," *J. Cryst. Growth,* vol. 177, no. 3-4, pp. 248-257, 1997.

[45] J. Suitor, W. Marner, and R. Ritter, "The history and status of research in fouling of heat exchangers in cooling water service," *The Canadian Journal of Chemical Engineering,* vol. 55, no. 4, pp. 374-380, 1977.

[46] F. N. Kemmer, "Nalco Chemical Company. The NALCO water handbook," ed: McGraw-Hill Book Co., New York, 1988.

[47]   W. Marshall and R. Slusher, "Solubility of Calcium Sulfate and its Hydrates in Sea Water and Saline Water Concentrates, and Temperature Concentration Limits," *Jour. Chem. & Eng. Data,* vol. 13, 1968.

[48]   Z. Amjad, *The science and technology of industrial water treatment*. CRC press, 2010.

[49]   M. E. Pilson, *An Introduction to the Chemistry of the Sea*. cambridge university press, 2012.

[50]   J. MacAdam and P. Jarvis, "Water-Formed Scales and Deposits: Types, Characteristics, and Relevant Industries," in *Mineral Scales and Deposits*: Elsevier, 2015, pp. 3-23.

[51]   R. Sheikholeslami, "Composite Fouling of Heat Transfer Equipment in Aqueous Media - A Review," *Heat Transfer Eng.,* vol. 21, no. 3, pp. 34-42, Jul. 2000. doi: https://doi.org/10.1080/014576300270889.

[52]   C. Gabrielli, G. Maurin, G. Poindessous, and R. Rosset, "Nucleation and growth of calcium carbonate by an electrochemical scaling process," *Journal of crystal growth,* vol. 200, no. 1-2, pp. 236-250, 1999.

[53]   M. Förster and M. Bohnet, "Influence of the interfacial free energy crystal/heat transfer surface on the induction period during fouling," *International journal of thermal sciences,* vol. 38, no. 11, pp. 944-954, 1999.

[54]   M. Förster, W. Augustin, and M. Bohnet, "Influence of the adhesion force crystal/heat exchanger surface on fouling mitigation," *Chemical Engineering and Processing: Process Intensification,* vol. 38, no. 4-6, pp. 449-461, Sept. 1999. doi: https://doi.org/10.1016/S0255-2701(99)00042-2.

[55]   S. Mitrouli, M. Kostoglou, and A. Karabelas, "Calcium carbonate scaling of desalination membranes: Assessment of scaling parameters from dead-end filtration experiments," *Journal of Membrane Science,* vol. 510, pp. 293-305, 2016.

[56]   K. Harouaka, Y. T. Lu, G. Ruan, H. D. Sriyarathne, W. Li, G. Deng, Y. Zhao, X. Wang, A. T. Kan, and M. Tomson, "The Effect of Surface Material on the Mechanics of Calcium Carbonate Scale Deposition," in *SPE International Oilfield Scale Conference and Exhibition*, 2018: Society of Petroleum Engineers.

[57]   J. W. Mullin, *Crystallization*. Elsevier, 2001.

[58]   G. Mazziotti di Celso, M. Prisciandaro, D. Karatza, A. Lancia, and D. Musmarra, "Salt scales on process equipment: Measurement of the induction time for calcium carbonate nucleation," *The Canadian Journal of Chemical Engineering,* vol. 95, no. 9, pp. 1671-1675, 2017.

[59]   T. Geddert, W. Augustin, and S. Scholl, "Induction time in crystallization fouling on heat transfer surfaces," *Chemical Engineering & Technology,* vol. 34, no. 8, pp. 1303-1310, 2011.

[60]   Q. Yang, Y. Liu, A. Gu, J. Ding, and Z. Shen, "Investigation of induction period and morphology of CaCO3 fouling on heated surface," *Chem. Eng. Sci.,* vol. 57, no. 6, pp. 921-931, 2002.

[61]   N. Epstein, "Thinking about heat transfer fouling: a 5× 5 matrix," *Heat Transfer Eng.,* vol. 4, no. 1, pp. 43-56, 1983.

[62]   M. Bohnet, "Influence of the Transport Properties of the Crystal/Heat Transfer Surface Interfacial on Fouling Behavior," *Chemical Engineering & Technology,* vol. 26, no. 10, pp. 1055-1060, 2003. doi: doi:10.1002/ceat.200301807.

[63]   M. Mayer, W. Augustin, and S. Scholl, "An approach to modeling induction period in crystallization fouling," *Heat Mass Transfer.,* vol. 49, no. 10, pp. 1419-1432, 2013.

[64]   J. Yang, "Computational fluid dynamics studies on the induction period of crude oil fouling in a heat exchanger tube," *Int. J. Heat Mass Transfer,* vol. 159, p. 120129, 2020.

[65]   B. Garrett-Price, "Fouling of heat exchangers: Characteristics, costs, prevention, control and removal," *Noyes Publications, 1985,* p. 417, 1985.

[66]   F. Brahim, W. Augustin, and M. Bohnet, "Numerical simulation of the fouling process," *International Journal of Thermal Sciences,* vol. 42, no. 3, pp. 323-334, Mar. 2003. doi: https://doi.org/10.1016/S1290-0729(02)00021-2.

[67]   M. Bohnet, W. Augustin, and H. Hirsch, "Influence of Fouling Layer Shear Strength on Removal Behavior," *Understanding Heat Exchanger Fouling and its Mitigation,* pp. 201-208, 1997.

[68]   J. Xiao, J. Han, F. Zhang, and X. D. Chen, "Numerical simulation of crystallization fouling: taking into account fouling layer structures," *Heat Transfer Eng.,* vol. 38, no. 7-8, pp. 775-785, 2017.

[69]   D. Kashchiev and G. Van Rosmalen, "Nucleation in solutions revisited," *Crystal Research and Technology: Journal of Experimental and Industrial Crystallography,* vol. 38, no. 7-8, pp. 555-574, 2003.

[70]   M. Mayer, W. Augustin, and S. Scholl, "Adhesion of single crystals on modified surfaces in crystallization fouling," *Journal of crystal Growth,* vol. 361, pp. 152-158, 2012.

[71]   P. Daudey, G. Van Rosmalen, and E. De Jong, "Secondary nucleation kinetcs of ammonium sulfate in a CMSMPR crystallizer," *J. Cryst. Growth,* vol. 99, no. 1-4, pp. 1076-1081, 1990.

[72]   E. Verdurand, C. Bebon, D. Colson, J.-P. Klein, A.-F. Blandin, and J.-M. Bossoutrot, "Secondary nucleation and growth of organic crystals in industrial crystallization," *J. Cryst. Growth,* vol. 275, no. 1-2, pp. e1363-e1367, 2005.

[73]   L.-C. Wang, S.-F. Li, L.-B. Wang, K. Cui, Q.-L. Zhang, H.-B. Liu, and G. Li, "Relationships between the characteristics of $CaCO_3$ fouling and the flow velocity in smooth tube," *Exp. Therm Fluid Sci.,* vol. 74, pp. 143-159, Jun. 2016. doi: https://doi.org/10.1016/j.expthermflusci.2015.12.001.

[74]   B. Bansal, X. D. Chen, and H. Müller-Steinhagen, "Analysis of 'classical' deposition rate law for crystallisation fouling," *Chemical Engineering and Processing: Process Intensification,* vol. 47, no. 8, pp. 1201-1210, 2008.

[75]   J. W. Morse, R. S. Arvidson, and A. Lüttge, "Calcium carbonate formation and dissolution," *Chem. Rev.,* vol. 107, no. 2, pp. 342-381, 2007.

[76]   J. Guo and S. J. Severtson, "Application of classical nucleation theory to characterize the influence of carboxylate-containing additives on CaCO3 nucleation at high temperature, pH, and ionic strength," *Industrial & engineering chemistry research,* vol. 42, no. 14, pp. 3480-3486, 2003.

[77]   P. M. Winkler, G. Steiner, A. Vrtala, H. Vehkamäki, M. Noppel, K. E. Lehtinen, G. P. Reischl, P. E. Wagner, and M. Kulmala, "Heterogeneous nucleation experiments bridging the scale from molecular ion clusters to nanoparticles," *Science,* vol. 319, no. 5868, pp. 1374-1377, 2008.

[78]   Q. Li, A. Fernandez-Martinez, B. Lee, G. A. Waychunas, and Y.-S. Jun, "Interfacial energies for heterogeneous nucleation of calcium carbonate on mica and quartz," *Environmental science & technology,* vol. 48, no. 10, pp. 5745-5753, 2014.

[79] M. G. Lioliou, C. A. Paraskeva, P. G. Koutsoukos, and A. C. Payatakes, "Heterogeneous nucleation and growth of calcium carbonate on calcite and quartz," *J. Colloid Interface Sci.,* vol. 308, no. 2, pp. 421-428, 2007.

[80] E. M. Pouget, P. H. Bomans, J. A. Goos, P. M. Frederik, and N. A. Sommerdijk, "The initial stages of template-controlled CaCO3 formation revealed by cryo-TEM," *Science,* vol. 323, no. 5920, pp. 1455-1458, 2009.

[81] J. Lee, J. Yang, S. G. Kwon, and T. Hyeon, "Nonclassical nucleation and growth of inorganic nanoparticles," *Nature Reviews Materials,* vol. 1, no. 8, p. 16034, 2016.

[82] R. S. Lam, J. M. Charnock, A. Lennie, and F. C. Meldrum, "Synthesis-dependant structural variations in amorphous calcium carbonate," *CrystEngComm,* vol. 9, no. 12, pp. 1226-1236, 2007.

[83] D. Gebauer, M. Kellermeier, J. D. Gale, L. Bergström, and H. Cölfen, "Pre-nucleation clusters as solute precursors in crystallisation," *Chem. Soc. Rev.,* vol. 43, no. 7, pp. 2348-2371, 2014.

[84] J. W. Mullin, "5.1.1 Homogeneous Nucleation," in *Crystallization (4th Edition)*: Elsevier, 2001, p. 182.

[85] M. S. Abd-Elhady, M. R. Jalalirad, and M. R. Malayeri, "Influence of injected projectiles on the induction period of crystallization fouling," *Heat Transfer Eng.,* vol. 35, no. 3, pp. 232-245, 2014.

[86] Y. Lv, M. Liu, and Y. Xu, "Corrosion and Fouling Behaviors on Modified Stainless Steel Surfaces in Simulated Oilfield Geothermal Water," *Protection of Metals and Physical Chemistry of Surfaces,* vol. 54, no. 3, pp. 526-535, 2018.

[87] D. Hasson, M. Avriel, W. Resnick, T. Rozenman, and S. Windreich, "Mechanism of calcium carbonate scale deposition on heat-transfer surfaces," *Industrial & Engineering Chemistry Fundamentals,* vol. 7, no. 1, pp. 59-65, Feb. 1968. doi: https://doi.org/10.1021/i160025a011.

[88] F. Fahiminia, A. P. Watkinson, and N. Epstein, "Early events in the precipitation fouling of calcium sulphate dihydrate under sensible heating conditions," *The Canadian Journal of Chemical Engineering,* vol. 85, no. 5, pp. 679-691, 2007.

[89] T. Pääkkönen, M. Riihimäki, C. Simonson, E. Muurinen, and R. Keiski, "Modeling CaCO3 crystallization fouling on a heat exchanger surface–Definition of fouling layer properties and model parameters," *Int. J. Heat Mass Transfer,* vol. 83, pp. 84-98, 2015.

[90] B. N. Opdyke and B. H. Wilkinson, "Carbonate mineral saturation state and cratonic limestone accumulation," *American Journal of Science,* vol. 293, no. 3, pp. 217-234, 1993.

[91] M. Mwaba, C. Rindt, A. Van Steenhoven, and M. Vorstman, "Experimental investigation of CaSO4 crystallization on a flat plate," *Heat Transfer Eng.,* vol. 27, no. 3, pp. 42-54, 2006.

[92] M. Mwaba, C. Rindt, A. Van Steenhoven, and M. Vorstman, "Validated numerical analysis of CaSO4 fouling," *Heat Transfer Eng.,* vol. 27, no. 7, pp. 50-62, 2006.

[93] J. W. Morse, "The kinetics of calcium carbonate dissolution and precipitation," *Reviews in Mineralogy and Geochemistry,* vol. 11, no. 1, pp. 227-264, 1983.

[94] J. Dirksen and T. Ring, "Fundamentals of crystallization: kinetic effects on particle size distributions and morphology," *Chem. Eng. Sci.,* vol. 46, no. 10, pp. 2389-2427, 1991.

[95] F. Frank, "On the kinematic theory of crystal growth and dissolution processes, II," *Z. Phys. Chem.,* vol. 77, no. 1-6, pp. 84-92, 1972.

[96] J. W. Gibbs, "The collected works of J. Willard Gibbs," Yale Univ. Press1948.

[97]   J. W. Mullin, "6.1.1 Surface Energy Theories," in *Crystallization (4th Edition)*: Elsevier, 2001, p. 216.

[98]   J. Curie and P. Curie, "Development by pressure of polar electricity in hemihedral crystals with inclined faces," *Bull. soc. min. de France,* vol. 3, p. 90, 1880.

[99]   G. Wulff, "On the question of speed of growth and dissolution of crystal surfaces," *Z. Kristallogr,* vol. 34, no. 5/6, p. 449, 1901.

[100] C. Goodman, *Crystal Growth*. Springer, 1974.

[101] M. Volmer, "Kinetic der Phasenbildung, Chap. 4," *Dresden and leipzig, Steinkopf,* 1939.

[102] B. Mutaftschiev, "Adsorption and crystal growth," *Cryst. Res. Technol.,* vol. 48, no. 10, pp. 706-726, 2013. doi: 10.1002/crat.201200703.

[103] A. A. Noyes and W. R. Whitney, "The rate of solution of solid substances in their own solutions," *J. Am. Chem. Soc.,* vol. 19, no. 12, pp. 930-934, 1897.

[104] A. Berthoud, "Théorie de la formation des faces d'un cristal," *Journal de Chimie Physique,* vol. 10, pp. 624-635, 1912.

[105] J. Valeton, "I. Wachstum und Auflösung der Kristalle. III," *Zeitschrift für Kristallographie-Crystalline Materials,* vol. 60, no. 1-6, pp. 1-38, 1924.

[106] J. N. Israelachvili, "Intermolecular and Surface Forces (with applications to colloidal and biological systems). London, Orlando, San Diego, New York, Toronto, Montreal," ed: Sydney, Tokyo: Academic Press, 1985.

[107] A. J. Karabelas, "Scale formation in tubular heat exchangers—research priorities," *International Journal of Thermal Sciences,* vol. 41, no. 7, pp. 682-692, 2002.

[108] M. A. Butt, A. Chughtai, J. Ahmad, R. Ahmad, U. Majeed, and I. Khan, "Theory of adhesion and its practical implications," *Journal of Faculty of Engineering & Technology,* vol. 2007, pp. 21-45, 2008.

[109] D. E. Packham, *Handbook of adhesion*. John Wiley & Sons, 2006.

[110] D. Packham and C. Johnston, "Mechanical adhesion: were McBain and Hopkins right? An empirical study," *Int. J. Adhes. Adhes.,* vol. 14, no. 2, pp. 131-135, 1994.

[111] H.-J. Butt and M. Kappl, *Surface and interfacial forces*. John Wiley & Sons, 2018.

[112] I. Collins, "A new model for mineral scale adhesion," in *International Symposium on Oilfield Scale*, 2002: Society of Petroleum Engineers.

[113] J. N. Israelachvili, *Intermolecular and surface forces*. Academic press, 2011.

[114] H. C. Hamaker, "The London—van der Waals attraction between spherical particles," *physica,* vol. 4, no. 10, pp. 1058-1072, 1937.

[115] T. R. Bott, "CHAPTER 6 - Adhesion," in *Fouling of Heat Exchangers*, T. R. Bott, Ed. Amsterdam: Elsevier Science B.V., 1995, pp. 45-54.

[116] Y. I. Rabinovich, J. J. Adler, A. Ata, R. K. Singh, and B. M. Moudgil, "Adhesion between nanoscale rough surfaces: I. Role of asperity geometry," *J. Colloid Interface Sci.,* vol. 232, no. 1, pp. 10-16, 2000.

[117] M. Crabtree, D. Eslinger, P. Fletcher, M. Miller, and A. Johnson, "Fighting scale: removal and prevention," *Oilfield review,* vol. 11, no. 03, pp. 30-45, 1999.

[118] M. Jordan, K. Sjursaether, M. Edgerton, and R. Bruce, "Inhibition of Lead and Zinc Sulphide Scale Deposits Formed during Production from High Temperature Oil and Condensate Reservoirs," in *SPE Asia Pacific Oil and Gas Conference and Exhibition*, 2000: Society of Petroleum Engineers.

[119] D. Kern, "A theoretical analysis of thermal surface fouling," *Br. Chem. Eng.,* vol. 4, pp. 258-262, 1959.

[120] J. Taborek, "Predictive methods for fouling behavior," *Chem. Eng. Prog. Chem. Eng. Prog.,* vol. 68, no. 7, pp. 69-78, 1972.

[121] M. L. Förster, *Verminderung des Kristallisationsfoulings durch gezielte Beeinflussung der Grenzfläche zwischen Kristallen und Wärmeübertragungsfläche*. Cuvillier, 2001.

[122] A. Al-Gailani, O. Sanni, T. V. J. Charpentier, R. Crisp, J. H. Bruins, and A. Neville, "Examining the effect of ionic constituents on crystallization fouling on heat transfer surfaces," *International Journal of Heat and Mass Transfer,* vol. 160, p. 120180, 2020/10/01/ 2020. doi: https://doi.org/10.1016/j.ijheatmasstransfer.2020.120180.

[123] H. Chen, C. Qing, J. Zheng, Y. Liu, and G. Wu, "Synthesis of calcium carbonate using extract components of croaker gill as morphology and polymorph adjust control agent," *Materials Science and Engineering: C,* vol. 63, pp. 485-488, 2016.

[124] S. Raharjo, S. Muryanto, J. Jamari, and A. P. Bayuseno, "Controlling of magnesium carbonate scale deposition on the piping system with laminar flow and in the presence of alumina," *AIP Conference Proceedings,* vol. 1977, no. 1, p. 020064, 2018/06/26 2018. doi: 10.1063/1.5042920.

[125] BC-Ground-Water-Association, "Hardness in Groundwater

" in "Water Stewardship Information Series " 2007.

[126] Y. Sano and D. Nakashima, "Prevention of calcium carbonate scale using electrolyzed water," *Int. J. Heat Mass Transfer,* vol. 127, pp. 1147-1156, 2018.

[127] S. B. Ahmed, M. Tlili, M. B. Amor, H. B. Bacha, and B. Elleuch, "Calcium sulphate scale prevention in a desalination unit using the SMCEC technique," *Desalination,* vol. 167, pp. 311-318, 2004.

[128] A. S. El Din, M. El-Dahshan, and R. Mohammed, "Scale formation in flash chambers of high-temperature MSF distillers," *Desalination,* vol. 177, no. 1-3, pp. 241-258, 2005.

[129] H.-J. Oh, Y.-K. Choung, S. Lee, J.-S. Choi, T.-M. Hwang, and J. H. Kim, "Scale formation in reverse osmosis desalination: model development," *Desalination,* vol. 238, no. 1-3, pp. 333-346, 2009.

[130] Scaleguard. (2020, August). *Hard Water Areas*. Available: https://www.scaleguard.co.uk/hard-water-areas.html

[131] N. Epstein, "Fouling in heat exchangers," in *Sixth International Heat Transfer Conference.*, 1977, vol. 6, pp. 235-253.

[132] L. Hiisvirta, "Metals in drinking water," *Vatten,* vol. 42, p. 201, 1986.

[133] H. Crumpton, "Chapter Five - Completion, Workover, and Intervention Fluids," in *Well Control for Completions and Interventions*, H. Crumpton, Ed. Boston: Gulf Professional Publishing, 2018, pp. 189-215.

[134] H.-P. Mattila and R. Zevenhoven, "Chapter Ten - Production of Precipitated Calcium Carbonate from Steel Converter Slag and Other Calcium-Containing Industrial Wastes and Residues," in *Adv. Inorg. Chem.*, vol. 66, M. Aresta and R. van Eldik, Eds.: Academic Press, 2014, pp. 347-384.

[135] L. Xiang, Y. Xiang, Y. Wen, and F. Wei, "Formation of CaCO3 nanoparticles in the presence of terpineol," *Mater. Lett.,* vol. 58, no. 6, pp. 959-965, 2004.

[136] J. Oddo and M. Tomson, "Why scale forms in the oil field and methods to predict it," *SPE Production & Facilities,* vol. 9, no. 01, pp. 47-54, 1994.

[137] T. Chen, A. Neville, and M. Yuan, "Calcium carbonate scale formation—assessing the initial stages of precipitation and deposition," *J. PETROL. SCI. ENG.,* vol. 46, no. 3, pp. 185-194, 2005.

[138] H. Li, M.-K. Hsieh, S.-H. Chien, J. D. Monnell, D. A. Dzombak, and R. D. Vidic, "Control of mineral scale deposition in cooling systems using secondary-treated municipal wastewater," *Water Res.,* vol. 45, no. 2, pp. 748-760, 2011.

[139] H. Müller-Steinhagen, "Heat transfer fouling: 50 years after the kern and seaton model," *Heat Transfer Eng.,* vol. 32, no. 1, pp. 1-13, 2011.

[140] K. Kadota, A. Shimosaka, Y. Shirakawa, and J. Hidaka, "Dehydration process in NaCl solutions under various external electric fields," *J. Nanopart. Res.,* vol. 9, no. 3, pp. 377-387, 2007.

[141] S. Yamanaka, N. Ito, A. Shimosaka, Y. Shirakawa, and J. Hidaka, "AFM investigation for the initial growth processes of calcium carbonate on hydrophilic and hydrophobic substrate," *Cryst. Growth Des.,* vol. 9, no. 7, pp. 3245-3250, 2009.

[142] H. Du, M. Steinacher, C. N. Borca, T. Huthwelker, A. Murello, F. Stellacci, and E. Amstad, "Amorphous CaCO3: Influence of the formation time on its degree of hydration and stability," *J. Am. Chem. Soc.,* 2018.

[143] M.-A. Popescu, R. Isopescu, C. Matei, G. Fagarasan, and V. Plesu, "Thermal decomposition of calcium carbonate polymorphs precipitated in the presence of ammonia and alkylamines," *Adv. Powder Technol.,* vol. 25, no. 2, pp. 500-507, 2014.

[144] K. N. Islam, M. Z. B. A. Bakar, M. M. Noordin, M. Z. B. Hussein, N. S. B. A. Rahman, and M. E. Ali, "Characterisation of calcium carbonate and its polymorphs from cockle shells (Anadara granosa)," *Powder Technol.,* vol. 213, no. 1-3, pp. 188-191, Nov. 2011. doi: https://doi.org/10.1016/j.powtec.2011.07.031.

[145] L. B. Gower, "Biomimetic model systems for investigating the amorphous precursor pathway and its role in biomineralization," *Chem. Rev.,* vol. 108, no. 11, pp. 4551-4627, 2008.

[146] A. Sarkar and S. Mahapatra, "Mechanism of unusual polymorph transformations in calcium carbonate: Dissolution-recrystallization vs additive-mediated nucleation," *Journal of Chemical Sciences,* vol. 124, no. 6, pp. 1399-1404, 2012.

[147] D. Chakraborty, V. Agarwal, S. Bhatia, and J. Bellare, "Steady-state transitions and polymorph transformations in continuous precipitation of calcium carbonate," *Industrial & engineering chemistry research,* vol. 33, no. 9, pp. 2187-2197, 1994.

[148] A. A. Al-Hamzah, C. P. East, W. O. Doherty, and C. M. Fellows, "Inhibition of homogenous formation of calcium carbonate by poly (acrylic acid). The effect of molar mass and end-group functionality," *Desalination,* vol. 338, pp. 93-105, 2014.

[149] T. Ogino, T. Suzuki, and K. Sawada, "The formation and transformation mechanism of calcium carbonate in water," *Geochim. Cosmochim. Acta,* vol. 51, no. 10, pp. 2757-2767, 1987.

[150] R. K. Dhir, J. d. Brito, R. Mangabhai, and C. Q. Lye, "4 - Use of Copper Slag as Concrete Sand," in *Sustainable Construction Materials: Copper Slag*, R. K. Dhir, J. d. Brito, R. Mangabhai, and C. Q. Lye, Eds.: Woodhead Publishing, 2017, pp. 87-163.

[151] P. A. Claisse, "Chapter 7 - Chemistry of construction materials," in *Civil Engineering Materials*, P. A. Claisse, Ed. Boston: Butterworth-Heinemann, 2016, pp. 65-72.

[152] Y. Choi, G. Naidu, S. Jeong, S. Lee, and S. Vigneswaran, "Effect of chemical and physical factors on the crystallization of calcium sulfate in seawater reverse osmosis brine," *Desalination,* vol. 426, pp. 78-87, 2018/01/15/ 2018. doi: https://doi.org/10.1016/j.desal.2017.10.037.

[153] D. H. Case, F. Wang, and D. E. Giammar, "Precipitation of magnesium carbonates as a function of temperature, solution composition, and presence of a silicate mineral substrate," *Environmental Engineering Science,* vol. 28, no. 12, pp. 881-889, 2011.

[154] T. R. Bott, "CHAPTER 2 - Basic Principles," in *Fouling of Heat Exchangers*, T. R. Bott, Ed. Amsterdam: Elsevier Science B.V., 1995, pp. 7-14.

[155] L. Sutherland, C. J. Johnston, and W. Taylor, "The influence of turbulence (or Hydrodynamic Effects) on barium sulphate scale formation and inhibitor performance," in *SPE International Symposium on Oilfield Chemistry*, 2013: Society of Petroleum Engineers.

[156] A. B. BinMerdhah, "Inhibition of barium sulfate scale at high-barium formation water," *J. PETROL. SCI. ENG.,* vol. 90, pp. 124-130, 2012.

[157] C. Chungcheng and G. Nancollas, "The crystallization of magnesium hydroxide, a constant composition study," *Desalination,* vol. 42, no. 2, pp. 209-219, 1982.

[158] B. Dabir, R. W. Peters, and J. D. Stevens, "Precipitation kinetics of magnesium hydroxide in a scaling system," *Industrial & Engineering Chemistry Fundamentals,* vol. 21, no. 3, pp. 298-305, 1982.

[159] J. S. Gill, "A novel inhibitor for scale control in water desalination," *Desalination,* vol. 124, no. 1, pp. 43-50, 1999/11/01/ 1999. doi: https://doi.org/10.1016/S0011-9164(99)00087-9.

[160] H. Müller-Steinhagen, *Heat exchanger fouling: Mitigation and cleaning techniques*. UK: IChemE, 2000.

[161] D. Hasson, "Fouling of heat transfer equipment," *Washington Hemisphere Publishing Corp,* vol. 1981, pp. 527-5681, 1981.

[162] S. Keysar, R. Semiat, D. Hasson, and J. Yahalom, "Effect of surface roughness on the morphology of calcite crystallizing on mild steel," *J. Colloid Interface Sci.,* vol. 162, no. 2, pp. 311-319, 1994.

[163] K. S. Song, J. Lim, S. Yun, D. Kim, and Y. Kim, "Composite fouling characteristics of CaCO3 and CaSO4 in plate heat exchangers at various operating and geometric conditions," *Int. J. Heat Mass Transfer,* vol. 136, pp. 555-562, 2019.

[164] K. Palanisamy and V. Subramanian, "CaCO3 scale deposition on copper metal surface; effect of morphology, size and area of contact under the influence of EDTA," *Powder Technol.,* vol. 294, pp. 221-225, 2016.

[165] S. Dash, L. Rapoport, and K. K. Varanasi, "Crystallization-Induced Fouling during Boiling: Formation Mechanisms to Mitigation Approaches," *Langmuir,* 2017.

[166] Z. Wu, J. H. Davidson, and L. F. Francis, "Effect of water chemistry on calcium carbonate deposition on metal and polymer surfaces," *J. Colloid Interface Sci.,* vol. 343, no. 1, pp. 176-187, 2010.

[167] T. Chen, A. Neville, and M. Yuan, "Assessing the effect of Mg2+ on CaCO3 scale formation–bulk precipitation and surface deposition," *J. Cryst. Growth,* vol. 275, no. 1-2, pp. e1341-e1347, 2005.

[168] K. Teng, A. Amiri, S. Kazi, M. Bakar, and B. Chew, "Fouling mitigation on heat exchanger surfaces by EDTA-treated MWCNT-based water nanofluids," *Journal of the Taiwan Institute of Chemical Engineers,* vol. 60, pp. 445-452, 2016.

[169] C. Wan, L.-T. Wang, J.-Y. Sha, and H.-H. Ge, "Effect of carbon nanoparticles on the crystallization of calcium carbonate in aqueous solution," *Nanomaterials,* vol. 9, no. 2, p. 179, 2019.

[170] F.-A. Setta and A. Neville, "Efficiency assessment of inhibitors on CaCO3 precipitation kinetics in the bulk and deposition on a stainless steel surface (316 L)," *Desalination,* vol. 281, pp. 340-347, 2011.

[171] M. Chaussemier, E. Pourmohtasham, D. Gelus, N. Pécoul, H. Perrot, J. Lédion, H. Cheap-Charpentier, and O. Horner, "State of art of natural inhibitors of calcium carbonate scaling. A review article," *Desalination,* vol. 356, pp. 47-55, 2015.

[172] J. MacAdam and S. A. Parsons, "The Effect of Metal Ions on Calcium Carbonate Precipitation and Scale Formation," in *Sustainability in Energy and Buildings*, Berlin, Heidelberg, 2009, pp. 137-146: Springer Berlin Heidelberg.

[173] P. G. Koutsoukos and C. G. Kontoyannis, "Precipitation of calcium carbonate in aqueous solutions," *Journal of the Chemical Society, Faraday Transactions 1: Physical Chemistry in Condensed Phases,* vol. 80, no. 5, pp. 1181-1192, 1984.

[174] E. J. Zeller and J. L. Wray, "Factors influencing precipitation of calcium carbonate," *AAPG Bulletin,* vol. 40, no. 1, pp. 140-152, 1956.

[175] O. Sanni, O. Bukuaghangin, T. Charpentier, N. Kapur, and A. Neville, "Using a real-time visualisation technique for the assessment of surface scale kinetics and mechanisms of inhibition," in *SPE International Oilfield Scale Conference and Exhibition*, 2016: Society of Petroleum Engineers.

[176] A. Neville, "Surface Scaling in the Oil and Gas Sector: Understanding the Process and Means of Management," *Energy & Fuels,* vol. 26, no. 7, pp. 4158-4166, 2012/07/19 2012. doi: 10.1021/ef300351w.

[177] O. S. Sanni, O. Bukuaghangin, T. V. Charpentier, and A. Neville, "Evaluation of laboratory techniques for assessing scale inhibition efficiency," *J. PETROL. SCI. ENG.,* p. 106347, 2019.

[178] K. Teng, S. Kazi, A. Amiri, A. Habali, M. Bakar, B. Chew, A. Al-Shamma'a, A. Shaw, K. Solangi, and G. Khan, "Calcium carbonate fouling on double-pipe heat exchanger with different heat exchanging surfaces," *Powder Technol.,* vol. 315, pp. 216-226, Jun. 2017. doi: https://doi.org/10.1016/j.powtec.2017.03.057.

[179] T. Waly, M. D. Kennedy, G.-J. Witkamp, G. Amy, and J. C. Schippers, "The role of inorganic ions in the calcium carbonate scaling of seawater reverse osmosis systems," *Desalination,* vol. 284, pp. 279-287, 2012/01/04/ 2012. doi: https://doi.org/10.1016/j.desal.2011.09.012.

[180] D. E. Packham, "Surface energy, surface topography and adhesion," *Int. J. Adhes. Adhes.,* vol. 23, no. 6, pp. 437-448, Aug. 2003. doi: https://doi.org/10.1016/S0143-7496(03)00068-X.

[181] A. Herz, M. R. Malayeri, and H. Müller-Steinhagen, "Fouling of roughened stainless steel surfaces during convective heat transfer to aqueous solutions," *Energy Convers. Manage.,* vol. 49, no. 11, pp. 3381-3386, 2008/11/01/ 2008. doi: https://doi.org/10.1016/j.enconman.2007.09.034.

[182] T. Geddert, W. Augustin, and S. Scholl, "Influence of surface defects and aging of coated surfaces on fouling behavior," *Heat Transfer Eng.,* vol. 32, no. 3-4, pp. 300-306, 2011.

[183] N. R. Chevalier, "Do surface wetting properties affect calcium carbonate heterogeneous nucleation and adhesion?," *The Journal of Physical Chemistry C,* vol. 118, no. 31, pp. 17600-17607, 2014.

[184] Q. Zhao, Y. Liu, C. Wang, S. Wang, and H. Müller-Steinhagen, "Effect of surface free energy on the adhesion of biofouling and crystalline fouling," *Chem. Eng. Sci.,* vol. 60, no. 17, pp. 4858-4865, 2005/09/01/ 2005. doi: https://doi.org/10.1016/j.ces.2005.04.006.

[185] A. Al-Janabi and M. R. Malayeri, "Environmentally Friendly Solvent- and Water-Based Coatings for Mitigation of Crystallization Fouling," *Chemical Engineering & Technology,* vol. 38, no. 1, pp. 147-154, 2015. doi: 10.1002/ceat.201400457.

[186] B. Bansal, "Crystallisation fouling in plate heat exchangers," ResearchSpace@ Auckland, 1994.

[187] S. Najibi, H. Muller-Steinhagen, and M. Jamialahmadi, "Calcium carbonate scale formation during subcooled flow boiling," *J. Heat Transfer,* vol. 119, no. 4, pp. 767-775, 1997.

[188] V. Eroini, A. Neville, N. Kapur, and M. Euvrard, "New insight into the relation between bulk precipitation and surface deposition of calcium carbonate mineral scale," *Desalination and water treatment,* vol. 51, no. 4-6, pp. 882-891, 2013.

[189] Y. Zhang, H. Shaw, R. Farquhar, and R. Dawe, "The kinetics of carbonate scaling—application for the prediction of downhole carbonate scaling," *J. PETROL. SCI. ENG.,* vol. 29, no. 2, pp. 85-95, 2001.

[190] M. Jamialahmadi and H. Müller-Steinhagen, "Scale formation during nucleate boiling-A review," ed: De Gruyter, 1993.

[191] A. Antony, J. H. Low, S. Gray, A. E. Childress, P. Le-Clech, and G. Leslie, "Scale formation and control in high pressure membrane water treatment systems: a review," *Journal of membrane science,* vol. 383, no. 1-2, pp. 1-16, 2011.

[192] A. Konak, "A new model for surface reaction-controlled growth of crystals from solution," *Chem. Eng. Sci.,* vol. 29, no. 7, pp. 1537-1543, 1974.

[193] S. Alsadaie and I. M. Mujtaba, "Crystallization of calcium carbonate and magnesium hydroxide in the heat exchangers of once-through Multistage Flash (MSF-OT) desalination process," *Computers & Chemical Engineering,* vol. 122, pp. 293-305, 2019.

[194] F. Zhang, J. Xiao, and X. D. Chen, "Towards predictive modeling of crystallization fouling: A pseudo-dynamic approach," *Food and Bioproducts Processing,* vol. 93, pp. 188-196, 2015.

[195] D. Kern and R. Seaton, "A theoretical analysis of thermal surface fouling," *Br. Chem. Eng.,* vol. 4, pp. 258-262, 1959.

[196] A. Bahadori, H. Vuthaluru, and M. Ang, "Predictive tool for estimation of potential precipitation from an equilibrated calcium carbonate aqueous phase," in *Trinidad and Tobago Energy Resources Conference*, 2010: Society of Petroleum Engineers.

[197] A. Eseosa and A. J. Atubokiki, "Prediction and Monitoring of Oilfield Carbonate Scales Using Scale Check," in *Nigeria Annual International Conference and Exhibition*, 2011: Society of Petroleum Engineers.

[198] I. RYZNER, "A New Index for Determining Amount of Calclum Carbonate Scale Formed by a Water," *J. Amer. Water Works Asso,* vol. 36, pp. 472-486, 1944.

[199] N. Andritsos, A. J. Karabelas, and P. G. Koutsoukos, "Morphology and Structure of CaCO3 Scale Layers Formed under Isothermal Flow Conditions," *Langmuir,* vol. 13, no. 10, pp. 2873-2879, 1997/05/01 1997. doi: 10.1021/la960960s.

[200] S. Muryanto, A. P. Bayuseno, H. Ma'mun, M. Usamah, and Jotho, "Calcium Carbonate Scale Formation in Pipes: Effect of Flow Rates, Temperature, and Malic Acid as Additives

on the Mass and Morphology of the Scale," *Procedia Chemistry,* vol. 9, pp. 69-76, 2014/01/01/ 2014. doi: https://doi.org/10.1016/j.proche.2014.05.009.

[201]   A. Fernandez-Martinez, H. Lopez-Martinez, and D. Wang, "Structural characteristics and the occurrence of polyamorphism in amorphous calcium carbonate," in *New Perspectives on Mineral Nucleation and Growth*: Springer, 2017, pp. 77-92.

[202]   A. Martinod, M. Euvrard, A. Foissy, and A. Neville, "Progressing the understanding of chemical inhibition of mineral scale by green inhibitors," *Desalination,* vol. 220, no. 1-3, pp. 345-352, 2008.

[203]   S.-H. Yu, "Bio-inspired crystal growth by synthetic templates," in *Biomineralization II*: Springer, 2006, pp. 79-118.

[204]   H. Meyer, "The influence of impurities on the growth rate of calcite," *J. Cryst. Growth,* vol. 66, no. 3, pp. 639-646, 1984.

[205]   T. Østvold and P. Randhol, "Kinetics of CaCO3 Scale Formation. The Influence of Temperature, Supersaturation and Ionic Composition," presented at the International Symposium on Oilfield Scale, Aberdeen, United Kingdom, 2001/1/1/, 2001. Available: https://doi.org/10.2118/68302-MS

[206]   J. Yu, M. Lei, B. Cheng, and X. Zhao, "Facile preparation of calcium carbonate particles with unusual morphologies by precipitation reaction," *J. Cryst. Growth,* vol. 261, no. 4, pp. 566-570, 2004.

[207]   L.-T. Wang, H.-H. Ge, Y.-T. Han, C. Wan, J.-Y. Sha, and K. Sheng, "Effects of Al2O3 nanoparticles on the formation of inorganic scale on heat exchange surface with and without scale inhibitor," *Appl. Therm. Eng.,* vol. 151, pp. 1-10, 2019.

[208]   S. M. Alsadaie and I. M. Mujtaba, "Dynamic modelling of Heat Exchanger fouling in multistage flash (MSF) desalination," *Desalination,* vol. 409, pp. 47-65, 2017.

[209]   D. Dawson, "Non-chemical water treatment system," *Corrosion Prevention & Control,* vol. 37, no. 3, pp. 61-64, 1990.

[210]   Z. Wang, A. Neville, and A. Meredith, "How and Why does Scale Stick-Can the Surface be Engineered to Decrease Scale Formation and Adhesion?," in *SPE International Symposium on Oilfield Scale*, 2005: Society of Petroleum Engineers.

[211]   B. Feng, A. K. Yong, and H. An, "Effect of various factors on the particle size of calcium carbonate formed in a precipitation process," *Materials Science and Engineering: A,* vol. 445, pp. 170-179, 2007.

[212]   M. B. Amor, D. Zgolli, M. Tlili, and A. Manzola, "Influence of water hardness, substrate nature and temperature on heterogeneous calcium carbonate nucleation," *Desalination,* vol. 166, pp. 79-84, Aug. 2004. doi: https://doi.org/10.1016/j.desal.2004.06.061.

[213]   M. Kitamura, "Controlling factor of polymorphism in crystallization process," *J. Cryst. Growth,* vol. 237, pp. 2205-2214, 2002.

[214]   M. Kellermeier, F. Glaab, R. Klein, E. Melero-García, W. Kunz, and J. M. García-Ruiz, "The effect of silica on polymorphic precipitation of calcium carbonate: an on-line energy-dispersive X-ray diffraction (EDXRD) study," *Nanoscale,* vol. 5, no. 15, pp. 7054-7065, 2013.

[215]   Y. S. Han, G. Hadiko, M. Fuji, and M. Takahashi, "Factors affecting the phase and morphology of CaCO3 prepared by a bubbling method," *J. Eur. Ceram. Soc.,* vol. 26, no. 4-5, pp. 843-847, 2006.

[216] C. Fan, A. Kan, P. Zhang, H. Lu, S. Work, J. Yu, and M. Tomson, "Scale Prediction and Inhibition for Oil and Gas Production at High Temperature/High Pressure," *SPE-130690-PA,* vol. 17, no. 02, pp. 379-392, Jun. 2012. doi: https://doi.org/10.2118/130690-PA.

[217] A. V. García, K. Thomsen, and E. H. Stenby, "Prediction of mineral scale formation in geothermal and oilfield operations using the Extended UNIQUAC model: Part II. Carbonate-scaling minerals," *Geothermics,* vol. 35, no. 3, pp. 239-284, 2006/06/01/ 2006. doi: https://doi.org/10.1016/j.geothermics.2006.03.001.

[218] S. J. Dyer and G. M. Graham, "The effect of temperature and pressure on oilfield scale formation," *J. PETROL. SCI. ENG.,* vol. 35, no. 1-2, pp. 95-107, 2002.

[219] M. Zahedzadeh, M. Karambeigi, E. Roayaei, M. Emadi, M. Radmehr, H. Gholamianpour, S. Ashoori, and S. Shokrollahzadeh, "Comprehensive management of mineral scale deposition in carbonate oil fields–A case study," *Chem. Eng. Res. Des.,* vol. 92, no. 11, pp. 2264-2272, 2014.

[220] K. Peyvandi, A. Haghtalab, and M. R. Omidkhah, "Using an electrochemical technique to study the effective variables on morphology and deposition of CaCO3 and BaSO4 at the metal surface," *J. Cryst. Growth,* vol. 354, no. 1, pp. 109-118, 2012/09/01/ 2012. doi: https://doi.org/10.1016/j.jcrysgro.2012.05.020.

[221] A. Kan and M. Tomson, "Scale prediction for oil and gas production," *SPE-130690-PA,* vol. 17, no. 02, pp. 362-378, 2012.

[222] A. B. B. Merdhah and A. A. M. Yassin, "Laboratory Study on precipitation of Barium Sulphate in Malaysia sandstone cores," *The Open Petroleum Engineering Journal,* vol. 2, no. 1, 2009.

[223] A. Watkinson and O. Martinez, "Scaling of heat exchanger tubes by calcium carbonate," *J. Heat Transfer,* vol. 97, no. 4, pp. 504-508, 1975.

[224] J. Moghadasi, M. Jamialahmadi, H. Müller-Steinhagen, and A. Sharif, "Scale formation in oil reservoir and production equipment during water injection (Kinetics of CaSO4 and CaCO3 crystal growth and effect on formation damage)," in *SPE European Formation Damage Conference*, 2003: Society of Petroleum Engineers.

[225] A. Helalizadeh, H. Müller-Steinhagen, and M. Jamialahmadi, "Mixed salt crystallisation fouling," *Chemical Engineering and Processing: Process Intensification,* vol. 39, no. 1, pp. 29-43, 2000.

[226] R. Jaouhari, A. Benbachir, A. Guenbour, C. Gabrielli, J. Garcia-Jareno, and G. Maurin, "Influence of water composition and substrate on electrochemical scaling," *J. Electrochem. Soc.,* vol. 147, no. 6, pp. 2151-2161, 2000.

[227] X. Si, J. Xi, and X. Tao, "The Study of Calcium Carbonate Scaling on Low Energy Surfaces," in *2010 14th International Heat Transfer Conference*, 2010, pp. 149-156: American Society of Mechanical Engineers.

[228] B. Rankin and W. Adamson, "Scale formation as related to evaporator surface conditions," *Desalination,* vol. 13, no. 1, pp. 63-87, 1973.

[229] B. Bhushan and Y. C. Jung, "Natural and biomimetic artificial surfaces for superhydrophobicity, self-cleaning, low adhesion, and drag reduction," *Prog. Mater Sci.,* vol. 56, no. 1, pp. 1-108, 2011.

[230] H. T. Phan, N. Caney, P. Marty, S. Colasson, and J. Gavillet, "Surface wettability control by nanocoating: the effects on pool boiling heat transfer and nucleation mechanism," *Int. J. Heat Mass Transfer,* vol. 52, no. 23-24, pp. 5459-5471, 2009.

[231] A. Koishi, A. Fernandez-Martinez, A. E. Van Driessche, L. J. Michot, C. M. Pina, C. Pimentel, B. Lee, and G. Montes-Hernandez, "Surface Wetting Controls Calcium Carbonate Crystallization Kinetics," *Chem. Mater.,* vol. 31, no. 9, pp. 3340-3348, 2019.

[232] C. Sandu and D. Lund, "Fouling of heat transfer equipment by food fluids: computational models," in *AIChE symposium series (USA). no. 218*, 1982.

[233] R. F. Brady Jr, "A fracture mechanical analysis of fouling release from nontoxic antifouling coatings," *Prog. Org. Coat.,* vol. 43, no. 1-3, pp. 188-192, 2001.

[234] J. W. MAYER and O. J. MARSH, "Ion implantation in Semiconductors," in *Applied Solid state science*, vol. 1: Elsevier, 1969, pp. 239-342.

[235] H. Müller-Steinhagen and Q. Zhao, "Investigation of low fouling surface alloys made by ion implantation technology," *Chem. Eng. Sci.,* vol. 52, no. 19, pp. 3321-3332, 1997.

[236] Q. Yang, J. Ding, and Z. Shen, "Investigation of calcium carbonate scaling on ELP surface," *J. Chem. Eng. Jpn.,* vol. 33, no. 4, pp. 591-596, 2000.

[237] Q. Zhao and X. Wang, "Heat transfer surfaces coated with fluorinated diamond-like carbon films to minimize scale formation," *Surf. Coat. Technol.,* vol. 192, no. 1, pp. 77-80, 2005.

[238] L. M. Al-Hadhrami, A. Quddus, and D. A. Al-Otaibi, "Calcium sulfate scale deposition on coated carbon steel and titanium," *Desalination and Water Treatment,* vol. 51, no. 13-15, pp. 2521-2528, 2013.

[239] K. I. Parsiegla and J. L. Katz, "Calcite growth inhibition by copper (II): I. Effect of supersaturation," *J. Cryst. Growth,* vol. 200, no. 1-2, pp. 213-226, 1999.

[240] M. M. Reddy and K. K. Wang, "Crystallization of calcium carbonate in the presence of metal ions: I. Inhibition by magnesium ion at pH 8.8 and 25 C," *J. Cryst. Growth,* vol. 50, no. 2, pp. 470-480, 1980.

[241] K. Zeppenfeld, "Prevention of CaCO3 scale formation by trace amounts of copper (II) in comparison to zinc (II)," *Desalination,* vol. 252, no. 1-3, pp. 60-65, 2010.

[242] A. Glasner and D. Weiss, "The crystallization of calcite from aqueous solutions and the role of zinc and magnesium ions—I. Precipitation of calcite in the presence of Zn2+ ions," *J. Inorg. Nucl. Chem.,* vol. 42, no. 5, pp. 655-663, 1980.

[243] B. Pernot, M. Euvrard, and P. Simon, "Effects of iron and manganese on the scaling potentiality of water," *Journal of Water Supply: Research and Technology-Aqua,* vol. 47, no. 1, pp. 21-29, 1998.

[244] C. Y. Tai and W.-C. Chien, "Effects of operating variables on the induction period of CaCl2–Na2CO3 system," *J. Cryst. Growth,* vol. 237, pp. 2142-2147, 2002.

[245] N. Wada, K. Yamashita, and T. Umegaki, "Effects of silver, aluminum, and chrome ions on the polymorphic formation of calcium carbonate under conditions of double diffusion," *J. Colloid Interface Sci.,* vol. 201, no. 1, pp. 1-6, 1998.

[246] O. Söhnel and J. W. Mullin, "Interpretation of crystallization induction periods," *J. Colloid Interface Sci.,* vol. 123, no. 1, pp. 43-50, 1988.

[247] C. Nalepa, R. Moore, G. Golson, T. Wolfe, and P. Puckorius, "A Comparison of Bromine-Based Biocides in a Medium Size Cooling Tower," *CTI JOURNAL,* vol. 20, pp. 42-61, 1999.

[248] A. G. I. Dalvi, N. K. Mohammad, S. Al-Sulami, K. Sahul, and R. Al-Rasheed, "Role of chemical constituents in recycle brine on the performance of scale control additives in MSF plants," *Desalination,* vol. 129, no. 2, pp. 173-186, 2000.

[249] E. Aoustin, A. Schäfer, A. G. Fane, and T. Waite, "Ultrafiltration of natural organic matter," *Sep. Purif. Technol.,* vol. 22, pp. 63-78, 2001.

[250] A. Zularisam, A. Ismail, and R. Salim, "Behaviours of natural organic matter in membrane filtration for surface water treatment—a review," *Desalination,* vol. 194, no. 1-3, pp. 211-231, 2006.

[251] E. M. Peña-Méndez, J. Havel, and J. Patočka, "Humic substances–compounds of still unknown structure: applications in agriculture, industry, environment, and biomedicine," *J. Appl. Biomed,* vol. 3, no. 1, pp. 13-24, 2005.

[252] M. M. Reddy and A. R. Hoch, "Calcite crystal growth rate inhibition by aquatic humic substances," in *Advances in crystal growth inhibition technologies*: Springer, 2002, pp. 107-121.

[253] R. Alvarez, L. A. Evans, P. J. Milham, and M. A. Wilson, "Effects of humic material on the precipitation of calcium phosphate," *Geoderma,* vol. 118, no. 3, pp. 245-260, 2004/02/01/ 2004. doi: https://doi.org/10.1016/S0016-7061(03)00207-6.

[254] F. J. Stevenson, *Humus chemistry: genesis, composition, reactions*. John Wiley & Sons, 1994.

[255] A. R. Hoch, M. M. Reddy, and G. R. Aiken, "Calcite crystal growth inhibition by humic substances with emphasis on hydrophobic acids from the Florida Everglades," *Geochim. Cosmochim. Acta,* vol. 64, no. 1, pp. 61-72, 2000/01/01/ 2000. doi: https://doi.org/10.1016/S0016-7037(99)00179-9.

[256] L. Fan, J. L. Harris, F. A. Roddick, and N. A. Booker, "Influence of the characteristics of natural organic matter on the fouling of microfiltration membranes," *Water Res.,* vol. 35, no. 18, pp. 4455-4463, 2001/12/01/ 2001. doi: https://doi.org/10.1016/S0043-1354(01)00183-X.

[257] D. Shen, D. Shcolnik, W. H. Steiner, D. G. Horstmann, G. N. Taylor, and M. Brown, "Evaluation of Scale Inhibitors in Marcellus Waters Containing High Levels of Dissolved Iron," in *SPE International Symposium on Oilfield Chemistry*, 2011: Society of Petroleum Engineers.

[258] S. Benslimane, H. Perrot, R. Bennezar, and K.-E. Bouhidel, "Thermodynamic study of Zn2+ inhibition properties and mechanism on calcium carbonate precipitation by chemical and electrochemical methods," *Desalination,* vol. 398, pp. 114-120, 2016.

[259] C. M. Fellows and A. Al-Hamzah, "Thermal Desalination: Current Challenges," in *Mineral Scales and Deposits*: Elsevier, 2015, pp. 583-602.

[260] A. P. Watkinson, "Water quality effects on fouling from hard waters," in *ICHMT DIGITAL LIBRARY ONLINE*, 1983: Begel House Inc.

[261] R. W. Morse and J. G. Knudsen, "Effect of alkalinity on the scaling of simulated cooling tower water," *The Canadian Journal of Chemical Engineering,* vol. 55, no. 3, pp. 272-278, 1977.

[262] R. L. Webb and W. Li, "Fouling in enhanced tubes using cooling tower water: Part I: long-term fouling data," *Int. J. Heat Mass Transfer,* vol. 43, no. 19, pp. 3567-3578, 2000.

[263] M. M. Reddy, L. N. Plummer, and E. Busenberg, "Crystal growth of calcite from calcium bicarbonate solutions at constant PCO2 and 25 C: a test of a calcite dissolution model," *Geochim. Cosmochim. Acta,* vol. 45, no. 8, pp. 1281-1289, 1981.

[264] W. Augustin and M. Bohnet, "Influence of the ratio of free hydrogen ions on crystallization fouling," *Chemical Engineering and Processing: Process Intensification,* vol. 34, no. 2, pp. 79-85, 1995.

[265] N. Andritsos and A. Karabelas, "The influence of particulates on CaCO3 scale formation," *J. Heat Transfer,* vol. 121, no. 1, pp. 225-227, 1999.

[266] C.-T. A. Chen, S.-L. Wang, W.-C. Chou, and D. D. Sheu, "Carbonate chemistry and projected future changes in pH and CaCO3 saturation state of the South China Sea," *Mar. Chem.,* vol. 101, no. 3-4, pp. 277-305, 2006.

[267] F. Albert, W. Augustin, and S. Scholl, "Roughness and constriction effects on heat transfer in crystallization fouling," *Chem. Eng. Sci.,* vol. 66, no. 3, pp. 499-509, 2011.

[268] M. Mayer, J. Bucko, W. Benzinger, R. Dittmeyer, W. Augustin, and S. Scholl, "Investigation and visualization of crystallization fouling in a micro heat exchanger," in *Proceedings of the 2nd European Conference on Microfluidics, Toulouse, France*, 2010.

[269] O. S. Sanni, "Calcium carbonate surface/bulk scaling mechanisms and kinetics in a once-through in-situ flow visualization rig," Ph.D. dissertation, Dept. MECH. ENG., University of Leeds, 2016.

[270] V. Erioni, "Kinetic study of calcium carbonate formation and inhibition by using an in-situ flow cell," *University of Leeds, Leeds, U.K.,* vol. Ph.D. Thesis, 2011.

[271] W. W. Frenier and M. Ziauddin, *Formation, removal, and inhibition of inorganic scale in the oilfield environment*. Society of Petroleum Engineers Richardson, TX, 2008.

[272] B. Bazin, N. Kohler, and A. Zaitoun, "Some insights into the tube-blocking-test method to evaluate the efficiency of mineral scale inhibitors," in *SPE Annual Technical Conference and Exhibition*, 2005: Society of Petroleum Engineers.

[273] J. Rinat, E. Korin, L. Soifer, and A. Bettelheim, "Electrocrystallization of calcium carbonate on carbon-based electrodes," *J. Electroanal. Chem.,* vol. 575, no. 2, pp. 195-202, 2005.

[274] A. Neville, T. Hodgkiess, and A. Morizot, "Electrochemical assessment of calcium carbonate deposition using a rotating disc electrode (RDE)," *J. Appl. Electrochem.,* vol. 29, no. 4, pp. 455-462, 1999.

[275] V. Tantayakom, T. Sreethawong, H. S. Fogler, F. De Moraes, and S. Chavadej, "Scale inhibition study by turbidity measurement," *J. Colloid Interface Sci.,* vol. 284, no. 1, pp. 57-65, 2005.

[276] R. Pawlowicz, "Calculating the conductivity of natural waters," *Limnology and Oceanography: Methods,* vol. 6, no. 9, pp. 489-501, 2008.

[277] J. Willis, "Determination of calcium and magnesium in urine by atomic absorption spectroscopy," *Anal. Chem.,* vol. 33, no. 4, pp. 556-559, 1961.

[278] C. W. Turner and D. W. Smith, "Calcium carbonate scaling kinetics determined from radiotracer experiments with calcium-47," *Industrial & engineering chemistry research,* vol. 37, no. 2, pp. 439-448, 1998.

[279] N. Andritsos, A. Karabelas, and P. Koutsoukos, "Morphology and structure of CaCO3 scale layers formed under isothermal flow conditions," *Langmuir,* vol. 13, no. 10, pp. 2873-2879, 1997.

[280] W. Sun, G. Liu, L. Wang, and Y. Li, "A mathematical model for modeling the formation of calcareous deposits on cathodically protected steel in seawater," *Electrochim. Acta,* vol. 78, pp. 597-608, 2012.

[281] M. Kawano and M. Miyashita, "Influence of glucuronic acid and galacturonic acid on the precipitation rate and polymorphism of calcium carbonate minerals in solutions with Mg2+ ions," *Clay Science,* vol. 22, no. 1, pp. 19-27, 2018.

[282] R. E. Anderson and A. R. Barron, "Effect of carbon nanomaterials on calcium carbonate crystallization," *Main Group Chem.,* vol. 4, no. 4, pp. 279-289, 2005.

[283] L. Wang and M. Liu, "Pool boiling fouling and corrosion properties on liquid-phase-deposition TiO2 coatings with copper substrate," *AlChE J.,* vol. 57, no. 7, pp. 1710-1718, 2011.

[284] S. M. Peyghambarzadeh, A. Vatani, and M. Jamialahmadi, "Application of asymptotic model for the prediction of fouling rate of calcium sulfate under subcooled flow boiling," *Appl. Therm. Eng.,* vol. 39, pp. 105-113, 2012/06/01/ 2012. doi: https://doi.org/10.1016/j.applthermaleng.2011.12.042.

[285] S. Wang, Z. Xu, and J. Wang, "Fouling characteristics of MgO particles under subcooled flow boiling," *Journal of Mechanical Science and Technology,* vol. 33, no. 3, pp. 1399-1407, 2019/03/01 2019. doi: 10.1007/s12206-019-0241-1.

[286] B. Zohuri and N. Fathi, "Convective Boiling," in *Thermal-Hydraulic Analysis of Nuclear Reactors*, B. Zohuri and N. Fathi, Eds. Cham: Springer International Publishing, 2015, pp. 375-412.

[287] O. Sanni, T. Charpentier, N. Kapur, and A. Neville, "Study of surface deposition and bulk scaling kinetics in oilfield conditions using an in-situ flow rig," in *NACE-International Corrosion Conference Series*, 2015, vol. 2015, no. 5916: Leeds.

[288] O. Bukuaghangin, "The kinetics of barium sulphate scale formation and inhibition in the bulk solution and on surfaces," University of Leeds, 2017.

[289] V. Eroini, "Kinetic study of calcium carbonate formation and inhibition by using an in-situ flow cell," Ph.D. dissertation, Dept. MECH. ENG., University of Leeds, 2011.

[290] S. M. Peyghambarzadeh, A. Vatani, and M. Jamialahmadi, "Influences of bubble formation on different types of heat exchanger fouling," *Appl. Therm. Eng.,* vol. 50, no. 1, pp. 848-856, 2013/01/10/ 2013. doi: https://doi.org/10.1016/j.applthermaleng.2012.07.015.

[291] M. Colombo and M. Fairweather, "Prediction of bubble departure in forced convection boiling: A mechanistic model," *Int. J. Heat Mass Transfer,* vol. 85, pp. 135-146, 2015/06/01/ 2015. doi: https://doi.org/10.1016/j.ijheatmasstransfer.2015.01.103.

[292] O. L. I. Brown, "The Clausius-Clapeyron equation," *J. Chem. Educ.,* vol. 28, no. 8, p. 428, 1951/08/01 1951. doi: 10.1021/ed028p428.

[293] P. De Moel, A. Van der Helm, M. Van Rijn, J. Van Dijk, and W. Van der Meer, "Assessment of calculation methods for calcium carbonate saturation in drinking water for DIN 38404-10 compliance," *Drinking Water Engineering & Science Discussions,* vol. 6, no. 2, 2013.

[294] F. J. Millero, D. Pierrot, K. Lee, R. Wanninkhof, R. Feely, C. L. Sabine, R. M. Key, and T. Takahashi, "Dissociation constants for carbonic acid determined from field measurements," *Deep Sea Research Part I: Oceanographic Research Papers,* vol. 49, no. 10, pp. 1705-1723, 2002.

[295] P. Undesser, "Softened Water Benefits Study (Energy and Detergent Savings)," in "Water Conditioning & Purification," Water Quality Research Foundation - Water Quality Association, Lisle, IL, USA,2011.

[296] K. E. Gubbins, "Thermodynamics. By K. S. Pitzer, 3rd ed., McGraw-Hill, New York, 1995, xvi+626 pp," *AlChE J.,* vol. 43, no. 1, pp. 285-285, 1997. doi: 10.1002/aic.690430137.

[297] R. G. Compton and C. A. Brown, "The inhibition of calcite dissolution/precipitation: Mg2+ cations," *J. Colloid Interface Sci.,* vol. 165, no. 2, pp. 445-449, Jul. 1994. doi: https://doi.org/10.1006/jcis.1994.1248.

[298] F. C. Meldrum and S. T. Hyde, "Morphological influence of magnesium and organic additives on the precipitation of calcite," *J. Cryst. Growth,* vol. 231, no. 4, pp. 544-558, Oct. 2001. doi: https://doi.org/10.1016/S0022-0248(01)01519-6.

[299] A. Fernandez-Martinez, H. Lopez-Martinez, and D. Wang, "Structural characteristics and the occurrence of polyamorphism in amorphous calcium carbonate," in *New Perspectives on Mineral Nucleation and Growth*, A. E. S. V. Driessche, M. Kellermeier, L. G. Benning, and D. Gebauer, Eds.: Springer, Cham, 2017, pp. pp. 77-92.

[300] J. Lédion, C. Braham, and F. Hui, "Anti-scaling properties of copper," *J. Water Supply Res. T.,* vol. 51, no. 7, pp. 389-398, Nov. 2002. doi: https://doi.org/10.2166/aqua.2002.0035.

[301] J. W. Mullin, "8.4.6.2 Reaction Crystallization," in *Crystallization (4th Edition)*: Elsevier.

[302] W. H. Organization, "Nutrients in drinking water," World Health Organization7117242299, 2005.

[303] A. Azoulay, P. Garzon, and M. J. Eisenberg, "Comparison of the mineral content of tap water and bottled waters," *Journal of general internal medicine,* vol. 16, no. 3, pp. 168-175, 2001.

[304] S. Raharjo, S. Muryanto, J. Jamari, and A. Bayuseno, "Controlling of magnesium carbonate scale deposition on the piping system with laminar flow and in the presence of alumina," in *AIP Conference Proceedings*, 2018, vol. 1977, no. 1, p. 020064: AIP Publishing.

[305] S. Ghizellaoui, M. Euvrard, J. Ledion, and A. Chibani, "Inhibition of scaling in the presence of copper and zinc by various chemical processes," *Desalination,* vol. 206, no. 1-3, pp. 185-197, 2007.

[306] B. Pernot, M. Euvrard, F. Remy, and P. Simon, "Influence of Zn (II) on the crystallisation of calcium carbonate application to scaling mechanisms," *Aqua- Journal of Water Services Research and Technology,* vol. 48, no. 1, pp. 16-23, 1999.

[307] S. Ghizellaoui and M. Euvrard, "Assessing the effect of zinc on the crystallization of calcium carbonate," *Desalination,* vol. 220, no. 1-3, pp. 394-402, 2008.

[308] W. Stumm and J. J. Morgan, *Aquatic chemistry: chemical equilibria and rates in natural waters*. John Wiley & Sons, 2012.

[309] L. Wenjun, F. Hui, J. Lédion, and W. Xingwu, "Anti-scaling properties of zinc ion and copper ion in the recycling water," *Ionics,* vol. 15, no. 3, pp. 337-343, 2009.

[310] knovel, "Physical Constants of Inorganic Compounds," ed, 2020.

[311] F. J. M. Prieto and F. J. Millero, "The values of pK1+ pK2 for the dissociation of carbonic acid in seawater," *Geochim. Cosmochim. Acta,* vol. 66, no. 14, pp. 2529-2540, 2002.

[312] F. J. Millero and R. N. Roy, "A chemical equilibrium model for the carbonate system in natural waters," *Croat. Chem. Acta,* vol. 70, no. 1, pp. 1-38, 1997.

[313] N. Boulay and M. Edwards, "Role of temperature, chlorine, and organic matter in copper corrosion by-product release in soft water," *Water Res.,* vol. 35, no. 3, pp. 683-690, Feb. 2001. doi: https://doi.org/10.1016/S0043-1354(00)00320-1.

[314] D. J. Kukulka and M. Devgun, "Fluid temperature and velocity effect on fouling," *Appl. Therm. Eng.,* vol. 27, no. 16, pp. 2732-2744, Nov 2007. doi: https://doi.org/10.1016/j.applthermaleng.2007.03.024.

[315] S. N. Kazi, G. G. Duffy, and X. D. Chen, "Mineral scale formation and mitigation on metals and a polymeric heat exchanger surface," *Appl. Therm. Eng.,* vol. 30, no. 14, pp. 2236-2242, Oct. 2010. doi: https://doi.org/10.1016/j.applthermaleng.2010.06.005.

[316] W. C. Wake, *Developments in adhesives*. Applied Science Publishers, 1977.

[317] N. DeLollis, "Handbook of Adhesive Bonding," *New York Mc-G rawHill,* 1973.

[318] D. H. Kaelble, *Physical chemistry of adhesion*. Wiley-Interscience, 1971.

[319] S. Najibi, H. Mü ller-Steinhagen, and M. Jamialahmadi, "Calcium carbonate scale formation during subcooled flow boiling," 1997.

[320] P. A. Schweitzer, *Corrosion Engineering Handbook, -3 Volume Set*. CRC Press, 1996.

[321] N. Birbilis and B. Hinton, "19 - Corrosion and corrosion protection of aluminium," in *Fundamentals of Aluminium Metallurgy*, R. Lumley, Ed.: Woodhead Publishing, 2011, pp. 574-604.

[322] J. M. Bryan, "The action of boiling distilled water on aluminium," *Journal of the Society of Chemical Industry,* vol. 69, no. 6, pp. 169-173, Jun. 1950. doi: https://doi.org/10.1002/jctb.5000690603.

[323] L. P. H. Jeurgens, W. G. Sloof, F. D. Tichelaar, and E. J. Mittemeijer, "Structure and morphology of aluminium-oxide films formed by thermal oxidation of aluminium," *Thin Solid Films,* vol. 418, no. 2, pp. 89-101, 2002/10/15/ 2002. doi: https://doi.org/10.1016/S0040-6090(02)00787-3.

[324] J. Gonzalez, V. Lopez, A. Bautista, E. Otero, and X. Nóvoa, "Characterization of porous aluminium oxide films from ac impedance measurements," *J. Appl. Electrochem.,* vol. 29, no. 2, pp. 229-238, Feb. 1999. doi: https://doi.org/10.1023/A:1003481418291.

[325] P. J. Anthony and A. C. Anderson, "The Thermal Conductivity of β-Alumina," in *Superionic Conductors*, G. D. Mahan and W. L. Roth, Eds. Boston, MA: Springer US, 1976, pp. 371-372.

[326] L. P. H. Jeurgens, W. G. Sloof, F. D. Tichelaar, and E. J. Mittemeijer, "Growth kinetics and mechanisms of aluminum-oxide films formed by thermal oxidation of aluminum," *J. Appl. Phys.,* vol. 92, no. 3, pp. 1649-1656, Jul. 2002. doi: https://doi.org/10.1063/1.1491591.

[327] S. B. Subramanyam, G. Azimi, and K. K. Varanasi, "Designing Lubricant-Impregnated Textured Surfaces to Resist Scale Formation," *Advanced Materials Interfaces,* vol. 1, no. 2, p. 1300068, Jan. 2014. doi: https://doi.org/10.1002/admi.201300068.

[328] S. Dash, L. Rapoport, and K. K. Varanasi, "Crystallization-Induced Fouling during Boiling: Formation Mechanisms to Mitigation Approaches," *Langmuir,* vol. 34, no. 3, pp. 782-788, Oct. 2017. doi: https://doi.org/10.1021/acs.langmuir.7b02936.

[329] M. R. Malayeri, H. Müller-Steinhagen, and T. H. Bartlett, "Fouling of tube bundles under pool boiling conditions," *Chemical Engineering Science,* vol. 60, no. 6, pp. 1503-1513, 2005/03/01/ 2005. doi: https://doi.org/10.1016/j.ces.2004.10.017.

[330] E. M. Ishiyama, F. Coletti, S. Macchietto, W. Paterson, and D. Wilson, "Impact of deposit ageing on thermal fouling: lumped parameter model," *AlChE J.,* vol. 56, no. 2, pp. 531-545, 2010.

[331] N. Raza, Z. I. Zafar, H. Najam ul, and R. V. Kumar, "Leaching of natural magnesite ore in succinic acid solutions," *Int. J. Miner. Process.,* vol. 139, pp. 25-30, 2015/06/10/ 2015. doi: https://doi.org/10.1016/j.minpro.2015.04.008.

[332] E. Abouali, O. Jean, and J. Lédion, "Influence du cuivre et du zinc sur le pouvoir entartrant de l'eau," *Journal européen d'hydrologie,* vol. 27, no. 2, pp. 109-126, 1996.

[333] H. J. Meyer, "The influence of impurities on the growth rate of calcite," *J. Cryst. Growth,* vol. 66, no. 3, pp. 639-646, 1984/05/01/ 1984. doi: https://doi.org/10.1016/0022-0248(84)90164-7.

[334] R. Sabzi and R. Arefinia, "Investigation of zinc as a scale and corrosion inhibitor of carbon steel in artificial seawater," *Corros. Sci.,* vol. 153, pp. 292-300, 2019/06/01/ 2019. doi: https://doi.org/10.1016/j.corsci.2019.03.045.